Event-by-Event Identified Particle Ratio Fluctuations in Pb–Pb Collisions with ALICE

Dissertation
zur Erlangung des Doktorgrades der Naturwissenschaften

vorgelegt beim Fachbereich Physik
der Johann Wolfgang Goethe-Universität
in Frankfurt am Main

von
Mesut Arslandok
aus Kayseri, Türkei

Frankfurt am Main (2017)
(D 30)

Vom Fachbereich Physik der Johann Wolfgang Goethe-Universität Frankfurt als Dissertation angenommen.

Dekan:	Prof. Dr. Owe Philipsen
Gutachter	Prof. Dr. Harald Appelshäuser
	Prof. Dr. Christoph Blume

Datum der Disputation:

Abstract

ALICE is the dedicated heavy-ion experiment among the experiments at the Large Hadron Collider (LHC) at CERN. It is, in particular, designed to exploit the physics of strongly interacting matter. The theory of strong interactions, Quantum Chromodynamics (QCD), predicts that at sufficiently high energy densities nuclear matter transforms into a deconfined state of quarks and gluons. One of the possible signatures of a transition between hadronic and partonic phases is the enhancement of fluctuations of the number of particles in the hadronic final state of relativistic heavy-ion collisions.

The observable ν_{dyn}, which is defined in terms of the moments of particle multiplicity distributions, is used to quantify the magnitude of the dynamical fluctuations in event-by-event measurements of particle ratios: K/π, p/π and K/p. It reflects deviations of the particle number distributions from those of a statistical distribution and also provides insight into the correlation between particle pairs. The ν_{dyn} fluctuation measure was previously studied at the Super Proton Synchrotron (SPS) and at the Relativistic Heavy-Ion Collider (RHIC) in Pb–Pb and Au–Au collisions, respectively. The ALICE detector is ideally suited to extend these measurements to higher collision energies. In particular, the excellent charged-particle tracking and particle identification (PID) capabilities in the central barrel of the detector allow for a precise and differential event-by-event analysis at mid-rapidity and low transverse momentum.

The standard approach of finding the moments is to count the number of particles event by event. However, this approach introduces difficulties such as incomplete particle identification due to overlapping energy loss ($\mathrm{d}E/\mathrm{d}x$) distribution functions in the Time Projection Chamber (TPC), which can be taken care of by either selecting suitable phase-space regions or by using additional detector information. These procedures reduce overall phase-space coverage and detection efficiencies. The present study is based on a novel experimental technique, the so-called Identity Method, which overcomes such limitations. The method follows a probabilistic approach using the inclusive $\mathrm{d}E/\mathrm{d}x$ distributions measured in the TPC, and determines the moments of the multiplicity distributions by an unfolding procedure. Therefore, understanding and calibration of the $\mathrm{d}E/\mathrm{d}x$ measurements in the TPC plays a significant role in the study of the ν_{dyn} observable.

The $\mathrm{d}E/\mathrm{d}x$ in the TPC is derived from the pulse height distributions of charged-particle tracks traversing the TPC. The so-called "Ion-tail" and "Common-mode" effects produce a significant deterioration in the measurement of $\mathrm{d}E/\mathrm{d}x$, and thus the PID performance of the TPC. Therefore, these effects need to be understood and corrected. The correction of this problem requires a good understanding of the TPC signal shape. To study this, the so-called "black events" with a non-zero-suppressed baseline from the TPC laser calibration system is used. The characteristic signal shape is then crosschecked with three-dimensional Garfield simulations for the first time. Following the signal shape analysis an offline correction procedure is developed, where a significant improvement in the $\mathrm{d}E/\mathrm{d}x$ resolution and thus the PID quality of the TPC is achieved. Moreover, these effects are implemented in the current simulation framework of the ALICE detector.

The Identity Method employs fits to inclusive $\mathrm{d}E/\mathrm{d}x$ distributions as an input for the calculation of the moments of particle multiplicity distributions. Therefore, a good understanding of the detector response of the TPC is required. For this, clean particle samples, which are retrieved from the decays with displaced vertices (pions from K^0_S decays, protons from Λ decays and electrons from photon conversions), are used. Additionally, for a better description of the detector response, a generalised Gauss function is chosen as fit function. It is the first time the TPC detector response is described with a generalised Gauss function. Based on the detector response functions obtained, an elaborate fitting procedure is developed to parametrize the TPC PID.

The Identity Method is successfully applied to ALICE data. The first results on the identified-particle-ratio fluctuations in Pb–Pb collisions at $\sqrt{s_{\mathrm{NN}}} = 2.76$ TeV as a function of centrality and pseudorapidity, as well as a comparison to calculations with the HIJING and AMPT event generators are presented. The results for p/π changes sign from positive to negative towards more peripheral collisions which indicates an increasing correlation between protons and pions. This behavior is not reproduced by the HIJING and AMPT models. On the other hand, for the most central collisions a change of sign for p/π and K/p observed compared to the measurements at lower energies from CERN-SPS and BNL-RHIC. A more detailed analysis of fluctuations with charge and species specific pairs is required to fully characterize the particle production dynamics in Pb–Pb collisions and understand, in particular, the origin of the sign changes reported in this thesis.

Zusammenfassung

Das gegenwärtige Verständnis der Elementarteilchen und ihrer Wechselwirkungen wird im sogenannten Standardtmodell der Elementarteilchenphysik zusammengefasst. Es beschreibt drei der vier bekannten fundamentalen Kräfte im Universum: die elektromagnetische, die schwache und die starke Wechselwirkung. Die starke Wechselwirkung ist für die Bindung von Quarks in Neutronen und Protonen verantwortlich. Die Quantenchromodynamik (QCD) ist die Theorie der starken Wechselwirkung und beschreibt die Wechselwirkungen zwischen Quarks und Gluonen. Sie teilt Hadronen in zwei Gruppen ein: die Baryonen und die Mesonen. Mesonen bestehen aus einem Quark und einem Antiquark ($q\bar{q}$) während Baryonen aus drei Quarks (qqq) oder ($\bar{q}\bar{q}\bar{q}$) bestehen. Die Quarks unterliegen der Fermi-Dirac Statistik. Um zu vermeiden, dass einige Baryonen aus drei identischen Quarks bestehen und damit das Pauli Prinzip verletzt würde, wurde eine zusätzliche Quantenzahl, die Farbladung, eingeführt. Die starke Wechselwirkung zwischen Quarks wird durch Gluonen vermittelt. Im Unterschied zu der elektromagnetischen Wechselwirkung, bei der das Photon keine elektrische Ladung trägt, tragen die Gluonen eine Farbladung. Daraus folgt, dass die Gluonen nicht nur mit den Quarks wechselwirken, sondern auch mit den Farbladungen anderer Gluonen. Daraus ergeben sich die speziellen Eigenschaften der starken Wechselwirkung "confinement" und asymptotische Freiheit (siehe Kapitel 1).

Die Gittereichtheorie (Gitter-QCD) ist eine Methode um Gleichgewichtseigenschaften stark wechselwirkender Systeme direkt aus der QCD Lagrangefunktion zu berechnen und sagt voraus, dass bei hinreichend hohen Energiedichten ein Übergang von hadronischer Materie zu einem Plasma ungebundener Quarks und Gluonen auftritt. Dies ist das sogenannte Quark-Gluon-Plasma (QGP). Im Rahmen des Standardmodells ist das Auftreten von Phasenbergängen, die elementare Quantenfelder betreffen, eng mit dem Brechen von fundamentalen Symmetrien der Natur und damit dem Ursprung der Masse verbunden. Bei hohen Temperaturen und verschwindendem baryo-chemischem Potential werden qualitative Eigenschaften des Überganges zum QCP von der chiralen Symmetrie der QCD Lagrangefunktion beeinflusst. Im Grenzfall von verschwindenden Quark Massen ist die QCD Lagrangefunktion chiral symmetrisch, d.h. invariant gegen getrennte flavor Drehungen von rechts oder links-händigen Quarks. Bei endlichen Quark Massen geht der Phasenübergang zweiter Ordnung in einen "crossover" von einem eingeschlossenen (confined) zu einem freien (deconfined) Zustand über, bei dem sich die Physik dramatisch aber kontinuierlich ändert und keine Korrelationslänge divergiert. Gitterrechnungen legen nahe, dass dieser "crossover" ziemlich abrupt in einem schmalen Temperaturintervall um $T_c \sim 154 \pm 9$ MeV stattfindet. Bei T_c treten zwei Effekte auf: der Farbeinschluss wird gebrochen, d.h. Farbfreiheitsgrade können über größere Entfernungen als der Radius von Hadronen propagieren, und die ungefähre chirale Symmetrie der QCD, die bei niedrigen Temperaturen und Dichten spontan gebrochen ist, wird wiederhergestellt.

In ultrarelativistischen Schwerionenreaktionen erwartet man hohe Energiedichten zu erreichen, die es ermöglichen den QCD Phasen-Übergang und die Physik des QGP Zustands zu untersuchen. Das in einer Schwerionenreaktion erzeugte System geht in einer schnellen dynamischen Evolution von den extremen Anfangsbedingungen in den verdünnten hadronischen Endzustand über. "Event-by-event" Fluktuationen von glob-

alen Observablen, wie mittlerer transversaler Impuls, Verhältnis identifizierter Teilchen und erhaltener Größen (Netto Ladung, Netto Baryonenzahl, Netto Seltsamkeit) im hadronischen Endzustand werden benutzt, um die Dynamik des Phasenübergangs zu untersuchen und das QCD Phasendiagramm abzutasten. Mit zunehmender Energie reicht die Phasentrennline von verschwindender Temperatur und hohem baryochemischen Potential zu endlicher Temperatur und kleinem baryochemischem Potential, wo die erste-Ordnung Phasen-Übergangslinie den sogenannten "kritischen Punkt" trifft. Dies ist eine spezielle thermodynamische Singularität, bei der die Suszeptibilitäten divergieren und der Ordnungsparameter bei großen Wellenlängen fluktuiert. Es wird erwartet, dass die entsprechenden Signaturen ein nicht-monotones Verhalten als Funktion der Kollisionsenergie, Zentralität, Rapidität oder Systemgröße zeigen. Das Feld der "event-by-event" Fluktuationen spielt also eine wichtige Rolle innerhalb des "Energie Scan Programms" der NA49/NA61 Kollaboration am CERN SPS und der STAR Kollaboration am RHIC beim Studium des QCD Phasenübergangs und insbesondere bei der Lokalisierung des kritischen Punkts.

"Event-by-event" Fluktuationen verschiedener Observablen wie z.B. mittleres p_{T}, (Netto) Ladung, Baryonenzahl, Seltsamkeit, Multiplizität usw. werden gegenwärtig sowohl experimentell als auch theoretisch untersucht. Diese Observable werden auf einer "event-by-event" Basis gemessen und im Rahmen der statistischen Physik mit Varianzen, Kovarianzen oder höheren Momenten charakterisiert. Diese Momente werden dann verglichen mit Erwartungen basierend auf thermischen Gleichgewichtsmodellen oder anderen statistischen Modellen. Auftretende Unterschiede können neuartigen dynamischen Effekten wie z.B. Variationen des Impact Parameters, "Baryonen Stopping", Fluktuationen der anfänglichen Energiedichte usw. zugeschrieben werden. Momente (oder Kumulanten) höher als zweiter Ordnung sind empfindlicher auf die zugrunde liegende Physik aber benötigen erhebliche Statistik. Man kann jedoch Observable unter Benutzung der Momente der Multiplizitätsverteilungen von Teilchen bis zur zweiten Ordnung konstruieren, um jegliches nicht-monotone Verhalten als Funktion der Energie oder des Systemvolumens zu erfassen.

Die Observable $\nu_{\mathrm{dyn}}[A, B]$, die in Einheiten der ersten und zweiten Momente der Multiplizitätsverteilungen der Teichen A und B definiert ist, wird zur Quantifizierung der dynamischen Fluktuationen der Teilchenverhältnisse benutzt und um Einblicke in die Korrelation von Teilchenpaaren, die mit dem Ladungsvorzeichen assoziiert sind, zu erhalten. Sie setzt die relative Stärke der Fluktuationen der Teilchensorte A und B zu der relativen Stärke der Korrelation zwischen diesen Teilchensorten. Sie verschwindet für statistisch unabhängige Produktion. Der Vorteil von ν_{dyn} ist die Robustheit gegen nicht-dynamische Beiträge, wie solche von Fluktuationen der Partizipantenzahl und endlichen Nachweiseffizienzen. Die ν_{dyn} Observable der netto-Ladungsfluktuationen wurde bereits von ALICE publiziert. Für identifizierte Teilchen wurde sie am Super-Proton-Synchrotron (SPS) und am Relativistic-Heavy-Ion-Collider (RHIC) in Pb–Pb und Au–Au Kollisionen gemessen. Der ALICE Detektor am LHC ist ideal dafür geeignet diese Messungen zu höheren Energien zu erweitern. Insbesondere die hervorragende Spurverfolgung und Teilchenidentifikation des Zentraldetektors erlauben eine genaue und differentielle "event-by-event" Analyse bei Midrapidität und kleinen Transversalimpulsen (p_{T}).

ALICE ist ein universell verwendbarer Detektor, jedoch insbesondere für die Un-

tersuchung von Schwerionenkollisionen geeignet. Er besteht aus verschiedenen Detektorkomponenten, aufgeteilt in das zentrale sowie das vorwärts/rückwärts Detektorsystem. Hauptdetektoren für die Spurverfolgung und Teilchenidentifikation im zentralen Detektorsystem sind das Innere Tracking System (ITS) und die Spurendriftkammer (Time Projection Chamber (TPC), die sich in einem großen Solenoiden (B = 0.5 T) befinden. Das ITS-TPC Spurverfolgungssystem deckt den mittleren Rapiditätsbereich ab und liefert Trajektorien und Impulsrekonstruktionen bis zu $p_{\mathrm{T}} = 100$ MeV/c. Der ITS erlaubt die Rekonstruktion des primären Vertex mit hoher Genauigkeit und verwirft sekundäre Vertices. Der relativistische Wiederanstieg des Energieverlustsignals der TPC wird für die Teilchenidentifikation in einem weiten Impulsbereich bis zu mehreren GeV/c durch die Messung des spezifischen Energieverlustes $\mathrm{d}E/\mathrm{d}x$ benutzt. Zwei Vorwärts-Szintillatorteleskope (V0) auf beiden Seite des Interaktionspunktes decken den Rapiditätsbereich $2.8 < \eta < 5.1$ und $-3.7 < \eta < -1.7$ ab. Die V0 Detektoren zusammen mit zwei Null-Grad Kalorimetern (ZDC) werden zum Triggern und zur Ereignisauswahl benutzt. Die Definition der Zentralität einer Kollision basiert auf der Amplitudenmessung in den V0 Detektoren und wird mithilfe einer Monte Carlo Simulation, basierend auf dem Glauber Modell, in Beziehung zur Geometrie der Kollision und zur Zahl der an der Kollision teilnehmenden Nukleonen gesetzt.

Der übliche Ansatz für das Finden der Momente ist das Zählen von Teilchen auf einer "event-by-event" Basis. Doch dieser Ansatz zeigt Unzulänglichkeiten, wie z.B. fehlerhafte Teilchenidentifikation durch überlappende Verteilungen des Energieverlusts ($\mathrm{d}E/\mathrm{d}x$) in der Zeitprojektionskammer (TPC), die entweder durch die Auswahl von geeigneten Phasenraumbereichen oder durch zusätzliche Detektorinformationen gelöst werden können. Diese Prozedur reduziert aber den erfassten Phasenraum und die Detektionseffizienzen. Die vorgestellte Arbeit basiert auf einer neuen experimentellen Methode, der sogenannten Identitätsmethode, welche die vorher genannten Unzulänglichkeiten beseitigt. Sie basiert auf einem Wahrscheinlichkeitsansatz in dem inklusive TPC $\mathrm{d}E/\mathrm{d}x$ Verteilungen gemessen und die Momente der Multiplizitätsverteilungen durch eine Entfaltungsprozedur extrahiert werden. Aus diesem Grund spielt das Verständnis und die Kalibration von Energieverlustsmessungen in der TPC eine wichtige Rolle bei der Untersuchung der Observable ν_{dyn}.

Die TPC ist der Hauptdetektor für Spurrekonstrunktion und Teilchenidentifikation in ALICE. Sie wurde entwickelt für Multiplizitäten von bis zu 20000 primären und sekundären geladene Teilchen, die in einer zentralen Pb–Pb Kollision erzeugt werden können. Ein geladenes Teilchen, das das Gas der TPC durchquert, hinterlässt eine Ionisationsspur entlang der Teilchentrajektorie. Die TPC erzeugt ein 3D Bild dieser Ionisation innerhalb des Detektors. Der Teilchenimpuls, der aus der Krümmung der Teilchentrajektorie berechnet werden kann, und der mittlere Energieverlust pro Spurlänge $\langle \mathrm{d}E/\mathrm{d}x \rangle$ erlauben es, die Teilchensorte zu bestimmen. Eine Einführung in das ALICE Experiment und die Details des TPC Detektors, insbesondere auch der $\mathrm{d}E/\mathrm{d}x$ Rekonstruktion und der Kalibration wird in Kapitel 2 gegeben.

Der Energieverlust in der TPC wird errechnet aus der Pulshöhenverteilung geladener Teilchen entlang der 159 Padreihen. Die Signale der "Multi-wire Proportional Chambers (MWPC)" zeigen nach dem eigentlichen Signal einen charakteristischen Unterschwinger, den sogenannten "Ion-tail", der durch die langen Ionendriftzeiten in der

MWPC-Verstärkungsregion verursacht wird. Eine zweite Beeinträchtigung ist der "Common-Mode" Effekt: die kapazitive Kopplung zwischen den Anodendrähten der MWPC und den Auslesepads induziert negative Signale auf den Pads eines gegebenen Anodendrahtsegments, die sich mit dem Signal überlagern. Diese zwei Effekte addieren sich auf und können signifikante Nulllinienverschiebungen und Fluktuationen erzeugen, die die $\mathrm{d}E/\mathrm{d}x$ Auflösung verschlechtern. Da die Effekte linear mit der lokalen Spurdichte ansteigen ist deren Einfluss bei den hohen Multiplizitäten in Pb–Pb Kollisionen besonders schwerwiegend. Die Korrektur dieser Effekte erfordert ein gutes Verständnis der TPC Signalform. Dazu werden sogenannte 'schwarze Events' mit einer nicht nullunterdrückten Nulllinie aus dem TPC Laserkalibrationssystem benutzt. Die charakteristische Signalform wird dann zum ersten Mal mit drei-dimensionalen Garfield Simulationen verglichen. Im Technischen Design Report (TDR) der TPC wurde angenommen, dass die derzeitige Front-End Elektronik ein Set von online Signalprozessalgorithmen haben wird, um die Nulllinienfluktuationen direkt auf dem hardwarelevel zu korrigieren. Diese Funktionalität war allerdings durch Softwareinstabilitäten nicht gegeben. Auf der Signalformanalyse basierend konnte aber eine offline Nulllinienkorrektur entwickelt werden, wodurch sich die Energieverlustsauflösung und damit Teilchenidentifikationsqualität signifikant verbessert haben. Darüber hinaus wurden die Korrekturen in das ALICE Simulationsframework implementiert. Kapitel 3 widmet sich der TPC Signalformuntersuchung, der offline Nulllinienkorrektur und der Implementierung des "Ion-tail" und des "Common-Mode" Effekts in das ALICE Simulationsframework.

Die Identitätsmethode verwendet Fits inklusiver $\mathrm{d}E/\mathrm{d}x$-Verteilungen als Eingangsgröße für die Berechnung der Momente von Teilchenmultiplizitäts-Verteilungen. Da die Überschneidungsregionen der $\mathrm{d}E/\mathrm{d}x$-Verteilungen verschiedener Teilchen ebenfalls genau berücksichtigt werden, ist eine sehr gute Beschreibung der inklusiven $\mathrm{d}E/\mathrm{d}x$ Spektren, und damit ein hervorragendes Verständnis des TPC Detektorverhaltens über den gesamten, für die Analyse der Fluktuationen des Verhältnisses identifizierter Teilchen abgedeckten kinematischen Bereich, möglich. Zu diesem Zweck werden die $\mathrm{d}E/\mathrm{d}x$-Verteilungen zuvor ausgewählter Stichproben aus Pionen, Protonen und Elektronen (identifiziert mittels der Rekonstruktion der V0 Topologie von K^0_S und Λ Zerfällen sowie Photonenkonversionen) mit einer verallgemeinerten Gaußfunktion gefittet. Zum ersten Mal wird hier das TPC Detektorverhalten mit fünf Parametern beschrieben. Die auf diese Art gewonnenen "Detector response-function" werden später für Fits der inklusiven $\mathrm{d}E/\mathrm{d}x$ Spektren verwendet. Um den Abhängigkeiten der $\mathrm{d}E/\mathrm{d}x$ Messung von Spurwinkel und Teilchenmultiplizität beizukommen, werden die Fits jeweils über eine Pseudorapiditätseinheit für jede Zentralitätsklasse durchgeführt. Des Weiteren wird die Breite der Impulsintervalle angemessen klein gewählt, um den Effekt der Impulsabhängigkeit von $\mathrm{d}E/\mathrm{d}x$ aufgrund der wachsenden Steigung der Spektren im Bereich niedriger Impulse zu minimieren. Beim Vergleich der durch die Identitätsmethode erhaltenen Teilchenspektren zu veröffentlichten Spektren wurde eine Übereinstimmung inneralb der systematischen Unsicherheiten festgestellt. Details der Fitprozedur werden in Kapitel 4 diskutiert.

Die in dieser Arbeit dargelegte Analyse basiert auf etwa 13 Millionen minimum-bias Pb–Pb Kollisionen bei Schwerpunktsenergien pro Nukleonenpaar von $\sqrt{s_{\mathrm{NN}}} = 2.76$ TeV, erfasst im Jahr 2010. Es werden geladene Teilchen über den vollen Azimuthalwinkel der TPC und einen Pseudorapiditätsbereich von $|\eta| < 0.8$ rekonstruiert. Des Weiteren wird der Impulsbereich auf $0.2 < p < 1.5$ GeV beschränkt, um die systematischen Unsicher-

heiten aufgrund sich überschneidender $\mathrm{d}E/\mathrm{d}x$-Verteilungen zu minimieren. Details der Datenanalyse wie Ereignis- und Spurauswahl, die Anwendung der Identitätsmethode auf ALICE Daten sowie die Fehlerabschätzung sind in Kapitel 5 dargelegt.Die Ergebnisse der ν_{dyn} Fluktuationsmessungen werden als Funktion der Kollisionszentralität dargestellt und mit Berechnungen der HIJING und AMPT Modelle verglichen. Ein wesentliches Merkmal des HIJING Modells ist die Behandlung von Nukleus-Nukleus Kollisionen als unabhängige Überlagerung von Nukleon-Nukleon Wechselwirkungen. Als solches berücksichtigt es keine Mechanismen für Wechselwirkungen der erzeugten Teilchen im Endzustand und daher treten Phänomene wie ein Gleichgewicht oder Kollektivität nicht auf. Die AMPT Berechnungen werden mit drei verschiedenen Szenarien durchgeführt, welche (i) Stringschmelze, (ii) hadronische Rückstreuung und (iii) hadronische Rückstreuung und Stringschmelze umfassen. Alle drei hier dargestellten Versionen des AMPT Modells verwenden harte Minijet Partonen und weiche Strings aus HIJING als Anfangsbedingungen. Aufgrund der intrinsischen Multiplizitätsabhängikeit von ν_{dyn} werden die ν_{dyn} Werte zusätzlich mit der Multiplizitätsdichte geladener Teilchen bei mittlerer Rapidität skaliert. Der Vollständigkeit halber wird ebenfalls die Skalierung bezüglich der Anzahl der mitwirkenden Teilchen, N_{part}, und der mittleren Multiplizität akzeptierter Teilchen untersucht.

Die $\nu_{\mathrm{dyn}}[\pi, \mathrm{K}]$ und $\nu_{\mathrm{dyn}}[\mathrm{K}, \mathrm{p}]$ Werte sind positiv für alle Zentralitäten. Dagegen ist $\nu_{\mathrm{dyn}}[\pi, \mathrm{p}]$ negativ für periphere Kollisionen und wechselt sein Vorzeichen bei mittlerer Zentralität. Dies deutet auf eine positive Korrelation zwischen Pionen und Protonen mit abnehmender Zentralität. Die dominierende Quelle korrelierter Pionen und Protonen sind baryonische Resonanzen. Die beobachtete Zentralitätsabhängigkeit der $\nu_{\mathrm{dyn}}[\mathrm{K}, \mathrm{p}]$ und $\nu_{\mathrm{dyn}}[\pi, \mathrm{p}]$ Verteilungen sind bezüglich ihrer Form ähnlich, d.h. flach von zentralen Kollisionen zu mittleren Zentralitäten mit einem systematischen Abfall zu peripheren Kollisionen. Im Gegensatz dazu ist $\nu_{\mathrm{dyn}}[\pi, \mathrm{K}]$ fast unabhängig von der Zentralität für periphere zu mittlerer Zentralität mit einem Anstieg zu zentralen Kollisionen. Ein ähnliches Verhalten wurde auch für $\nu_{\mathrm{dyn}}[\pi, \mathrm{K}]$ für ein Pseudorapiditätsintervall von $|\eta| < 1$ und einem Impulsintervall $0.2 < p < 0.6$ GeV/c in Au–Au Kollisionen bei einer Schwerpunktsenergie von $\sqrt{s_{\mathrm{NN}}} = 200$ GeV von der STAR Kollaboration beobachtet. Dies könnte auf eine zunehmende Antikorrelation zwischen Pionen und Kaonen oder auf verstärkte dynamische Fluktuationen für zentrale Kollisionen hindeuten. Um diese Beiträge zu unterscheiden, sind spezielle Studien mit unterschiedlichen Ladungs-Kombinationen notwendig, welche auch die Untersuchung von Beiträgen von Resonanzzerfällen und globaler Ladungserhaltung erlauben.

Die ν_{dyn} Ergebnisse für sehr zentrale Pb–Pb Kollisionen wurden mit den Ergebnissen bei niedrigeren Schwerpunktsenergien, CERN-SPS und BNL-RHIC, verglichen. Die ALICE Ergebnisse zeigen für alle Teilchen-Paarkombinationen positive Werte auf, was im Vergleich zu den Ergebnissen bei niedrigeren Energien auf einen Vorzeichenwechsel für $\nu_{\mathrm{dyn}}[\pi, \mathrm{K}]$ und $\nu_{\mathrm{dyn}}[\pi, \mathrm{K}]$ bei $\sqrt{s_{\mathrm{NN}}} = 2.76$ TeV hindeutet. Eine solche Änderung des Vorzeichens wurde von den Transportmodellen HSD und UrQMD für den RHIC Energiebereich vorhergesagt. Auch sagen die Modellrechnungen HIJING und AMPT einen Vorzeichenwechsel bei LHC Energien voraus, abgesehen von $\nu_{\mathrm{dyn}}[\pi, \mathrm{p}]$ in der AMPT-Simulation mit den Einstellungen hadronischer Streuung und ohne Stringschmelze. Die NA49 Kollaboration hat die starke Abhängigkeit von ν_{dyn} von der Phasenraumabdeckung untersucht, um die Diskrepanz zwischen der Messung von STAR und NA49 bei niedrigen Energien zu erklären. Entsprechend wurde auch die Abhängigkeit von ν_{dyn}

von der Akzeptanz für die ALICE Messung durch Variation der Phasenraumabdeckung untersucht. Eine Erhöhung des Pseudorapiditätsintervalles von bis zu $|\eta| < 1$ führt zu einer Reduktion von ν_{dyn} um 10-20%. Allerdings erklärt dies nicht den Unterschied, und vor allem nicht die Änderung des Vorzeichens mit steigender Schwerpunktsenergie. Zur Vollständigkeit wurden die Unterschiede zwischen den Ergebnissen von ALICE und STAR im Detail durch den Vergleich der Analysestrategien und der Detektoreigenschaften untersucht. Weiterführende Diskussionen der Physik sind in Kapitel 6 zu finden.

In Zukunft werden detaillierte Untersuchungen der Teilchenverhältnisfluktuationen, welche kleinere Kollisionssysteme, gleich- und unterschiedlich geladene Teilchenpaare und unterschiedliche Kollisionsenergien berücksichtigen, weitergehende Schlussfolgerungen erlauben und Verbindungen zu anderen Beobachtungsgrößen wie dem radialen Fluss, der Seltsamkeitsverstärkung, den Netto-Teilchenfluktuationen und Resonanzzerfälle ermöglichen.

Contents

1. Introduction

In the early decades of the twentieth century, particle-beam energies from accelerators reached only a few MeV, and their resolution was so poor that protons and neutrons could themselves be regarded as elementary and point-like. However, in the early 1970s deep-inelastic electron scattering experiments on protons indicated that nucleons (protons and neutrons) have an internal structure−they are built of quarks and gluons [1].

The current understanding of the elementary particles and their interactions is encapsulated in the so-called "Standard Model" of particle physics. It describes three of the four known fundamental forces in the universe (Table 1.1). According to this model, all matter is built from a small number of fundamental spin 1/2 particles, or fermions: six quarks and six leptons (Table 1.2). The different interactions are described in quantum language in terms of the exchange of characteristic bosons (particles of integer spin) between the fermion constituents. The force-carrying bosons: gluons, photons, and the W and Z have spin 1 since they go with vector fields, while the recently discovered Higgs boson [3, 4] corresponds to a scalar field and has spin 0. The Higgs boson is the visible manifestation of the so-called Higgs field which pervades the universe and explains how the particles gain mass.

Force	**Range**	**Strength**	**Mediator boson**	**Mass (GeV/c^2)**	**Spin**
Strong	$< 10^{-15}$ m	1	gluon	0	1
Electromagnetic	∞	10^{-2}	photon	0	1
Weak	$< 10^{-18}$ m	10^{-7}	$W^{\pm}$, Z^0	80, 90	1

Table 1.1.: A comparison of the range, relative strength, and some properties of mediators of the fundamental forces in the Standard Model [2].

The Standard Model also comprises the interactions of fundamental particles. Strong interactions are responsible for binding the quarks into the neutron and proton. Electromagnetic interactions occur between any two particles that have electric charge. Weak interactions are typified by the process of nuclear β-decay, involving the emission of an electron and neutrino by a radioactive nucleus [2]. In this sense, the electroweak theory (unified theory of weak and electromagnetic interactions) together with the Quantum Chromodynamics (QCD) form the Standard Model which is a relativistic quantum field theory based on the local gauge group SU(3) $\otimes$ SU(2) $\otimes$ U(1). i.e. the direct product of three simple groups. SU(3) is the gauge group or colour group describing the strong interactions and SU(2) $\otimes$ U(1) is the gauge group describing the electroweak interactions [5].

1.1. Strongly interacting matter and the Quark Gluon Plasma (QGP)

QCD describes the interactions of colored quarks and gluons. The quark model, based on symmetries and quantum numbers, was introduced by M. Gell-Mann and G. Zweig

[6]. It categorizes hadrons (color-singlet bound states of quarks and antiquarks) into two groups; the baryons and mesons. Mesons are composed of a quark and an anti-quark ($q\bar{q}$) while baryons consist of three quarks (qqq) or ($\bar{q}\bar{q}\bar{q}$). The quarks obey the Fermi-Dirac statistics. Since some of the baryons consist of three identical quarks, an additional quantum number was introduced, called color, in order to preserve the Pauli principle. There are three different colors a quark can carry: red, green, and blue. In SU(3) hadronic wave functions are color-neutral states and can be constructed either from anti-color+color (mesons) or three different colors (baryons). The strong interaction between the quarks is mediated by eight massless gauge bosons called gluons. The fundamental difference from the electromagnetic interaction, where the photon itself carries no electrical charge, is that gluons themselves carry color charges. It follows that gluons do not interact only with quarks but also couple to the color charges of other gluons, which is the reason for many special properties of the strong interaction.

The demand for color neutrality also means that free quarks can not be observed. To

	1^{st} Generation		**2^{nd} Generation**		**3^{rd} Generation**	
Quarks	**up (u)**	**down (d)**	**strange (s)**	**charm (c)**	**bottom (b)**	**top (t)**
Mass (GeV/c^2)	0.0018−0.003	0.0045−0.0053	0.09−0.1	1.275±0.025	4.18±0.03	173.21±0.51±0.71
Charge (e)	+2/3	−1/3	−1/3	+2/3	−1/3	+2/3
Weak Isospin	+1/2	−1/2	−1/2	+1/2	−1/2	+1/2
I_3	+1/2	−1/2	0	0	0	0
S	0	0	-1	0	0	0
C	0	0	0	+1	0	0
B	0	0	0	0	-1	0
T	0	0	0	0	0	+1
Leptons	**electron (e)** **electron neutrino (ν_e)**		**muon (μ)** **muon neutrino (ν_μ)**		**tau (τ)** **tau neutrino (ν_τ)**	

Table 1.2.: Basic properties of quarks; mass, electric charge, weak isospin, the third component of the isospin (I_3), strangeness (S), charm (C), bottom (B), and top (T). All quarks have spin $\frac{1}{2}\hbar$, baryon number 1/3 , and lepton number 0. Quarks and Leptons come in three generations of doublets [4].

separate a single, color-charged quark from a hadron would require an infinite work done against the color field. This increases the energy of the color field to such an extent that new quark-antiquark pairs are created out of the vacuum to keep the color-neutral form of the hadron (Figure 1.1). This phenomenon is called ***confinement***.

The strength of the strong interaction is given by the QCD running coupling constant (Figure 1.1):

$$\alpha_s(Q^2) = \frac{12\pi}{(33 - 2n_f) \cdot \ln\left(Q^2/\Lambda^2_{\mathrm{QCD}}\right)} \tag{1.1}$$

where Q is the momentum transfer, n_f is the number of active quark flavors and Λ_{QCD} (~ 250 MeV/c) is a free parameter, which must be determined experimentally [7]. In case of large momentum transfer ($Q^2 \to \infty$) i.e. asymptotically short distances, the coupling vanishes. In these circumstances quarks can be regarded as free particles. This is known as ***asymptotic freedom*** [8], which explains scaling at short distances and offers a mechanism for confinement at large distances (Wilczeck and Politzer, Nobel Price in 2004).

Even though the standard model accounts for an enormous body of experimental data, as a complete theory of physics it does have some significant shortcomings. For instance,

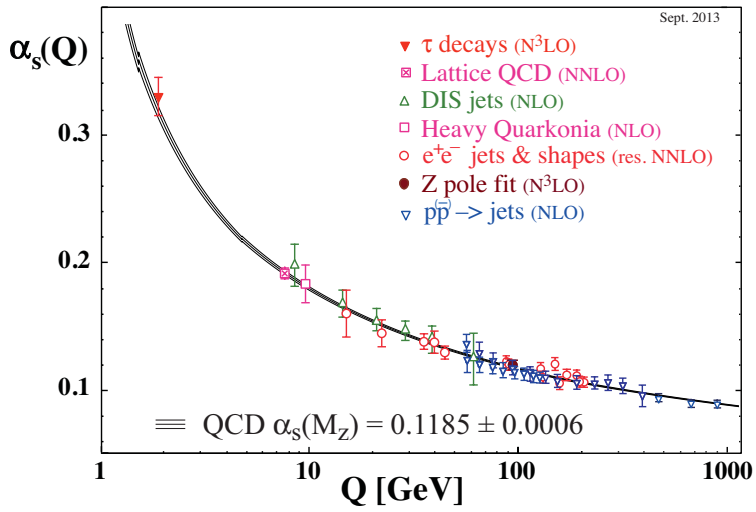

Figure 1.1.: Summary of measurements of the running coupling constant α_s as a function of the energy scale Q. The respective degree of QCD perturbation theory used in the extraction of α_s is indicated in brackets (NLO: next-to-leading order; NNLO: next-to-next-to leading order and so on and so forth. M_Z is the mass of the Z boson) [4].

it does not include gravity and has nearly twenty parameters that cannot be calculated within its framework. Also, in the standard model, neutrinos are assumed to be massless, but there is evidence from the solar and atmospheric anomalies, that neutrinos do have finite masses. In other words, it appears that in trying to understand some of the major features of our universe, such as the preponderance of 'dark matter' and the large matter-antimatter asymmetry, one would also require new and presently unknown physics beyond that of the Standard Model.

1.2. Probing the QCD phase diagram

The Lattice QCD, which is a method for calculating equilibrium properties of strongly interacting systems directly from the QCD Lagrangian by numerical evaluation of the corresponding path integrals, predicts that at sufficiently high energy densities there will be a transition from hadronic matter to a plasma of deconfined quarks and gluons. This is the so called Quark-Gluon Plasma (QGP). Within the framework of the Standard Model, the appearance of phase transitions involving elementary quantum fields is intrinsically connected to the breaking of fundamental symmetries of nature and thus to the origin of mass.

Figure 1.2 shows the phase diagram of strongly interacting matter in the temperature vs. baryon chemical potential plane (T, μ_B). At high temperature T and vanishing μ_B, qualitative aspects of the transition to the QGP are controlled by the chiral symmetry of the QCD Lagrangian. In the limit of vanishing quark masses the QCD Lagrangian is chirally symmetric, i.e. invariant under separate flavor rotations of right and left-handed quarks. Lattice calculations suggest that this crossover is rather rapid, taking place in a narrow temperature interval around $T_c \sim 154 \pm 9$ MeV [9]. At T_c two phenomena happen: color confinement is broken, i.e. colored degrees of freedom can propagate over distances much larger than the size of a hadron, and the approximate chiral symmetry of QCD, which is spontaneously broken at low temperatures and densities, gets restored [10]. On

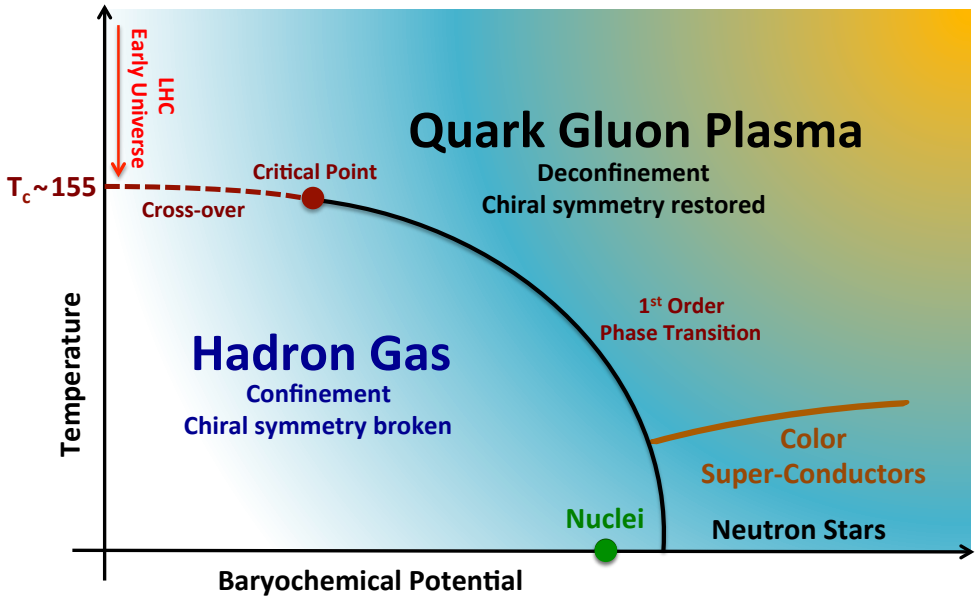

Figure 1.2.: The schematic phase diagram of the QCD.

the other hand, at very low temperatures and asymptotically large baryon densities quarks are also deconfined, although not in a quark-gluon plasma state but rather in a color superconductor [11].

1.3. Ultra-relativistic heavy-ion collisions

In ultra-relativistic heavy-ion collisions one expects to attain energy densities which reach and exceed the critical energy density ε_c ($\sim$1 GeV), thus making it possible to study the QCD phase transition and the physics of the QGP state. The system created in heavy-ion collisions undergoes a fast dynamical evolution from the extreme initial conditions to the dilute final hadronic state. The space-time evolution of an ultra-relativistic heavy-ion collision is shown in Figure 1.3.

At the first instants of the collision, called pre-equilibrium, the energy deposited in the collision volume is redistributed into other degrees of freedom. After the so-called "formation time" ($\sim$1 fm/c), the deposited energy may lead to the formation of the QGP. As the reaction zone expands, the collision fireball cools down and goes through a mixed phase where the formed hadrons coexist with the deconfined quarks and gluons and which can be subsequently described by hydrodynamics. Finally, all quarks and gluons condensate into a state of highly interacting hadron gas which further expands and cools to the point called **chemical freeze-out**, where the last inelastic collisions occur. At this point abundances of all hadrons are fixed and only elastic collisions between particles continue. The final stage, **kinetic freeze-out**, where all elastic collisions vanish is reflected in the momenta of the measured particles [12].

Since heavy-ion collisions are highly complex processes, connections with other fields of physics may show up and become important [1]. The most striking connection is to the studies of the models of the early universe. According to Big-Bang cosmology, the universe evolved from an initial state of extreme energy density to its present state through rapid expansion and cooling, just as in the case of ultra-relativistic heavy-ion collisions. It is

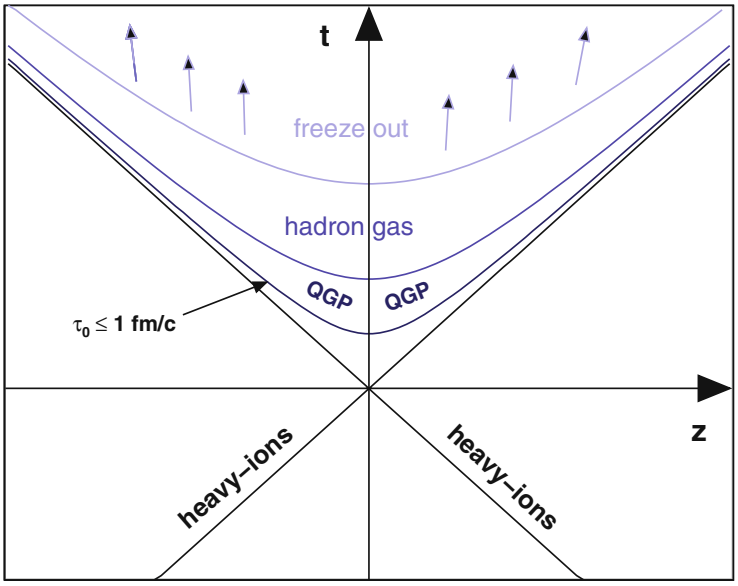

Figure 1.3.: Space-time diagram of a nucleus-nucleus collision, showing the various stages of the evolution of expanding matter [12].

believed that the QGP phase existed in the early universe up to few microseconds after the Big Bang. Moreover, the knowledge of the equation of state for nuclear matter at extreme density is relevant for astrophysics in understanding the dynamics of supernovae explosions and the stability of neutron stars [13]. In this sense, the information that can be extracted from ultra-relativistic heavy-ion reactions may provide a deeper insight into the models of the early universe and astrophysical phenomena.

The LHC provides an ideal tool for the study of this new state of matter, QGP. It brings heavy-ion physics into such a high-energy region ($\sqrt{s} = 5.5$ TeV per nucleon pair in Pb–Pb collisions) that the net-baryon density in the central rapidity region vanishes and the experimental conditions become close to the ones of lattice QCD calculations as well as to those of the expanding early universe.

1.4. Event-by-event fluctuations

In general, one can classify fluctuations into two parts. First, dynamical fluctuations which result from correlated particle production reflecting the underlying dynamics of the system. Second, statistical fluctuations induced by the measurement process itself due to the finite event multiplicity. On the other hand, there are also quantum fluctuations which play almost negligible role in heavy-ion collisions but might be relevant in pp collisions.

Event-by-event fluctuations of global observables, such as mean transverse momentum, identified particle ratios and conserved quantities (net-charge, net-baryon, net-strangeness), in the hadronic final state are used to study the dynamics of the phase transition and probe the QCD phase diagram (Figure 1.2). With increasing energy the phase separation line ranges from zero temperature and large baryo-chemical potential to finite temperature and smaller baryo-chemical potential where the first-order phase transition line hits to a so-called “critical point” [14]. This is a genuine thermodynamic singularity at which susceptibilities diverge and the order parameter fluctuates on long

wavelengths. Accordingly, the resulting signatures are expected to show non-monotonic behaviour as a function of collision energy, centrality, rapidity or ion size [14–16]. The field of event-by-event fluctuations, thus, plays a significant role within the energy scan program of the NA49 Collaboration at the CERN SPS and STAR Collaboration at RHIC, in order to study the QCD phase diagram and in particular locate the critical point.

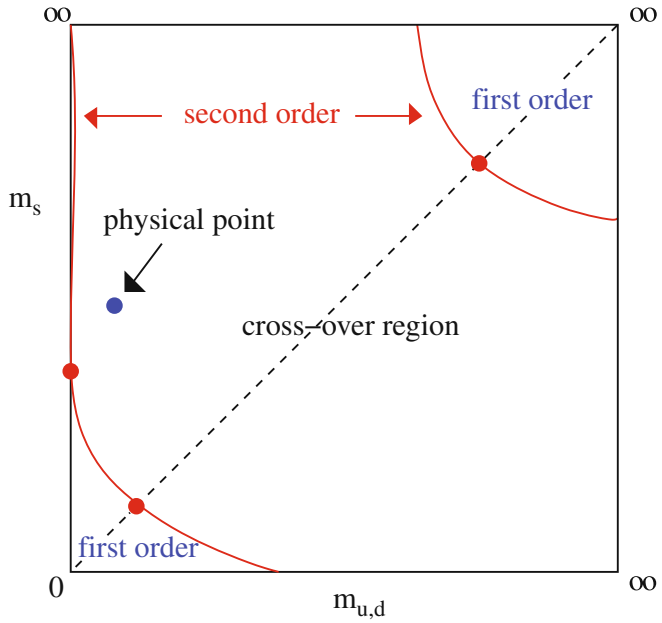

Figure 1.4.: The QCD phase diagram of 3-flavour QCD [17].

At LHC energies, i.e. at vanishing baryo-chemical potential, $\mu_B \approx 0$ (Figure 1.2), the properties of the QCD phase transition depend on the number of quark flavours and their masses. The global symmetries of the QCD Lagrangian only exist in the limits of either infinite or vanishing quark masses. For $m_q \to 0$ for all quark masses, the Lagrangian becomes chirally symmetric, while for $0 < m_q < \infty$ the second order phase transition is replaced by a rapid crossover from confinement to deconfinement where physics changes dramatically but smoothly and no correlation length diverges. In other words, there is no thermal singularity and no genuine phase transition, and restoration of chiral symmetry is only approximate. The overall behavior of the QCD phase transition is illustrated in Figure 1.4. The "physical point", which falls into the cross-over region, corresponds to small u, d masses and a larger s-quark mass.

Although there is no genuine phase transition at $\mu_{\mathrm{B}} \approx 0$, recent Lattice QCD calculations predict a critical behavior at the crossover region. As shown in Figure 1.5, the chiral condensate susceptibilities show well defined peaks corresponding to a (pseudo-)critical temperature T_{pc} [9].

On the other hand, the functional dependence of the pressure on T and μ_{B}, i.e. the equation of state of strongly interacting matter, allows for linking the thermodynamic quantities to ensemble fluctuations: derivatives of the pressure with respect to the chemical potential to the susceptibilities

$$\chi_n = \frac{\partial^n (P/T^4)}{\partial(\mu/T)}, \tag{1.2}$$

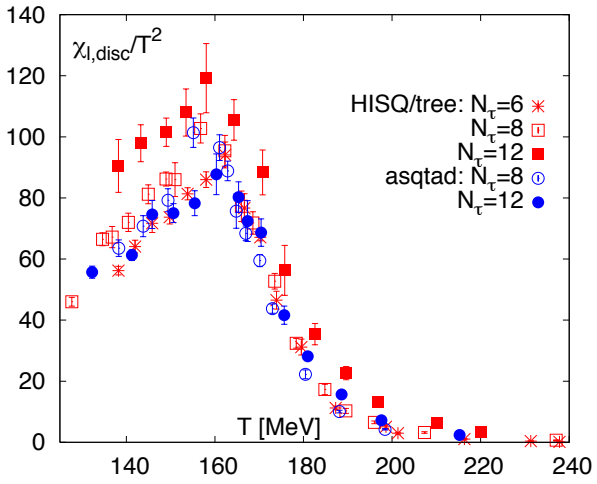

Figure 1.5.: Recent calculations of the chiral susceptibility for $m_l = m_s/20$ and different N_τ, where N_τ is temporal extent and m_l, m_s are the light and strange quark masses, respectively [9].

where

$$\frac{P}{T^4} = \frac{1}{VT^3} \ln Z(V, T, \mu) \tag{1.3}$$

and Z is the grandcanonical partition function. Here, within the framework of statistical physics, one can show that the susceptibilities relate to cumulants of the event-by-event multiplicity distributions via

$$\chi_1 = \frac{1}{VT^3}\langle N \rangle, \quad \chi_2 = \frac{1}{VT^3}\langle (\Delta N)^2 \rangle, \quad \chi_3 = \frac{1}{VT^3}\langle (\Delta N)^3 \rangle \cdots, \tag{1.4}$$

where N is the number of the measured particles or any conserved quantity (e.g. charge, baryon number, strangeness) and $\Delta N = N - \langle N \rangle$ is the fluctuation around the event-averaged mean. The sixth and eighth order cumulants of the net baryon number fluctuations are shown to be sensitive probes for the analysis of the crossover phase transition in Figure 1.6 [19]. Moreover, since Lattice QCD allows for the calculation of susceptibilities of conserved quantities, one can make a quantitative comparison between Lattice QCD and event-by-event fluctuations of conserved quantities which can be measured experimentally via cumulants [20].

All in all, measuring event-by-event fluctuations over the ensemble of events via cumulants or moments of particle multiplicity distributions, one can study the freeze-out conditions in heavy-ion collisions and clarify their relation to the QCD phase transition.

1.4.1. Fluctuation measures

The event-by-event fluctuations of several observables are currently being studied experimentally and theoretically, such as mean-p_{T}, (net) charge, baryon number, strangeness, multiplicity etc.. These observables are measured on an event-by-event basis and, in the framework of statistical physics, characterized by variances, covariances or higher moments. These moments are then compared to expectations based on thermal-equilibrium or other statistical models. Any difference can be attributed to novel dynamic effects such as variations of impact parameter, baryon stopping, initial energy density fluctuations etc. [21, 22].

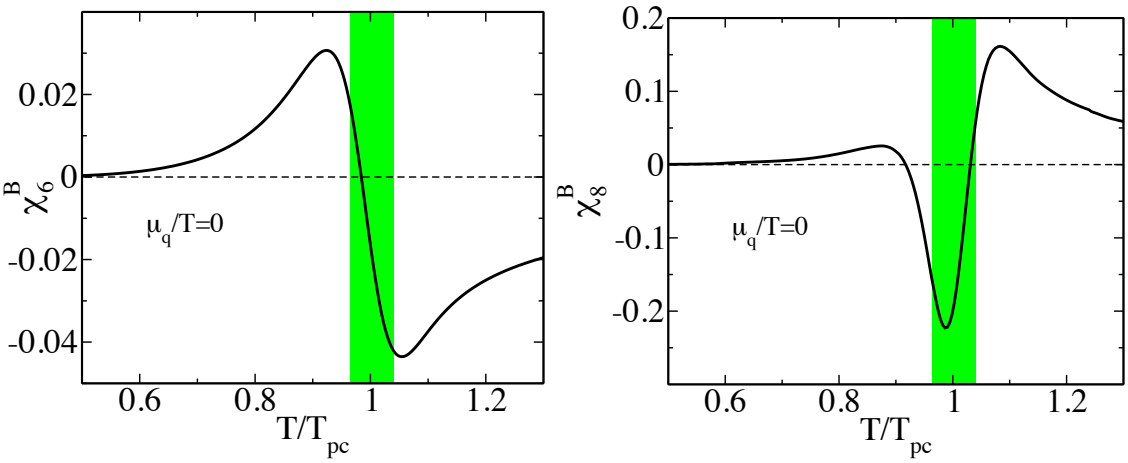

Figure 1.6.: The sixth and eighth order cumulants of the net baryon number fluctuations at $\mu_q/T = 0$ in the Polyakov Quark Meson (PQM) model [18]. The temperature is given in units of the pseudo-critical temperature T_{pc} corresponding to a maximum of the chiral susceptibility. The shaded area indicates the chiral crossover region [19].

Moments (or cumulants) higher than second order are more sensitive to the underlying physics but require significant statistics. Yet, one can construct observables using the moments of the particle multiplicity distributions up to second order to address any non-monotonic behavior as a function of energy or system volume.

A number of statistical measures which consist of the moments up to second order, have been suggested to study particle number fluctuations in experiments such as $\sigma_{\rm dyn}$, $\nu_{\rm dyn}$, Σ, Δ, Φ etc. [23]. However, each measure exhibits different dependences on collision centrality, detector acceptance, particle detection efficiency, and susceptibility to experimental biases. Because of the following advantages $\nu_{\rm dyn}$ was studied in this thesis:

- To first order it is free of detection efficiency losses.
- Provides information on the correlations between particle pairs.
- Contains the moments of particle multiplicity distributions up to second order, and thus does not require too much statistics.

The dynamical event-by-event fluctuations of particle ratios were first studied by the NA49 collaboration at the SPS [24] using the $\sigma_{\rm dyn}$ quantity, which is defined as

$$\sigma_{\rm dyn} = sgn(\sigma^2_{\rm data} - \sigma^2_{\rm mixed})\sqrt{|\sigma^2_{\rm data} - \sigma^2_{\rm mixed}|} \tag{1.5}$$

where $\sigma_{\rm data}$ and $\sigma_{\rm mixed}$ are the relative width of the event-by-event particle ratio distribution for the data and artificially generated mixed events, respectively. The STAR experiment at RHIC studied the related event-by-event fluctuation measure $\nu_{\rm dyn}$ [25], which was originally proposed to study net-charge fluctuations [26].

$\nu_{\rm dyn}[a,b]$ is determined by intrinsic correlations between particle types a and b averaged over the phase space of interest and given as

$$\nu_{\rm dyn}[a,b] = \frac{\langle N_a^2\rangle}{\langle N_a\rangle^2} + \frac{\langle N_b^2\rangle}{\langle N_b\rangle^2} - 2\frac{\langle N_a N_b\rangle}{\langle N_a\rangle\langle N_b\rangle} - \left(\frac{1}{\langle N_a\rangle} + \frac{1}{\langle N_b\rangle}\right) \tag{1.6}$$

where $\langle N_a \rangle$ and $\langle N_b \rangle$ are the event-averaged multiplicities of particle types a and b, respectively. It vanishes when the multiplicity distributions of a and b are Poissonian and independent of each other. Moreover, a negative value of $\nu_{\rm dyn}[a,b]$ [1] indicates that a and b are correlated, whereas anti-correlation is signaled when $\nu_{\rm dyn}[a,b]$ is positive. By definition, Eq. 1.6 is symmetric under the transposition of particles a and b. Although it is free from volume fluctuations, it has an intrinsic multiplicity dependence which has to be taken into account.

For sufficiently high particle multiplicities one finds the approximate relation [27];

$$\nu_{\rm dyn} \approx sgn(\sigma_{\rm dyn})\sigma^2_{\rm dyn}. \tag{1.7}$$

However, this relation is only approximate and its accuracy decreases inversely with multiplicity. In order not to rely on this approximation, the NA49 collaboration published also the $\nu_{\rm dyn}$ results in Ref [28].

As shown in Figure 1.7, measurements from NA49 and STAR show a smooth evolu-

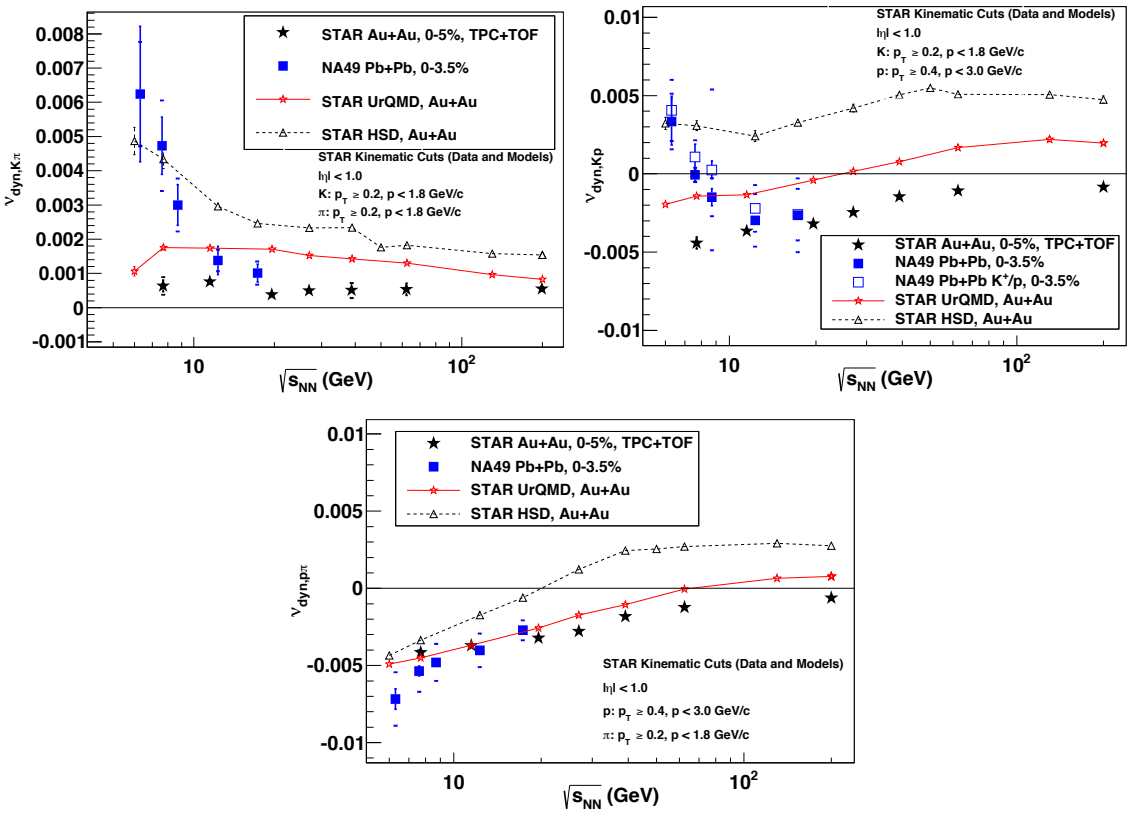

Figure 1.7.: $\nu_{\rm dyn}$ results of NA49 [28] and STAR [25] collaborations.

tion with beam energy and do not reveal an indication for critical behavior in the range $6.3 < \sqrt{s_{\rm NN}} < 200$ GeV. Disagreement between NA49 and STAR data for $\nu_{\rm dyn}[{\rm K,p}]$ and $\nu_{\rm dyn}[\pi,{\rm K}]$ at $\sqrt{s_{\rm NN}} < 10$ GeV was explained in Ref [28] with the acceptance dependence of $\nu_{\rm dyn}$. Above this energy, both experiments report positive values for $\nu_{\rm dyn}[\pi,{\rm K}]$ and a weak energy dependence, whereas $\nu_{\rm dyn}[{\rm K,p}]$ is negative and approaches zero as $\sqrt{s_{\rm NN}}$ increases.

[1] In this thesis, $\nu_{\rm dyn}[a,b]$ was taken to be $\nu_{\rm dyn}[a+\overline{a},b+\overline{b}]$, where $\overline{a}$ and $\overline{b}$ are the anti-particles of a and b, respectively.

The results for $\nu_{\rm dyn}[\pi, {\rm p}]$ are also negative and approach zero, while the hadronic transport models HSD [29] and UrQMD [30] indicate a sign change in the RHIC energy regime.

The ALICE detector at the LHC is ideally suited to extend these measurements to higher collision energies. In particular, the excellent charged-particle tracking and particle identification (PID) capabilities in the central barrel of the detector allow for measurements of π, K and p on an event-by-event basis at mid-rapidity and low transverse momentum ($p_{\rm T}$). The ALICE results for $\nu_{\rm dyn}$ in Pb–Pb collisions at $\sqrt{s_{\rm NN}}$ =2.76 TeV are presented in Chapter 6.

1.4.2. A solution for misidentification: the Identity Method

Unlike single-particle spectra measurements, the results on second and higher moments of particle multiplicity distributions cannot be corrected in a model-independent way for the limited experimental acceptance. Therefore, one keeps the acceptance reasonably high by combining the information of several detectors, for instance ITS+TPC+TOF. However, this costs a reduction in the particle detection efficiency, which is also difficult to correct for. Namely, the main challenge in the fluctuation analyses is to identify each particle track uniquely keeping the acceptance and detection efficiency large.

Thereby, the particle identification (PID) in ALICE is mostly based on the TPC, which provides a momentum resolution better than 2% and single particle detection efficiencies up to 80% for $p_{\rm T} > 0.3$ GeV/c. The PID in the TPC is based on the specific energy loss (dE/dx), charge, and momentum of each particle traversing the detector gas. When the dE/dx distributions of different particle species are well separated, a unique particle identification is possible which allows for finding the moments by counting the number of particles on an event-by-event basis. However, it suffers from the misidentification problem when the measured particle dE/dx distributions overlap. Although it is impossible to identify particles uniquely in the overlap region, one can determine with high accuracy the percentage of a given particle type among others. Below, it will be shown that this probability information is sufficient to overcome misidentification problem.

A new experimental technique called the Identity Method was proposed in Ref. [31] as a solution to the misidentification problem for the analysis of events with two measured particle species. In Ref. [32] the method was further developed to calculate the second moments of the multiplicity distributions of more than two particle species. Finally, in Ref. [33] it was generalized to second and higher moments of the multiplicity distributions in events consisting of an arbitrary number of different particle species. First experimental results using the Identity Method was published by the NA49 collaboration in Ref. [28].

Instead of identifying every detected particle event-by-event, the Identity Method calculates the moments of particle multiplicity distributions by means of an unfolding procedure using only two basic experimentally measurable event-by-event quantities, ω and W. They are defined as

$$\omega_j(x_i) = \frac{\rho_j(x_i)}{\rho(x_i)} \in [0,1], \quad \rho(x_i) = \sum_j \rho_j(x_i), \quad W_j \equiv \sum_{i=1}^{N(n)} \omega_j(x_i), \tag{1.8}$$

where x_i stands for the dE/dx of a given track i, $\rho_j(x)$ is the dE/dx distribution of particle j within a given phase-space bin and $N(n)$ is the number of tracks in the $n^{\rm th}$ event. In other words, ω_j is a Bayesian probability measure of being particle type j for a given track. Thus, in case of perfect identification one expects $W_i = N_i$, while this does

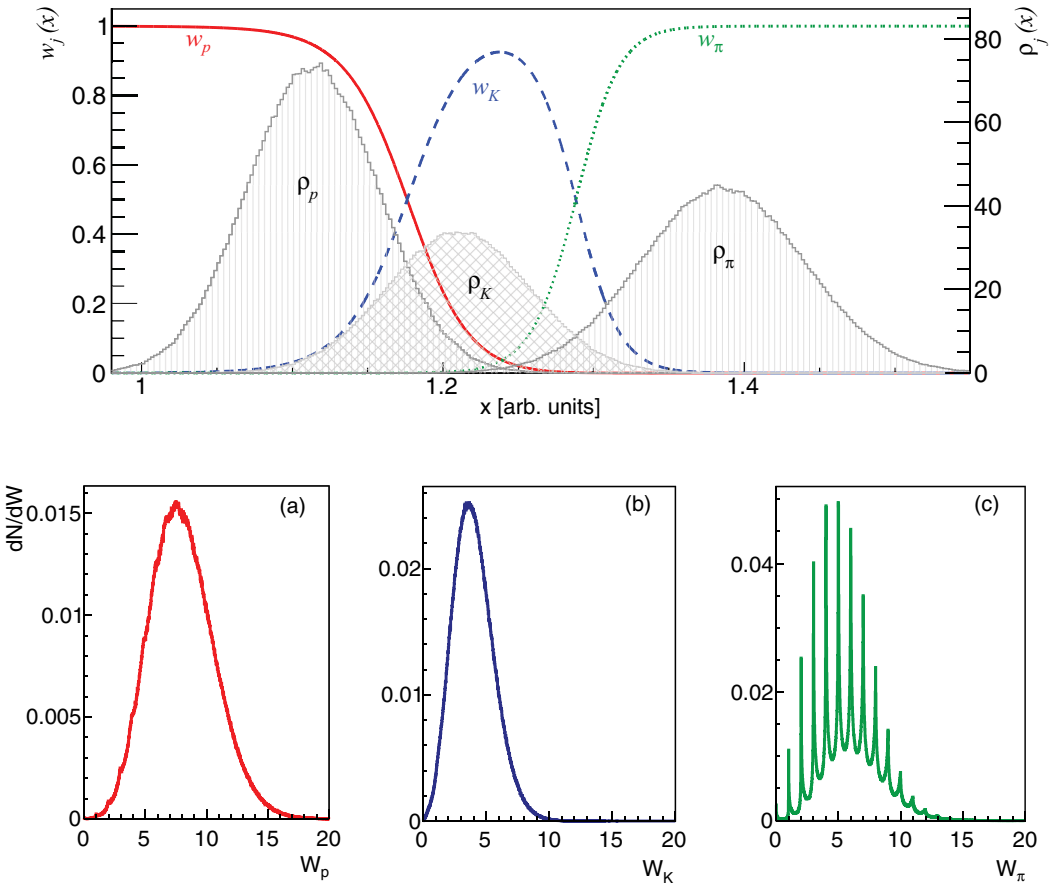

Figure 1.8.: A toy simulation of particle energy loss for pions, kaons and protons where unique particle identification is impossible. Upper panel: The inclusive distribution $\rho_j(x)$ of the particle identification variable x for protons, kaons, and pions, used as an input to the simulation, are depicted with shaded histograms. The distributions of identities $\omega_j(x)$ for protons, kaons, and pions are presented with red solid, blue dashed, and green dotted lines respectively. Lower panel: The distribution of event variables W_j with j standing for (a) protons, (b) kaons, and (c) pions.[34].

not hold in case of misidentification. Figure 1.8 illustrates ω and W quantities for pions, kaons and protons in a given phase space where unique particle identification is impossible. As expected the W distribution of protons shows a more discrete structure because the proton $\mathrm{d}E/\mathrm{d}x$ distribution has the least overlap.

The moments of the W distributions $\langle W_i ... W_j \rangle$ can be easily constructed directly from experimental data. The Identity Method provides the real moments $\langle N_i ... N_j \rangle$ of the particle multiplicity distributions using the moments of these W distributions. Details of the mathematical derivation as well as a verification of the method by means of a toy Monte-Carlo simulation, can be found in Ref. [32, 33]. In the next section an application of the Identity Method to experimental data will be given.

1.4.3. Application of the Identity Method to experimental data

As seen in Eq. 1.6, the fluctuation measure ν_{dyn} depends on the first and all second (pure and mixed) moments of the multiplicity distributions of the studied particles pairs. For

particle types a and b the second moments are defined as

$$\langle N_a^2 \rangle = \sum_{N_a=0}^{\infty} N_a^2 P(N_a), \tag{1.9}$$

$$\langle N_a N_b \rangle = \sum_{N_a=0}^{\infty} \sum_{N_b=0}^{\infty} N_a N_b P(N_a, N_b). \tag{1.10}$$

where N_a and N_b are the multiplicities of particles types a and b, respectively. $P(N_a)$ stands for the probability distribution of the multiplicity of a, while $P(N_a, N_b)$ is the joint probability distribution for the multiplicities of particles a and b. These moments can be calculated by counting the particles event-by-event in case of a unique identification.

The Identity Method proposes a general way of calculating the moments in spite of misidentification. It follows an iterative unfolding procedure. Below the mathematical derivation of only the first and second moments are given, since the third and higher moments are out of the scope of the thesis.

Derivation of the first moments:

The Identity Method employs the fitted $\mathrm{d}E/\mathrm{d}x$ distribution functions of each particle, $\rho_j(x)$, with j ($j = 1, ..., k \geq 2$) standing for different particle species. The values of ρ and ρ_j are calculated using the parameters stored in the lookup table of fitted distribution functions in the appropriate phase-space bin. Since the $\mathrm{d}E/\mathrm{d}x$ measurement is of finite resolution, the normalization of $\rho_j(x)$ is given as

$$\int dx \rho_j(x) = \langle N_j \rangle. \tag{1.11}$$

The first moment of the W quantities for particle type a can be written as

$$\begin{aligned}
\langle W_a \rangle = & \sum_{N_1=0}^{N_1=\infty} \sum_{N_2=0}^{N_2=\infty} \cdots \sum_{N_k=0}^{N_k=\infty} \mathcal{P}\left(N_1, N_2, ..., N_k\right) \int dx_1^1 P_1(x_1^1) \cdots \int dx_{N_1}^1 P_1(x_{N_1}^1) \\
& \times \int dx_1^2 P_2(x_1^2) \cdots \int dx_{N_2}^2 P_2(x_{N_2}^2) \times \cdots \times \int dx_1^k P_k(x_1^k) \cdots \int dx_{N_k}^k P_k(x_{N_k}^k) \\
& \times \left[\omega_a(x_1^1) + \cdots + \omega_a(x_{N_1}^1) + \omega_a(x_1^2) + \cdots + \omega_a(x_{N_2}^1) + \omega_a(x_{N_1}^k) + \cdots + \omega_a(x_{N_k}^k) \right] \\
= & \sum_{j=1}^{k} \langle N_j \rangle \overline{\omega_{a,j}},
\end{aligned} \tag{1.12}$$

where $\mathcal{P}\left(N_1, N_2, ..., N_k\right)$ is the multiplicity distribution, $P_j(x) \equiv \rho_j(x)/\langle N_j \rangle$ are the $\mathrm{d}E/\mathrm{d}x$ probability density functions, x_i is the $\mathrm{d}E/\mathrm{d}x$ of the track i and

$$\overline{\omega_{a,j}} = \frac{\int \omega_a(x) \rho_j(x) dx}{\int \rho_j(x) dx}. \tag{1.13}$$

The Eq. 1.12 can be written in matrix form:

$$\begin{pmatrix} \langle W_1 \rangle \\ \langle W_2 \rangle \\ ... \\ \langle W_k \rangle \end{pmatrix} = \begin{pmatrix} \overline{\omega_{1,1}} & \overline{\omega_{1,2}} & ... & \overline{\omega_{1,k}} \\ \overline{\omega_{2,1}} & \overline{\omega_{2,2}} & ... & \overline{\omega_{2,k}} \\ ... & ... & ... & ... \\ \overline{\omega_{k,1}} & \overline{\omega_{k,2}} & ... & \overline{\omega_{k,k}} \end{pmatrix} \begin{pmatrix} \langle N_1 \rangle \\ \langle N_2 \rangle \\ ... \\ \langle N_k \rangle \end{pmatrix} \tag{1.14}$$

Here, the only unknowns are the first moments $\langle N_j \rangle$ which can easily be obtained by matrix inversion. Also, by substituting Eq. 1.13 to the right hand side of Eq. 1.12 one can obtain

$$\begin{aligned}\langle W_a \rangle &= \sum_{j=1}^{k} \langle N_j \rangle \overline{\omega_{a,j}} \\ &= \sum_{j=1}^{k} \int \frac{\rho_a \rho_j}{\rho} dx \\ &= \int \rho_a dx \\ &= \langle N_a \rangle \end{aligned} \tag{1.15}$$

Namely, the first moments of the multiplicity distributions are identical to the first moments of the W quantities similar to the case of unique identification while this does not hold for the second and higher moments.

Derivation of the second moments:

Using the definition of W_j quantity, one can introduce the second moments W_j^2 with $j = 1, ..., k$ and $W_a W_b$ with $1 \leq a < b \leq k$,

$$\langle W_j^2 \rangle \equiv \frac{1}{N_{\rm ev}} \sum_{n=1}^{N_{\rm ev}} \left[\sum_{i=1}^{N(n)} \omega_j(x_i) \right]^2 , \tag{1.16}$$

$$\langle W_a W_b \rangle \equiv \frac{1}{N_{\rm ev}} \sum_{n=1}^{N_{\rm ev}} \left(\left[\sum_{i=1}^{N(n)} \omega_a(x_i) \right] \times \left[\sum_{i=1}^{N(n)} \omega_b(x_i) \right] \right) , \tag{1.17}$$

where $N_{\rm ev}$ is the number of events and $N(n)$ is the total multiplicity in the nth event. Similar to the derivation of the first moments of W quantities, Eq. 1.16 and Eq. 1.17 can be calculated as follows:

$$\begin{aligned}\langle W_a^2 \rangle = & \sum_{N_1=0}^{\infty} \sum_{N_2=0}^{\infty} \cdots \sum_{N_k=0}^{\infty} \mathcal{P}\left(N_1, N_2, ..., N_k\right) \int dx_1^1 P_1(x_1^1) \cdots \int dx_{N_1}^1 P_1(x_{N_1}^1) \\ & \times \int dx_1^2 P_2(x_1^2) \cdots \int dx_{N_2}^2 P_2(x_{N_2}^2) \times \cdots \times \int dx_1^k P_k(x_1^k) \cdots \int dx_{N_k}^k P_k(x_{N_k}^k) \\ & \times \left[\omega_a(x_1^1) + \cdots + \omega_a(x_{N_1}^1) + \omega_a(x_1^2) + \cdots + \omega_a(x_{N_2}^1) + \omega_a(x_{N_1}^k) + \cdots + \omega_a(x_{N_k}^k) \right]^2 \end{aligned} \tag{1.18}$$

$$\begin{aligned}\langle W_a W_b \rangle = & \sum_{N_1=0}^{\infty} \sum_{N_2=0}^{\infty} \cdots \sum_{N_k=0}^{\infty} \mathcal{P}\left(N_1, N_2, ..., N_k\right) \int dx_1^1 P_1(x_1^1) \cdots \int dx_{N_1}^1 P_1(x_{N_1}^1) \\ & \times \int dx_1^2 P_2(x_1^2) \cdots \int dx_{N_2}^2 P_2(x_{N_2}^2) \times \cdots \times \int dx_1^k P_k(x_1^k) \cdots \int dx_{N_k}^k P_k(x_{N_k}^k) \\ & \times \left[\omega_a(x_1^1) + \cdots + \omega_a(x_{N_1}^1) + \omega_a(x_1^2) + \cdots + \omega_a(x_{N_2}^1) + \omega_a(x_{N_1}^k) + \cdots + \omega_a(x_{N_k}^k) \right] \\ & \times \left[\omega_b(x_1^1) + \cdots + \omega_b(x_{N_1}^1) + \omega_b(x_1^2) + \cdots + \omega_b(x_{N_2}^1) + \omega_b(x_{N_1}^k) + \cdots + \omega_b(x_{N_k}^k) \right] \end{aligned} \tag{1.19}$$

Thus one obtains

$$\langle W_a^2\rangle = \sum_{j=1}^{k}\langle N_j\rangle\left[u_{aj}^2-(u_{aj})^2\right]+\sum_{j=1}^{k}\langle N_j^2\rangle(u_{aj})^2+2\sum_{1\le j<l\le k}\langle N_jN_l\rangle u_{aj}u_{al}, \tag{1.20}$$

$$\langle W_aW_b\rangle = \sum_{j=1}^{k}\langle N_j\rangle\left[u_{abj}-u_{aj}u_{bj}\right]+\sum_{j=1}^{k}\langle N_j^2\rangle u_{aj}u_{bj}+\sum_{1\le j<l\le k}\langle N_jN_l\rangle\left[u_{aj}u_{bl}+u_{al}u_{bj}\right], \tag{1.21}$$

where experimentally measurable quantities u_{ji}^s $(s=1,2)$ and u_{abi} are defined as

$$\begin{aligned} u_{aj}^s &= \frac{1}{\langle N_j\rangle}\int dx\omega_a^s(x)\rho_j(x)\\ u_{abj} &= \frac{1}{\langle N_j\rangle}\int dx\omega_a(x)\omega_b(x)\rho_j(x). \end{aligned} \tag{1.22}$$

In case of unique identification one finds that

$$u_{aj}^s=\delta_{aj}, \qquad u_{abj}=0, \tag{1.23}$$

and Eq. 1.20 and Eq. 1.21 reduces then to $\langle W_a^2\rangle=\langle N_a^2\rangle$ and $\langle W_aW_b\rangle=\langle N_aN_b\rangle$, respectively.

The right hand side of Eq. 1.20 and Eq. 1.21 are linear combinations of all the first and second moments, $\langle N_j\rangle$, $\langle N_j^2\rangle$ and $\langle N_iN_j\rangle$. By introducing the experimentally measurable quantities r_j and r_{ab}, which are defined as

$$r_a \equiv \langle W_a^2\rangle-\sum_{j=1}^{k}\langle N_j\rangle\left[u_{aj}^2-(u_{aj})^2\right] \tag{1.24}$$

$$r_{ab} \equiv \langle W_aW_b\rangle-\sum_{j=1}^{k}\langle N_j\rangle\left[u_{abj}-u_{aj}u_{bj}\right], \tag{1.25}$$

one can transform Eq. 1.20 and Eq. 1.21 to the following form:

$$\sum_{j=1}^{k}\langle N_j^2\rangle u_{aj}^2+2\sum_{1\le j<l\le k}\langle N_jN_l\rangle u_{aj}u_{al}=r_a \tag{1.26}$$

$$\sum_{j=1}^{k}\langle N_j^2\rangle u_{aj}u_{bj}+\sum_{1\le j<l\le k}\langle N_jN_l\rangle\left[u_{aj}u_{bl}+u_{al}u_{bj}\right]=r_{ab}. \tag{1.27}$$

Here, the only unknowns are the second moments $\langle N_j\rangle$, $\langle N_j^2\rangle$ and $\langle N_jN_l\rangle$. Therefore, Eq. 1.26 and Eq. 1.27 represent a system of of $k+k(k-1)/2$ linear equations which can be written as a matrix equation $\mathcal{N}=\mathcal{A}^{-1}\mathcal{R}$

$$\begin{pmatrix} \langle N_1^2\rangle \\ \vdots \\ \langle N_k^2\rangle \\ \langle N_1N_2\rangle \\ \vdots \\ \langle N_{k-1}N_k\rangle \end{pmatrix} = \left(\begin{array}{ccc:ccc} a_1^1 & \cdots & a_1^k & a_1^{12} & \cdots & a_1^{(k-1)k} \\ \vdots & \vdots & \vdots & \vdots & \vdots & \vdots \\ a_k^1 & \cdots & a_k^k & a_k^{12} & \cdots & a_k^{(k-1)k} \\ \hdashline a_{12}^1 & \cdots & a_{12}^k & a_{12}^{12} & \cdots & a_{12}^{(k-1)k} \\ \vdots & \vdots & \vdots & \vdots & \vdots & \vdots \\ a_{12}^k & \cdots & a_{(k-1)k}^k & a_{(k-1)k}^{12} & \cdots & a_{(k-1)k}^{(k-1)k} \end{array}\right)^{-1} \begin{pmatrix} r_1 \\ \vdots \\ r_k \\ r_{12} \\ \vdots \\ r_{(k-1)k} \end{pmatrix}, \tag{1.28}$$

where

$$a_j^i \equiv u_{ji}^2, \quad 1 \leq i, \quad j \leq k; \tag{1.29}$$

$$a_i^{ab} \equiv 2u_{ia}u_{ib}, \quad 1 \leq a < b \leq k, \quad i = 1, ..., k; \tag{1.30}$$

$$a_{ab}^i \equiv u_{ai}u_{bi}, \quad 1 \leq a < b \leq k, \quad i = 1, ..., k; \tag{1.31}$$

$$a_{ab}^{lm} \equiv u_{al}u_{bm} + u_{bl}u_{am}, \quad 1 \leq a < b \leq k, \quad 1 \leq l < m \leq k. \tag{1.32}$$

As an example, for the case of a two-particle system ($k = 2$) Eq. 1.28 takes the form

$$\begin{pmatrix} \langle N_1^2 \rangle \\ \langle N_2^2 \rangle \\ \langle N_1 N_2 \rangle \end{pmatrix} = \begin{pmatrix} u_{11}^2 & u_{12}^2 & 2u_{11}u_{12} \\ u_{21}^2 & u_{22}^2 & 2u_{21}u_{22} \\ u_{11}^{12} & u_{12}u_{22} & u_{11}u_{22} + u_{12}u_{21} \end{pmatrix}^{-1} \begin{pmatrix} r_1 \\ r_2 \\ r_{12} \end{pmatrix}. \tag{1.33}$$

This linear equation system has a unique solution for all the second moments, if $\det A \neq 0$. On the other hand, in an extereme case, the so-called "random identification", the ω_j probability for each track is equal to $p_j = \langle N_j \rangle / \langle N \rangle$, where $N = \Sigma_{i=1}^k N_i$, and thus one obtains

$$u_{ji} = \frac{\langle N_j \rangle}{\langle N \rangle} \equiv p_j, \quad j = 1, ..., k. \tag{1.34}$$

This leads to $\det A = 0$ and Eq. 1.28 does not define the second moments in a unique way. In other words, if all $\mathrm{d}E/\mathrm{d}x$ distribution functions $\rho_j(x)$ have the same shape but different normalization, the Identity Method fails to calculate the second moments [32].

In Ref [33] 100 toy simulations, with $6 \cdot 10^6$ events each, with different mean multiplicities of protons, kaons and pions were performed in order to verify the method. The number of particles for each particle species was simulated from a Poisson distribution and the number of kaons in each event was taken to be equal to the number of protons, in order to induce a correlation between particles. Moreover, to simulate the misidentification problem, a certain amount of overlap of the particle distribution functions was allowed. As a conclusion, the results reconstructed with the Identity Method up to the third moment provided an agreement with the Poisson expectation on the level of a few per mille. In Chapter 5 a MC-Closure test was also performed within this thesis to verify the Identity Method through an internal check.

1.5. Outline of the thesis

An introduction to the ALICE apparatus and the details of the TPC detector, as well as the $\mathrm{d}E/\mathrm{d}x$ reconstruction and calibration procedures are given in Chapter 2. Chapter 3 is dedicated to the investigation of the TPC signal shape, the offline baseline correction procedure and the implementation of ion-tail and common-mode effects into the ALICE simulation framework. In Chapter 4, a new parametrization of the TPC $\mathrm{d}E/\mathrm{d}x$ and the so-called "Iterative PID" procedure are introduced. Details of the analysis such as event and track selection, application of the Identity Method to ALICE data and error estimation are given in Chapter 5. The thesis concludes in Chapter 6 with the first results on identified-particle-ratio fluctuations in Pb–Pb collisions at $\sqrt{s_{\mathrm{NN}}}$ =2.76 TeV as a function of centrality and pseudorapidity as well as a comparison to calculations with the HIJING and AMPT event generators. Moreover, the ALICE results for the most central events are compared to the lower-energy measurements at the CERN-SPS and RHIC.

2. ALICE, A Large Ion Collider Experiment

ALICE [35] has been specifically designed to study the physics of strongly interacting matter and particularly the QCD phase diagram and the properties of the QGP in an environment with large charged-particle multiplicities. The experiment has been designed to cope with up to 8000 charged particles per unit of rapidity at mid-rapidity ($\mathrm{d}N_{\mathrm{ch}}/\mathrm{d}\eta$) in Pb–Pb collisions at $\sqrt{s_{\mathrm{NN}}} = 5.5$ TeV [13, 36, 37].

Due to its excellent tracking and particle identification capabilities, the ALICE pp and p–Pb programs complement those of the dedicated pp experiments. Not only the successful completion of the heavy-ion programme requires the study of these systems in order to establish the benchmark processes under the same experimental conditions, but they are also interesting in themselves. For instance, they open up possibilities to study fundamental aspects of the interaction of colour-neutral objects related to non-perturbative strong phenomena, like confinement and hadronic structure. Moreover, recent results from high-energy pp collisions indicate collective behaviour even in pp collisions [38].

2.1. Sub-detectors of ALICE

ALICE is capable of tracking and identifying particles from very low (∼100 MeV/c) up to fairly high (∼100 GeV/c) transverse momentum (p_{T}). Its subdetectors use mostly three-dimensional hit information and continuous tracking with many points. It consists of a central part, which is enclosed in a solenoid magnet with a nominal field of 0.5 T along the beam direction, a forward muon spectrometer and several smaller detectors in the forward region. The overview of the detector systems is shown in Figure 2.1.

In the following a short description of the main detector components, which are summarized in Table 2.1, is given. The data taking model of ALICE and the coordinate systems commonly used within ALICE are introduced in Appendix A and Appendix B, respectively.

2.1.1. Central detectors

Inner Tracking System (ITS)

The ITS [39] is a set of silicon detectors. It is composed of six cylindrical layers located at radii between 4cm and 44cm. The main purpose of these layers starting from the beam pipe are:

- *Silicon Pixel Detector (SPD):* The SPD constitutes the two innermost layers of the ITS. They are fundamental elements for the determination of the primary vertex as well as for measurement of the impact parameter of secondary tracks originating from weak decays of strange, charm and beauty particles. Moreover it is used as L0 trigger (See Appendix A for trigger definitions).

- *Silicon Drift Detector (SDD):* The SDD equips the two intermediate layers of the ITS. They have a very good multi-track capability and provide two out of the four

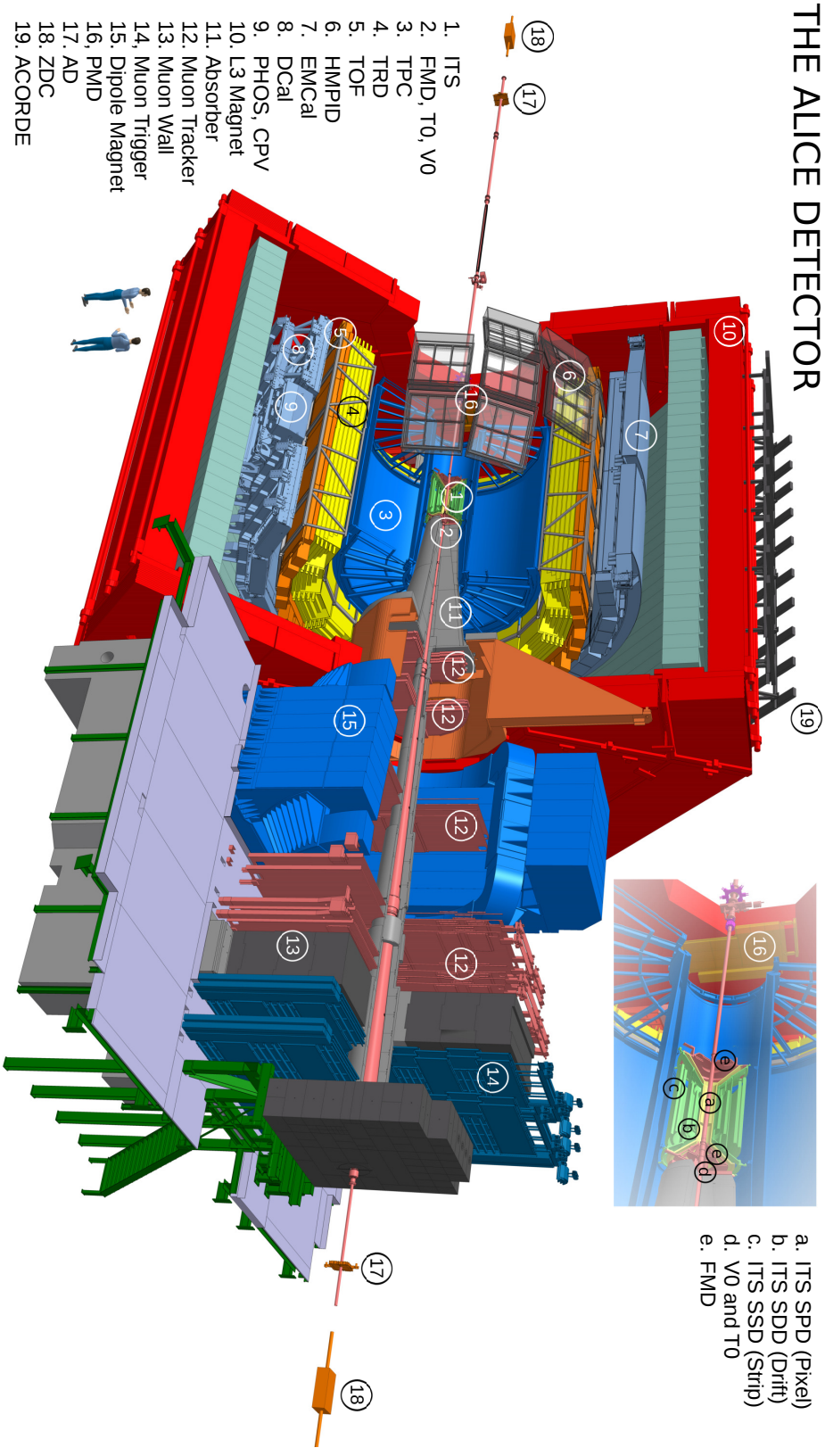

Figure 2.1.: Overview of the ALICE detector.

$\mathrm{d}E/\mathrm{d}x$ samples needed for the ITS particle identification.

- *Silicon Strip Detector (SSD):* The SSD represents the two outermost layers equipped with double-sided silicon micro-strip detectors. The SSD is crucial for the matching of tracks from the TPC to the ITS. It also provides $\mathrm{d}E/\mathrm{d}x$ information to assist particle identification for low-momentum particles.

Time Projection Chamber (TPC)
The TPC [40] is a gaseous detector. It is the main tracking detector of the ALICE central barrel. The main goal of the TPC is to provide charged-particle momentum measurements with good two-track separation, particle identification, and vertex determination together with the other central barrel detectors. A detailed description of the TPC will be given in Section 2.2.

Transition Radiation Detector (TRD)
The TRD [41] is also a gas-based detector. The main goal of the TRD is to provide electron identification in the central barrel for momenta above 1 GeV/c. Further, it takes part in tracking and also used as a fast trigger for charged particles with high momenta and electrons.

Time-Of-Flight (TOF) detector
The TOF [42] is a large-area array of Multi-gap Resistive-Plate Chambers (MRPC) surrounding the TRD. It improves the PID in the intermediate momentum range from 0.2 to 2.5 GeVc^{-1}. Together with the ITS and TPC for track and vertex reconstruction and for $\mathrm{d}E/\mathrm{d}x$ measurements in the low-momentum range (up to about 0.5 GeVc^{-1}), it provides event-by-event identification of large samples of pions, kaons, and protons.

High-Momentum Particle Identification Detector (HMPID)
The HMPID [43] is a Ring Imaging Cherenkov (RICH). It enhances the PID capability of ALICE in a limited acceptance range beyond the momentum range attainable through the energy loss (in ITS and TPC) and time of flight (in TOF) measurements.

2.1.2. Calorimeters

ElectroMagnetic Calorimeter (EMCal)
The EMCal [44] is a Pb-scintillator sampling calorimeter. It improves the jet energy resolution and increases the existing ALICE capabilities to measure high-momentum photons and electrons.

PHOton Spectrometer (PHOS)
The PHOS [45] is a lead-tungstate calorimeter. It is a high-resolution electromagnetic spectrometer detecting electromagnetic particles in a limited acceptance domain at central rapidity and provides photon identification as well as neutral meson identification.

Zero Degree Calorimeter (ZDC)
The ZDC [46] is a Quartz (fiber) calorimeter. It detects the spectator (non-interacting) nucleons in the collision and thus provides information about the event centrality. It is also used as a fast trigger to enhance the sample of central collisions.

2.1.3. Spectrometers

Photon Multiplicity Detector (PMD)

The PMD [47] consists of a preshower detector with a charged particle veto detector in front. It measures the multiplicity and spatial $(\eta - \phi)$ distribution of photons on an event-by-event basis in forward direction.

Forward Multiplicity Detector (FMD)

The FMD [48] is a silicon strip detector (Lead converter). It provides (offline) charged-particle multiplicity information. High radial detector segmentation allows for the study of multiplicity fluctuations on an event-by-event basis while azimuthal segmentation allows for the determination of the reaction plane for each event and the analysis of flow within the FMD's pseudorapidity coverage. Further, it can be used as a trigger at the L2 trigger level or above (due to a readout time of $\sim$13 μs).

Forward Muon Spectrometer

The muon spectrometer [48] is designed to detect muons in the forward direction. It consists of a passive front absorber (tungsten, lead and stainless steel) to absorb hadrons and photons from the interaction vertex, a high-granularity tracking system (gaseous) of 10 detection planes, a large dipole magnet, with a nominal field of 0.7 T and a horizontal field perpendicular to the beam axis, a passive muon filter wall followed by four planes of trigger chambers (Resistive-Plate Chambers (RPCs)) and an inner beam shield to protect the chambers from particles and secondaries produced at large rapidities.

2.1.4. Other detectors

Vertex 0 (V0) detector

The V0 [48] is a scintillator counter. It is a small angle detector consisting of two arrays; called V0A and V0C, that are installed on either side of the ALICE interaction point. It provides a minimum-bias trigger for the central-barrel detectors in pp and Pb–Pb collisions and two centrality triggers in Pb–Pb collisions at the trigger level L0. It serves as a centrality indicator via the multiplicity recorded in the event. Further, it contributes to the rejection of beam-gas interactions and provides background rejection for the di-muon spectrometer.

Time 0 (T0) detector

The T0 is [48] a Cherenkov counter. It generates a T0 signal for the TOF detector with a resolution of about 50 ps. It measures the vertex position (with a precision $\pm$1.5 cm) for each interaction and provides a L0 trigger when the position is within the preset values. It gives a fast evaluation of the multiplicity in Pb–Pb collisions. It also provides an early wake-up signal to the TRD, prior to L0.

ALICE COsmic Ray DEtector (ACORDE)

ACORDE [35] is a plastic-scintillator counter. It is placed on the upper surface of the L3 magnet. It provides a fast L0 trigger signal, when atmospheric muons impinge upon the ALICE detector. Further, It detects, in combination with the ITS, TPC, TRD and TOF, very rare high multiplicity muon events [49].

Subdetector	**Acceptance**		Position	Technology	Main Purpose
	Polar	Azimuthal			
ITS	$\|\eta\| < 0.9$	full	$3.9 < r/\text{cm} < 43$	Si (pixel, drift, strip)	tracking, vertex, PID
TPC	$\|\eta\| < 0.9$	full	$85 < r/\text{cm} < 247$	Ar(Ne) drift + MWPC	tracking, PID
TRD	$\|\eta\| < 0.8$	full	$290 < r/\text{cm} < 368$	TR+Xe drift + MWPC	tracking, $e^{\pm}$ ID
TOF	$\|\eta\| < 0.9$	full	$370 < r/\text{cm} < 399$	MRPC	tracking, PID
EMCAL	$\|\eta\| < 0.7$	$80^{\text{o}} < \phi < 187^{\text{o}}$	$430 < r/\text{cm} < 455$	Pb+Scintillator	photons and jets
PHOS	$\|\eta\| < 0.12$	$220^{\text{o}} < \phi < 320^{\text{o}}$	$460 < r/\text{cm} < 478$	Ar(Ne) drift + MWPC	tracking, PID
HMPID	$\|\eta\| < 0.6$	$1^{\text{o}} < \phi < 59^{\text{o}}$	$r = 490$ cm	C_6F_{14}+RICH+MWPC	PID
ACORDE	$\|\eta\| < 1.3$	$30^{\text{o}} < \phi < 150^{\text{o}}$	$r = 850$ cm	Scintillator	Cosmic trigger
PMD	$2.3 < \|\eta\| < 3.9$	full	$z = 367$ cm	Pb + PC	photons
FMD	$3.6 < \|\eta\| < 5$	full	$z = 320$ cm	Si strip	charged particles
	$1.7 < \|\eta\| < 3.7$	full	$z = 80$ cm	Si strip	charged particles
	$-3.4 < \|\eta\| < -1.7$	full	$z = -70$ cm	Si strip	charged particles
V0	$2.8 < \|\eta\| < 5.1$	full	$z = 340$ cm	Scintillator	charged particles
	$-3.7 < \|\eta\| < -1.7$	full	$z = -90$ cm	Scintillator	charged particles
T0	$4.6 < \|\eta\| < 4.9$	full	$z = 370$ cm	Quartz	time, vertex
	$-3.3 < \|\eta\| < -3$	full	$z = -70$ cm	Quartz	time, vertex
ZDC	$\|\eta\| > 8.8$	full	$z = \pm 113$ m	W+quartz	forward neutrons
	$6.5 < \|\eta\| < 7.5$	$\|\phi\| < 10^{\text{o}}$	$z = \pm 113$ m	brass+quartz	forward protons
	$4.8 < \|\eta\| < 5.7$	$\|2\phi\| < 32^{\text{o}}$	$z = 7.3$ m	Pb+quartz	photons
MCH	$-4 < \|\eta\| < -2.5$	full	$-14.2 < z/\text{m} < -5.4$	MWPC	muon tracking
MTR	$\|\eta\| < 0.12$	full	$-17.1 < z/\text{m} < -16.1$	RPC	muon trigger

Table 2.1.: The ALICE sub-detectors. The transverse and longitudinal coordinates r, z are measured with respect to the ALICE interaction point (IP2). The z axis points along the counterclockwise LHC beam.

2.2. Time Projection Chamber (TPC)

The ALICE TPC [40] is the main tracking, pattern recognition, and particle identification device in ALICE. It was designed to perform well at multiplicities of up to $\mathrm{d}N_{\mathrm{ch}}/\mathrm{d}\eta = 8000$, which would result in about 20000 charged primary and secondary tracks emerging from Pb–Pb collisions at a center of mass energy of $\sqrt{s_{\mathrm{NN}}} = 5.5$ TeV. The TPC covers the momentum range $0.1 - 100$ GeV/c within the pseudorapidity range $|\eta| < 0.9$. The details about the TPC are given below.

2.2.1. Layout of the TPC

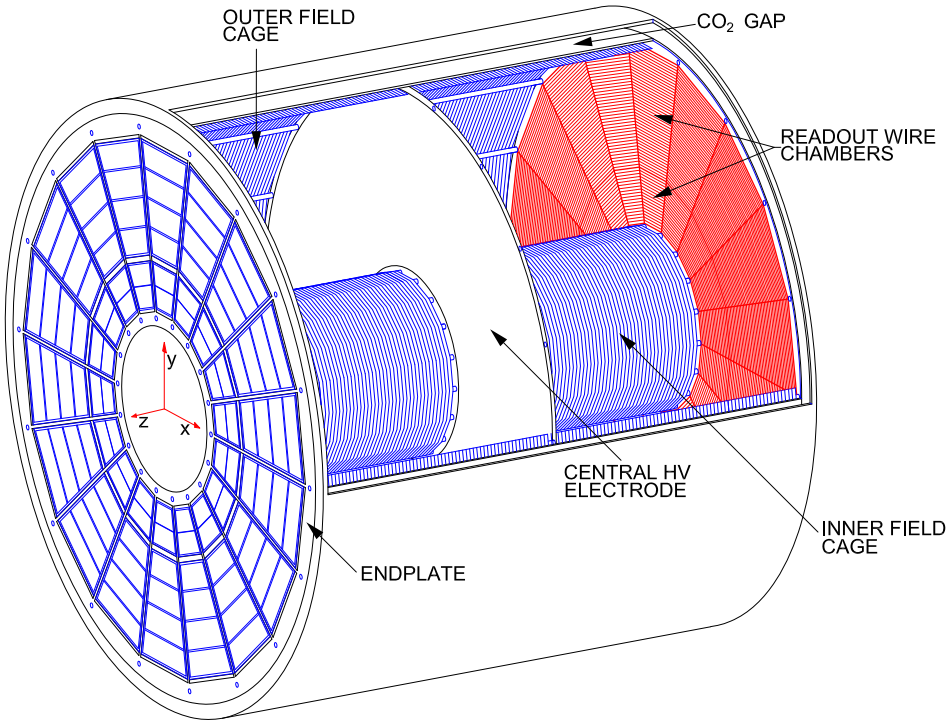

Figure 2.2.: Layout of the TPC [50].

The layout of the TPC is shown in Figure 2.2. The TPC, which has a volume of 88 m^3, an active radial range from about 85 to 247 cm (See Table 2.1) and an overall length along the beam direction of 500 cm, is made of a large cylindrical vessel filled with a gas mixture of Ar-CO_2 (88-12). It is divided equally into two readout sides (A- and C- Side) by a Central Electrode (CE). The readout chambers are positioned on the endplates.

The main purposes of the field cage [50–52] is to define a uniform electrostatic field in the gas volume and, together with the endplates, to provide a stable mechanical structure for precise positioning of the chambers and other detector elements. At the center of the field cage the central electrode, made of a stretched 30 μm thick aluminised mylar foil, is located perpendicularly to the beam axis with a mechanical stability and precision of 250 μm in the position (Figure 2.2).

Owing to the choice of the gas composition used in the TPC, the field cage has to be operated at a rather high drift field of 400 V/cm, with a high voltage of 100 kV at the

CE. This results in a drift time of about 96 μs. Four opposite axial potential degraders with suspended strips provide the uniformity of the drift field on either side of the central electrode. This minimizes the electric field distortions inside the drift volume.

Readout chambers:

The overall design of the readout plane, which is based on conventional multi-wire proportional chambers, has been optimized with respect to the high-multiplicity environment of a central Pb–Pb collision. The azimuthal segmentation of the readout plane is common with the subsequent ALICE detectors TRD and TOF, i.e. 18 trapezoidal sectors, each covering 20° in azimuth. Further, the radial dependence of the track density leads to a radial segmentation of the readout plane into Inner (IROC) and Outer (OROC) ReadOut Chambers within one sector. The TPC thus has 36 sectors each having 159 radial pad rows, resulting in a total of 570132 pads and a total active area of ∼32.5 m^2.

Chamber Type	Pad Size [mm^2]	Number of Pad Rows
IROC (81.1 – 132.1 cm)	4×7.5	63
OROC (134.6 – 198.6 cm)	6×10	64
OROC (198.6 – 246.6 cm)	6×15	32

Table 2.2.: Pad sizes and number of pad rows within a sector.

In the offline code a specific numbering convention [53], with the view point of the interaction point, is used for the 72 ROCs as seen in Figure 2.3. Numbering always starts with zero, from left to right, and from bottom to top. For instance, the pads are aligned in rows numbering from left to right while the padrows are counted from small to large radii.

The readout chambers [50] are made of standard wire planes: a grid of anode wires

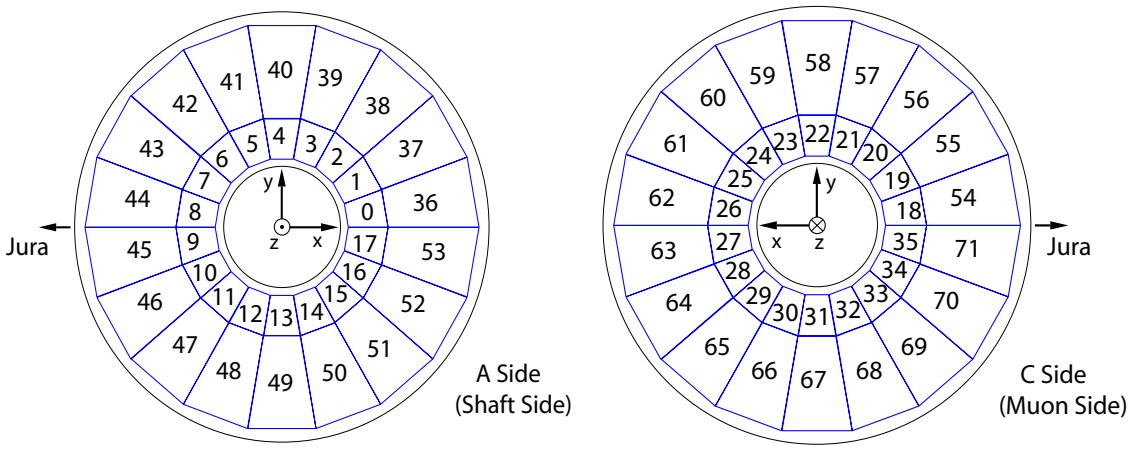

Figure 2.3.: Numbering of the 72 ROCs in the offline code [53].

above the pad plane, a cathode-wire grid, and a gating grid facing the drift volume (Figure 2.4). All wires run in the azimuthal direction. Since the design constraints are different for the inner and outer chambers, their wire geometry is different (Figure 2.5).

In view of cost and the granularity resulting from the diffusion, the pad size cannot be chosen arbitrarily. The goal is to find a pad configuration for which the resulting

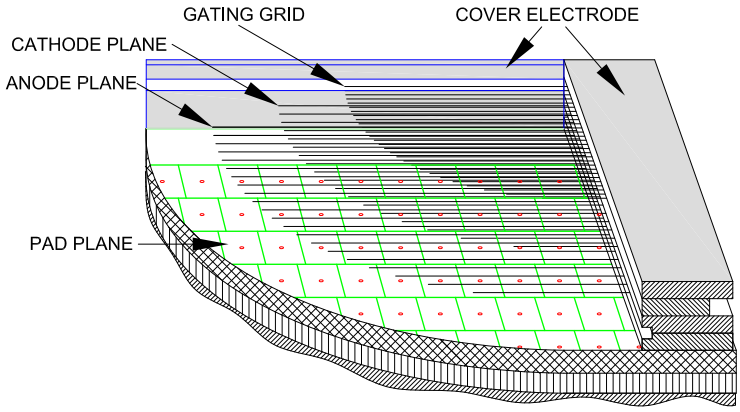

Figure 2.4.: Cross section through a readout chamber showing the pad plane, the wire planes and the cover electrode [50].

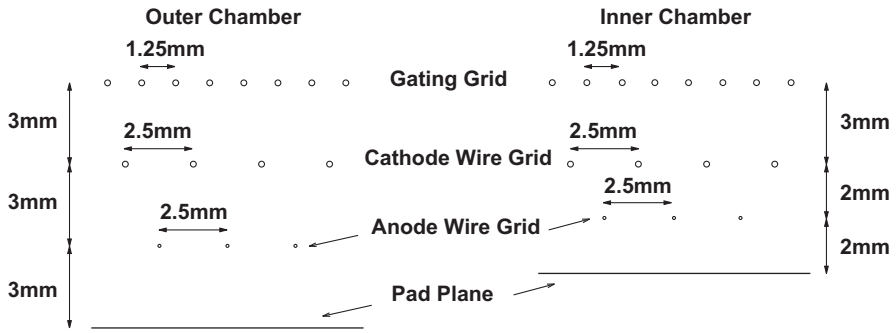

Figure 2.5.: Wire geometries of the outer and inner readout chambers [50].

single-track cluster area is minimal. The readout pad structure, therefore, has been optimized for signal-to-noise ratio and position resolution at the desired gas gain. The adopted pad sizes and number of pad rows, as well as the effective active radial length (taking edge effects into account) of the ROCs are summarised in Table 2.2.

Front-End Electronics (FEE):

The Front-end Electronics (FEE) reads out the charge detected by the 570132 pads from the cathode pad plane of the readout chambers. It can be divided into two parts; the Front-end Cards (FECs) and the Read-out Control Units (RCUs).

FEC: The actual signal processing is done by the FECs located 7 cm away from the pad plane and connected via flexible Kapton cables. The FEC contains the complete readout chain for the amplification, shaping, digitization, processing and buffering of the TPC signals. The main parts of the FEC are Pre-Amplifier/Shaper chips (PASAs) and Alice TPC Readout Chips (ALTRO) each of which handles 16 channels. Each FEC houses 8 PASAs and 8 ALTRO chips, 128 channels in total [54].

A scheme of the data flow of one channel is displayed in Figure 2.6. The charge signal from the pads is passed to the FECs and transformed into a differential semi-Gaussian voltage signal by the PASA with a rise time of 120 ns and a shaping time (FWHM) of

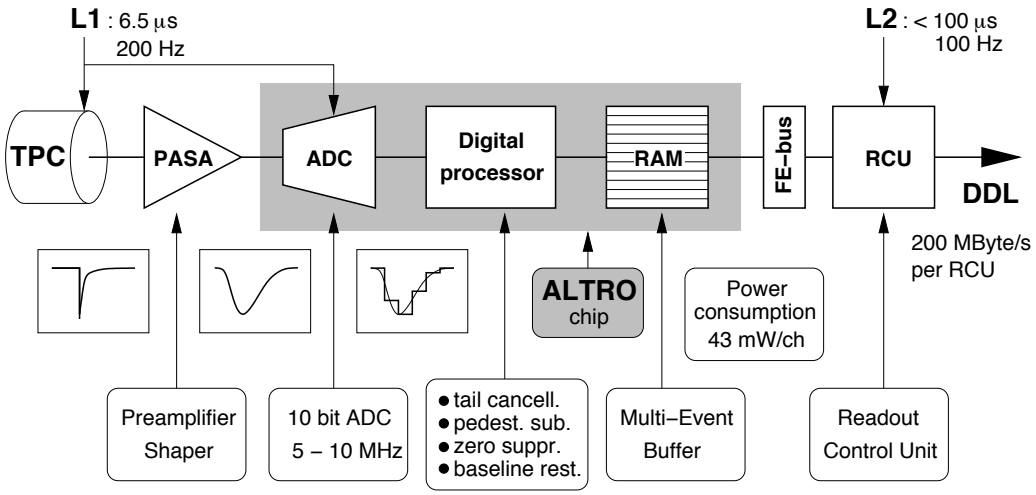

Figure 2.6.: Block diagram of the TPC front-end electronics [55].

about 190 ns. The shaping function is illustrated in Figure 2.7. Each channel of the ALTRO chip has three components; a 10 bit Analogue-Digital-Converter (ADC), a digital circuit with several digital filters and a multi-event buffer. The output signal of the PASA chip is digitized by a 10 bit ADC capable of 10 million samples per second. The digitized signal is then processed by a set of circuits that perform: first baseline correction, tail cancellation, second baseline correction, zero-suppression and data formating, respectively. An important feature is that processing parameters and algorithms can be reconfigured.

RCU: One TPC sector is subdivided into 6 partitions; two for the IROC and four for

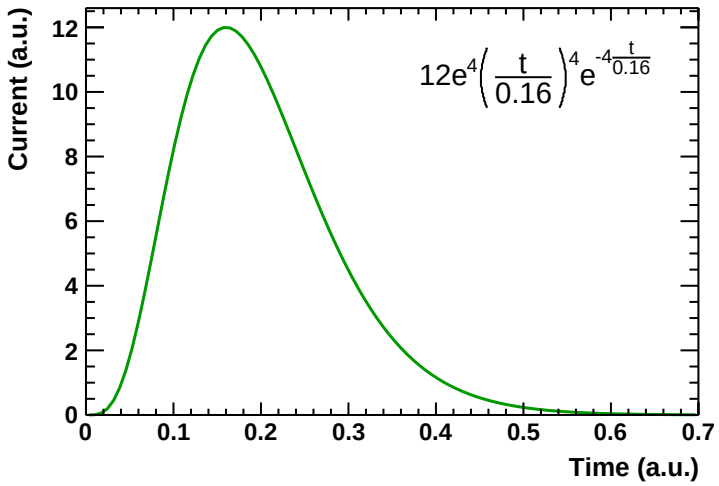

Figure 2.7.: Shaping function used in the FEE.

the OROC, each controlled by one RCU. Depending on the radial position in the sector, one partition may have 18 to 25 FECs. The RCU provides core functionality to configure, trigger, readout, monitor and debug the FEE. It acts as a bridge between the FECs and the DAQ, DCS and the trigger system of the TPC (Appendix A). Data are forwarded from the RCU by means of an optical fiber, the Detector Data Link (DDL), to the DAQ.

A DCS board equipped with an embedded ARM processor running Linux is attached to the RCU for control and monitoring. From the readout and control point of view, each partition represents an independent system.

The TPC data acquisition is started either upon a L0 or upon a L1 trigger, according to the configuration of the trigger detectors participating in the run, whereas the readout process starts after a L2 trigger (Appendix A). Between triggers, the data stream is processed by the digital filter circuits and then stored temporarily in a buffer. When the L2 trigger is received, this data is frozen in memory and shipped to the data acquisition system. Otherwise the data is overwritten. This process defines two contributions to the dead-time generated by the TPC: detector dead-time, i.e. the drift time, and the FEE dead-time (event readout time). Whenever the TPC cannot process any further events, a signal (busy signal) is asserted to prevent the Central Trigger Processor (CTP) from issuing subsequent triggers.

Gas mixture:

The gas mixture of the ALICE TPC is expected to provide saturated high electron drift velocity, low electron diffusion, high gain and resolution, high ionisation rate, high stability, large ion mobility, low-Z and low dependence to the external parameters. But unfortunately it is impossible to handle all those requirements at the same time. Therefore an optimization process had to be carried out [56].

The selection of the main gas component and the quencher was made by a process of elimination rather than choosing the gas by its merits. The resulting candidates for the ALICE TPC, on grounds of ageing, inflammability, toxicity, neutron capture, density and price, are Argon, Neon and CO_2. But none of them is satisfactory as sole ingredient in view of operational stability, drift velocity and diffusion. Therefore a mixture, such that Argon or Neon nobel gases as main component and CO_2 as the quencher, was chosen.

Adding CO_2 reduces the transverse diffusion due to its large electron scattering cross

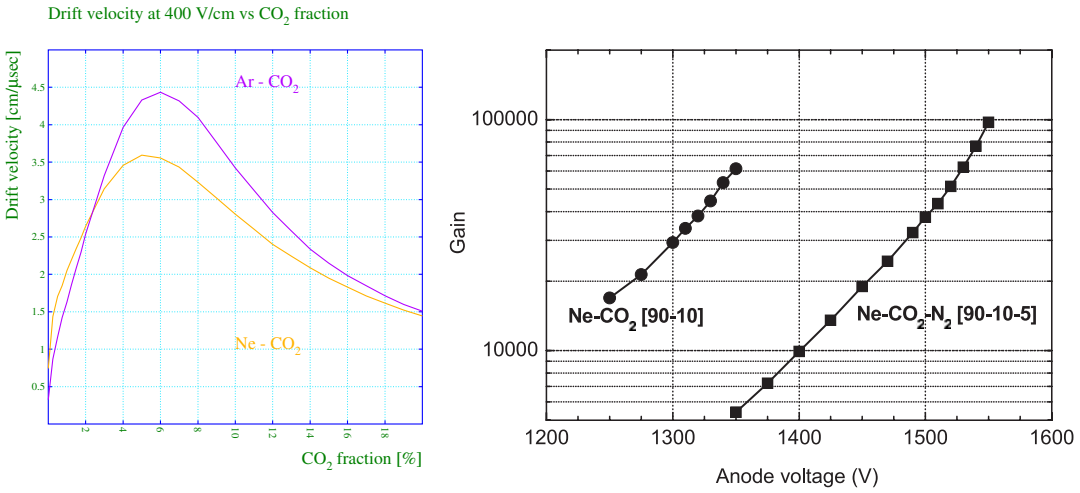

Figure 2.8.: (Left) CO_2 dependence of the relative change of the drift velocity for the Ne-CO_2 and Ar-CO_2 gas mixtures [56]. (Right) Comparison of gas gain as a function of the anode wire voltage for a Ne-CO_2 and a Ne-CO_2-N_2 gas mixture [52].

section. This results in an increase in the drift velocity up to a CO_2 fraction of about 6% and then a decrease as seen in Figure 2.8. Eventually, as a compromise for as much CO_2

as possible to increase operation stability and little enough CO_2 to have a reasonable drift velocity the CO_2 concentration was tuned to be 10%.

Owing to the non-saturated drift velocity in the TPC, the exact composition of the

Gas	Symbol	Density ($mgcm^{-3}$)	E_x (eV)	E_I (eV)	W_I (eV)	$dE/dx\ \|_{min}$ ($keVcm^{-1}$)	N_P (cm^{-1})	N_T (cm^{-1})
Neon	(Ne)	0.839	16.7	21.6	37	1.45	13	40
Argon	(Ar)	1.66	11.6	15.7	26	2.53	25	97

Table 2.3.: Properties of Argon and Neon at normal temperature and pressure (20°, 1 atm). E_x: first excitation energy, E_I: first ionization energy; W_I: average energy per ion pair; $dE/dx|_{min}$, N_P, N_T: differential energy loss, primary and total number of electron-ion pairs per cm, for unit-charge minimum-ionizing particles [4].

gas needs to be monitored carefully. The TPC uses a recirculating gas system due to its large volume [50] and the price of Neon. This makes the external gases, mainly N_2, O_2 and H_2O, mix in the system indispensable. Since O_2 has the very unfavorable effect of causing electron attachment, they have to be removed from the gas. One should also note that 100 ppm H_2O is nevertheless kept, in spite of its feature of reducing the ion mobility [57], because it reduces the discharge probabilities at the inner surfaces of the TPC.

Short story of the gas mixture in view of the High Voltage (HV) trips and damage in the electronics:

The Argon-based mixtures have higher number of ionization ions per unit length and a lower ion mobility. These ions, a factor of ∼1.7 slower than the ions in Neon, enhance the space-charge effect and thus lead to sizeable field distortions and spatial corrections of the order of few cm. The gas mixture, hence, was chosen to be Ne-CO_2 (90-10) in the TDR [40]. Throughout the RUN1 (2009–2013) period of the LHC running Neon was used as the noble gas.

Besides, it was decided to add N_2 to the gas mixture [52] in order to improve the stability of the readout chambers at relatively higher gains of about 2×10^4, with the cost of reduction of the drift velocity at the nominal field by about 5% (Figure 2.8). Moreover, N_2 supports CO_2 as a quencher by reducing the undesirable Penning effect [56] in the avalanche. Therefore, it was decided to keep ∼5% N_2 in the mixture. Consequently, from 2009 to 2011, the gas mixture of Ne-CO_2-N_2 (85.7%-9.5%-4.8%) was used.

Later in the beginning of 2011, increasing interaction rates resulted in High Voltage (HV) trips of the ROCs. The usual suspects were the read-out chambers, gas mixture and beam conditions and quality. From the TPC side, it was first decided to investigate the gas mixture. Initial suspicion was that the N_2 might cause the so-called Self-Quenching Streamer (SQS) discharge [58], and consequently the HV trips. Therefore, first N_2 was removed. This resulted in no change in the rates of neither HV trips nor damage in electronics. Then, the HV capacitors, which is used as a protection for the Common-mode effect (See Section 3.3), were removed. After that, no more damage to electronics were observed but the HV trips remained the same. Additionally, the HV power supplies were replaced. Tuning of the new power supplies drastically decreased the HV trips.

The following attempt was the replacement of Neon with Argon, which is known to be more stable due to its lower excitation energy level (Table 2.3), during the LHC first long shutdown (2013–2015), before the start of RUN2 (2015–2018) period. In the mean

time there were some improvements in the beam line at the beginning of RUN2. On the other hand the increase in the energy, which resulted in lower emittance, i.e. smaller beam radius, also had a positive influence. These two effects dramatically removed the beam background, thus the load in the TPC. Eventually, the trip problem has disappeared, except for the first fills at high luminosity, where many HV trips were observed. All in all, the HV trip problem has disappeared without a full understanding of the main reason.

Currently, the gas mixture Ar-CO_2 (88-12) satisfies most of the requirements of the ALICE TPC, except for the inevitable space-charge distortions which are due to primary ionisation in the TPC volume. Indeed, the known gas properties of Argon-based mixtures allowed for a reasonable estimate for the shape of these distortions and thus a reasonable correction. The correction procedure, as well as the investigation of recently observed local spatial distortions, are detailed in a public note which is currently in preparation.

2.2.2. The TPC laser calibration system

A laser system was constructed for the ALICE TPC as a versatile tool for calibration purposes, which is used to generate straight tracks, similar to ionizing particle tracks, at known positions in the drift volume of the TPC [59]. An overview of the system is shown in Figure 2.9. (Details about the laser system can be found in Appendix E.)

To obtain the best precision of the measured tracks, the geometry is chosen such

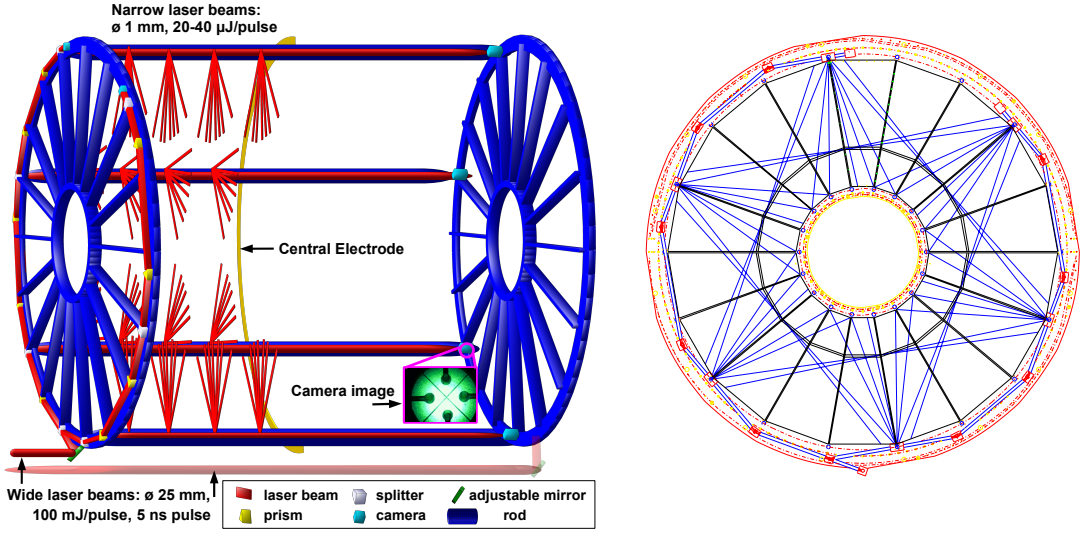

Figure 2.9.: (Left) Schematic 3D view of the TPC and the laser system. (Right) Ideal laser tracks projected to the endcap. The pattern repeats eight times through the full length of the TPC [50].

that the tracks have constant drift times and are perpendicular to the wires. For this configuration, clusters are smallest and the electronics and reconstruction programs give the best possible single-point resolution [60]. In total 336 tracks are generated by two-photon ionization (Appendix D) of the drift gas. For this a pulsed UV laser beam with a wavelength of 266 nm, which is obtained from a Nd:YAG laser (1064 nm), is used [60]. This wavelength corresponds to an energy of $E = h\nu = 4.66$ eV. Most metallic surfaces have work functions below 4.66 eV. Therefore, a considerable amount of low-energy photo-electrons are expected from the CE synchronously with the laser pulse. After a characteristic drift time, nearly each of the readout pads receives this signal.

The reconstructed laser tracks, together with the CE signal, are used for the calibration of the electronics, alignment of the ROCs, studying field distortions and $E \times B$ effects, gain and drift velocity calibration [59]. In this thesis, the signals from the laser tracks are used for the investigation of the TPC signal response.

The data taking system of ALICE is designed to take data in various run configurations, either in dedicated calibration runs with laser triggered events only or in a mode where the laser events are interspersed between physics events. For stand-alone calibration runs, a fixed total number of events (typically 1000-5000) is recorded. In case of physics runs, a set of laser events, a so-called burst, with a fixed number of events (e.g. 100 events) are interleaved between physics triggers. After one burst is taken, the laser is put into a standby mode for a period of about 1 hour. Therefore, depending on the length of the run, one run can include more than one burst. This burst mode of operation is handled automatically by the DCS (Appendix A) and is designed to ensure a reasonably long laser flashlamp lifetime [59].

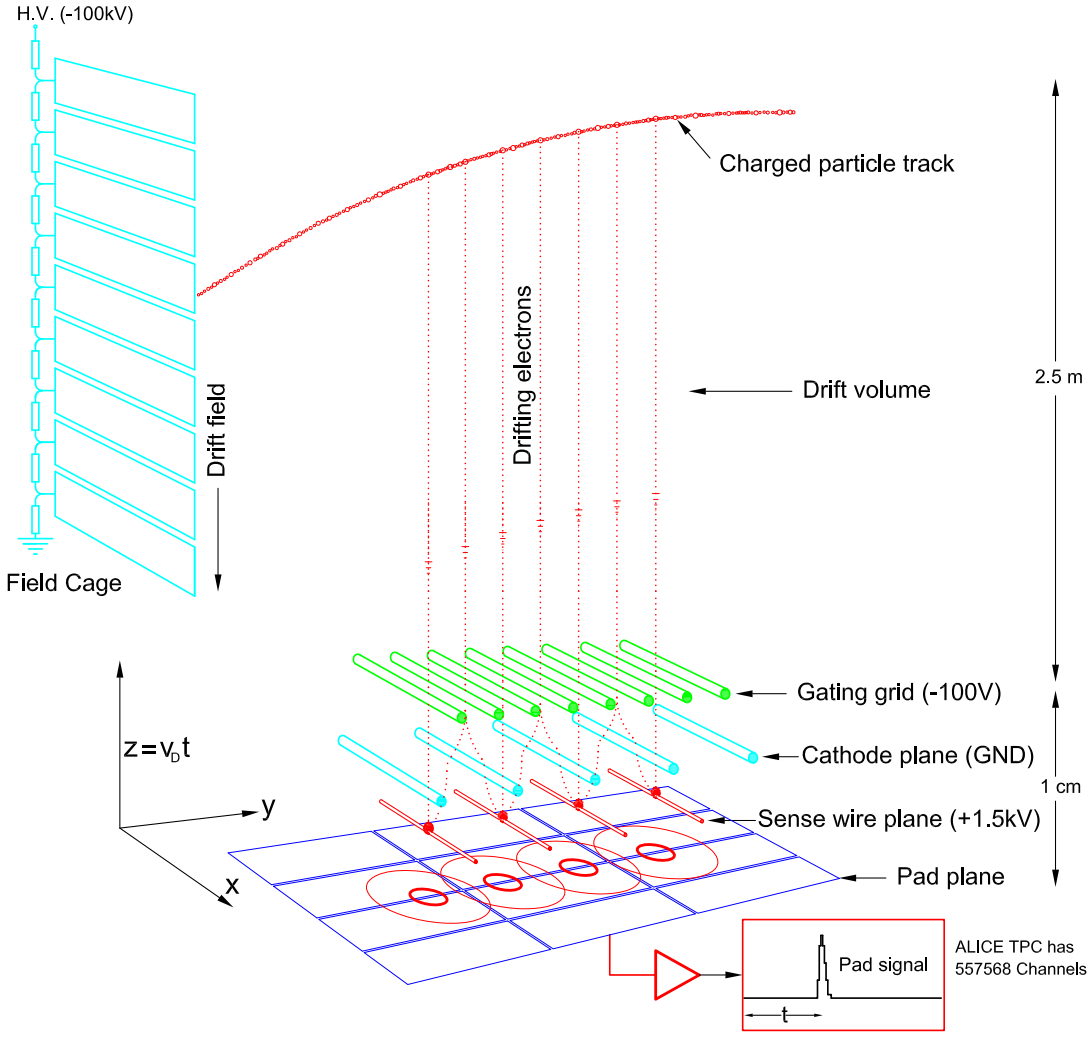

Figure 2.10.: Schematic illustration of the working principle of TPC [61].

2.2.3. Signal creation and readout

A charged particle that traverses the gas in the TPC leaves a track of ionization along its flight path. The TPC provides a complete 3D picture of the ionization deposited in the chamber. The energy loss by ionization reduces the particle's kinetic energy and is typically a few keV per centimeter of gas under normal conditions. The density of the ionization along the track depends on the momentum and type of the particle.

Under the influence of the electric field, ionization electrons drift to either of the two endplates and are amplified at the wires in avalanches (see Appendix C). The electrical signal, obtained by means of the gas amplification, allows the readout electronics to provide the projection of the track. Together with an accurate measurement of the drift time of the electron clusters, with respect to some external reference such as the collision time, a reconstruction software calculates the origin of the ionisation as three-dimensional space points. Afterwards, the complete trajectory of the particle can be determined with precision from the reconstructed space points by a tracking algorithm. Because of the applied magnetic field parallel to the E field inside the TPC, the actual path of the charged-particle is bent according to its charge and momentum. The momentum can then be deduced from the bending radius of the particle trajectory. Finally, together with the known momentum, the measurement of the mean energy loss per track length $\langle \mathrm{d}E/\mathrm{d}x \rangle$ allows for the particle identification.

The energy loss per unit of pathlength due to Coulomb interactions is given by the

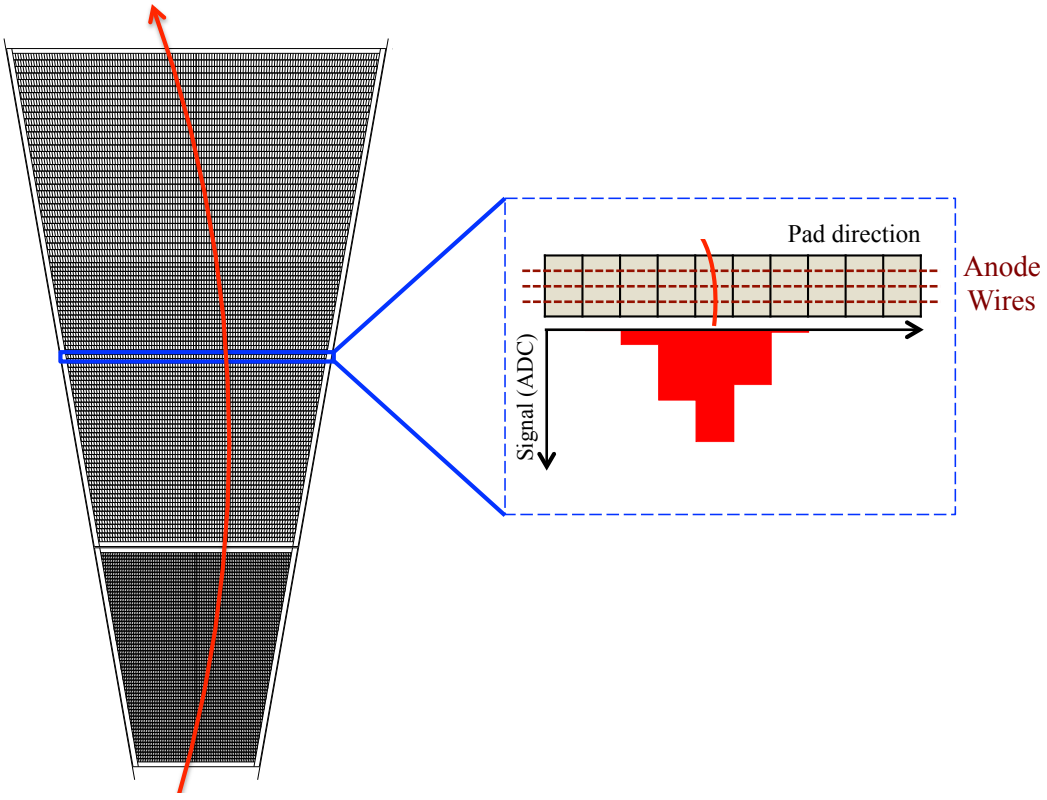

Figure 2.11.: Illustration of a track passing through 159 padrows of a given sector and the corresponding pulse height distribution of a cluster on one padrow. The shape of the signal shown in red is taken form a laser track cluster.

Bethe-Bloch approximation which describes the integral over all the energies lost to the

individual atoms of the medium in the framework of relativistic quantum theory of collisions.

As the drift electrons approach the vicinity of the anode wires, they encounter an electric field increasing with the decreasing distance to the wires. After some point, the energy gained by the electrons between collisions becomes so large that they ionise the gas, producing secondary electrons. This causes an avalanche to start and the initial charge is amplified by a factor of about several thousands depending on the anode high voltage.

The amplification region is defined by the cathode wires, anode wires and the pad plane, as shown in Figure 2.10. The gating grid is located between the cathode wires and the drift region to prevent positive ions, generated in the amplification process, to drift back into the drift volume and create field distortions. The anode wire voltage is chosen such that the produced signal is proportional to the original charge while the signal-to-noise ratio has to be good for position resolution. The proportionality is given as long as the field of the produced ions is negligible compared to that of the wire.

The gating grid works between two modes; closed and open. In the open gate mode, all gating grid wires are held at the same potential V_g, which is defined by the potential of the drift field at the place of the gating grid. In this case, the grid is transparent to charge transport between amplification and drift regions. Therefore the gating grid is closed by default and only opened in case of a triggered event. The opening duration is given by the drift time over the full TPC length $\sim$96 μs. In the closed gate mode a voltage of $V_g \pm \Delta V$ is applied to alternating wires. The necessary value of ΔV, which is given by the magnetic field, the wire spacing, and the drift field, is $\pm$90 V. Further, a gate pulser system has been devised to enable the rapid transition of the gating grid from the closed to the open mode upon the receipt of a trigger [50].

On the other hand, UV photons are also produced in the avalanche. A fraction of these photons are energetic enough to lead to further ionisation. This results in some additional undesired ionisation in the gas and photo electrons from the cathode pads. This effect is removed by the quencher gases (CO_2 and N_2) which have a large number of rotational and vibrational modes i.e. large photoabsorption coefficients.

The ions produced in the amplification process are collected at the cathode wires and the secondary electrons with about 1000 times larger drift velocity of the primaries at the anode wires. The field of the ions induces a mirror charge on the pads which creates the pad signal. The wire geometry is chosen such that on average the signal spreads over three adjacent pads. Determining the center of gravity of the charge distribution, a position resolution much better than the actual pad size is achieved.

2.2.4. Track reconstruction procedure in the TPC

The overall data taking and reconstruction scheme is briefly given in Appendix A. Below, the track reconstruction process in the TPC is summarized.

Clusterization:

The track reconstruction in the TPC starts with the cluster finding. A charged-particle traversing the TPC induces a maximum number of 159 clusters on the padrows. Figure 2.11 shows a schematic view of a charged-particle track and a cluster along its path. A cluster, which is regarded as hit points in the TPC, is defined as peaked deposited charge within a search window of 5 bins in pad and 5 bins in time direction.

In Figure 2.12 a cluster, created by a laser track, before pedestal subtraction and zero-suppression is shown. Because the distribution of primary electrons arriving at the anode wires cannot be considered as point-like, the size and shape of a cluster depend on the diffusion and the track inclination which both spread the ionization in the gas.

In order to reconstruct particle tracks, the space point of each cluster has to be determined. For this, first the local position of a cluster is calculated as the center of gravity in 5×5 pad-time matrix with maxima at the central bin using the following equations

$$C_t = \frac{\sum_{t,b} m_{tb} r_t}{\sum_{t,b} m_{tb}}, \qquad C_p = \frac{\sum_{t,b} m_{tb} r_p}{\sum_{t,b} m_{tb}} \tag{2.1}$$

where r_t, r_p are the positions of the bins in time and pad direction, weighted by the bin content m_{tb} of the corresponding bin, and C_t, C_p are the center of gravity coordinates in time and pad directions, respectively. Each pad and its local coordinate are well defined in the Offline Calibration Data Base (OCDB) with respect to its specific pad number. Accordingly, the center of the pad with the nearest integer number to the C_p was taken to be the center of gravity to obtain the local (x, y) position of the cluster. Second, the z position of the cluster is evaluated from the time-bin and the default drift velocity information, which are also retrieved from the OCDB. Lastly, the final space point of the cluster is calculated making use of the coordinate transformations given in Appendix B.

Moreover, the total charge Q_{tot} (sum of all digits in a cluster) or the maximum

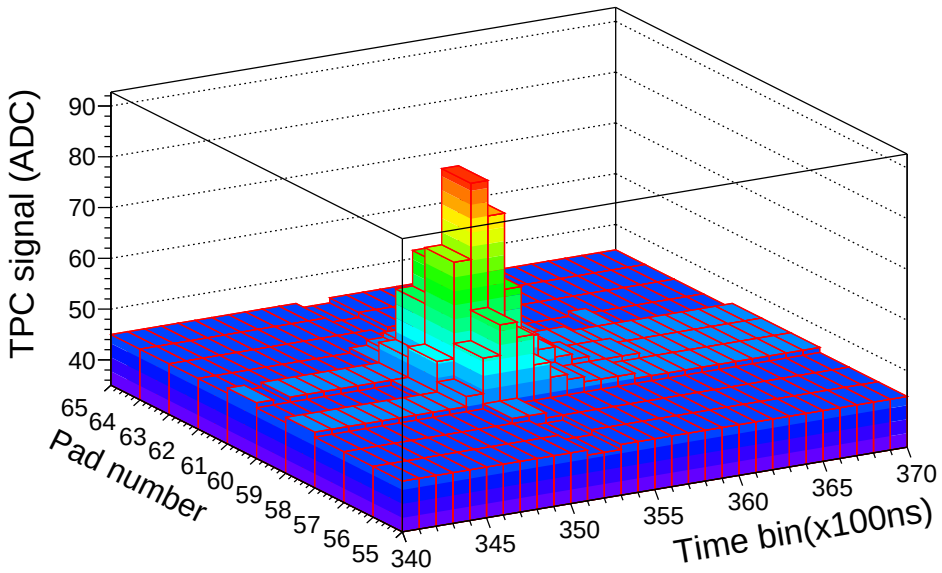

Figure 2.12.: A laser cluster before pedestal subtraction and zero-suppression.

charge Q_{max} (maximum value among all digits in a cluster) of a cluster is used in the calculation of specific energy loss measurement $\mathrm{d}E/\mathrm{d}x$ in the TPC gas. One should also note that, high particle density in the TPC results in an increase in the number of closely spaced tracks, thus overlapping clusters in pad-time space. These clusters are identified using the width of clusters. The characteristics of a cluster are listed in Table 2.4

y, z	Center of gravity
σ_y, σ_z	Shape of the cluster (characterize cluster background for overlapped clusters)
Q_{tot}, Q_{max}	Total charge and maximum amplitude in cluster
C_{type}	Cluster type – characterize the overlap factor (ratio of the charge supposed to be deposited by the track and total charge in cluster)

Table 2.4.: Characteristics of a cluster.

Track finding:

After the reconstruction of clusters containing the space-point information of primary ionisation, particle track finding is carried on. For this, the Kalman-filter approach, which is a method for simultaneous track recognition and fitting is used [62, 63]. Due to the longitudinal magnetic field of the ALICE experiment, charged particles follow a helix trajectory. Therefore in the Kalman-filter approach each track is parametrized with 5 track parameters which are;

- y : local y coordinate of the track at the reference plane $x = x_{\mathrm{ref}}$,
- z : local z coordinate of the track at the reference plane $x = x_{\mathrm{ref}}$,
- k : track curvature. $k = 1/R$, where R is the radius of the circle obtained projecting the track on the bending plane,
- γ : $k \cdot x_0$, being x_0 the local x coordinate of the center of the circle on the bending plane,
- $\tan\lambda$: tangent of the track angle with the bending plane ($\tan\lambda = p_z/p_{\mathrm{T}}$).

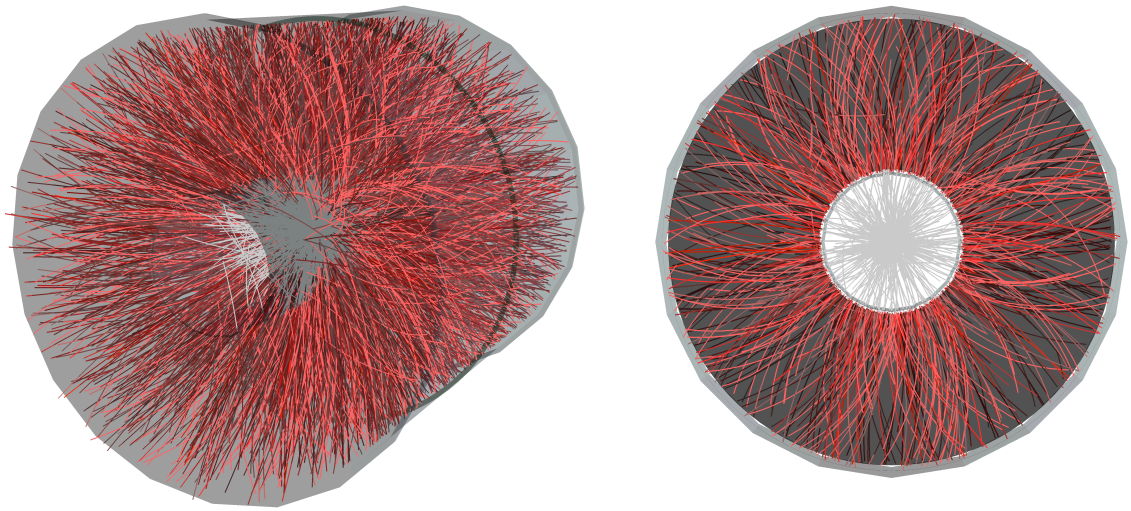

Figure 2.13.: Reconstructed TPC and ITS tracks in a Pb–Pb event at $\sqrt{s_{\mathrm{NN}}} = 2.76$ TeV. TPC and ITS tracks are shown in red and light grey, respectively.

The track finding starts with the determination of the "seed clusters" on the outermost padrows of the TPC (see Appendix A). For each track candidate the prolongation to the next padrow and corresponding nearest cluster is found. The track is then updated according to current cluster parameters and errors. In each padrow several track hypotheses are formed by connecting clusters on neighboring padrows. If the cluster overlap factor, which is defined as the ratio of the clusters shared between two track candidates and the number of all clusters, is greater than a given threshold, track candidate with higher χ^2 or significantly lower number of points is rejected. The χ^2 per cluster is defined as

$$\frac{\chi^2}{n_{\mathrm{cl}}} = \frac{1}{n_{\mathrm{cl}}} \sum_{i=0}^{n_{\mathrm{cl}}} \frac{(y_{i,\mathrm{cluster}} - y_{i,\mathrm{track}})^2}{\sigma_{i,y}^2} + \frac{(z_{i,\mathrm{cluster}} - z_{i,\mathrm{track}})^2}{\sigma_{i,z}^2}, \tag{2.2}$$

where n_{cl} is the number of clusters along the track, σ_y, σ_z are the width of the clusters in pad and drift direction, respectively.

In this way, the prolongation of the track is continued down to the innermost padrow. Also, the Kalman-filter approach makes it possible to reject incorrect space points, which are due to the imperfections of the cluster finder, already at the tracking level. Moreover, it allows for the extrapolation of a track from one detector to another. Reconstructed TPC and ITS tracks in a central Pb–Pb event at $\sqrt{s_{\mathrm{NN}}}$ =2.76 TeV are shown in Figure 2.13.

The performance of the Kalman-filter strongly depends on the occupancies, which is expected to be up to 40% in IROCs and up to 20% in OROCs in the TPC. These high occupancies cause an increase in the number of overlapping clusters. Therefore a certain number of the clusters is lost, and the others may be significantly displaced, which in turn reduces the tracking efficiency. On the other hand, due to the high-voltage setting of the read-out chambers or the baseline fluctuations (see Chapter 3), the collected charge on some padrows might be lower than the zero-suppression threshold and thus causes some clusters to be lost. These missing clusters[1] are identified by looking into the neighboring padrows.

The relative p_{T} resolution is estimated as

$$\frac{\Delta p_{\mathrm{T}}}{p_{\mathrm{T}}} = \frac{r\delta\varphi}{0.3 \cdot B \cdot L^2} \sqrt{\frac{720}{N+4}}, \tag{2.3}$$

where L is the total visible track length, N is the number of space points on the track trajectory, B is the magnetic field and $r\delta\varphi$ is the azimuthal position resolution of a single space point [40]. As can be seen in Eq. 2.3, the relevant quantity for the p_{T}-resolution of a track is the effectively sampled track length of a particle in the TPC. Therefore, the effective track length is taken to be the number of padrows which a track crosses and given as follows

$$n_{\mathrm{eff}} = n_{\mathrm{cl}} + n_{\mathrm{miss}}, \tag{2.4}$$

where n_{cl} is the found clusters and n_{miss} are the missing clusters along the track. Here, one should note that inclusion of the ITS, TRD and TOF in tracking improves the p_{T} resolution significantly.

[1] if there is no reconstructed cluster on pad row i, but clusters are found on the pad rows $i-r$ and $i+r$. The number of padrows between $i-r$ and $i+r$ is considered to be the n_{miss}. The minimum charge of the cluster $i-r$ and $i+r$ is assigned to all missing clusters to be used in the final $\mathrm{d}E/\mathrm{d}x$ calculation of the given track. Consequently, the missing clusters introduce a non-linear effect on the TPC $\mathrm{d}E/\mathrm{d}x$ response.

Specific energy loss dE/dx:

Charged particles passing through the TPC gas lose kinetic energy by ionization processes. The mean rate of energy loss is described by the "Bethe-Bloch formula",

$$\left\langle \frac{\mathrm{d}E}{\mathrm{d}x} \right\rangle = \frac{4\pi N\rho}{mc^2}\frac{Z}{A}\frac{1}{\beta^2}z^2\left(\ln\frac{2mc^2}{I}\beta^2\gamma^2 - \beta^2 - \frac{\delta(\beta)}{2}\right), \tag{2.5}$$

where mc^2 is the rest energy of electron, e is the elementary charge, z is the charge of the traveling particle, β is the velocity of the traveling particle in units of c, γ is the Lorentz factor, N is the Avagadro number, Z and A are the atomic number and mass of the medium, ρ is the gas density, I is the mean excitation energy of the atom calculated by using the Thomas-Fermi theory of the atom and $\delta(\beta)$ is the correction term which accounts for the so-called density effect [64]. It describes the integral over all the energies lost to the individual atoms of the medium in the framework of relativistic quantum theory of collisions. For a given momentum, the mean energy loss of a particle depends only on the charge and mass of the particle.

The $\delta(\beta)$ describes how much the extended transverse electric field of the propagating

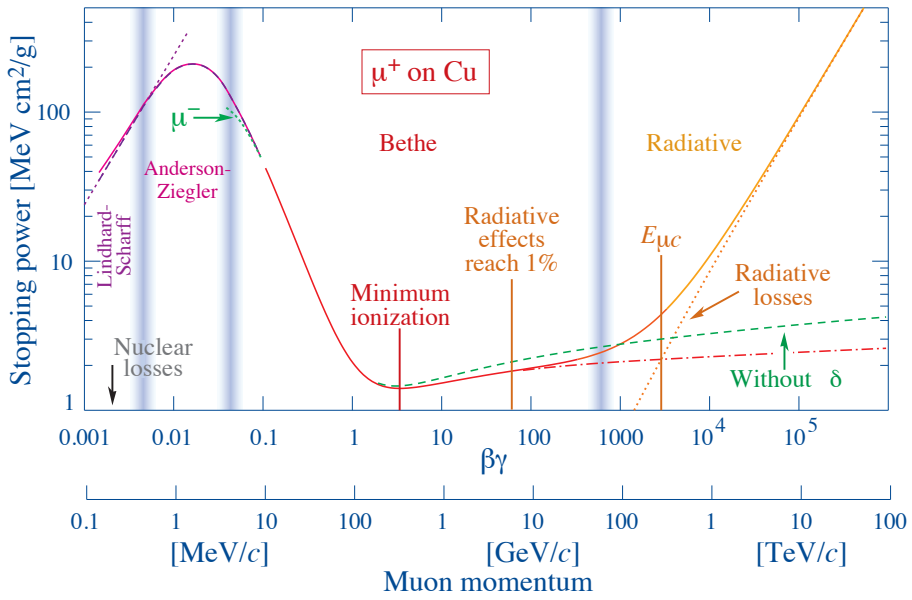

Figure 2.14.: Stopping power ($\langle -\mathrm{d}E/\mathrm{d}x\rangle$) for positive muons in copper as a function of $\beta\gamma$ over nine orders of magnitude in momentum (12 orders of magnitude in kinetic energy) [4].

particle is screened by the charge density of the atomic electrons. As the particle energy increases, its electric field flattens and extends, so that the distant-collision contribution to Eq. 2.5 increases as $\ln\beta\gamma$. However, real media become polarized, limiting the field extension and effectively truncating this part of the logarithmic rise. Therefore, the density effect is important in dense absorber materials and can be neglected for gases under normal pressure and for not too high energies.

The Bethe-Bloch function as computed for muons on copper is shown as the "Bethe" region of Figure 2.14. The mean energy loss behavior is a function of β alone only in this region; the mass dependence is more complicated elsewhere. In practical cases, most relativistic particles (e.g. cosmic-ray muons) have mean energy loss rates close to the

minimum at about $\beta\gamma \approx 3.6$; they are "Minimum-Ionizing Particles (MIPs)". Moreover, in the limit $\beta \longrightarrow 1$ one observes a complete cancellation of the γ dependence and eventually the energy loss reaches a constant value, the so-called "Fermi plateau".

Due to its statistical nature, the energy loss of a particle by ionization deviates from the mean energy loss. The probability distribution of resulting energy loss is described by an asymmetric, so-called "straggling function" [65]. It differs from the Landau distribution in its width, because it takes into account the density correction $\delta(\beta)$. Figure 2.15 shows an example of this distribution which clearly deviates from a Gaussian and slightly differ from a Landau distribution.

Because of the long tail towards higher energy losses in the distribution, the average energy loss is not a good estimator for the mean energy loss of a given track as it would be for a Gaussian distribution. Therefore, a so-called "truncated mean" procedure is applied for each track, where only the smallest 60% of the clusters are used for the $\mathrm{d}E/\mathrm{d}x$ calculation. The threshold of 60% is found to provide the best $\mathrm{d}E/\mathrm{d}x$ resolution [66].

In Pb–Pb events, to avoid drawbacks resulting from the overlapping clusters, the $\mathrm{d}E/\mathrm{d}x$ calculation is based on Q_{max} of the clusters, which provides slightly less separation power for peripheral events, but better separation power in central events. On the other hand, for low multiplicity environments like pp Q_{tot} is used, since it provides the best separation power.

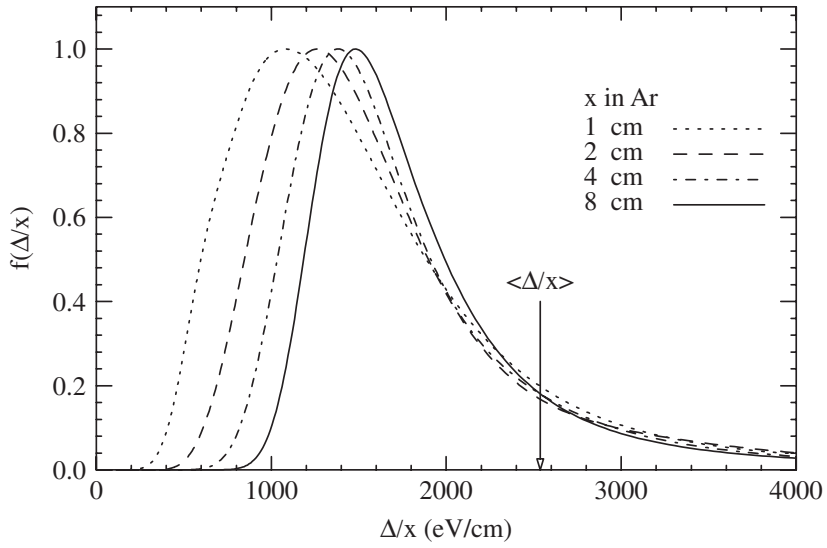

Figure 2.15.: Calculated straggling functions $f(\Delta/x)$ (note that Δ/x is equivalent to $\mathrm{d}E/\mathrm{d}x$) for $\beta\gamma$=3.6 particles (MIPs), traversing layers of Argon in different widths [65].

Separation power and $\mathrm{d}E/\mathrm{d}x$ resolution:

To quantify the performance of particle identification via energy loss $\mathrm{d}E/\mathrm{d}x$, two quantities are used; separation power and $\mathrm{d}E/\mathrm{d}x$ resolution. They are defined as

$$S_{i,j} = \frac{|\mu_i(p) - \mu_j(p)|}{\frac{1}{2}(\sigma_{\mathrm{d}E/\mathrm{d}x,i}(p) + \sigma_{\mathrm{d}E/\mathrm{d}x,j}(p))}, \tag{2.6}$$

$$\sigma_{\mathrm{d}E/\mathrm{d}x} = \frac{\sigma_{\mathrm{d}E/\mathrm{d}x,\mathrm{MIP}}}{\mu_{\mathrm{d}E/\mathrm{d}x,\mathrm{MIP}}}, \tag{2.7}$$

respectively, where $S_{i,j}$ is the separation between particle types i and j, $\mu_i(p)$ is the $\mathrm{d}E/\mathrm{d}x$ signal of particle i at momentum p and MIP stands for the minimum-ionizing particles (pions at $p \approx 400$ MeV/c). Since the best particle identification performance is required in the relativistic-rise region, a quantitative separation power estimate is usually done between minimum-ionizing particles and particles on the Fermi plateau. However, in case of lack of sufficient statistics at the Fermi plateau (in particular for quick performance checks), electrons at $p \approx 300$ MeV/c are used instead. Since the separation power intrinsically contains the $\mathrm{d}E/\mathrm{d}x$ resolution information, it is used as the main quantity for the PID performance checks. Figure 2.16 shows an illustration of a separation power calculation for a small statistics test of HIJING simulation with GEANT3 implementation of the TPC detector setup for central Pb–Pb collisions.

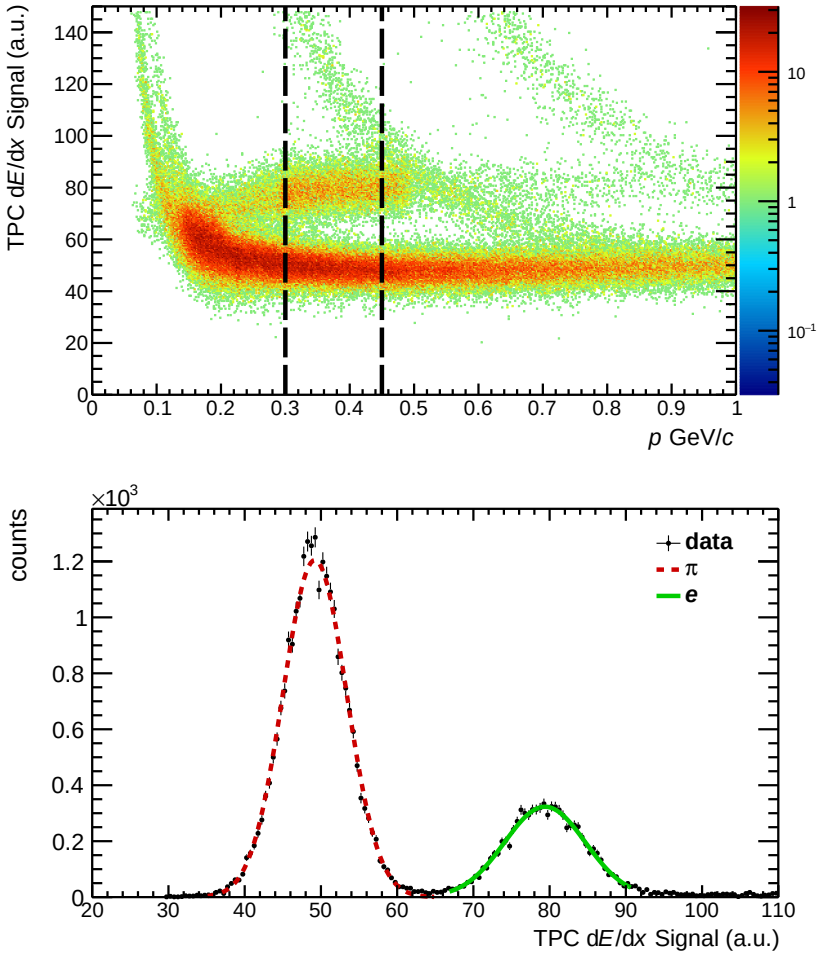

Figure 2.16.: (Top) $\mathrm{d}E/\mathrm{d}x$ spectrum of simulated central Pb–Pb events obtained via HIJING simulation with GEANT3 implementation of the TPC detector setup, where electrons are enhanced by embedding γ conversions in order to obtain sufficient statistics for the fit. Dashed lines depict the momentum range where the separation power calculation is performed. (Bottom) The projection of the marked area of the left plot on the $\mathrm{d}E/\mathrm{d}x$ axis. Red dashed line for the π fit, green solid line for the e fit. Resulting separation power is 6.4 ± 0.04.

2.2.4.1. $\mathrm{d}E/\mathrm{d}x$ calibration in TPC

High values of the separation power can be either achieved by increasing the distance between minimum-ionizing particles and the Fermi plateau or by minimizing the $\mathrm{d}E/\mathrm{d}x$ resolution. The first is mainly due to threshold effects and the baseline fluctuations while the latter is essentially affected by the number of clusters used for PID (n_{PID}) calculation, gain uniformity, cluster shape and primary ionization process. Since the geometrical factors such as pad size and the wire geometry are fixed by construction, the $\mathrm{d}E/\mathrm{d}x$ measurement has to be calibrated for a better and stable PID performance. The following $\mathrm{d}E/\mathrm{d}x$ calibration steps are currently performed in the ALICE TPC:

- **Gas-gain calibration:** To achieve a homogeneous detector response in azimuth, the chamber high-voltages must be adjusted accordingly. For this, standalone Krypton runs, where a radioactive Krypton source is released into the TPC gas, are used. The Krypton clusters, which are measured as the product of radioactive decay processes, produce a similar signal as ordinary charged particles traversing the TPC gas. These clusters homogeneously occupy the TPC gas volume and allows for the extraction of the gain map. All chamber gains agree within 2%

- **Corrections depending on the track topology:** The Pad Response Function (PRF) describes the pulse height distribution on adjacent pads induced by a point-like avalanche, which can be approximated with a Gaussian distribution with a width of 2 mm and 3 mm for IROCs and OROCs, respectively. This approximation holds only if the track passes a padrow perpendicularly. However, the inclination of each track with respect to padrow is different. Thus, the PRF shape deviates from the Gaussian. (Note that, the response in time direction is assumed to be Gaussian for simplicity.) Cosmic tracks have very high momenta ($p > 25$ GeV/c) with vanishing curvature and cover homogeneously all angles and drift lengths, Therefore their $\mathrm{d}E/\mathrm{d}x$ signal is binned in the relevant variables and then fitted to extract the corresponding dependences.

- **Temperature and pressure dependence of gain:** The gas gain depends on the pressure and temperature. The event-by-event $\mathrm{d}E/\mathrm{d}x$ distributions of tracks with a momentum corresponding to minimum-ionizing pions are fitted with a Gaussian function. The mean of this fit as a function of time is used later to extract the time dependence of the gas gain.

- **Electron drift-length dependence (electron attachment):** Due to the electron attachment on oxygen and water contaminations in the TPC gas, a signal loss of several percent per meter of drift occurs. The magnitude of this effect is estimated and corrected by fitting the peak position of the $\mathrm{d}E/\mathrm{d}x$ signal of minimum-ionizing pions in several bins of the drift length.

- **Overlapping clusters:** These clusters are removed by a cut on $\sigma_{\mathrm{meas}}/\sigma_{\mathrm{exp}} < 1.5$, where σ_{meas} and σ_{exp} are the measured and expected cluster width, respectively. The cut value 1.5 is determined in pp collisions where the small tail due to overlapping clusters is clearly visible in the distribution.

- ***Threshold effects and baseline fluctuations due to ion-tail and common-mode effects:*** The details on the $\mathrm{d}E/\mathrm{d}x$ calibration can be found in [66], while calibration procedures developed for the baseline fluctuations due to ion-tail and

common-mode effects are extensively discussed in the next chapter. One should also be aware of the interdependency between calibration parameters. For instance, a change in the gas mixture not only requires a recalibration of the chamber gain but also a new parametrization of the ion-tail response.

2.2.5. Performance of the TPC

Since the TPC is the main tracking and PID detector in ALICE, its performance is crucial for the overall PID quality of the ALICE experiment in particular for the high-multiplicity environment. However, its performance goals are limited by operational concerns such as the choice of gas mixture, acceptable drift time, allowed maximum gain etc. Therefore, to achieve a high and stable performance for the physics analysis, an elaborate calibration of the TPC data is necessary. The main goal of the calibration is to provide the information needed for the offline software for the reconstruction of the particle tracks with sufficient precision. To this end, several calibration passes are applied to the TPC data during the raw data reconstruction. In each calibration step several observables such as MIP position, Distance-of-Closest Approach (DCA), separation power etc. are monitored run-by-run as a part of an automatized TPC Quality Assurance (QA) procedure. Automatically generated plots are also available via a web interface.

The three most important parameters to judge the performance of the TPC are track-

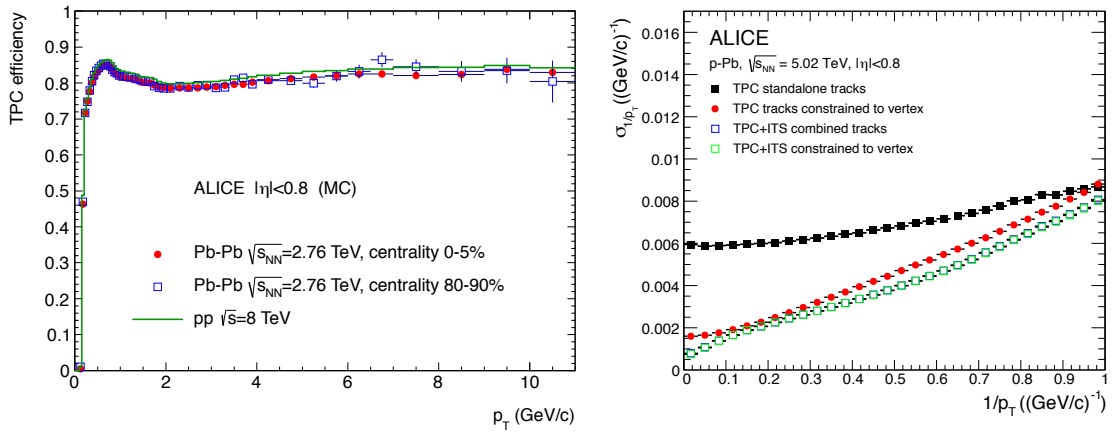

Figure 2.17.: (Left) TPC track finding efficiency for primary particles in pp and Pb–Pb collisions (simulation). (Right) The p_{T} resolution measured in p–Pb collisoins for standalone TPC and ITS–TPC matched tracks with and without constraint to the vertex [67].

ing efficiency, momentum resolution and the separation power. The p_{T} resolution for TPC standalone tracks and ITS–TPC combined tracks measured in p–Pb collisions, is shown in Figure 2.17 right plot. The effect of constraining the tracks to the primary vertex is shown as well. The inverse-p_{T} resolution, plotted in this figure, is connected to the relative transverse-momentum resolution via $\sigma_{p_{\mathrm{T}}}/p_{\mathrm{T}} = p_{\mathrm{T}}\sigma_{1/p_{\mathrm{T}}}$. In central Pb–Pb collisions, the p_{T} resolution is expected to deteriorate by about 10–15% at high p_{T} due to the loss (or reduction) of clusters sitting on ion tails, cluster overlap and fake clusters attached to the tracks.

The left plot in Figure 2.17 shows the tracking efficiency of the TPC as a function of transverse momentum. The drop below 0.5 GeV/c is caused by the energy loss in the detector material, while the characteristic shape at larger p_{T} is determined by the loss of

clusters in the dead zones between readout sectors. The efficiency is almost independent of the occupancy in the detector. Further details on the TPC design performance goals and the recent performance can be found in [40] and [67], respectively.

Figure 2.18 shows the separation power performance of the TPC in the RUN1 Pb–Pb data taking period in 2010. The mean dE/dx signal for minimum-ionizing pions, the separation between electrons and minimum-ionizing pions and resulting separation power measured in the TPC are shown on a run-by-run basis. Different lines indicate allowed ranges for the given quantity. Additionally, electron drift velocity, ITS–TPC track matching efficiency, mean number of clusters per track etc. shown on the bottom of each plot are also monitored for a global evaluation of the data quality of a given run. Green color refers to runs that can be considered as "GOOD" for the physics analysis while red is "BAD".

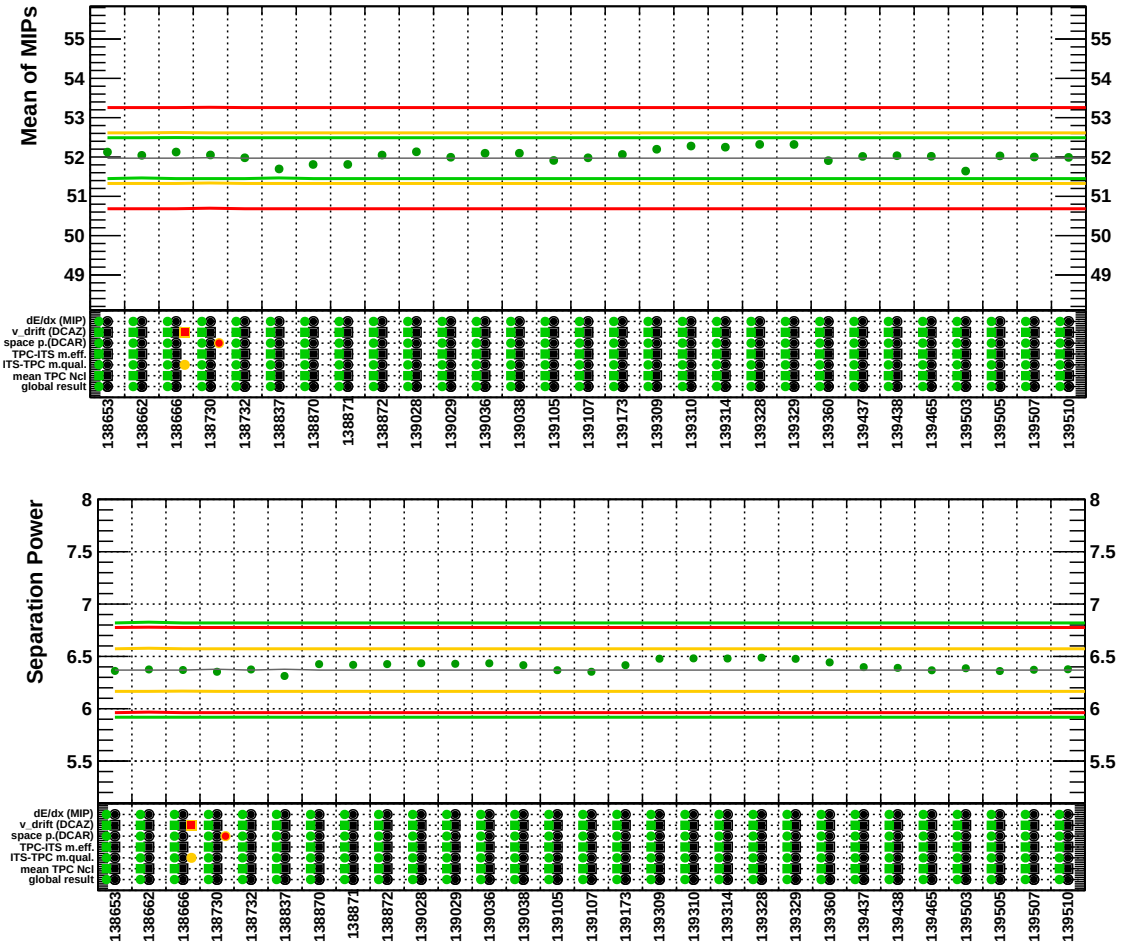

Figure 2.18.: (Top) Mean dE/dx signal for minimum-ionizing pions and (Bottom) separation power between electrons and minimum-ionizing pions measured in the TPC for the first runs of the 2010 Pb–Pb data taking.

3. The Effect of the TPC Signal Shape Distortions on the Particle Identification and its Correction

The most relevant correction of the charge measurement in the TPC in a high-multiplicity environment was found to be the so-called "Ion-tail" and "Common-mode" effects which cause significant baseline shifts and fluctuations. Below the nature of these effects in view of the investigation of the TPC signal characteristics is described in detail. Results are also crosschecked with three-dimensional Garfield simulations. Following the detailed analysis of the TPC signal shape, an offline correction procedure for ion-tail and common-mode effects, as well as two alternative online correction approaches for common-mode effect only, are discussed below.

3.1. "Black" laser data for the TPC signal shape analysis

As explained in Section 2.2, the mirror charge induced on the pads by the ions produced in the avalanche creates the pad signal. This signal is subsequently shaped in the FEE and finally the zero-suppression is applied to cut the electronic noise in order to reduce the data size for online data handling and storage. For the study of signal shape the so-called "black" data is used, which is the pad signal after shaping and before the zero-suppression. An example black event with an additional pedestal shift of 50 ADC is shown in Figure 3.1.

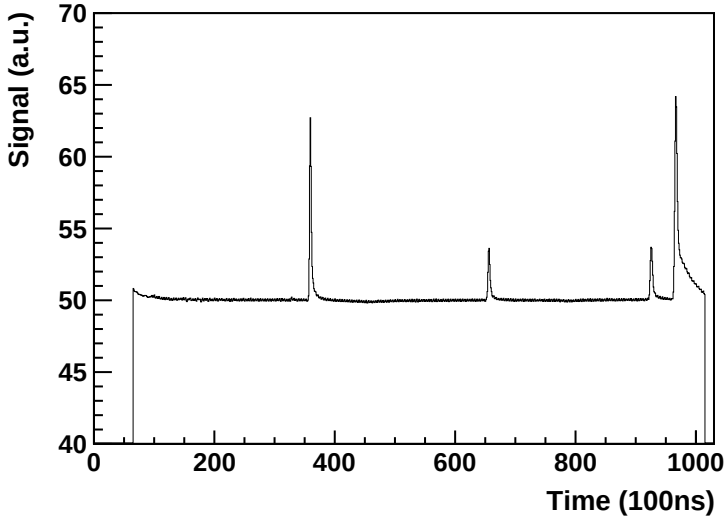

Figure 3.1.: A non-zero-suppressed TPC laser signal from a single pad.

There are several challenges in the signal shape analysis. Since the characteristic un-

dershoot due to the ion-tail spreads over tens of microseconds and the magnitude of the undershoot is comparable to the electronics noise, one requires a data set with low track density so that the signal tail is not distorted by other tracks and high statistics to get a better resolution of the tail shape. Moreover, the sensitivity of the signal shape to the geometry (distance between the wires and pad width) and gas mixture rules out the usage of any external prototype. Therefore, in the past, either cosmic or pp events were used. The TPC laser data was not considered due to the repetitive structure of the laser tracks in the drift direction of the TPC and the short distances between the laser layers as seen in Figure 3.1. Details on the TPC laser system are given in Section 2.2 and Appendix E. The ideal laser track positions stored in the Offline Calibration Database (OCDB) and the reconstructed clusters of the laser tracks read out in a stand-alone laser calibration run are shown in Figure 3.2.

It was found that the imperfections in the positioning of laser tracks lead to a number

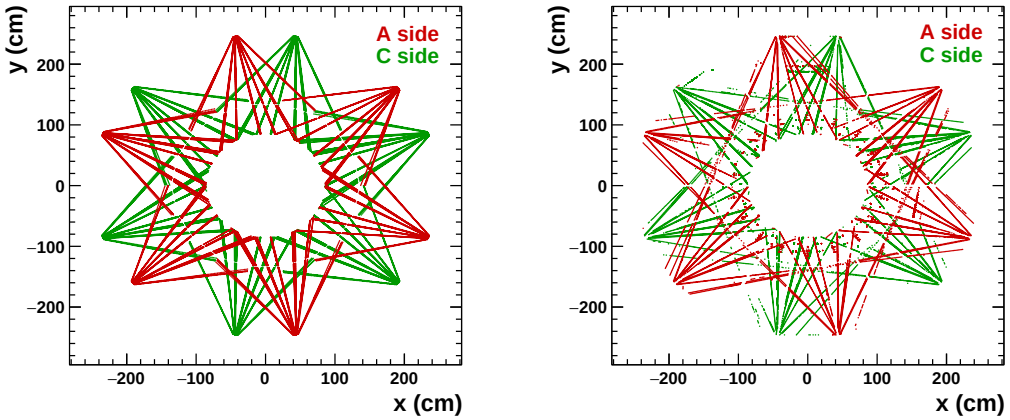

Figure 3.2.: (Left) Ideal laser track positions stored in the Offline Calibration Database (OCDB). (Right) Reconstructed clusters of the laser tracks read out in a stand-alone laser calibration run. The pattern repeats eight times through the full length of the TPC.

of pads with clean tails. Figure 3.3 shows an example sector and a typical laser signal including the ion-tail. The sharp dip at ∼680 μs corresponds to the common-mode signal which is induced by the other pads in the same anode wire segment. The common-mode effect will be discussed later in this chapter.

Since the laser system can run standalone it has several advantages:

- a typical standalone laser run takes about 5-10 minutes,
- data size can be minimized by using only two (one IROC and one OROC) sectors which is enough for the whole signal shape analysis,
- it allows for the study of the same pad signals which eliminates possible chamber-to-chamber fluctuations.
- this allows for tuning of the signal-to-noise ratio by changing the laser beam intensity and number of events.

All these arguments make the laser system an ideal tool for the analysis of the TPC signal shape.

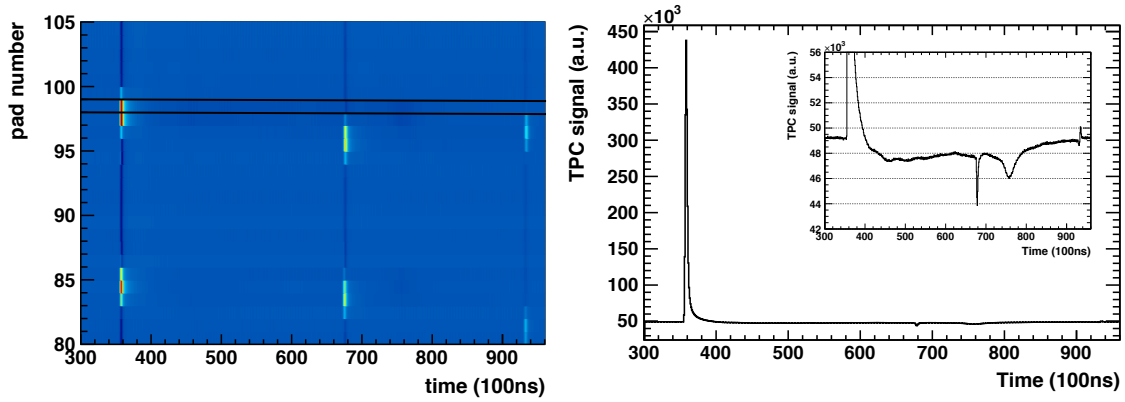

Figure 3.3.: Typical laser signal integrated over 1000 laser events. Non-zero-suppressed TPC signals for 25 pads are shown in the left plot, where the two solid horizontal black lines indicate the pad whose signal is shown in the right. The ion-tail (zoom into signal (y) axis) structure of the main pulse is shown as the inset of the right plot.

3.2. Ion-tail effect

Ion-tail shape analysis was performed in one IROC (16) and one OROC (61) which were found to have a weak third laser layer, thus a clean signal tail of the second layer. To have a better signal-to-noise ratio, first the number of events was increased to 2000 (a typical standalone laser run has 1000 events). Second, a pad signal amplitude of about 800 ADC was achieved by increasing the laser intensity (Figure 3.4).

Moreover, an additional high-frequency electronics noise was observed. It was removed

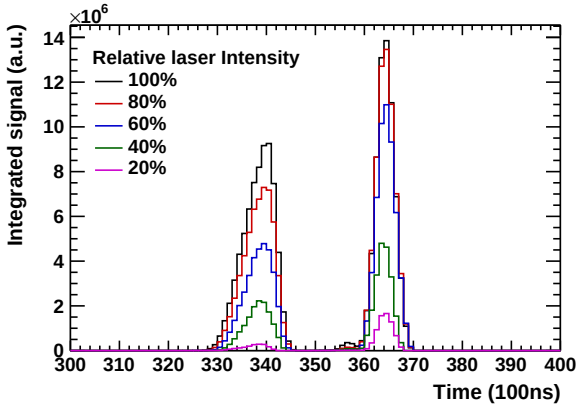

Figure 3.4.: Integrated TPC signals of the second laser layers on the A and C side of the TPC for different laser intensities. For each intensity a stand-alone laser calibration run was taken with a total number of 2000 events.

making use of the Fast Fourier Transform (FFT), functionality in the ROOT Framework [68] in three steps:

- apply Fourier transformation to the normalized pad signal,
- detect and smooth the outlier high frequency in the frequency domain,
- apply backward Fourier transformation to the signal domain.

The high frequency removal procedure is illustrated in Figure 3.5.

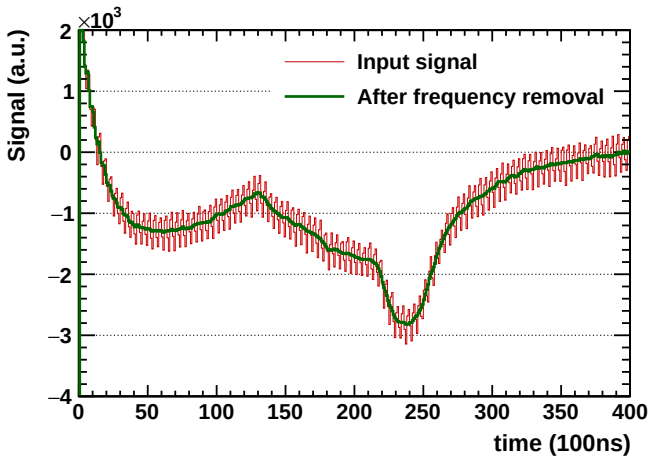

Figure 3.5.: (Color Online) The ion-tail signal before (red solid line) and after (green solid line) the removal of the high frequencies.

3.2.1. Ion movement in the amplification region

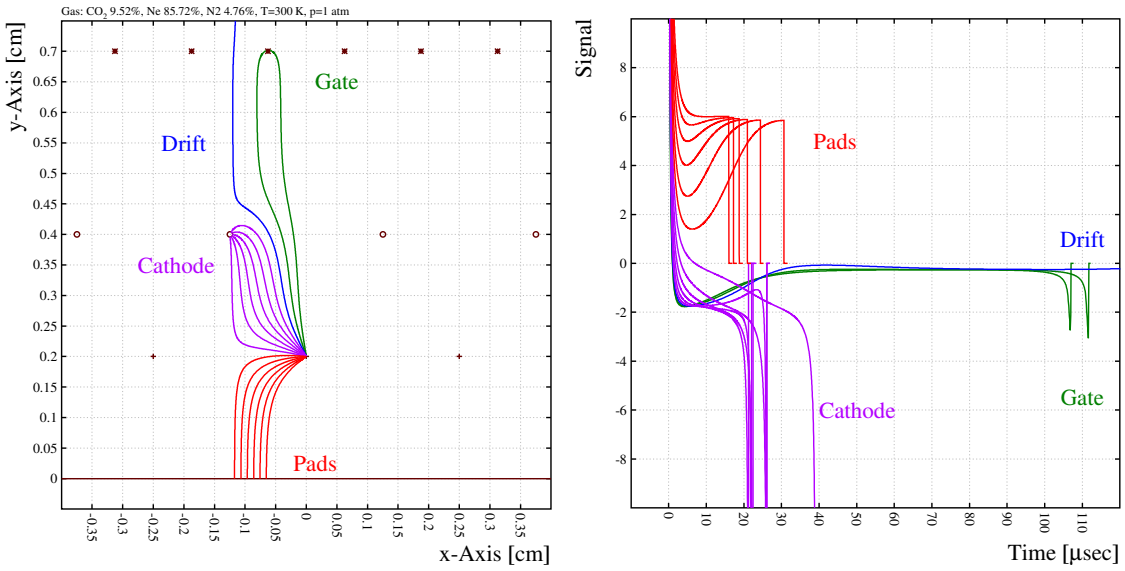

Figure 3.6.: (Left) The drift lines of ions. (Right) Corresponding ion signals induced on the pads [69, 70].

As explained earlier in Section 2.2, the large number of positive ions, created during the gas amplification by the incoming primary electrons at the vicinity of the anode wires, induces a positive signal on the pads. The electrons are immediately collected by the anode wire, while the ions leave the anode wire under various angles following different paths and eventually reach the pad plane, cathode wire or even gate wires in several tens of microseconds. The signal shape for individual ions, as well as a particle track traversing the TPC volume, were simulated using Garfield as shown in Figure 3.6 [69, 70]. Ions drifting towards the pad plane make a positive contribution to the signal tail, while back-drifting ions make a negative contribution.

The mobility of the electrons is several orders of magnitude larger than the mobility of

ions, therefore electrons are immediately removed from the amplification region and thus the pad signal is characterized by a fast rise due to ions in the high field in the vicinity of the anode wire and a long tail due to the motion of positive ions. The amplitude of the ion-tail is usually less than 1% of the original signal, however, it can cause a significant degradation of the following signal of the same pad in a high-multiplicity environment due to pile-up. Eventually, part of the pad signal remains under the zero-suppression threshold and gets lost. Such losses of signal amplitude eventually cause significant deterioration in the $\mathrm{d}E/\mathrm{d}x$ resolution and thus the PID performance.

Additionally, a number of baseline perturbations such as the systematic pattern created by the switching of the gating grid might also be present. Pads with such effects were either discarded or the additional frequencies removed by means of a Fast Fourier Transform (FFT), as explained above.

Previously, the ion-tail effect was studied in the NA49 Vertex TPC (using laser tracks)

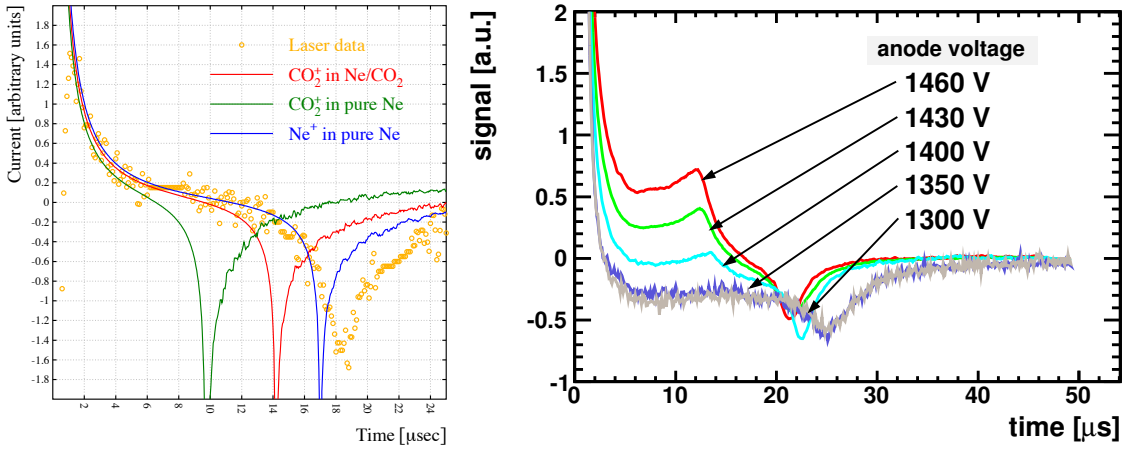

Figure 3.7.: (Left) The laser signal shape measured in the NA49 Vertex TPC at the SPS is shown with orange markers while the solid lines show the Garfield simulations for different assumptions on the drifting ion type and gas mixtures [57]. (Right) Ion-tail signals measured in a ALICE-TPC IROC with Ne-CO_2-N_2 (90-10-5) gas mixture for different anode voltages [69].

[71] and in the ALICE-TPC (using cosmic and pp events). Several dependencies were observed like on the gas mixture, the anode voltage settings, the geometry (gap size between anode and cathode wires) and the avalanche spread. Figure 3.7 shows the ion-tail shape observed in the NA49-TPC in comparison with Garfield simulations for different assumptions on the drifting ions and the gas mixture, as well as the voltage and gas mixture dependencies observed in the ALICE-TPC.

3.2.2. Ion-tail shape dependencies

There are two important aspects which determine the ion-tail shape: gas mixture and the settings which influence the drift field within the MWPC and thus the drift path of the ions. Since this thesis is aimed to develop an offline correction for the ion-tail effect, only the following first-order effects, which play a significant role in the ion movement in the amplification region, are investigated:

- gas mixture,
- voltage settings on the anode wires,

- gap sizes between the anode and cathode wires,
- position of a given pad signal with respect to the center-of-gravity of the cluster.

Gas mixture dependence:

The left plot in Figure 3.8 shows a significant difference in the ion-tail shapes of the gas mixtures: Ar-CO_2 (88-12) and Ne-CO_2 (90-10). The primary ionization in Ar-CO_2 is a factor of ∼2.4 higher than Ne-CO_2 (See Table 2.3), therefore the gas gain was tuned accordingly to a factor of ∼1.66 lower value [72], as shown in the right plot in Figure 3.8. This results in a significant modification in the avalanche spread around the anode wires, and eventually increases the amount of back drifting ions up to a factor of ∼1.3 more in Ar-CO_2. On the other hand, the shift of the second minimum can be explained with the different ion mobilities. The remainder of the sinal shape analysis is based on the Ne-CO_2 gas mixture.

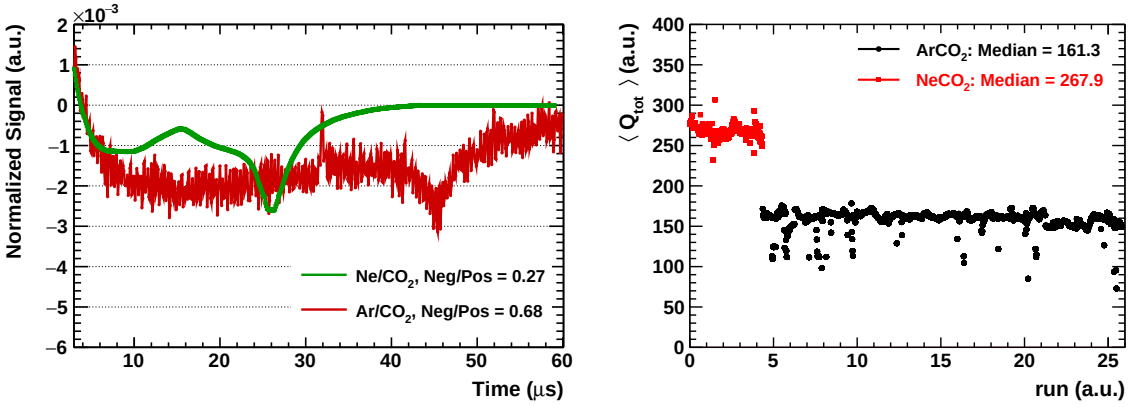

Figure 3.8.: (Color Online) Left: Normalized pad signals with zoom into the y-axis for Ar-CO_2 (88-12) and Ne-CO_2 (90-10) gas mixtures. Right: Mean total charge of clusters for Ar-CO_2 and Ne-CO_2 gas mixtures as a function of run [72]. Ar-CO_2 values are scaled with the relative ratio of primary ionization values ($N_{T,ArCO_2}/N_{T,NeCO_2}$=97/40, where N_T is the total number of electron-ion pairs per cm) taken from [4].

Geometry dependence:

The ALICE TPC MWPC has two different geometries, for IROCs and OROCs, where the difference lies in the gap sizes between the cathode wires, anode wires and pad plane (See Figure 2.5). The two normalized signals for IROC and OROC geometries are shown in Figure 3.9. The ratio of the negative to positive parts of the signals, which scales with the amount of the ions shared by the cathode-gate wires and the pad plane, are comparable. Due to larger distances between anode-cathode wires and anode wires-pad plane (i.e. different drift times), the time positions of the local maximum and the second minimum shifts to larger values in case of OROC geometry.

Anode voltage dependence:

Since the ion drift velocity increases with higher fields, the anode wire voltage has a somewhat similar effect as the wire geometry. However, the first-order effect reveals itself in a change of the avalanche spread around the anode wire. An increase in the anode wire

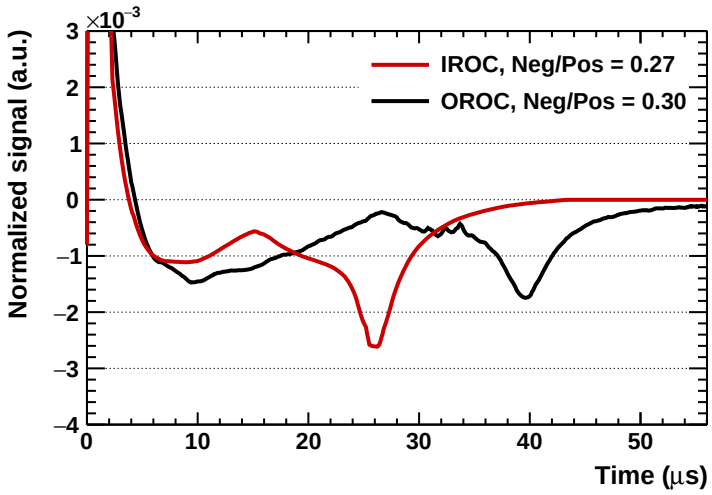

Figure 3.9.: (Color Online) Normalized pad signals with zoom into the y-axis for IROC and OROC geometries (See Section 2.2).

voltage does not only lead to higher gains but also to an earlier start of the avalanche due to the higher fields and thus an enlarged avalanche spread around the anode wire. This can be seen in the ratio of the integral of the undershoot to the integral of the signal as a function of the anode wire voltage, as shown in Figure 3.10.

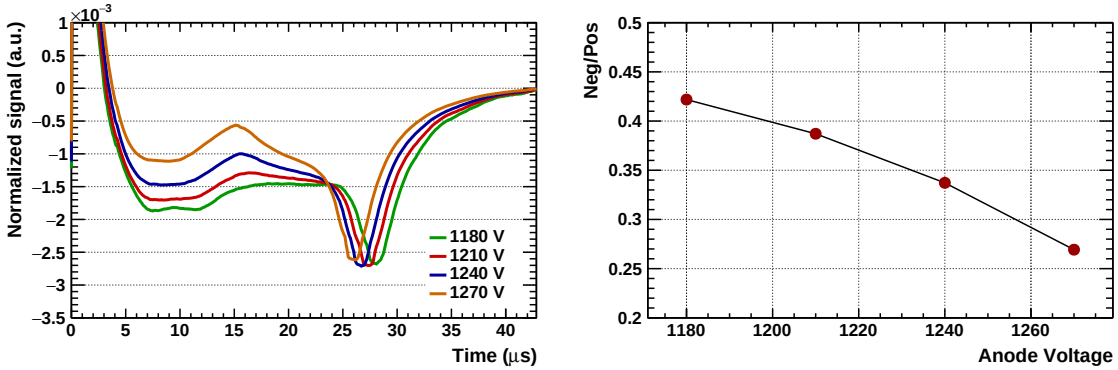

Figure 3.10.: (Color Online) Normalized pad signals with zoom into the y-axis for different anode voltage settings. (Left) Ion-tail shape. (Right) Ratio of the undershoot to the pulse as a function of anode voltage.

Pad position dependence:

Since the anode voltage, the geometry of the wires and the gas mixture are all fixed for a given run and the offline signal correction is applied on the cluster level, the main focus of the shape analysis study in this thesis is the dependence of the ion-tail on the pad position with respect to the center-of-gravity of the cluster. The principle of this dependence is that each pad of a given cluster sees a different fraction of the ions ending up on the pad plane and accordingly on the cathode wires because of the nature of the avalanche spread around the anode wire. This eventually changes the ion-tail shape of each pad signal of the cluster. Normalized pad signals measured at different distances to the center-of-gravity of the cluster are shown in Figure 3.11. The ratio of the undershoot

to the pulse as a function of distance to the center-of-gravity of the cluster shows almost a linear behavior, where most central pads receive more ions than the peripheral ones as expected.

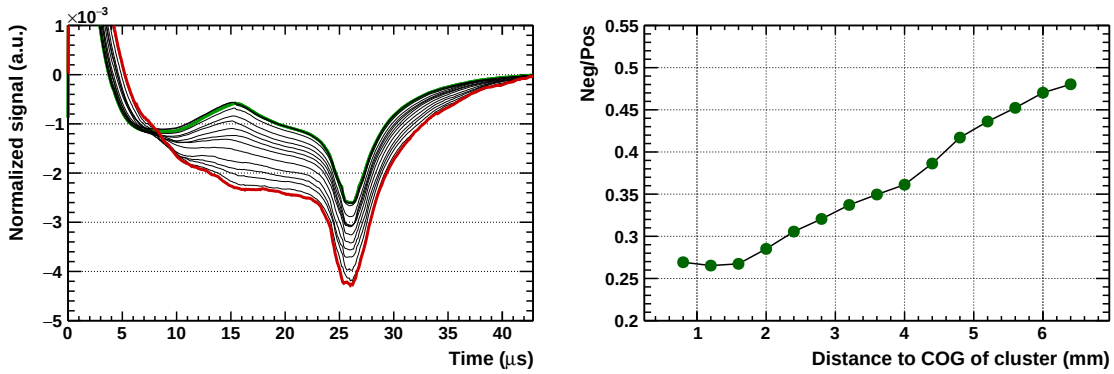

Figure 3.11.: Normalized pad signals with zoom into the y-axis measured at different distances to the center of gravity of the cluster. (Left) Ion-tail shape where solid green and red lines indicate the most central and peripheral pad signals, respectively. (Right) Ratio of the undershoot to the pulse as a function of distance to the center of gravity of the cluster.

3.2.3. Signal shape simulations

Pad signals in MWPCs can be simulated with Garfield [73], which allows for a detailed simulation of the detector response including primary ionization, electron drift, diffusion and signal induction on different electrodes for the geometry of interest. Originally, Garfield was written for two-dimensional chambers made of wires and planes where the exact fields are known. However for three-dimensional configurations the dielectric media and complex electrode shapes are difficult to handle with analytic techniques. To cope with this problem, Garfield is interfaced with the neBEM (A nearly exact Boundary Element Method) [74] program, which provides the field maps as basis for the calculations of Garfield. The three-dimensional pad read-out set-up of the TPC-IROC created using the neBEM program is shown in Figure 3.12. In addition to the five read-out pads two pads were added on each side in order to avoid boundary effects.

The ion distributions around the anode wires are not known precisely. For this a better simulation of electron transport in the amplification region is required. Therefore, one has to make some assumptions about the positions of the ions in the vicinity of the anode wires. To create a more realistic scenario, a number of primary electrons distributed similarly to the TPC Pad Response Function (PRF) (Figure 3.13) originates at a sufficient distance from the amplification region. The arrival points of the electrons at 3 different angles, as shown in Figure 3.13, was taken to be the peak positions of 3 generalised Gauss functions (Eq. 4.4), which were then used as the ion distributions around the wire.

By tuning the mean positions and peakedness parameter of the Gauss functions, a reasonable agreement between the data and Garfield simulations is achieved, as shown in Figure 3.14. In particular, the pad position dependence is reproduced. Besides, the following two main differences were also observed:

1. In contrast to the measurements, simulated signal shapes display a sharp negative spike. The smearing of these spikes can be attributed to fluctuations of the wire

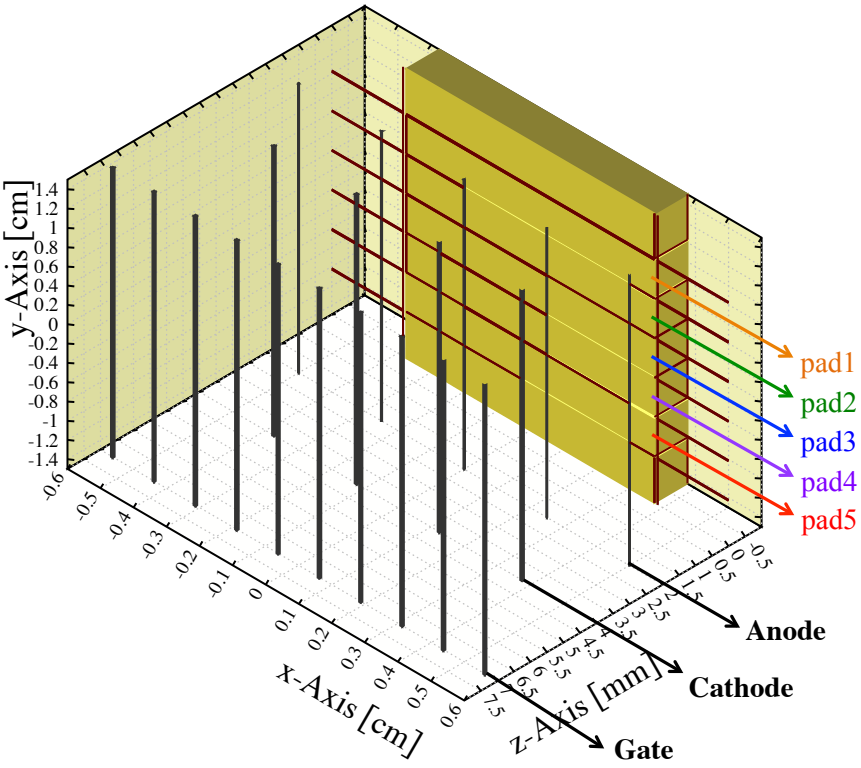

Figure 3.12.: Three dimensional setup of the TPC pad read-out used in the Garfield simulations.

positions. These fluctuations are assumed to be Gaussian and are in the range of $\sigma_{\text{geom}} \approx 50\mu$m. For further details see [70].

2. The time position of the negative spike in the simulations is at ∼22 μs while in the data it is at ∼26 μs. Also there is a slight difference in the overall peak and ion-tail shape. These differences are due to the assumptions on the gas media used in the simulation. There is a lack of information on the identity of the drifting ions in the literature. Therefore, as a fair approximation, gas-detector simulations usually simplify the treatment of ions to the extreme by taking only the noble gas ions (Ne^+) into account, neglecting the role of the quencher (CO_2) (See Figure 3.7). However, avalanches in gas-based detectors operating at atmospheric pressure and using Ne-CO_2 (90-10) as drift medium produce at the first instance mainly Ne^+ and CO_2^+ ions. The noble Ne^+ ions transfer their charge to CO_2 in a few ns. In [57], clusters of CO_2^+ ions are proposed as a solution to this problem.

All in all, the ion movement in the amplification region is well understood and also confirmed by three-dimensional Garfield simulations. Even though the identity of drifting ions and the ion distributions around the anode wires are not precisely known, one can approximate the ion mobilities, which is the relevant information for the ion movement measurements, with a proper scaling based on the measured ion drift velocities. Figure 3.15 shows an excellent agreement between the data and simulation, which is obtained by applying this scaling and, in addition, taking the fluctuations of wire positions into account. Note that, here the position uncertainty of only one out of three wires is considered.

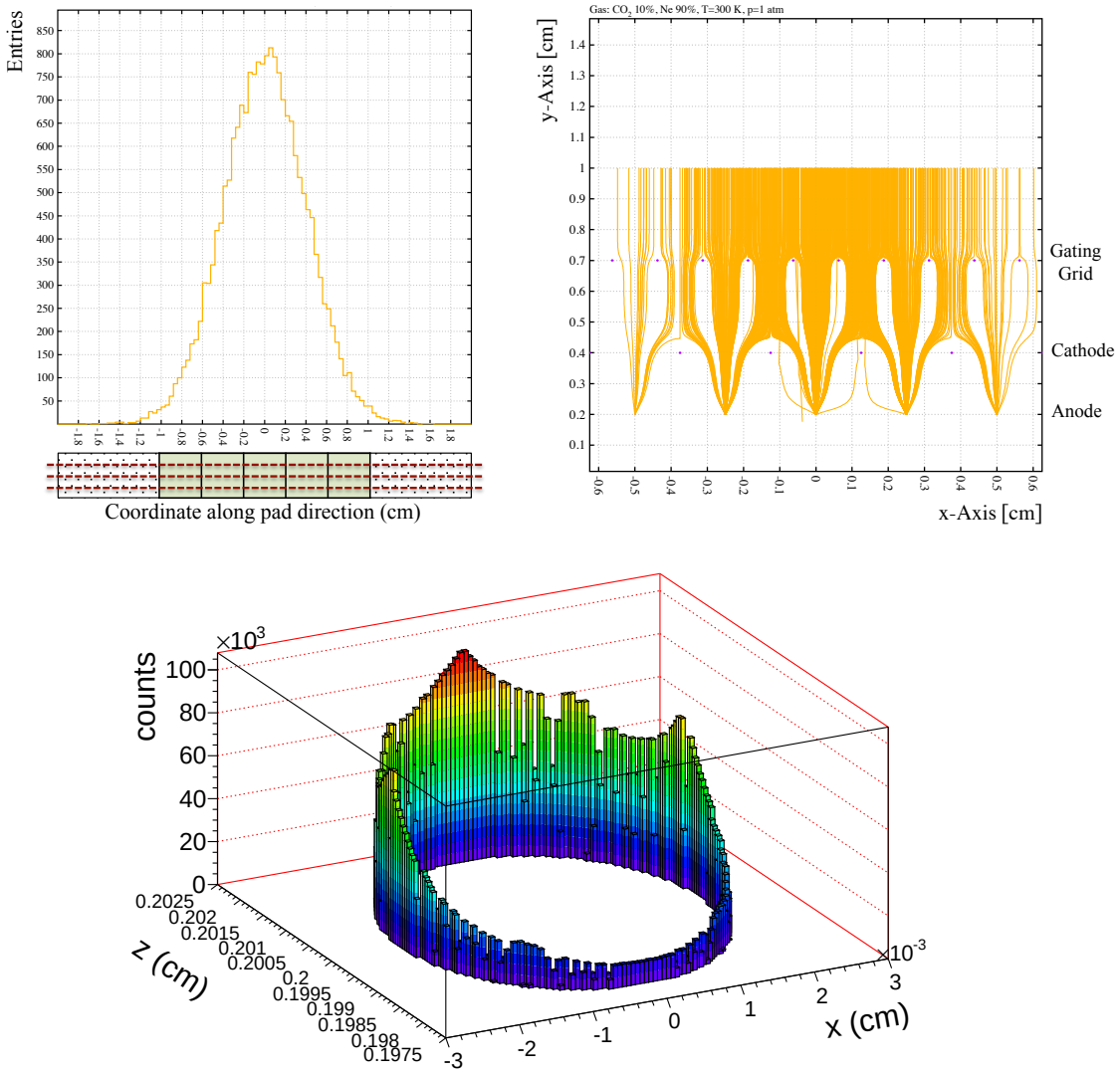

Figure 3.13.: (Upper panel:Left) Distribution of ions along the anode wires with the shape of the TPC PRF. The parameters of the PRF are taken from the OCDB. (Upper panel: Right) Drift lines of electrons in the amplification region (without diffusion), where the primary electrons are assumed to be distributed with a Gaussian shape. (Lower panel) Distribution of ions around the anode wire at the start of drift.

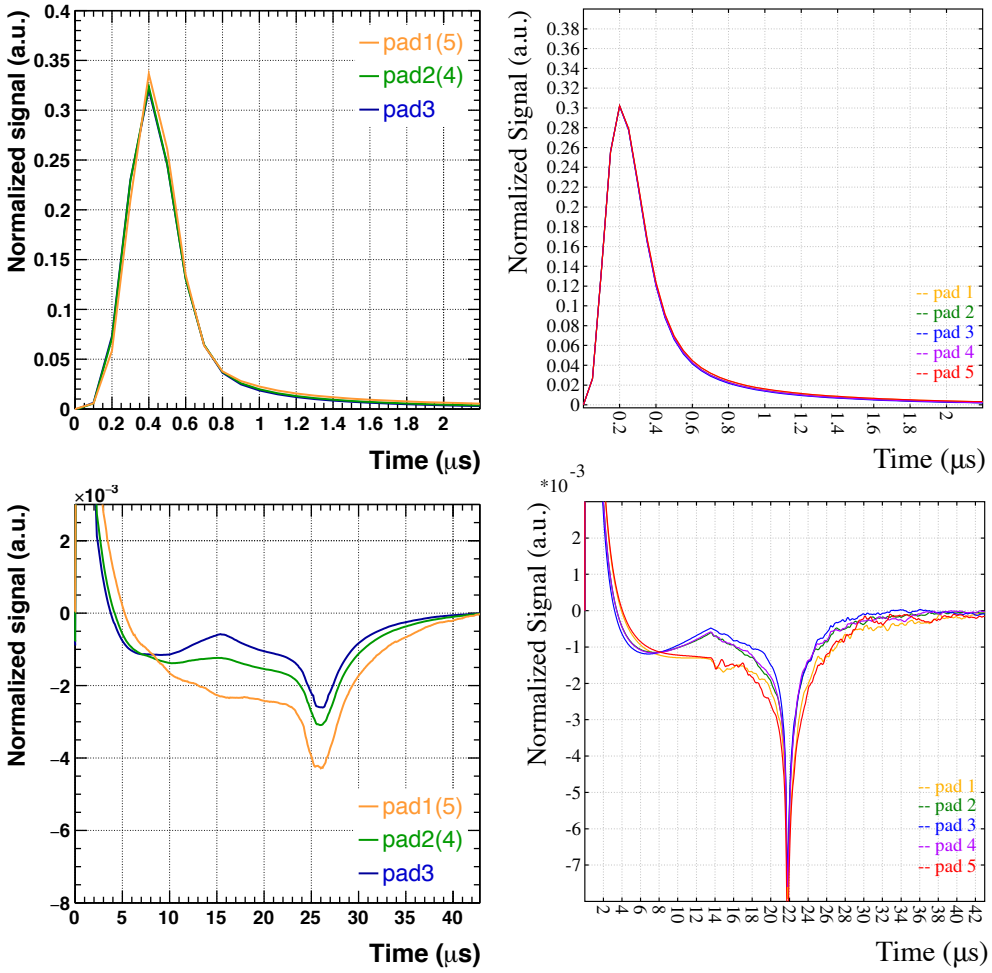

Figure 3.14.: Comparison of the measured and simulated signal shapes in five pads of a cluster where pad number 3 is the center of the cluster. Upper panel: Pulse shape. Lower panel: Ion-tail. Left: data. Right: Garfield simulation.

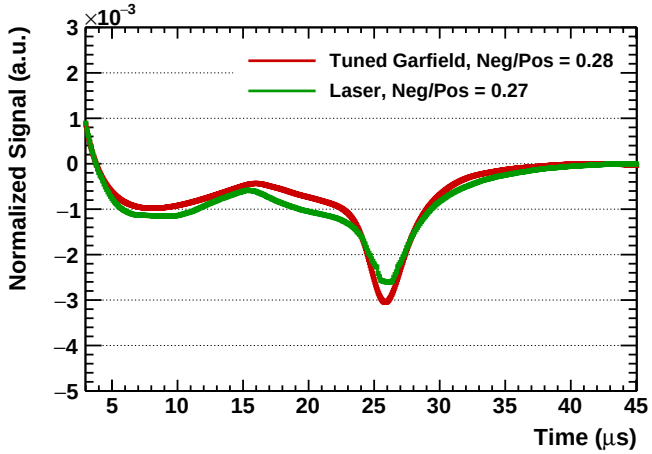

Figure 3.15.: (Color Online) Comparison of the normalized pad signal to the Garfield simulations in Ne-CO_2 (90-10) gas mixture for the most central pad of a cluster. Simulation result is scaled to match the measured ion drift velocity, and also smeared taking the fluctuations of the wire positions into account.

3.3. Common-mode effect

The common-mode effect is a basic property of wire chambers. Like the ion-tail effect, it causes a multiplicity-dependent deterioration of the $\mathrm{d}E/\mathrm{d}x$ resolution, thus the PID quality in the TPC. It occurs due to capacitive coupling of the anode wires to the readout pads. Below, the common-mode effect is investigated in detail using the laser data.

3.3.1. Proof of principle: Charge conservation

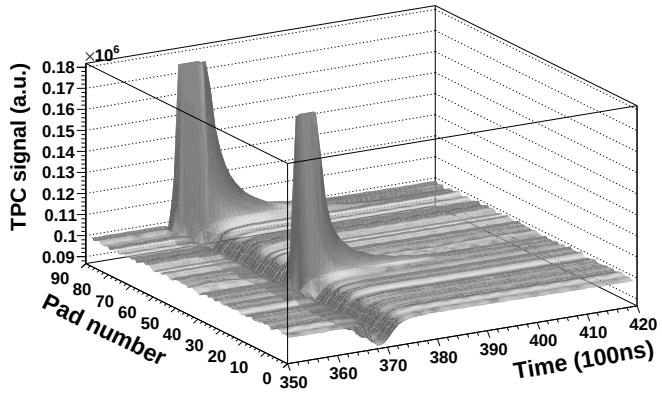

Figure 3.16.: Integrated laser track signal on a given pad-row which illustrates the common-mode effect.

Anode wires of a given read-out chamber are grouped into several so-called "anode wire segments", each of which is connected to a single high-voltage supply via a 10 kΩ protection resistors. IROCs have 4 and OROCs have 7 segments as shown with black solid lines in Figure 3.20. The arrival of the electrons on a given anode wire leads to an effective change of the anode wire voltage on the time scale of less than a time-bin (100 ns). The potential is then restored by the high-voltage supply feeding the anode wire segment. Due to the capacitive coupling of the anode wires to the readout pads, discharging and charging of the wires induces a bipolar signal on all pads facing the same anode wire segment in which the original signal is detected.

The fast rise time of the discharging process causes a simultaneous undershoot. Fig-

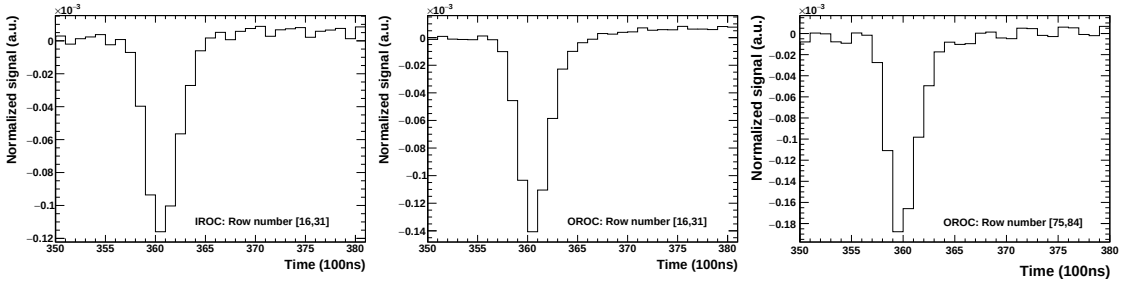

Figure 3.17.: Normalised common-mode response functions for three different pad-size regions: IROC (left), inner OROC (middle) and outer OROC (right).

ure 3.16 shows two laser track clusters (integrated over 2000 events) on a given pad row

and the undershoot induced on the other pads. Normalized common-mode response functions for three different pad-size regions are shown in Figure 3.17. This effect causes a reduction in all signals measured in the same time plane by all pads facing the same anode wire segment.

The common-mode signal, in principle, can be damped by a buffer capacitor for each

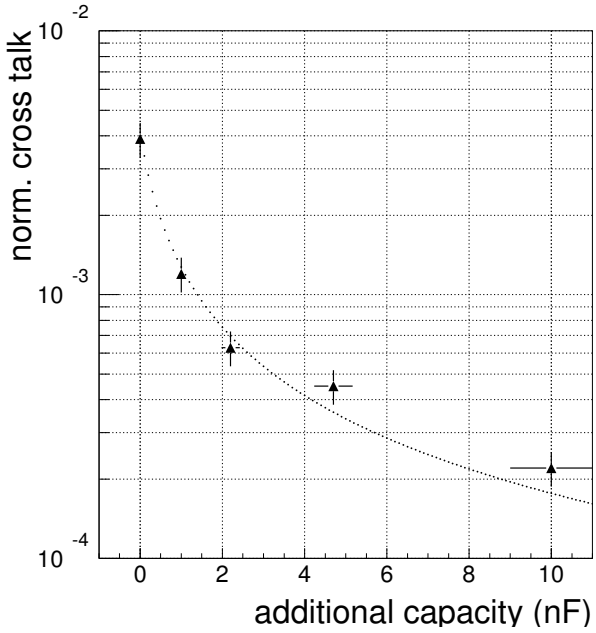

Figure 3.18.: Normalized common-mode signal as function of an additional capacity directly connected to the anode wires (Measured in NA49 experiment [75]). The expected behavior due to a parallel capacity is shown by the dotted line.

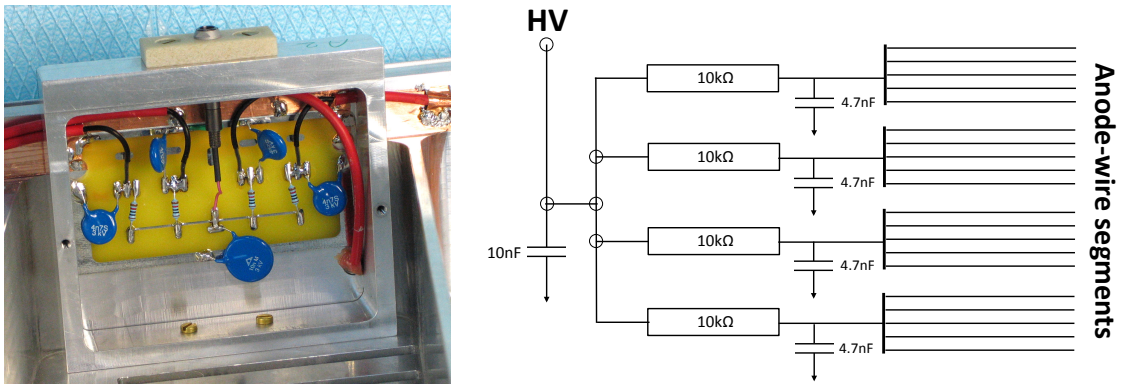

Figure 3.19.: Picture (Left) and diagram (Right) of an electric circuit of an IROC [61, 71].

segment. Figure 3.18 shows the normalized common-mode signal as a function of the additional capacity. Indeed, these capacitors were used in the ALICE-TPC before 2011 (Figure 3.19). However, discharges in the wire chambers due to highly-ionizing particles injected the charge stored in the buffer capacitors into the input stage of a given PASA chip, which eventually damaged the corresponding FEC. Therefore, they were eventually

removed in order to improve operational stability and safety.

In the absence of this capacitance, the total positive and the induced negative signal

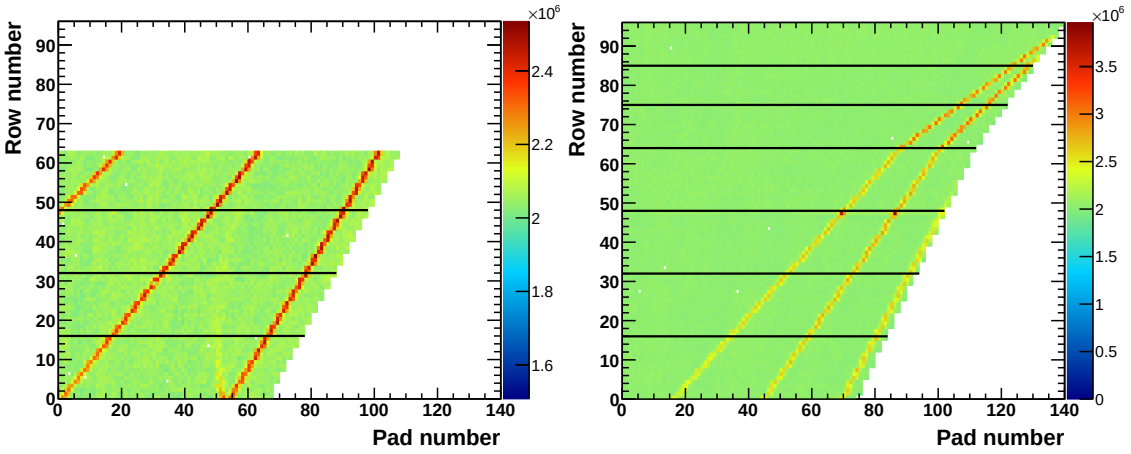

Figure 3.20.: Anode wire segmentation of the IROC (left) and OROC (right) geometries.

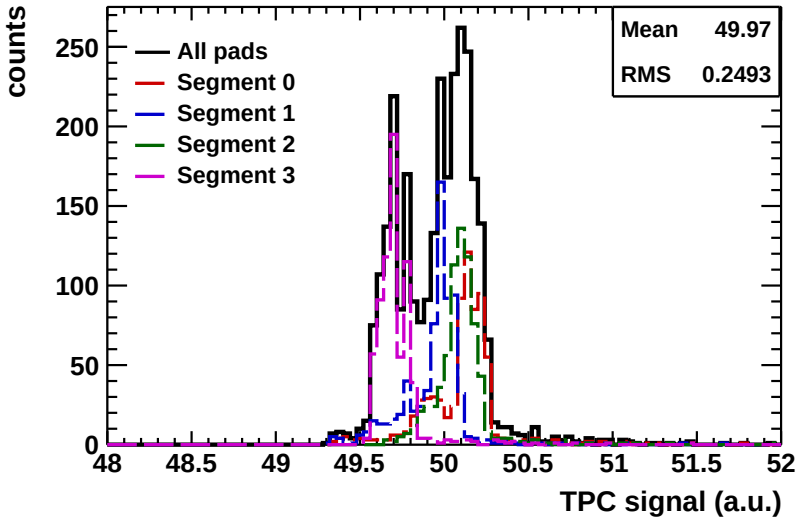

Figure 3.21.: Integrated charge of the four anode wire segments on a given IROC.

on a given anode wire segment has to be 0 due to charge conservation. To verify this, the total charge in a given anode wire segment for each time-bin of a given pad was calculated using the nonzero-suppressed laser data with a pedestal value of 50 ADC. The distribution of the integrated charge is shown in Figure 3.21. Since some of the pad-rows are shared by two neighboring segments, the distributions are not perfectly peaked at 50 ADC. Nevertheless, the RMS of 0.25 ADC is enough to conclude that the charge conservation holds.

Given the charge conservation, the amplitude of the common-mode signal on a given pad is suppressed by N^{-1} with respect to the original signal, where N is the number of pads facing the anode wire segment. Therefore, in a high-multiplicity environment, the common-mode signals lead to an average baseline drop, as well as an effective noise contribution.

3.4. Offline correction for the ion-tail and common-mode effects

In the Technical Design Report (TDR) of the TPC [40] it was assumed that the current front-end electronics will have a set of online signal processing algorithms (Moving Average Filter (MAF)) to correct for these baseline fluctuations on the hardware level [76]. However, the given functionality was not enabled due to instabilities in the firmware. Therefore, as an alternative solution, an offline correction was proposed. Below this offline correction, as well as two online correction algorithms for the common-mode effect alone are given.

3.4.1. Offline correction algorithms

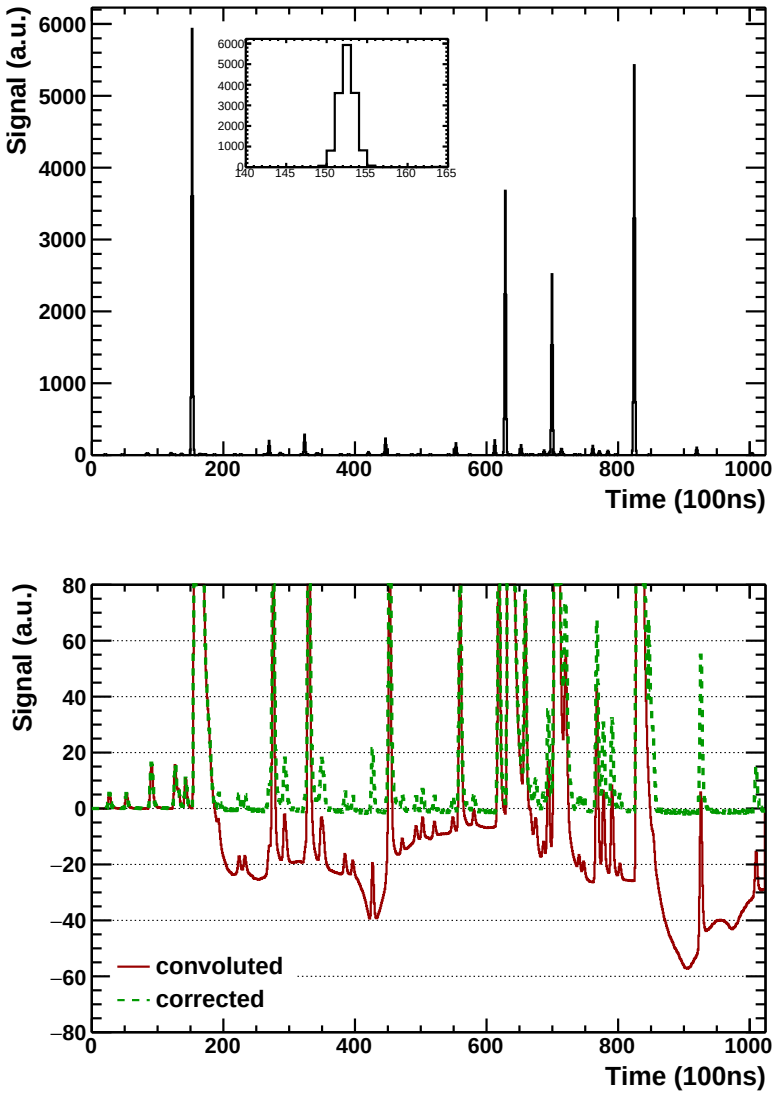

Figure 3.22.: Toy simulation of a single pad read-out. Top: input signal. Bottom: Convoluted (red solid line) and corrected (dashed green line) signals.

The ion-tail effect correction uses the so-called "Time Response Functions (TRFs)", i.e.

normalized pad signals including the ion-tail, as the sole input. The procedure is applied on the cluster level. For a given pad, each cluster is corrected with the following vector operation:

$$\mathbf{A} = \mathbf{A}_{\text{in}} + \alpha_{\text{IT}} \cdot Q_{\text{tot,pad}} \cdot \mathbf{T}, \tag{3.1}$$

where $\mathbf{A}$ and $\mathbf{A}_{\text{in}}$ are the corrected and input pad signals, respectively, $Q_{\text{tot,pad}}$ is the integral of the positive part of the input pad signal and $\mathbf{T}$ is the TRF for the given relative pad position to the center-of-gravity of cluster. After cluster finding the coordinates of the center-of-gravity, Q_{tot} and Q_{max} of each cluster are available but pad-by-pad information is lost. Therefore, the shape of a given cluster is approximated with the so-called "Pad Response function (PRF)", which has a Gaussian shape, in both time and pad direction for simplicity. This allows for an easy calculation of the relative position of each pad and its $Q_{\text{tot,pad}}$.

On the other hand, threshold effects, i.e. zero-suppression, lead to missing charge and clusters, which are then compensated by the fudge factor α_{IT}. Also, since a cluster is defined by five pads, the tails of clusters, which spread over more than 5 pads, are ignored. Moreover, because the TRFs are produced by laser tracks from a single IROC or OROC with a certain angle, some second-order effects such as chamber-by-chamber fluctuations in the wire positioning and voltages, as well as the cluster shape variations stemming from the track angles can not be covered. A test of the offline ion-tail correction procedure with a toy simulation of the TPC pad signal is illustrated in Figure 3.22. The correction is applied from left to right, so that each signal's $Q_{\text{tot,pad}}$ is recovered initially.

The common-mode effect correction relies on the charge conservation on a given anode-

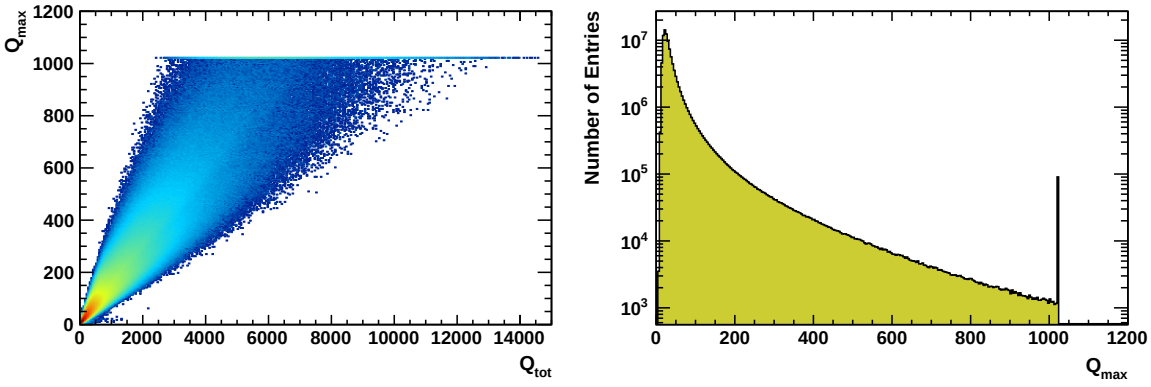

Figure 3.23.: (Left) Total vs maximum charge of TPC clusters. (Right) Distribution of the maximum charge of TPC clusters.

wire segment. The correction factor β for each time bin of a given pad signal is calculated as follows:

$$\beta = \alpha_{\text{CM}} \cdot \frac{Q_{\text{tot,segment}}}{N}, \tag{3.2}$$

where α_{CM} is a fudge factor standing for the missing charge and clusters while $Q_{\text{tot,segment}}$ and N are the total charge and pads of the current anode wire segment, respectively. Since only the coordinates of center-of-gravity of clusters are known, the bin contents along the time direction is also estimated by assuming that the clusters have a Gaussian shape in the time direction.

Due to missing charges and lost clusters, as well as the aforementioned approximations,

these algorithms can only provide a first-order correction. On the other hand, one should note that the performance of the corrections is also effected by unavoidable saturated signals [1] created by the highly-ionizing particles which can be attributed to the missing information as well.

3.4.2. Results from 2010 Pb–Pb and 2013 p–Pb data

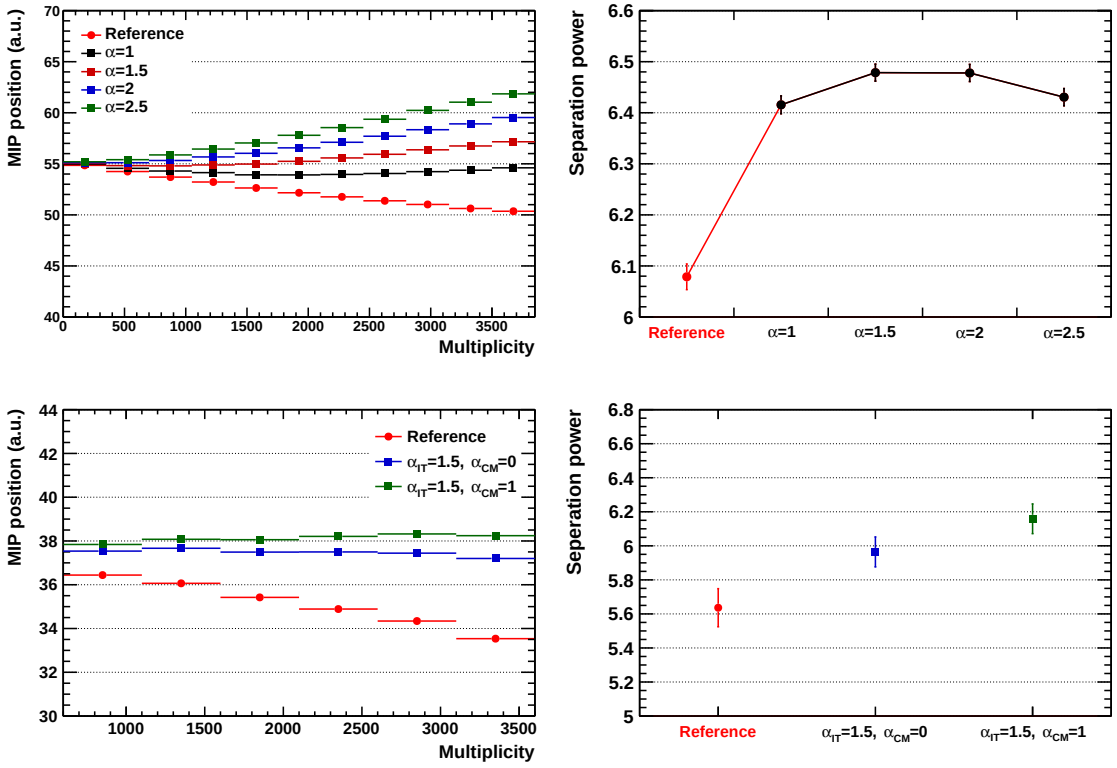

Figure 3.24.: Improvement achieved in the separation power and mean dE/dx positions. Upper Panel: for a given run from the 2010 Pb–Pb data taking period after the offline ion-tail correction with different fudge factors. Lower Panel: for a given run from the 2013 p–Pb data taking period after the offline ion-tail and common-mode corrections.

To quantify the performance of the particle identification after the offline correction, two quantities are used: electron-pion separation power and mean dE/dx position of the minimum-ionizing pions. The definition of the separation power is given in Section 2.2.4. Tests were performed on two different data sets:

- 2010 Pb–Pb: Gas mixture is Ne-CO_2-N_2 (90-10-5). Ion-tail effect exists, but common-mode effect does not due to additional capacitors.
- 2013 p–Pb: Gas mixture is Ne-CO_2 (90-10). Both ion-tail and common-mode effects exist.

[1] The front-end electronics of the TPC reads out a maximum of 1024 ADC (10 bits), if there is a signal which exceeds this limit, the channel stays in saturation for several time-bins at a certain value (in simulation at 1024 ADC as shown in Figure 3.23). These signals are labeled as "saturated signal".

The mean $\mathrm{d}E/\mathrm{d}x$ position results are shown in Figure 3.24 left column as a function of event multiplicity, where the number of primary particles for the Pb–Pb and the number of primary and secondary particles for the p–Pb data are used as multiplicity estimator. As shown by the red data points, both effects cause a linear decrease in the mean $\mathrm{d}E/\mathrm{d}x$ position as a function of multiplicity. For the highest multiplicity events the ion-tail alone results in a reduction of about 10% in Pb–Pb data, while in p–Pb data ion-tail and common-mode effects together cause a drop of about 6%.

The separation power results are calculated for the integrated multiplicity. As a compromise between the separation power and mean $\mathrm{d}E/\mathrm{d}x$ position results, the optimal value of the fudge factor for the Pb–Pb data can be taken as 1.3. However, in the coming section, it will be seen that this factor is actually 1.8. This is because the TRFs used here are produced with the laser data where the gas mixture was Ne-CO_2 (90-10) not Ne-CO_2-N_2 (90-10-5) (See Figure 3.7). Therefore, the Pb–Pb results can be further improved by using the proper TRFs. On the other hand for the p–Pb data quasi-optimal values of the fudge factors are used, thus there is also some room for improvement.

Eventually, choosing reasonable values of the fudge factors, improvements of about 7% and 10% are achieved in the separation power for the Pb–Pb and p–Pb data sets, respectively. Besides, the multiplicity-dependent deterioration of the mean $\mathrm{d}E/\mathrm{d}x$ position is removed.

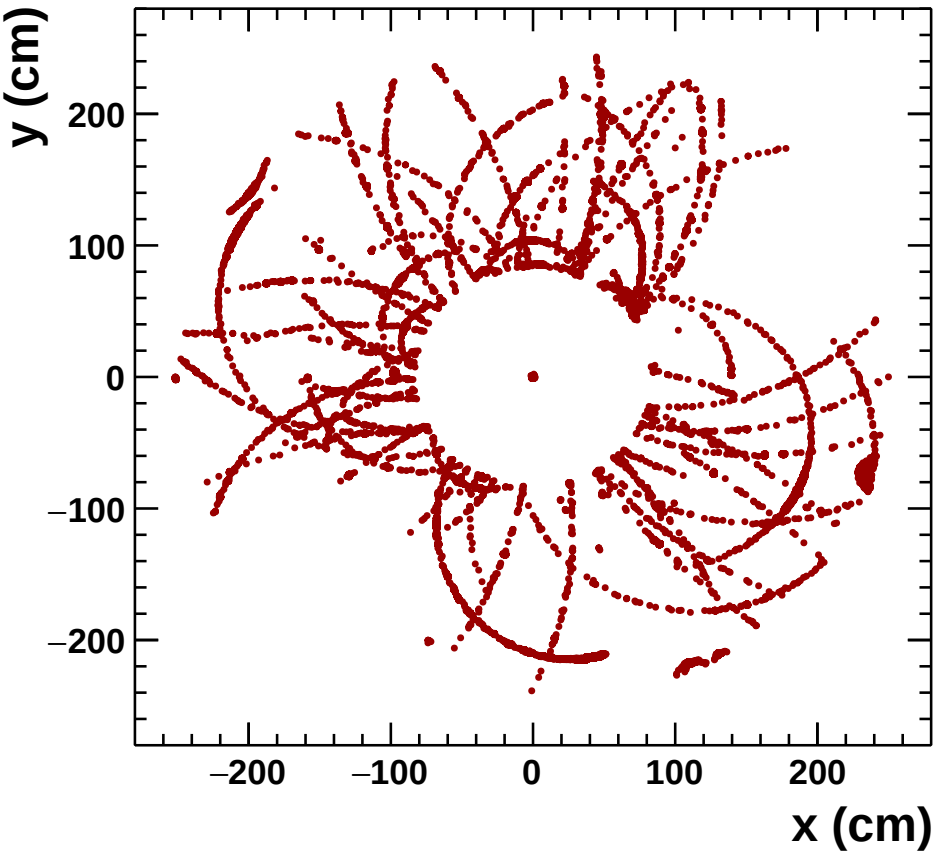

Figure 3.25.: TPC event display of a simulated Monte-Carlo event with 100 tracks.

3.5. Implementation of the ion-tail and common-mode effects into the ALICE simulation framework

The ALICE detector requires detailed simulations to design and optimize its sub-detectors, develop and test the reconstruction and analysis software and also interpret the experimental data. In particular for the efficiency studies the detector response has to be described as precisely as possible. For this, several event generators, such as HIJING and AMPT, employing a GEANT3 setup of the ALICE experiment are used. GEANT [77] is a program which accepts events simulated by Monte-Carlo generators and transports particles through the detector setup, taking into account geometrical volume boundaries and physical effects according to the nature of the particles, their interactions with matter and the magnetic field. It also visualizes the particle trajectories and records the response of each sub-detector. Figure 3.25 illustrates a simulated HIJING-MC event with 100 tracks. Each point illustrates a detected hit (primary ionization) in the TPC. For more details of the simulation chain in ALICE see Appendix A.

Note that each individual detector effect is measured and implemented in the frame-

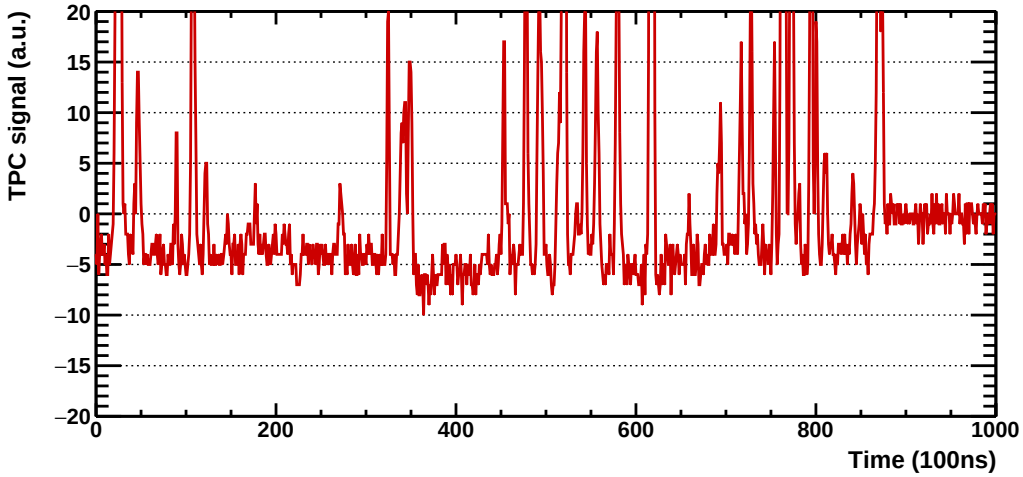

Figure 3.26.: Simulation of a pad signal for a central event where only the common-mode effect is implemented.

work by each sub-detector group. From the TPC side the following effects are succesfully implemented in the Aliroot framework:

- gain map which is produced by means of the Krypton calibration data,
- temperature and pressure dependence of gain,
- hardware settings such as high-voltage,
- effects related to track topology.

Causing significant deteriorations on the TPC signal and thus on the overall detector response, ion-tail and common-mode effects need to be implemented in the Aliroot framework as well in order to have a more realistic MC description. Figure 3.26 shows an example pad signal of a central HIJING event, where only the common-mode effect is included. Below the implementation of these effects in the Aliroot framework and the results

obtained are given. Ion-tail and common-mode effects are multiplicity dependent, therefore, for the simulation tests, the HIJING event generator was used since it describes the event multiplicities rather well, as shown in Figure 6.11. The simulation of the common-mode signal was based on the charge conservation in a given anode-wire segment. The simulated common-mode signal β_{sim} in each time bin was calculated with the following expression:

$$\beta_{\text{sim}} = \frac{Q_{\text{seg}}}{N}, \tag{3.3}$$

where Q_{seg} and N are the total simulated charge and number of pads in the given anode wire segment. On the other hand, the ion-tail was implemented by convoluting each simulated signal on the digits level (See Appendix A for the simulation process in ALICE) with the TRFs stored in the OCDB for the given geometry and high-voltage settings, which were also taken from the OCDB for each run. Both effects, first implemented individually and then together were investigated. Note that, since the common-mode effect is a result of the charge conservation it should be implemented first.

The effects were first included in the simulation and then the simulated events were reconstructed back as in the case of real data. The final performance in the electron-pion separation power and mean $\mathrm{d}E/\mathrm{d}x$ position of the minimum ionizing pions as a function of multiplicity are shown in Figure 3.27. The reference data without common-mode and ion-tail shown with black solid markers in the separation power plots displays the known degradation introduced by cluster merging at increasing occupancy. As expected, introduction of both effects leads to an additional significant deterioration of the separation power and also a linear decrease of the mean $\mathrm{d}E/\mathrm{d}x$ position as a function of multiplicity. The number of primary particles are used as multiplicity estimator. For the highest multiplicity events the following conclusions can be made:

Mean $\mathrm{d}E/\mathrm{d}x$ position:

- the common-mode effect alone causes a reduction of ∼12%, where ∼6% of it is recovered with a fudge factor of 1,
- the ion-tail effect alone causes a reduction of ∼13% (Figure 3.24 suggests that this number is ∼10%. The difference can be attributed to the TRFs being for a different gas mixtures, as discussed earlier), which is totally recovered with a fudge factor of 1.8,
- Ion-tail and common-mode effect together cause a reduction of ∼25%, where ∼18% of it is recovered.

Separation power:

- the common-mode effect alone causes a reduction of ∼18%, where ∼12% of it is recovered,
- the ion-tail effect alone causes a reduction of about ∼22%, where ∼18% of it is recovered,
- Ion-tail and common-mode effect together cause a reduction of ∼37%, where ∼25% of it is recovered.

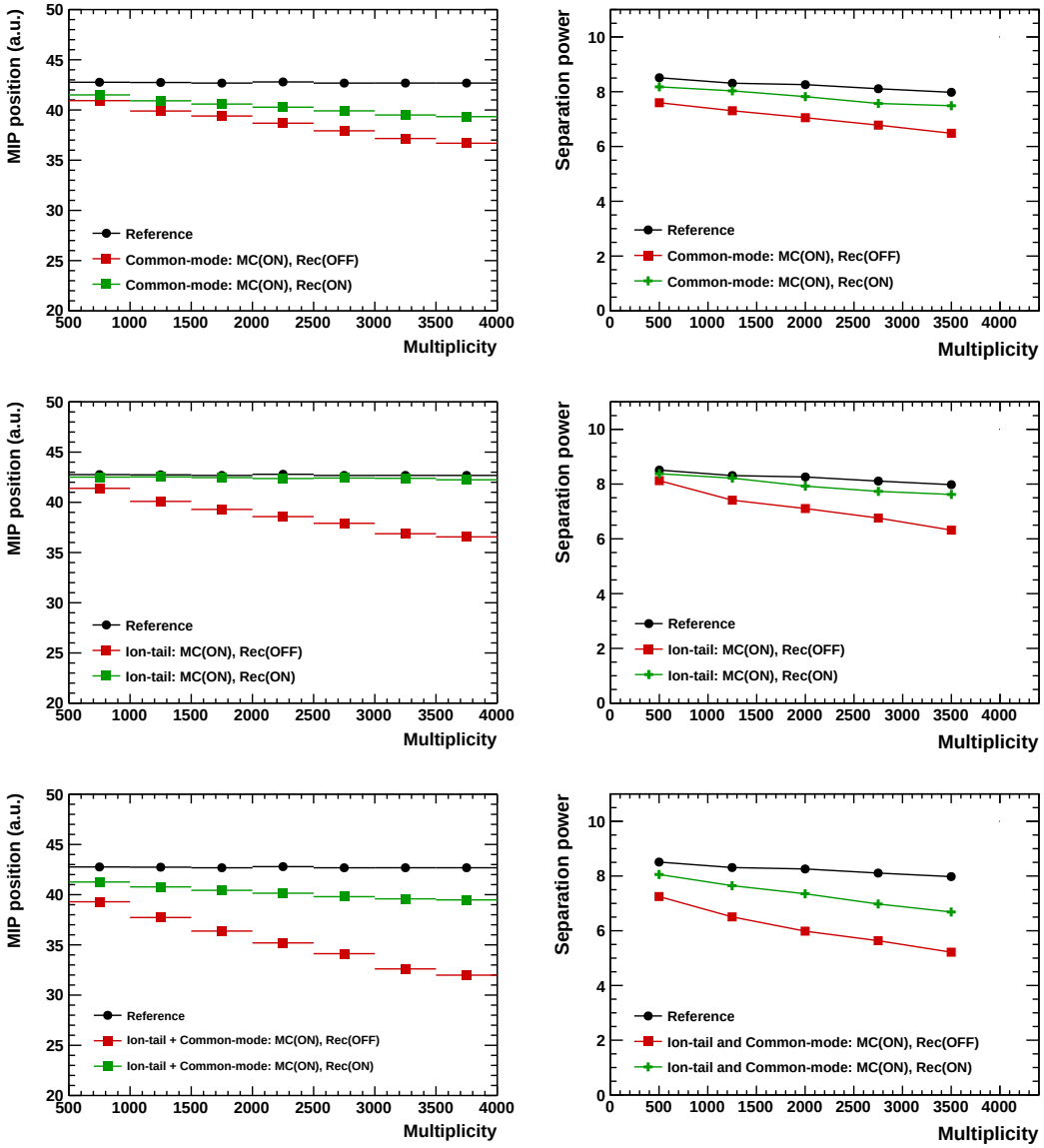

Figure 3.27.: Separation power (left column) and mean dE/dx position (right column) results of a HIJING simulation including common-mode and ion-tail effects. Achieved performances for common-mode effect only (upper panel), ion-tail effect only (middle panel) and both effects together (lower panel) are shown as a function of the multiplicity (number of primary tracks).

Here one should note that the additional noise contribution as a result of the common-mode effect, as shown in Figure 3.28, requires a higher zero-suppression threshold, which results in more missing charge. This effect reveals itself in the mean dE/dx position, where a fudge factor of 1 can recover only half of the total reduction.

Moreover, lost clusters as a function of multiplicity were also investigated as shown in Figure 3.29. As expected they can not be recovered by this procedure. For the highest multiplicity events, the common-mode effect alone leads to an additional cluster loss of about 3.5%, while the ion-tail effect alone 4.5% and accordingly the two effects together 8%. Since the common-mode signal causes an average baseline shift, it results in less

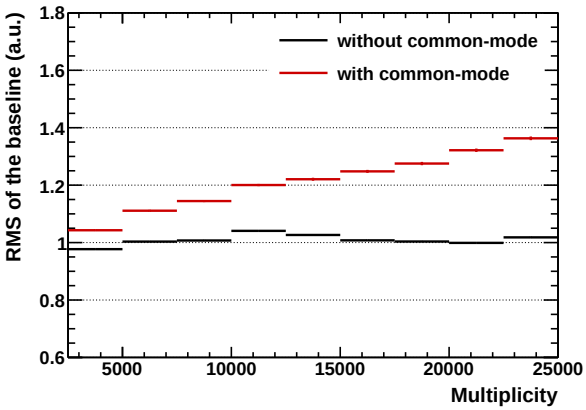

Figure 3.28.: Additional noise resulting from the common-mode effect as a function of multiplicity (total number of primary and secondary tracks).

missing clusters in comparison to the ion-tail effect which is more localized and thus can reach larger local drops in the baseline.

All in all, both ion-tail and common-mode effects were successfully implemented in the Aliroot framework, where the obtained simulation results agree well with the expectations based on the real data. Also, it is confirmed that the offline correction provides sizeable improvement in the TPC detector performance.

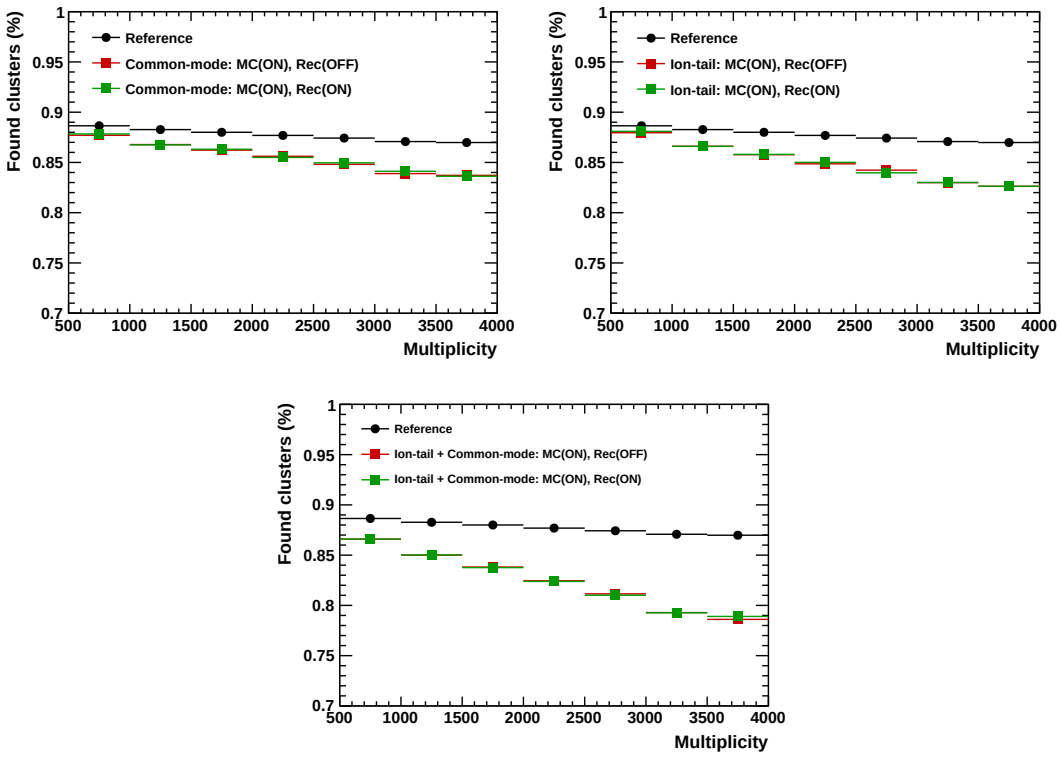

Figure 3.29.: Relative number of missing clusters for common-mode effect only (upper panel left), ion-tail effect only (upper panel right) and both effects together (lower panel) as function multiplicity (number of primary tracks).

3.6. An online algorithm for the baseline correction

Lost clusters due to the aforementioned baseline fluctuations do not only deteriorate the PID performance but also reduce the particle detection efficiencies in the TPC. Therefore, an online correction applied in the FEE prior to zero-suppression can restore the baseline and thus prevent loss of clusters. Below, it is shown that a single-channel-based online correction can not be a solution to common-mode effect.

ALICE will record Pb–Pb collisions at a rate of 50 kHz in the RUN3 period of the LHC

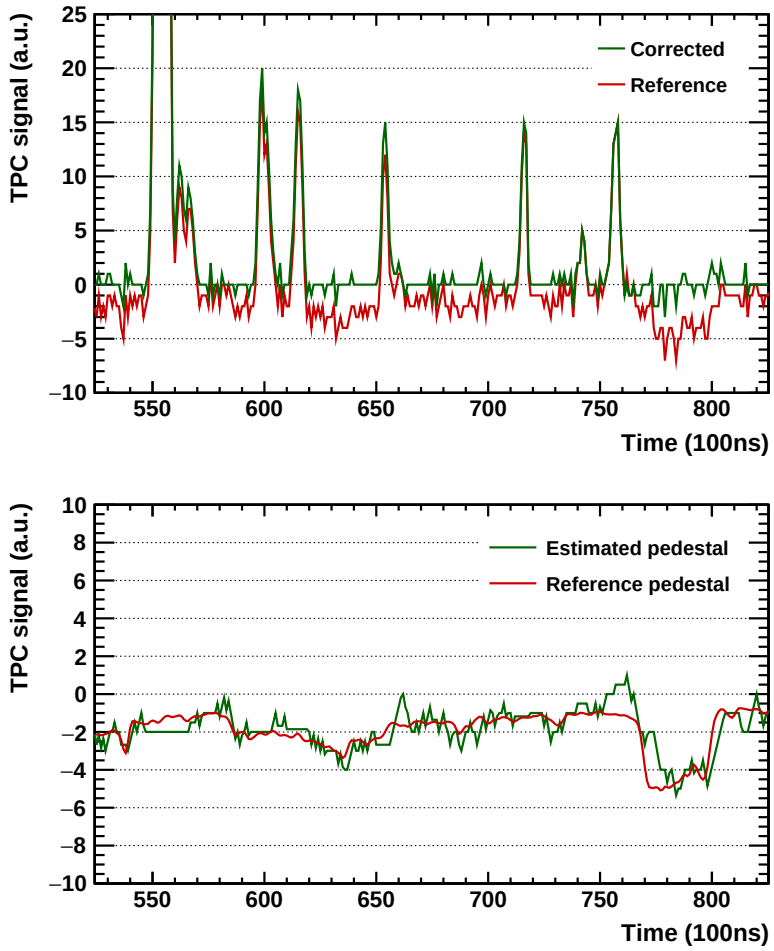

Figure 3.30.: (Upper plot) Pad signal before (red line) and after (green line) the online correction. (Lower plot) Comparison of the corresponding baseline (signals removed) of the pad signal with common-mode effect (red line) to the estimated baseline (green line).

after the LHC second long shutdown in 2019/20. This implies that a TPC operation with a gating grid is no longer possible, since it limits the TPC readout to trigger rates below about 3 kHz. This motivates the choice of Gas Electron Multiplier (GEM) technology instead of MWPC. The possibility to use a stack of 4 GEM foils and operate them with optimized voltages avoid massive charge accumulation in the drift volume from back-drifting ions, and prevent excessive space-charge distortions [78]. In GEM detectors, the signal is produced by the electrons, therefore there will be no ion-tail component. However common-mode effects will remain to play a significant role. Moreover, these high rates

and a continuous read-out scheme result in a significant increase in the charge density and eventually severe cluster losses and baseline shifts.

Here, a single-channel-based approach, which aims for the correction of both ion-tail and in particular common-mode effects, is described. For this, first, an interface was implemented in the Aliroot simulation framework which allows for the test of any online algorithm. In this approach the baseline calculation is paused in case of rapid changes, i.e. pulses are detected in the input pad signal. An illustration of the baseline estimation and comparison of the distorted and corrected signals are shown in Figure 3.30.

The performance achieved in terms of electron-pion separation power, mean dE/dx

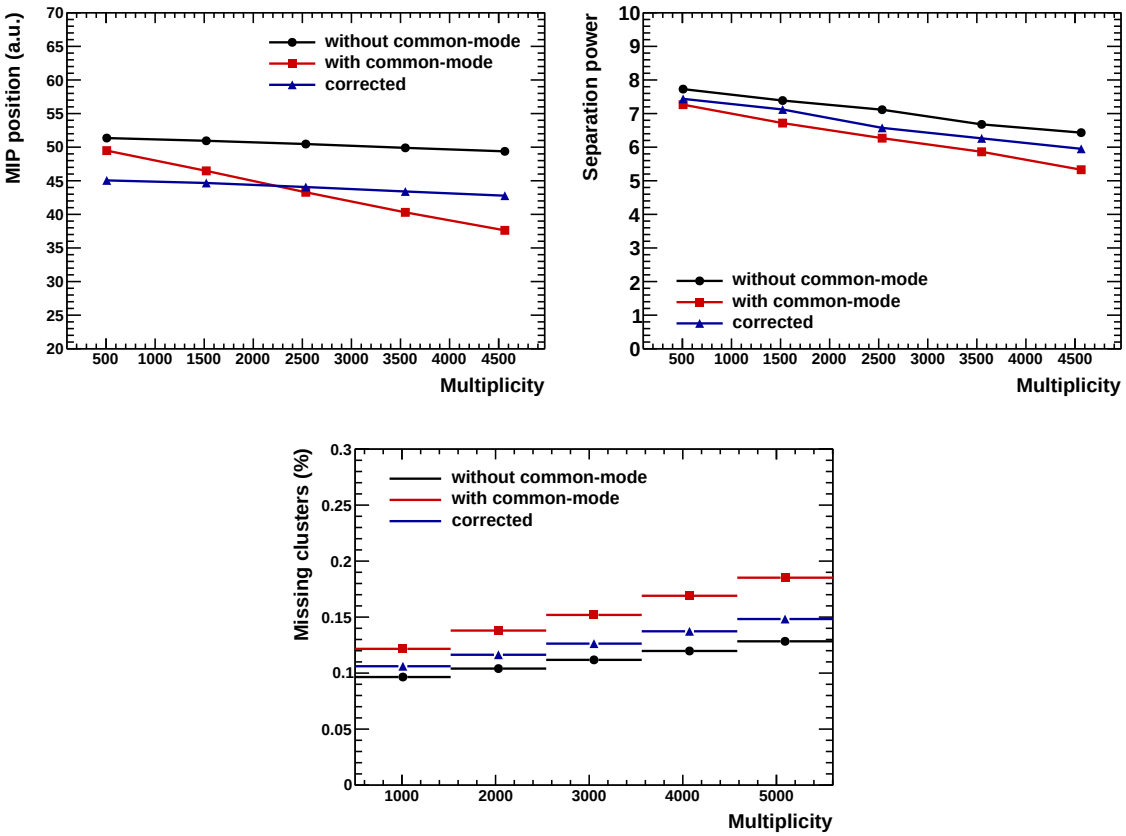

Figure 3.31.: Achieved performance in mean dE/dx position (top left), separation power (top right) and relative number of missing clusters (bottom) after the online correction applied to a HIJING simulation including the common-mode effect. Results are shown as a function of multiplicity.

position of the minimum-ionizing pions and fraction of the missing clusters as a function of multiplicity are shown in Figure 3.31. The total number of primary particles are used as the multiplicity estimator, where 4500 tracks correspond to a central Pb–Pb collision at 50 kHz (expected highest multiplicity in the RUN3 period of LHC running), i.e. pile-up of 5 minimum bias events. The black data points show the known degradation introduced by cluster merging with increasing occupancy. The introduction of common-mode noise leads to an additional significant deterioration of the separation power. The multiplicity dependence of the mean dE/dx position is recovered with a systematic shift. However, missing clusters and the separation power were only partially recovered. The overall

performance is comparable with the offline correction.

All in all, in the presence of the common-mode effect, it is impossible to recover the full performance with a single-channel-based online signal processing because of the correlated nature of the common-mode signal between the pads of a given anode-wire segment. Given that the calculation of the baseline is blind during the duration of pulses, the performance of the approach is limited by the signal occupancy. Below, an ideal correction, which is considered to be used in RUN3, for the common-mode effect is discussed.

3.7. Ideal approach for the common-mode correction

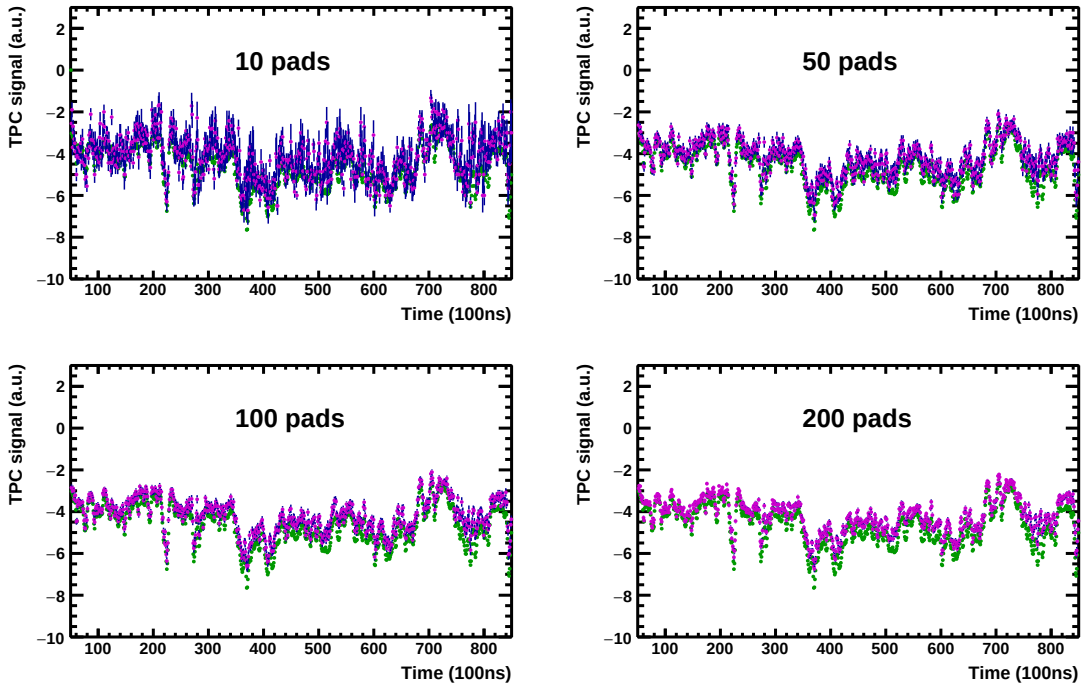

Figure 3.32.: (Color Online) Reference baseline (green points) of a given pad signal with common-mode effect in comparison to the estimated baselines (magenta points) where a different number of pads is used for the estimation.

Since the common-mode signal is the same on all pads facing the same anode voltage segment, due to the charge conservation, one needs to correlate a number of pads to estimate the common-mode effect contribution to the baseline for a given segment. (Note that, the same layout of the readout chambers will be used for the GEM detector with different anode voltage segmentation. The algorithm was tested for both GEM and MWPC settings.) Figure 3.32 shows the comparison of the common-mode noise to the estimated baselines calculated by averaging over a different number of pads of a given anode voltage segment. Also, Figure 3.33 shows a 0.03 ADC bias in the baseline estimation for 10 pads with an additional noise contribution of 0.46 ADC. By increasing the number of pads included in averaging the noise contribution can be reduced to ∼0.1 ADC (Figure 3.34 left plot).

That is, the baseline can be restored with negligible residual bias and noise contribution by averaging over about 100 pads. Note that, while averaging the true particle signals are

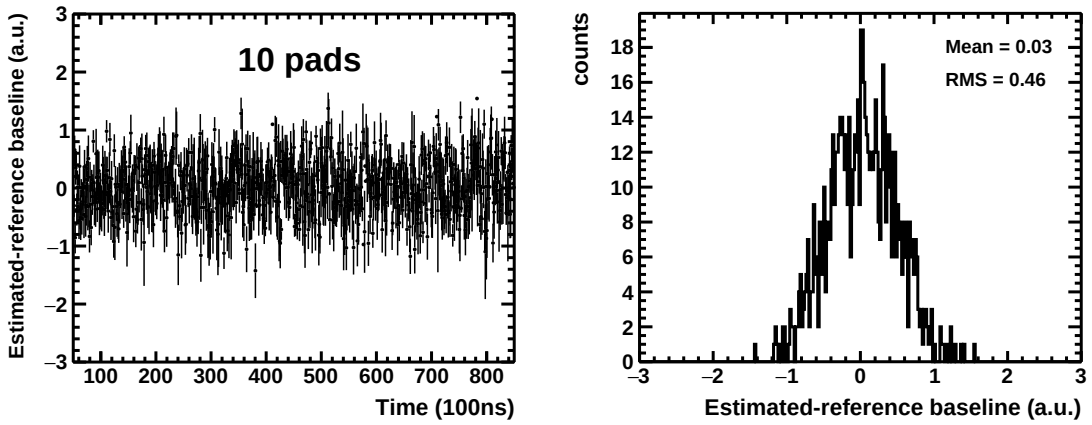

Figure 3.33.: (Left) Baseline of a pad signal with common-mode effect subtracted from the estimated baseline averaging over 10 pads. (Right) Projection of the left plot to the signal (y) axis.

filtered out by a simple peak detection algorithm because of the aforementioned reason.

Such averaging over a large number of pads is not possible in case of single input channel processing only. On the other hand, the data of up to 1600 pads are merged in a Common Reaout Unit (CRU). Therefore, the whole raw data need to be recorded without any compression. Figure 3.34 right plot shows the signal occupancy in the IROCs as a function of multiplicity, where about 16% is reached at the innermost rows. This number goes up to 25% for the highest multiplicities expected in RUN3. In summary, at the cost of about four times more raw data buffering, one can completely eliminate the common-mode effect. Note that, with a sampling frequency of 5 MHz, i.e. using 500 time-bins instead of 1000 time-bins along z-direction, one can gain a factor of 2 reduction in the raw data buffering.

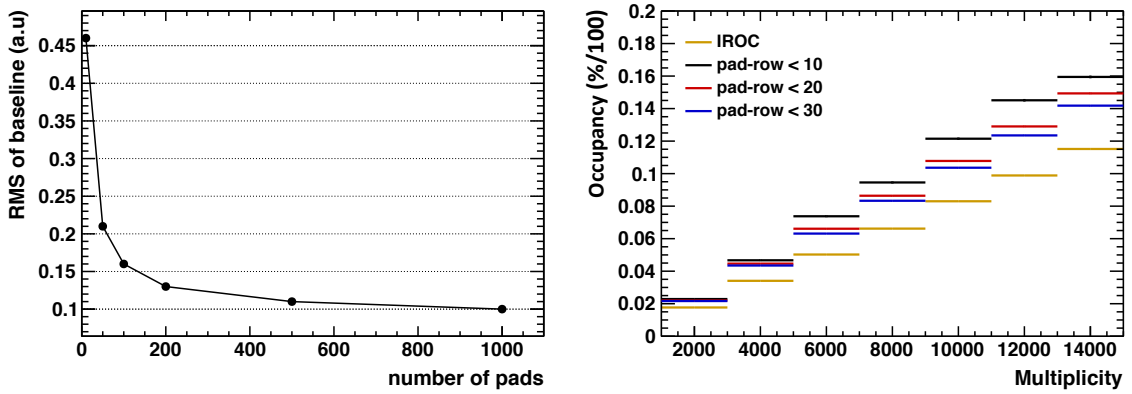

Figure 3.34.: (Left) Effective common-mode noise contribution as a function of the number of pads used for the average calculation. (Right) Signal occupancy in IROCs as a function of multiplicity (total number of primary and secondary tracks).

4. A new parameterization of the TPC $\mathrm{d}E/\mathrm{d}x$ response and "Iterative PID" procedure

The ALICE detector has a number of different subsystems for identifying charged hadrons, electrons and muons. Making use of all known PID techniques, it allows for excellent particle identification over a wide momentum range covering three orders of magnitude, from $\sim$100 MeV/c to $\sim$100 GeV/c. Figure 4.2 shows the PID performance of the experiment as a function of momentum in terms of several particle ratios.

The particle identification in the central barrel of ALICE is based on ITS, TPC, TRD,

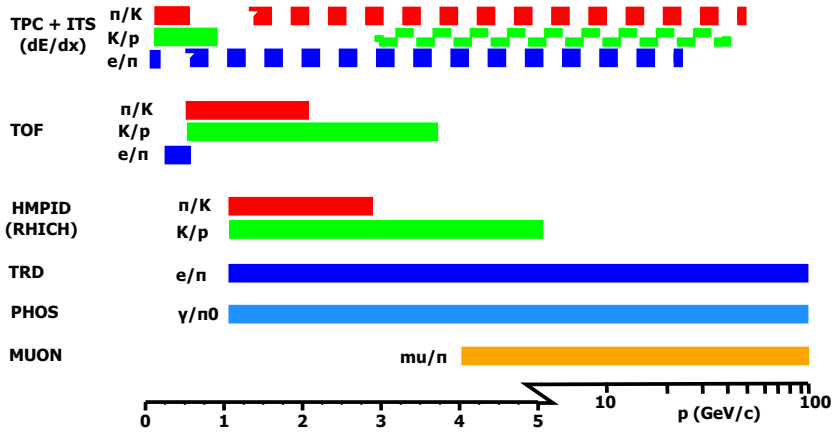

Figure 4.1.: Particle identification capabilities of the subdetectors of ALICE as a function of momentum. Solid bars and dashed regions mark regions of a separation better than 3σ and 2σ, respectively [79].

TOF, EMCal and HMPID. The PID techniques used in these detectors are summarized in Table 4.1. Since, ITS, TPC, TRD and TOF detectors have the adequate pseudorapidity coverage of $|\eta| < 0.8$ for the event-by-event fluctuation analyses, only the PID procedures for these subdetectors are covered in this thesis. Detatils on the PID techniques used in ITS, TOF and TRD are given in Appendix G, while the TPC, which is mainly used in this analysis, is discussed in detail below.

4.1. Particle identification in the TPC

The TPC is the main tracking and particle identification detector in ALICE. It provides specific energy loss ($\mathrm{d}E/\mathrm{d}x$), charge, and momentum of each particle traversing the detector gas. The transverse momentum of the particle is determined using the following relation

$$p_{\mathrm{T}}[\mathrm{GeV}/c] = 0.3 \cdot B \cdot r[\mathrm{Tm}], \tag{4.1}$$

Detector	PID Technique
ITS	specific energy loss, dE/dx, in silicon
TPC	specific energy loss, dE/dx, in gas Ar-CO_2 (88-12)
TRD	specific energy loss, dE/dx, in gas Xe-CO_2 (85-15) and transition radiation
TOF	β via time of flight
HMPID	β via Cherenkov angle
EMCAL	energy of EMCAL cluster (E) / momentum of matched track (p),

Table 4.1.: Charged hadron identification techniques and corresponding sub-detectors used in ALICE.

where, r is the curvature of the particle trajectory and B is the magnetic field parallel to the beam direction. The mean dE/dx value of a given track is calculated using the truncated mean procedure which is applied over a maximum number of 159 clusters attached to the track (Section 2.2.3). As shown in Figure 4.2, different particle species can be separated from each other in a wide momentum range. One should note that, the momentum at the inner wall of the TPC is used in order not to be influenced by energy loss in the material before the TPC. The energy loss dE/dx, described by the Bethe-Bloch

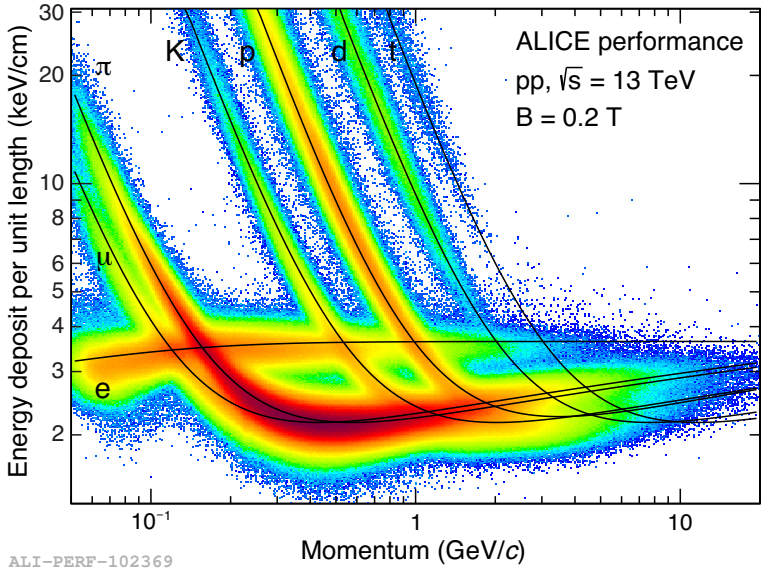

Figure 4.2.: Specific energy loss in the TPC at magnetic field of 0.2 T and $\sqrt{s} = 13$ TeV as a function of momentum with superimposed Bethe-Bloch lines for various particle species [4].

formula (See Section 2.2), is parametrized by a function originally proposed by the ALEPH collaboration [61],

$$f(\beta\gamma) = \frac{P_1}{\beta^{P_4}}(P_2 - \beta^{P_4} - \ln(P_3 + \frac{1}{(\beta\gamma)^{P_5}})), \tag{4.2}$$

where β is the particle velocity, γ is the Lorentz factor, and P_{1-5} are fit parameters. The parametrization of the dE/dx signal vs $\beta\gamma$ allows for the determination of the response for all particles by means of a scaling: $p/z = \beta\gamma \cdot m/z$.

The Bethe-Bloch parameterization is obtained making use of clean samples of electrons, pions, kaons and protons which cover different regions of the Bethe-Bloch curve. They are reconstructed using different detector information as well as the decay topologies of V^0 particles (see next chapter for clean sample extraction). The mean energy loss information

of these clean samples are extracted with a Gaussian fit and plotted as function of $\beta\gamma$. The graph obtained is then fitted with a least χ^2 minimization to obtain the parameters of the ALEPH parameterization (Figure 4.3). The solid lines in Figure 4.2 indicate the final parameterization for different particle species. For each data taking period, the corresponding parameterizations are extracted and used in the offline reconstruction framework.

In order to identify tracks reconstructed in the TPC, the measured energy loss of a

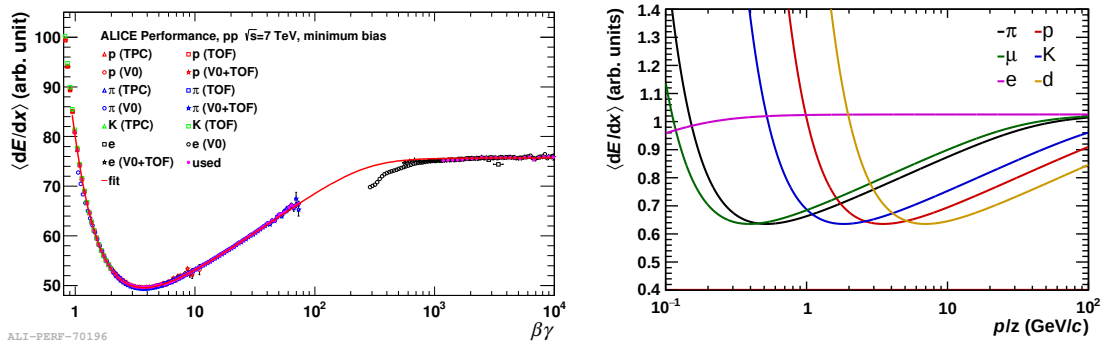

Figure 4.3.: (Left) Bethe-Bloch fit to the TPC $\mathrm{d}E/\mathrm{d}x$ signal from various clean samples covering the different regions of the Bethe-Bloch curve. (Right) Typical Bethe-Bloch curves of the ionization signal as a function of particle momentum for different particle species. A parameterization like the one suggested in [64] was used to calculate the curves.

given track is compared to the expected energy loss of the different particle species, namely to the Bethe-Bloch fits. Tracks are identified by means of a so-called "$n\sigma$-cut", which is defined as the distance of the track's mean $\mathrm{d}E/\mathrm{d}x$ information to the Bethe-Bloch fits. $n\sigma$ is expressed in terms of the detector resolution $\sigma_{\mathrm{d}E/\mathrm{d}x}$

$$n\sigma = \frac{\mathrm{d}E/\mathrm{d}x_{\mathrm{measured}} - \mathrm{d}E/\mathrm{d}x_{\mathrm{fit}}}{\sigma_{\mathrm{d}E/\mathrm{d}x}}, \tag{4.3}$$

where $\sigma_{\mathrm{d}E/\mathrm{d}x}$ depends on the track properties. In case of a 3σ cut, an underestimation of the resolution of up to 0.5σ results only in a systematic error of 1%. Namely, the $n\sigma$-cut approach is robust against miscalibration effects and also errors in the Bethe-Bloch parametrization procedure. On the other hand, contaminations from other particle species resulting from the overlap of $\mathrm{d}E/\mathrm{d}x$ distributions bias the results. This has to be taken into account in the systematic uncertainty estimation of a given physics analysis.

4.2. TPC $\mathrm{d}E/\mathrm{d}x$ response determination

As explained in Chapter 1, the Identity Method requires only the event-by-event quantity ω_i, which is a probabilistic measure of a given track for being particle type i. Therefore, in the first place, one needs to decide on the PID technique which allows for the calculation of ρ_j and ρ quantities (Eq. 1.23), which require inclusive $\mathrm{d}E/\mathrm{d}x$ spectra fits. This requirement rules out the usage of combined Bayesian PID (See Appendix G). Eventually, because of resolution, efficiency and acceptance concerns, the optimum choice remains to be the PID via the specific energy loss $\mathrm{d}E/\mathrm{d}x$ in the TPC.

ρ quantities in the TPC are obtained via a multi-Gaussian fit of the inclusive $\mathrm{d}E/\mathrm{d}x$ spectra in a given phase-space. Since the overlap regions in the $\mathrm{d}E/\mathrm{d}x$ distributions are

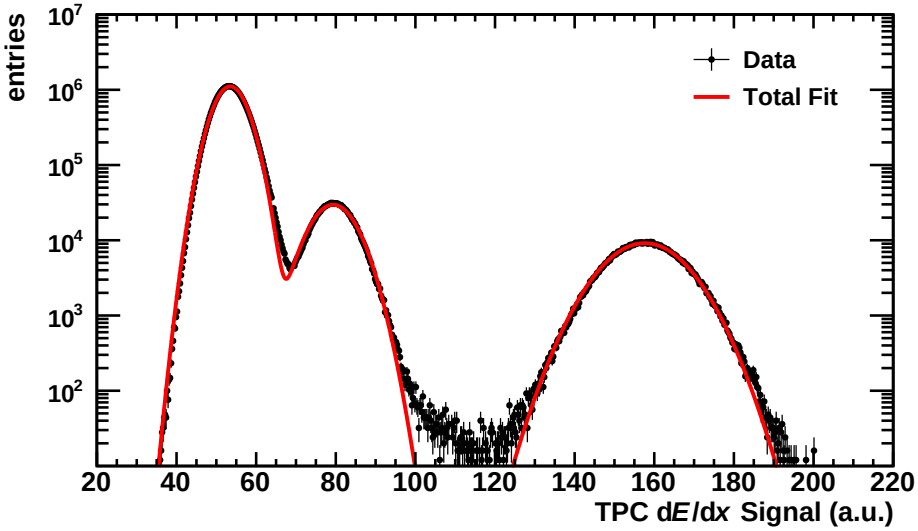

Figure 4.4.: Multi-Gaussian fit of the inclusive $\mathrm{d}E/\mathrm{d}x$ distribution of TPC in the phase-space region of $0.35 < p < 0.37$ GeV/c and $0 < \eta < 0.2$ for the most central events. The overlap region is not covered properly because of the symmetric shape of the Gauss function.

also allowed in the Identity Method, one needs very good fits of inclusive $\mathrm{d}E/\mathrm{d}x$ spectra over the full momentum range covered in the analysis. As can be seen in Figure 4.4, the TPC detector response has an asymmetric behavior. In order to cope with this asymmetric shape, a good understanding of the detector response of the TPC is required. To this end, the detector response of the TPC was determined as follows:

- a generalized Gauss function was chosen in order to describe the response shape better,
- the source of the asymmetry was first investigated by means of a toy-MC study, where the truncated mean procedure in the TPC was simulated,
- the parametrization of the detector response was estimated making use of clean particle samples and partially the inclusive spectra

4.2.1. Generalized Gauss function

Since the Gauss function is not sufficient to describe the TPC detector response, the so-called "Generalized Gauss" function was chosen for a better description of the response shape. In addition to the normal distribution it has two additional parameters, α to cope with the asymmetry and β to describe the width better. The functional form is the following:

$$f(x) = Ae^{-(|x-\mu|/\sigma)^{\beta}} \left(1 + \mathrm{erf}\left(\alpha \frac{|x-\mu|}{\sigma\sqrt{2}}\right)\right) \tag{4.4}$$

where A, μ and σ stand for the abundance, mean and width of the distribution, respectively. The distribution is right-skewed for $\alpha > 0$, left-skewed for $\alpha < 0$ and symmetric for $\alpha = 0$. Besides, the tails of the distribution, compared to a Gauss function, are either heavier for $\beta < 2$, lighter for $\beta > 2$ and recover the symmetric shape for $\beta = 2$. Figure 4.5

shows how it accommodates the asymmetry and the tails.

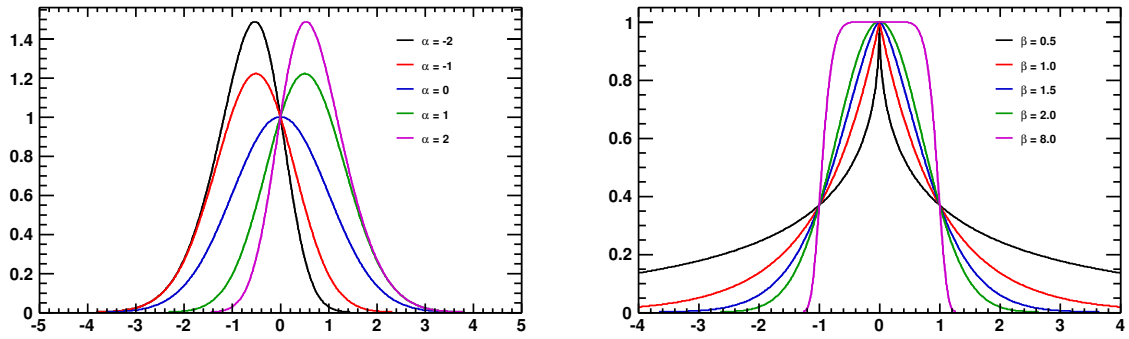

Figure 4.5.: Generalised Gauss function for different skewness (α) parameters at fixed $\beta = 2$ (left) and for different kurtosis (β) parameters at fixed $\alpha = 0$ (right).

4.2.2. Toy simulation of the truncated mean procedure

The most fundamental concept determining the TPC detector response is the truncated mean procedure (See Section 2.2). To quantify the effect of this procedure on the detector response shape, a toy-MC simulation was performed. The truncated mean procedure for a single particle track is illustrated in Figure 4.6.

In order to address also the effect of the rising slope of the $\mathrm{d}E/\mathrm{d}x$ spectrum, two

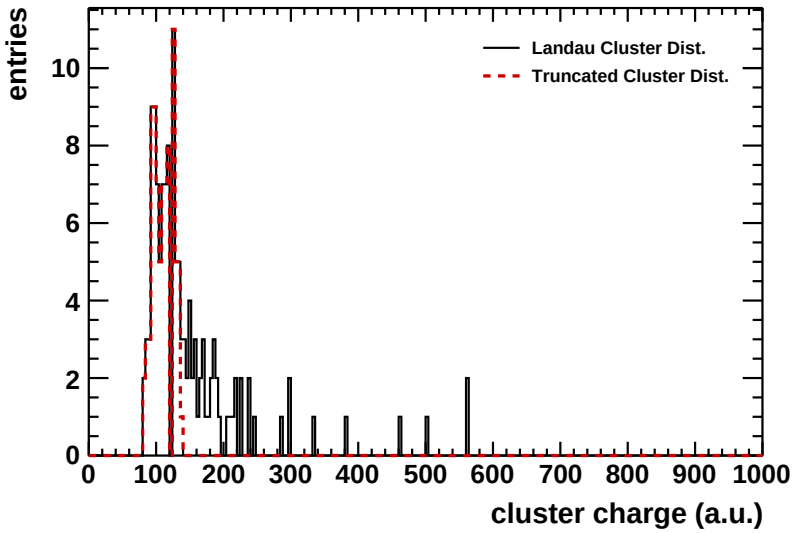

Figure 4.6.: Toy simulation of a given track's charge distribution, which has a Landau shape (black solid line) and the charge distribution after the truncated mean procedure (red dotted line).

simulations were performed. First, the mean $\mathrm{d}E/\mathrm{d}x$ values are taken from Monte-Carlo (MC) protons and, second, fixed at 100, as illustrated in Figure 4.7.

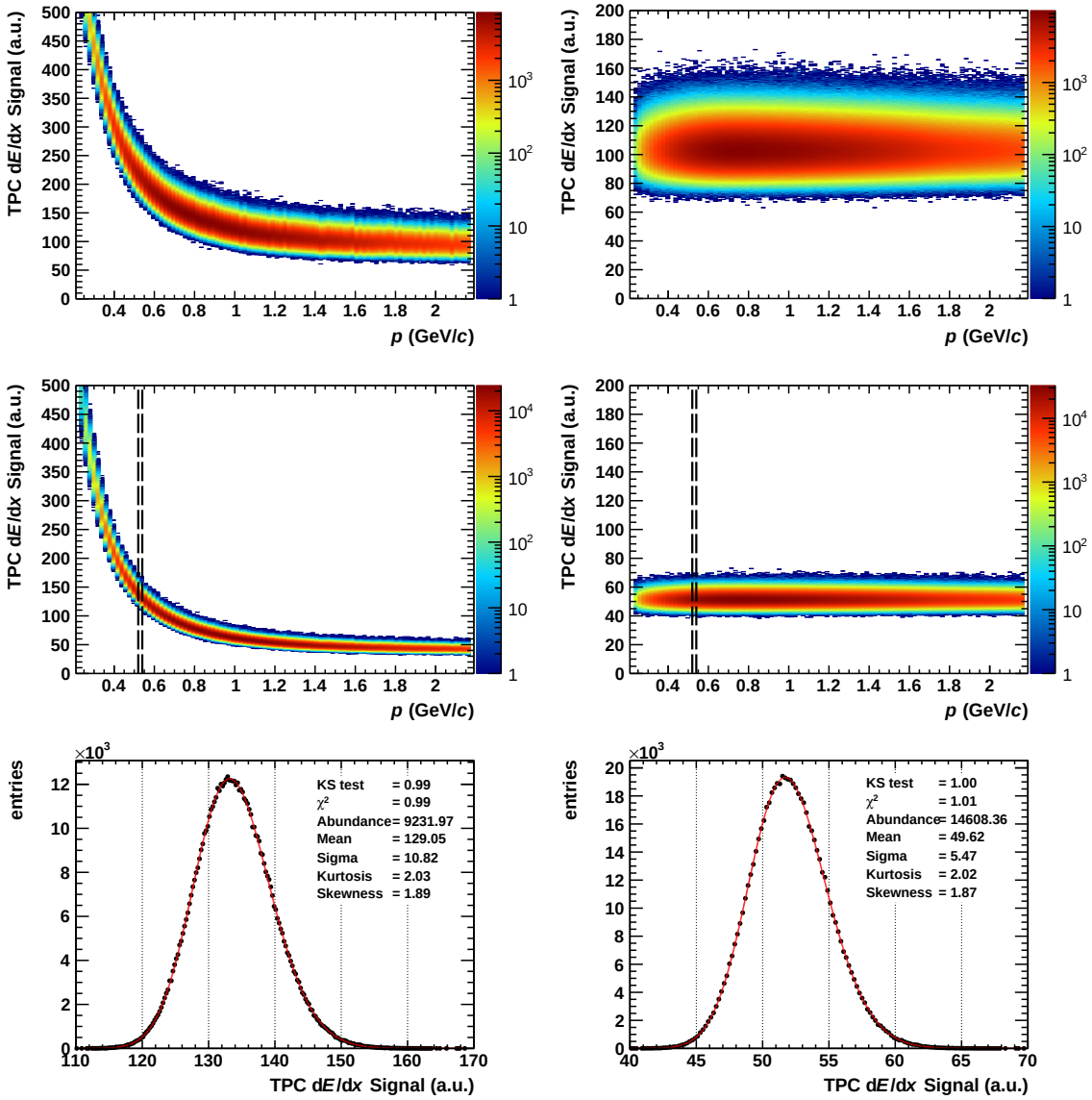

Figure 4.7.: Toy simulation of particle tracks illustrating the effect of truncated mean procedure on the TPC $\mathrm{d}E/\mathrm{d}x$. The mean $\mathrm{d}E/\mathrm{d}x$ values are taken from Monte-Carlo (MC) protons in the left column and are fixed at 100 in the right column. The $\mathrm{d}E/\mathrm{d}x$ distributions before and after the truncated mean procedure are shown in the upper and middle panels, respectively. The lower panel illustrates the Generalized Gauss function fits of the $\mathrm{d}E/\mathrm{d}x$ distributions in the momentum intervals indicated in the middle panel by dashed lines.

The usage of relatively small momentum slices (bin width of 20 MeV/c) eliminates the effect of the rising slope to a large extent. Most importantly, it is also seen that the bare truncation procedure introduces an asymmetry to the detector response, thus the Generalized Gauss as the fit function is indeed a powerful tool. Moreover, a quantitative investigation of the kurtosis and skewness parameters, as shown in Figure 4.8, suggests that the asymmetry and the tails of the fit functions in the momentum interval of $0.5 < p < 2.2$ GeV/c demonstrates a stationary behavior, while the width (σ), as expected, decreases as the slope flattens.

Even with this simplest picture one concludes that the TPC PID response can not be described by a Gauss function. Below, a detailed investigation of the TPC detector response is discussed in view of the clean and MC samples, where to a large extent, detector effects are taken into account, respectively.

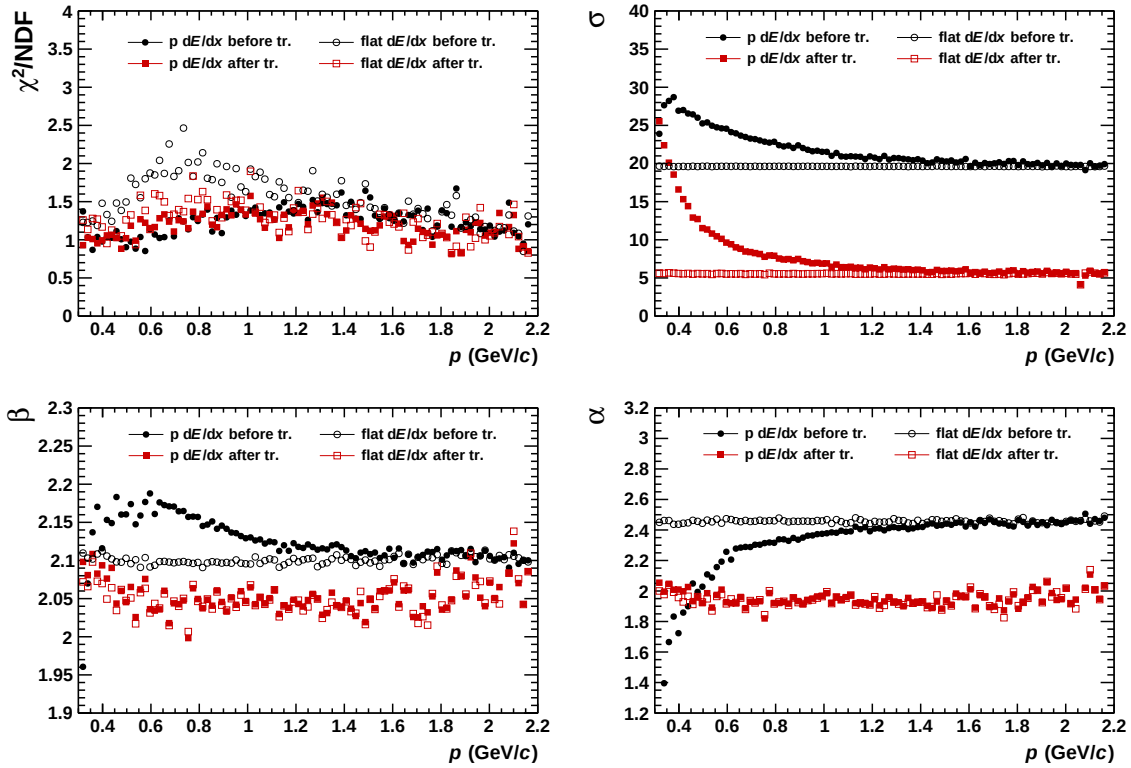

Figure 4.8.: Distribution of the fit parameters α, β and σ as well as the fit quality measure χ^2/NDF along the full momentum range used in Figure 4.7 for before (black markers) and after (red markers) the truncated mean procedure. Closed symbols show the results for the rising dE/dx slope and the open symbols for the fixed dE/dx.

4.2.3. Clean samples

A V^0 is the name given to a neutral particle which decays into two charged tracks, such as K^0_S ($K^0_S \longrightarrow \pi^+\pi^-$), $\bar{\Lambda}$ ($\bar{\Lambda} \longrightarrow \bar{p}\pi^+$) and Λ ($\Lambda \longrightarrow p\pi^+$). Clean samples of electrons, pions and protons were extracted from the decays of these V^0 particles, by means of the Armenteros-Podolanski phase-space (for details see Appendix F).

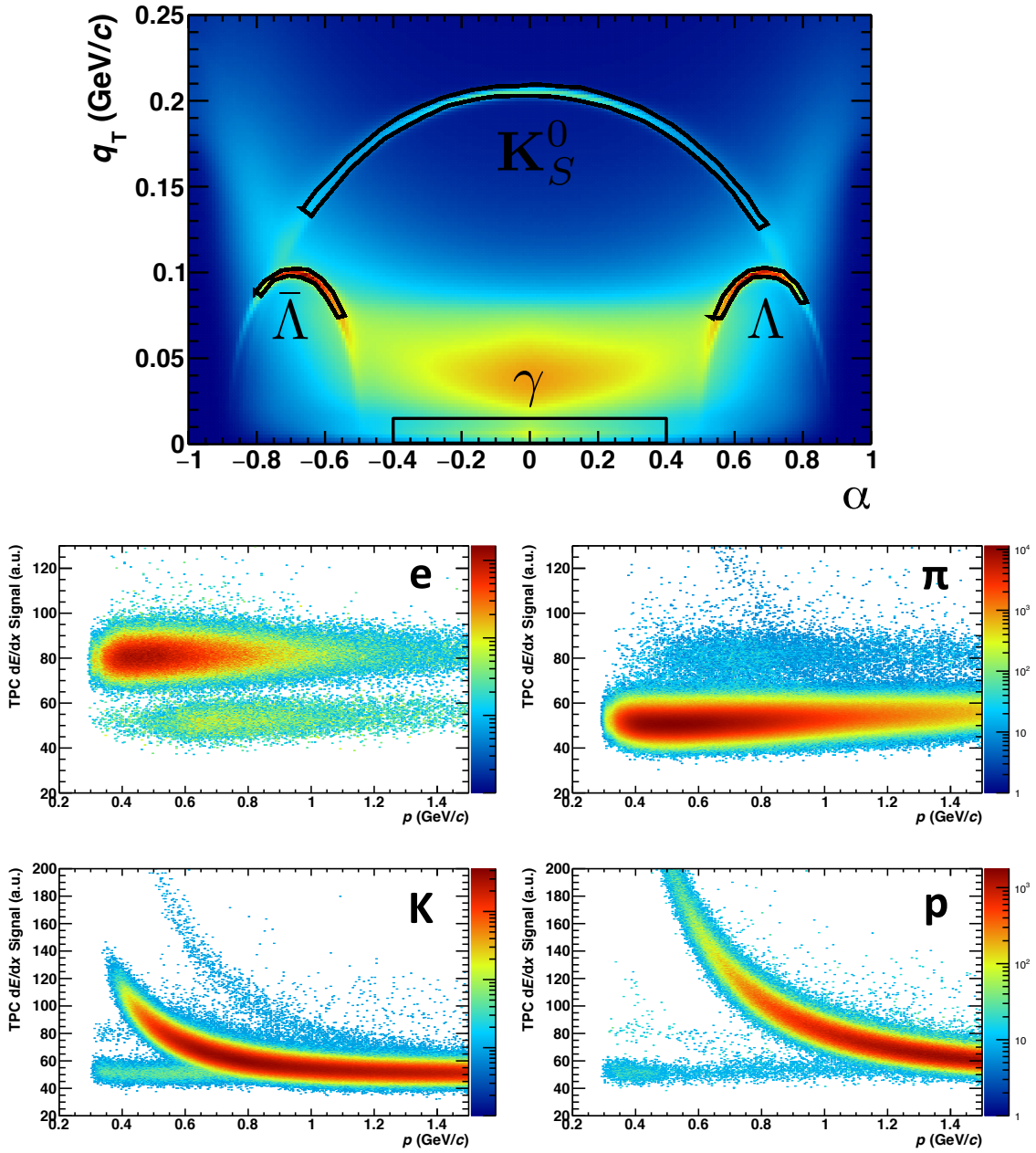

Figure 4.9.: (Upper panel) Armenteros-Podolanski plot obtained from the V0 decay particles. Black lines indicates the graphical cuts used to select K^0_S, $\bar{\Lambda}$ and Λ. The $\mathrm{d}E/\mathrm{d}x$ distributions of clean electron samples (Middle panel left) from the γ conversions, pion samples (Middle panel right) from the decay of $\mathrm{K}^0_S \longrightarrow \pi^+\pi^-$, proton samples (Lower panel right) from the decays of $\bar{\Lambda} \longrightarrow \bar{p}\pi^+$ and $\Lambda \longrightarrow p\pi^+$ and kaon samples (Lower panel left) obtained using TOF and TRD information.

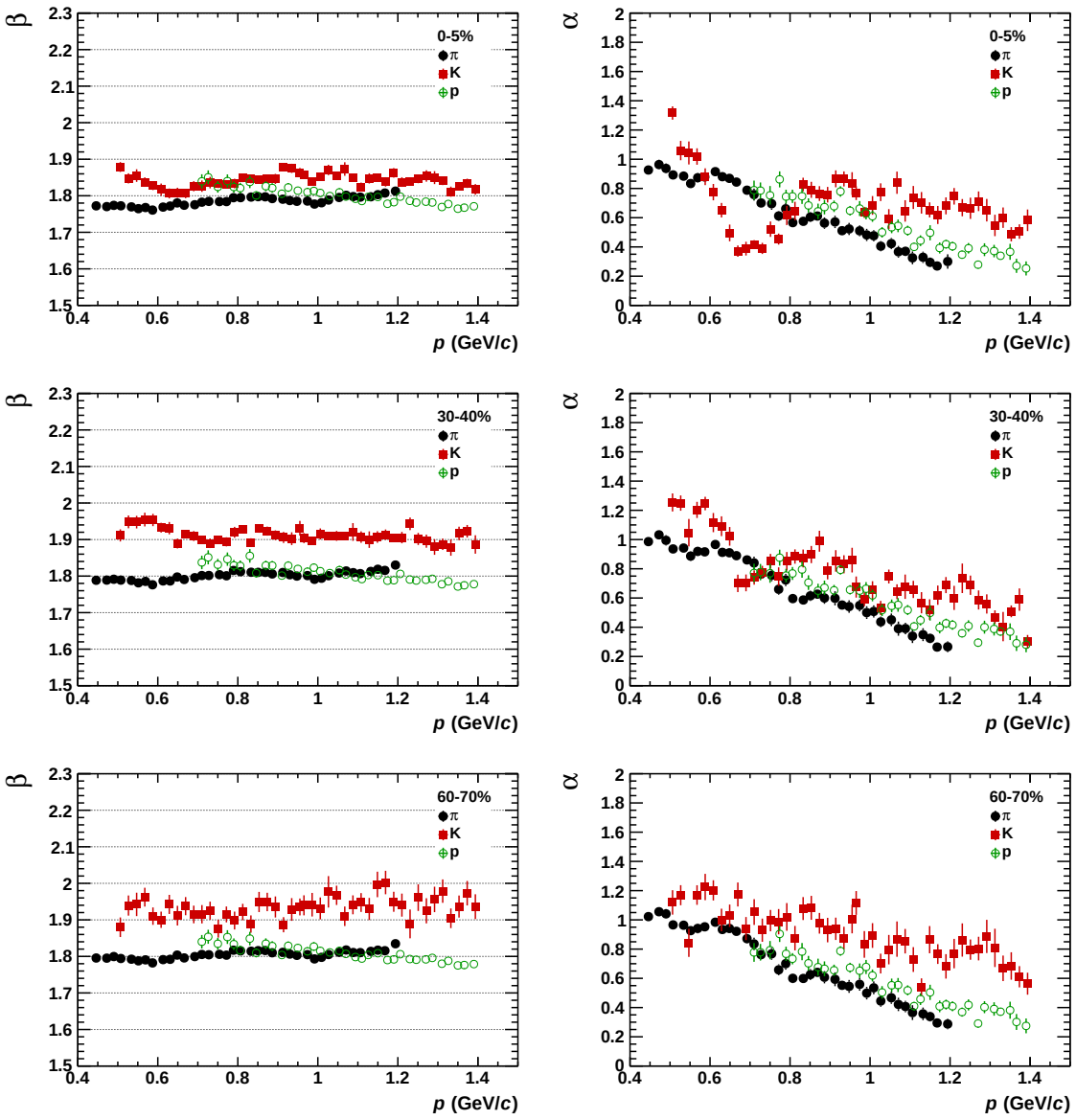

Figure 4.10.: Distribution of the fit parameters β (left column) and α (right column) for clean pions (black markers), kaons (red markers) and protons (green markers) in three different centrality bins: 0-5% (upper panel), 30-40% (middle panel) and 60-70% (lower panel).

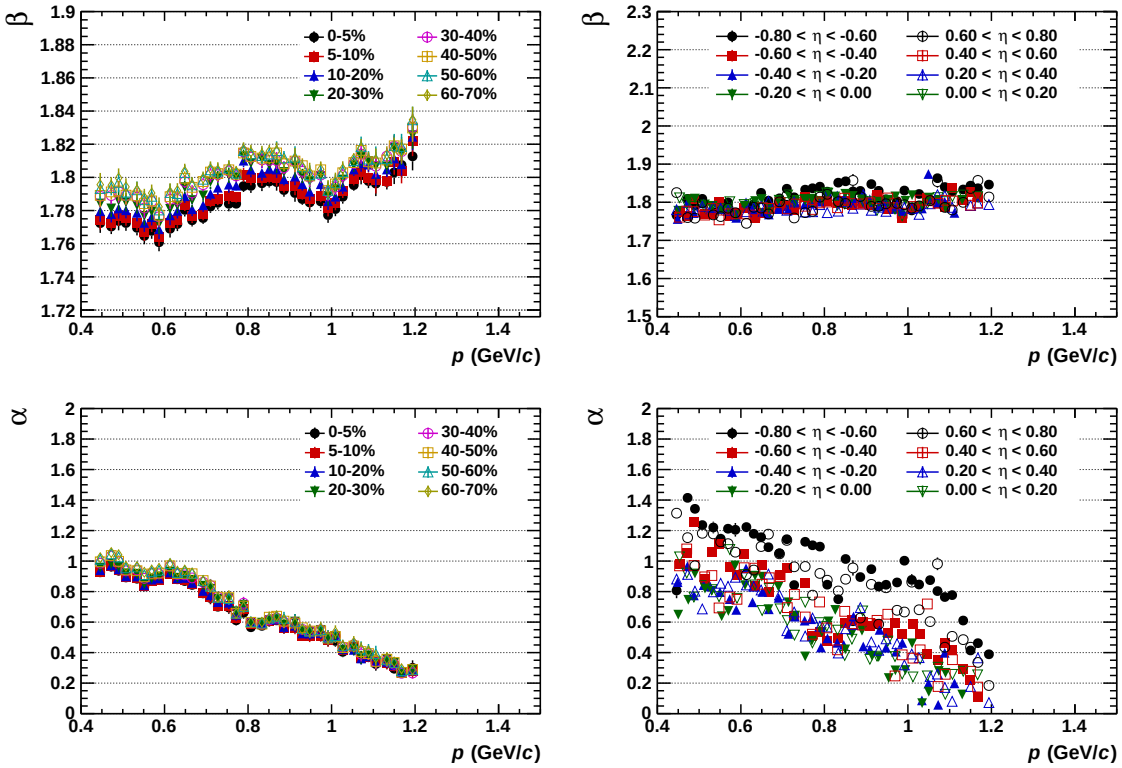

Figure 4.11.: Distribution of the fit parameters β (upper panel) and α (lower panel) for clean pions. Centrality and pseudorapidity dependence of both parameters are shown in the left and right columns, respectively.

The Figure 4.9 shows the Armenteros-Podolanski plot which illustrates the yields as a function of q_{T} and α, where q_{T} is defined as the transverse momentum of either of the V^0 decay particles relative to the direction of the V^0 and α is defined as

$$\alpha = \frac{q_{\mathrm{L}}^{+} - q_{\mathrm{L}}^{-}}{q_{\mathrm{L}}^{+} + q_{\mathrm{L}}^{-}} \tag{4.5}$$

where q_{L}^{+} and q_{L}^{-} are the longitudinal momentum components of the positive and negative decay tracks respectively relative to the direction of the V^0. The α parameter measures the momentum asymmetry in the decay.

Clean samples of pions and protons are retrieved from the decays of K^0_S, $\bar{\Lambda}$ and Λ through the Armenteros-Podolanski phase-space, as depicted with solid black lines in Figure 4.9, while for the electrons γ conversions in $q_{\mathrm{T}} < 0.015$ and $|\alpha| < 0.4$ were used. Since the achieved purity was sufficient, additional cuts on the invariant mass were not performed. The clean kaon samples were extracted making use of the TOF and TRD detectors. For this, cuts on the $n\sigma$ in TOF ($n\sigma_{\mathrm{TOF}} < 2$) and on the number of clusters measured in TRD ($n_{\mathrm{cl,TRD}} < 80$) were used (see Appendix G for the details about the PID in TRD and TOF detectors). The reason to use the number of clusters cut in the TRD was to have a cleaner sample by selecting the kaons which decay after passing through the TRD.

The $\mathrm{d}E/\mathrm{d}x$ distributions of the clean samples is shown in Figure 4.9. To investigate the detector response, each sample was fitted with the generalised Gauss function in momentum slices of 20 MeV/c. In particular, the kurtosis and skewness parameters of the pions,

kaons and protons were examined, since they are the main focus of this thesis. As shown in Figure 4.10, the kurtosis values stay more or less constant as a function of momentum, where clean kaons have slightly more pronounced tails than pions and protons. This might be due to the resulting cluster shape difference arising from the track topologies of the V^0 decay particles. On the other hand, the skewness parameter decreases with the momentum for all three samples, where kaons again show slightly larger values which can be explained by the fact that the kaon samples are less pure than pions and protons due to their selection procedure.

The centrality and pseudorapidity dependence of the kurtosis and skewness parameters for clean pions are displayed in Figure 4.11. The kurtosis shows a clear centrality but no pseudorapidity dependence as function of momentum. Most central events have a narrower peak shape. The reason for this centrality dependence can be attributed to the aforementioned baseline fluctuations which are not yet corrected in this data sample. On the other hand the skewness parameter shows no centrality but a clear pseudorapidity dependence. This is quite intuitive because more inclined tracks smear the shape of the clusters and thus introduce a larger asymmetry for the large η.

In summary, additional detector effects on top of the truncated mean procedure introduce a significant momentum dependence of the skewness parameter, i.e. asymmetry, as a function of momentum. Besides, the kurtosis parameter remains constant but has a narrower peak width compared to a Gauss function. Not to mention, the pseudorapidity and centrality dependences should be taken care of in the inclusive $\mathrm{d}E/\mathrm{d}x$ spectra fits.

4.2.4. Monte-Carlo (MC) samples

It is a big challenge to properly describe and simulate each individual detector effect particularly for such a huge and complex detector system like ALICE. As discussed in Section 3.5, several detector effects, such as gain map, hardware settings, effects related to track topology etc. have already been implemented in the Aliroot simulation framework unlike those ion-tail and common-mode effects. The main motivation to investigate the TPC $\mathrm{d}E/\mathrm{d}x$ response by means of the MC samples was to see how well the currently observed detector effects are described in MC and also, if the MC information helps for the inclusive spectra fits.

Since GEANT [77] allows for the simulation of the TPC $\mathrm{d}E/\mathrm{d}x$ of a given track, the identities of each particle and corresponding $\mathrm{d}E/\mathrm{d}x$ values are available in the simulation output. Therefore one can easily produce the inclusive and individual particle $\mathrm{d}E/\mathrm{d}x$ distributions as shown in Figure 4.12.

To investigate the simulated detector response, as in the case of clean samples, each MC sample was fitted with the generalised Gauss function in momentum slices of 20 MeV/c. As shown in Figure 4.13, the kurtosis values stays more or less constant with a very slight decreasing slope as a function of momentum for pions, kaons and protons, while the statistics in the most peripheral events are not sufficient to draw a firm conclusion. On the other hand, the skewness parameter decreases with the momentum for all three samples, where protons show slightly larger values.

The centrality and pseudorapidity dependence of the kurtosis and skewness parameters for clean pions are displayed in Figure 4.14. Both skewness and kurtosis show a centrality but no pseudorapidity dependence as function of momentum. Most central events have a narrower peak shape and smaller asymmetry. The deviations at large momenta are due to lack of statistics as can be seen in Figure 4.12.

In summary, MC samples agree with the overall behavior of the clean samples but small differences that can be attributed to additional detector effects, which are not yet included in the Aliroot simulation framework, remain.

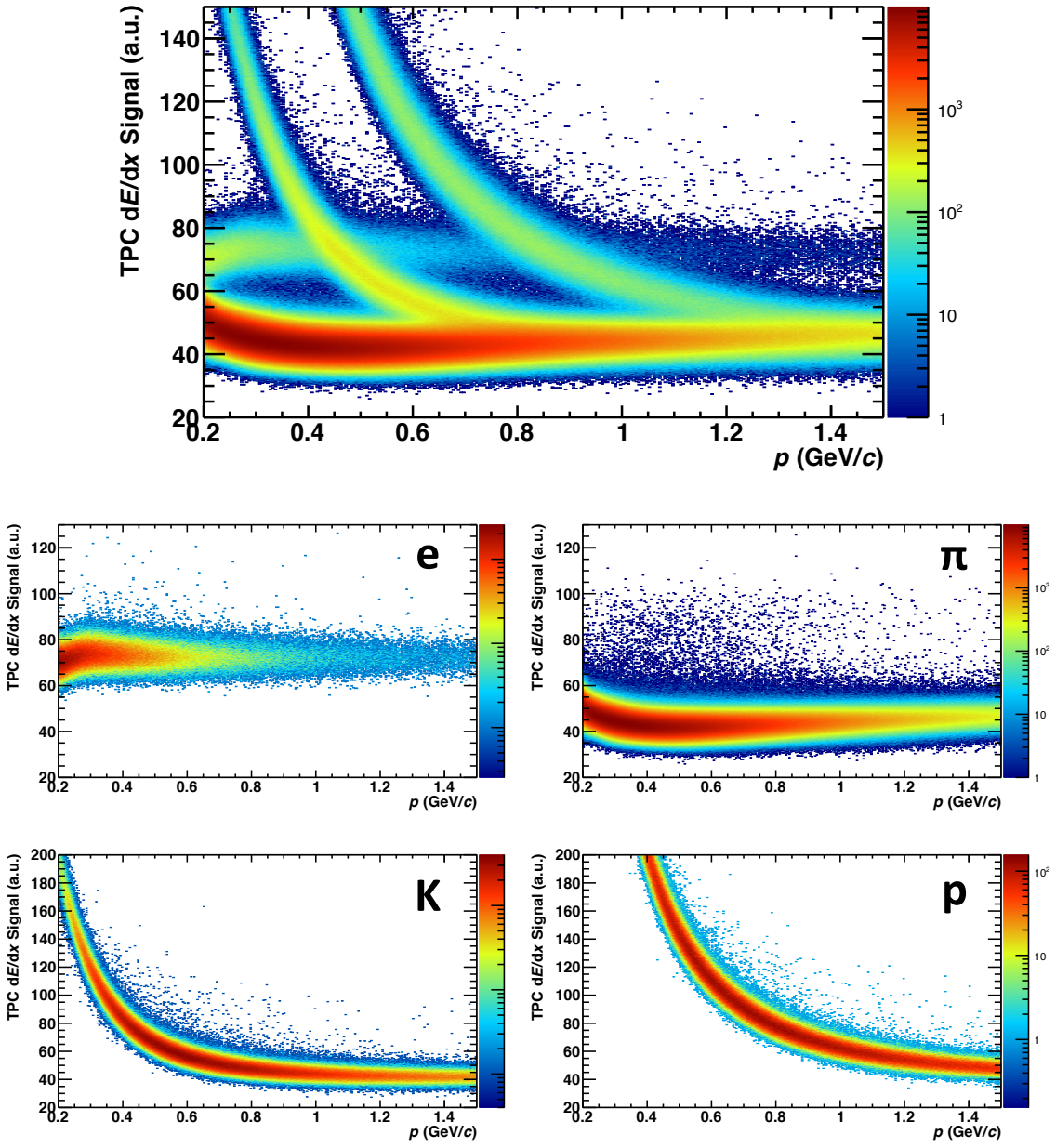

Figure 4.12.: $\mathrm{d}E/\mathrm{d}x$ distributions of inclusive MC particles (Upper panel), electrons (Middle panel left), pions (Middle panel right), kaons (Lower panel left) and protons (Lower panel right).

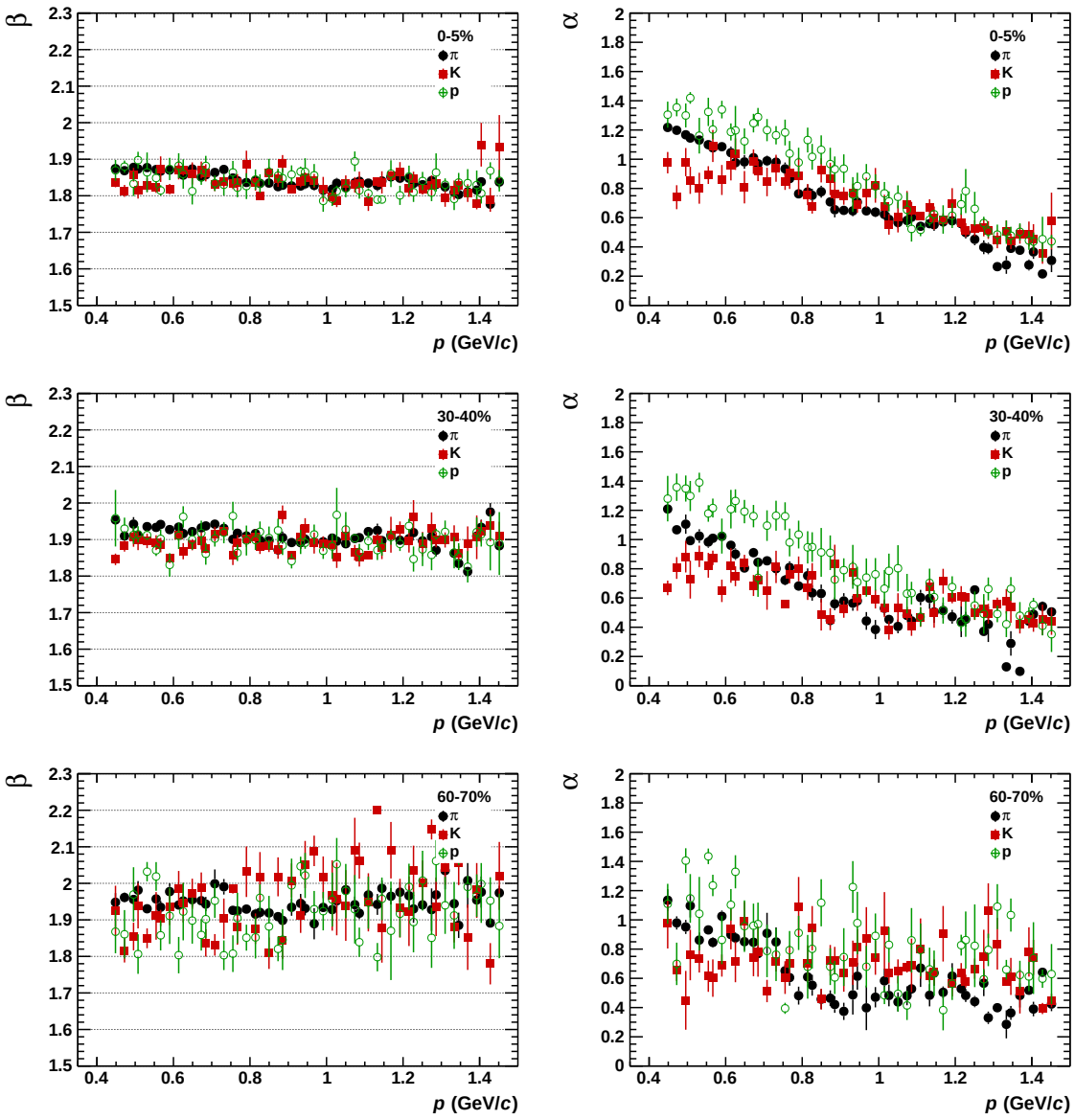

Figure 4.13.: Distribution of the fit parameters β (left column) and α (right column) for MC pions (black markers), kaons (red markers) and protons (green markers) in three different centrality bins: 0-5% (upper panel), 30-40% (middle panel) and 60-70% (lower panel).

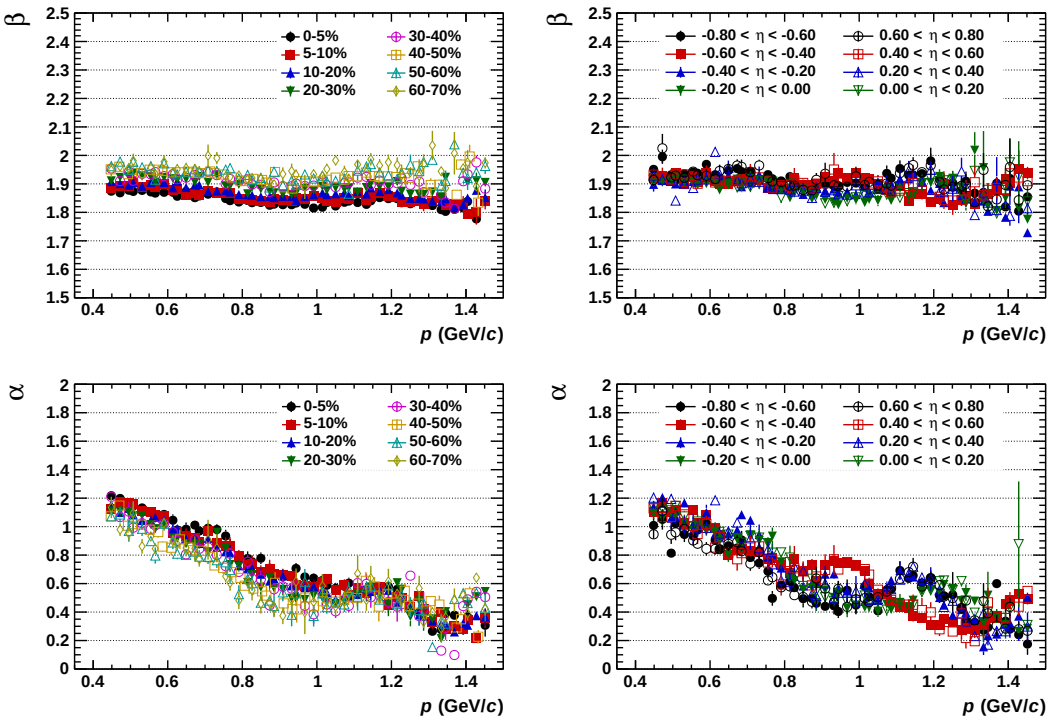

Figure 4.14.: Distribution of the fit parameters β (upper panel) and α (lower panel) for MC pions. Centrality and pseudorapidity dependence of both parameters are shown in the left and right columns, respectively.

4.3. Inclusive $\mathrm{d}E/\mathrm{d}x$ spectra fits of the TPC

The main topic of this thesis, particle-ratio fluctuation analysis, was performed as a function of pseudorapidity and centrality. Accordingly the quality of the inclusive spectra fits as a function of η and centrality play an important role for the final physics output. Therefore, these dependencies of the TPC $\mathrm{d}E/\mathrm{d}x$ response, in view of the MC and clean samples, as well as the inclusive spectra, was investigated prior to the iterative fitting procedure.

4.3.1. Pseudo-rapidity and centrality dependence of the TPC $\mathrm{d}E/\mathrm{d}x$

Neither MC nor clean samples are solely able to provide a perfect description of the detector response in terms of the kurtosis and skewness parameters due to the aforementioned reasons. Therefore results from MC and clean samples are compared to the so-called "safe momentum intervals" of the inclusive spectra where there is no overlap of the $\mathrm{d}E/\mathrm{d}x$ distributions of individual particles. This comparison is illustrated in Figure 4.15 for the pions only.

Clean pion samples, which were retrieved from the K^0_S decays ($\mathrm{K}^0_S \longrightarrow \pi^+\pi^-$), do not agree with the inclusive spectra, because of the cut applied to the TOF information which allows for a better separation of the pions and electrons at low momenta. On the other hand, MC samples do not describe the centrality dependence observed in the data. This can be attributed to detector effects, such as ion-tail and common-mode, which are not

yet included in the MC framework. Furthermore, the slight centrality dependence of the asymmetry with respect to the inclusive spectra is not described by neither MC nor clean pions, while the qualitative behavior of the decreasing asymmetry as a function of the momentum is.

Moreover, a significant pseudorapidity dependence of the mean dE/dx positions were

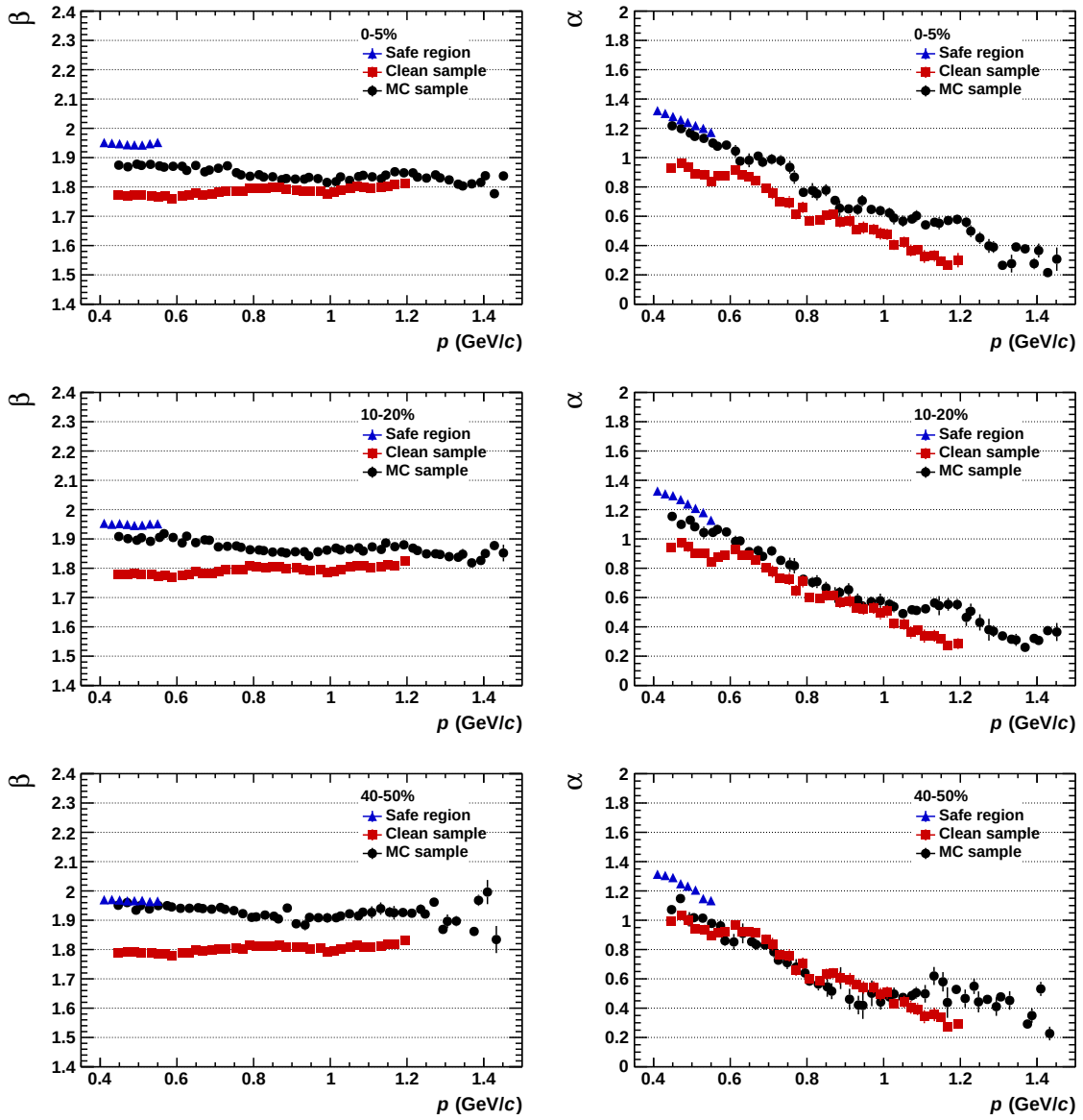

Figure 4.15.: Distribution of the fit parameters β (left column) and α (right) for MC (black markers), clean sample (red markers) and inclusive spectra pions in three different centrality bins: 0-5% (upper panel), 30-40% (middle panel) and 60-70% (lower panel).

observed, as shown in Figure 4.16. Here, the clean samples provide a reasonable estimate for the inclusive spectra while the MC samples agree only qualitatively in spite of a systematic shift.

Taking these dependencies into account, a step-by-step procedure for the inclusive spectra fits has been developed.

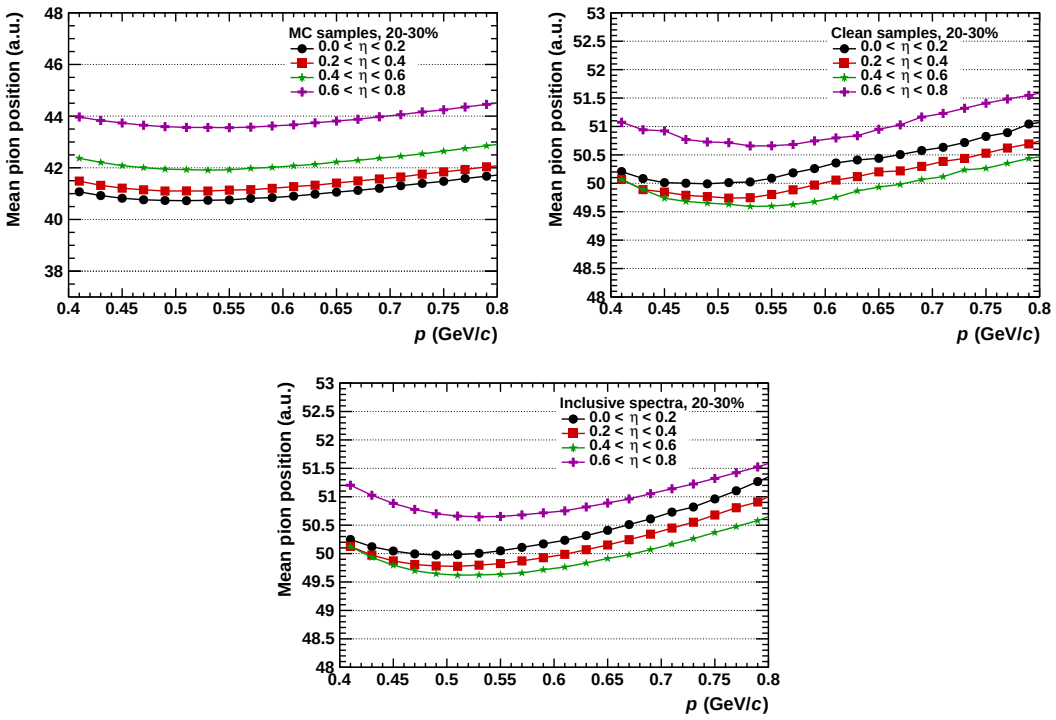

Figure 4.16.: Pseudorapidity dependence of the mean $\mathrm{d}E/\mathrm{d}x$ positions of the MC simulation (top left), clean sample (top right) and inclusive pion spectra (bottom) in the centrality bin of 20-30%.

4.3.2. Iterative fitting procedure

In order to cope with the pseudorapidity, multiplicity and momentum dependence of the TPC $\mathrm{d}E/\mathrm{d}x$, the inclusive spectra fits were applied in sixteen pseudorapidity, nine centrality and 65 momentum bins in the kinematic range $0.2 < p < 1.5$ GeV/c and $|\eta| < 0.8$. For a given phase-space bin, $\mathrm{d}E/\mathrm{d}x$ distributions of five particle species (electron, pion, kaon, proton, deuteron) were fitted with a generalised Gauss function each of which requires an a priori estimate for the fit parameters. For this, an iterative procedure was developed where one or two parameters are estimated in each step. Details of the procedure is given below.

1st iteration: Determination of kurtosis and skewness parameters

For a given data set the Bethe-Bloch parameterization of each particle species, i.e. mean $\mathrm{d}E/\mathrm{d}x$ position and expected width around it are available in the Aliroot framework. First of all, making use of these information, initial fits of the inclusive spectra and clean samples are performed in momentum slices with a width of 20 MeV/c. This allows for the determination of the $\mathrm{d}E/\mathrm{d}x$ responses of clean particle samples as well as the inclusive spectra in the safe momentum intervals: $0.3 < p < 0.5$ GeV/c for pions, $0.6 < p < 0.8$ GeV/c for protons and $0.3 < p < 0.4$ GeV/c for kaons. Then the kurtosis parameter was estimated, because it is not only the most sensitive parameter but also does not change as a function of momentum unlike others. For pions and protons the safe momentum intervals were used, while for kaons the clean samples. This is because kaons start to merge with the electrons at about 0.4 GeV/c, where the rising slope of the

dE/dx distribution does not lose its effect. Note that, clean samples, in general, are not a good estimator for the kurtosis therefore the kurtosis of the kaons is further studied in the systematic uncertainty analysis part in Chapter **??**.

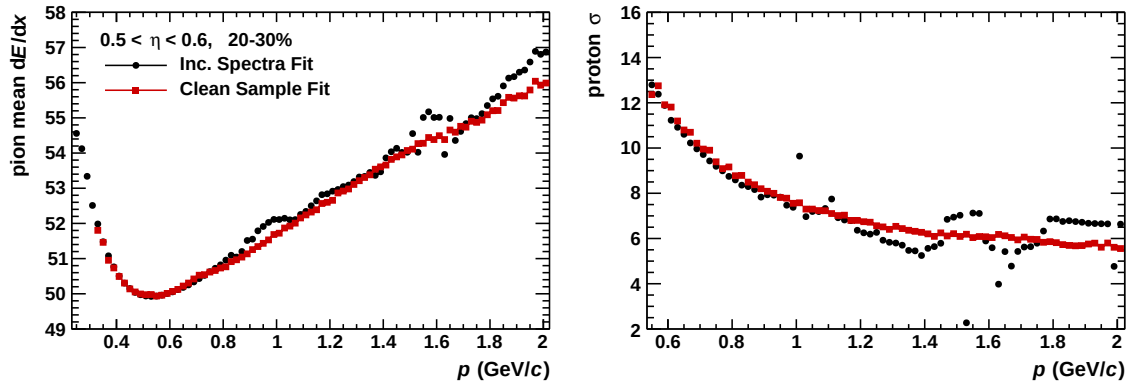

Figure 4.17.: Comparison of the first iteration fit results (black markers) and the clean sample fits (red markers). Left: mean dE/dx position for pions. Right: width (σ) of the generalized Gauss function fit for protons.

Following the estimation of the kurtosis for each particle, the skewness parameter is also determined with the same data samples as used for the kurtosis. Here additionally, MC samples were used, since they allow for an extrapolation to the momentum slices where there are overlaps of the dE/dx distributions. Although, skewness is not constant as a function of momentum, in the current study, it was taken to be an optimized fixed value for simplicity. Nevertheless, a reasonable fit performance is achieved with this assumption (See next section). Therefore, one can conclude that the final fit performance is not so sensitive to the skewness parameter.

2nd Iteration: Determination of mean and sigma parameters

The official PID response parametrization is based on the Gaussian fits and they are determined for a given data sample (See Section 4.1). Therefore, they might be somewhat biased for a given analysis. In this study they were used only as a rough estimate for the initial fits. The clean particle samples were used as the main estimator for the mean dE/dx positions for all particle species, and also for the sigma parameter of protons, as shown in Figure 4.17. It is clearly seen that the dE/dx overlap regions are recovered completely. Note that, a change in the kurtosis and skewness parameters results in a systematic shift in the mean dE/dx position and sigma of a given fit function. This was compensated by a simple scaling with respect to the safe regions of the inclusive spectra.

3rd Iteration: Determination of abundance

Having fixed the kurtosis, skewness, mean, and sigma parameters for each particle making use of the clean-MC samples and safe regions of the inclusive spectra, the remaining parameter is the abundance. For this, neither clean nor MC particles can be used, since they do not represent the physics of the inclusive spectra. The assumption here is that the yield of each particle shows a smooth behavior as a function of momentum. Taking this

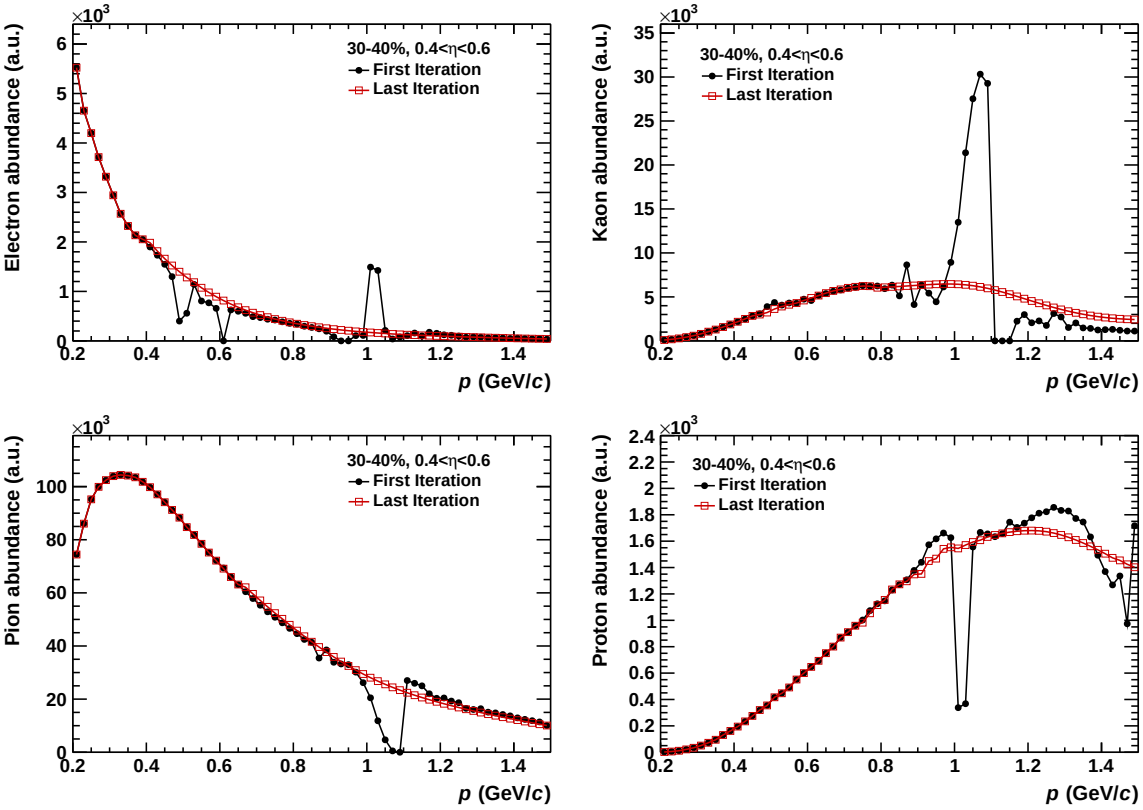

Figure 4.18.: Comparison of the abundances of each particle species in the first (black markers) and last (red markers) iteration.

into account, an iterative interpolation procedure is applied to the abundance parameter of each particle subsequently. The resulting abundances for each particle species in a given phase-space interval for the first and last iteration is shown in Figure 4.18. The integral of the fit functions, i.e the pion yields are also shown in Figure 4.19 for several iterations. The outliers in the momentum interval of $0.6 < p < 1.5$ GeV/c are recovered in the final iteration.

4.3.3. Discussion of the fit results

The quality of the fits were monitored by both Kolmogorov-Smirnov (K-S) and χ^2 tests, as well as the residuals which are defined as the difference between data points and the total fit function, normalized to the statistical error of the data points. In each iteration, the fit quality from the K-S test statistics was guaranteed to fall in a confidence band of 90%.

Two example $\mathrm{d}E/\mathrm{d}x$ distribution fits, as well as the corresponding residuals, in a given phase-space bin are shown in Figure 4.20. These two have the worst χ^2 performance at low and high momenta regions considered in this thesis. Since the kurtosis parameter for a given phase space along the full momentum range is just a fixed approximated value, the shoulders of the peaks are not fully covered. This results in such a wavy structure in the residuals as seen in Figure 4.20 bottom plots. Nevertheless, the maximum deviation is less than 5σ of the statistical uncertainty.

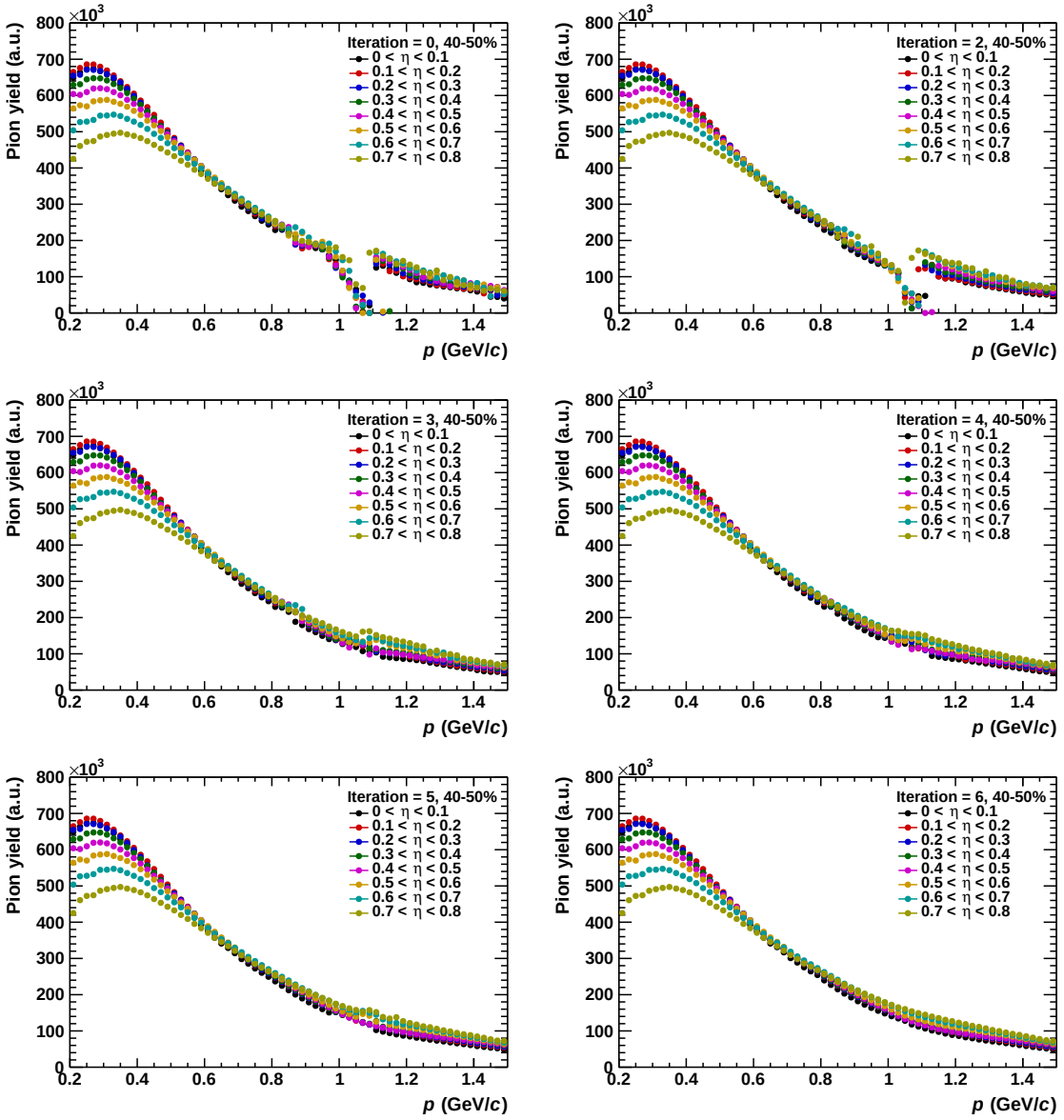

Figure 4.19.: Integral of the fit functions of inclusive pion spectra for several fit iterations.

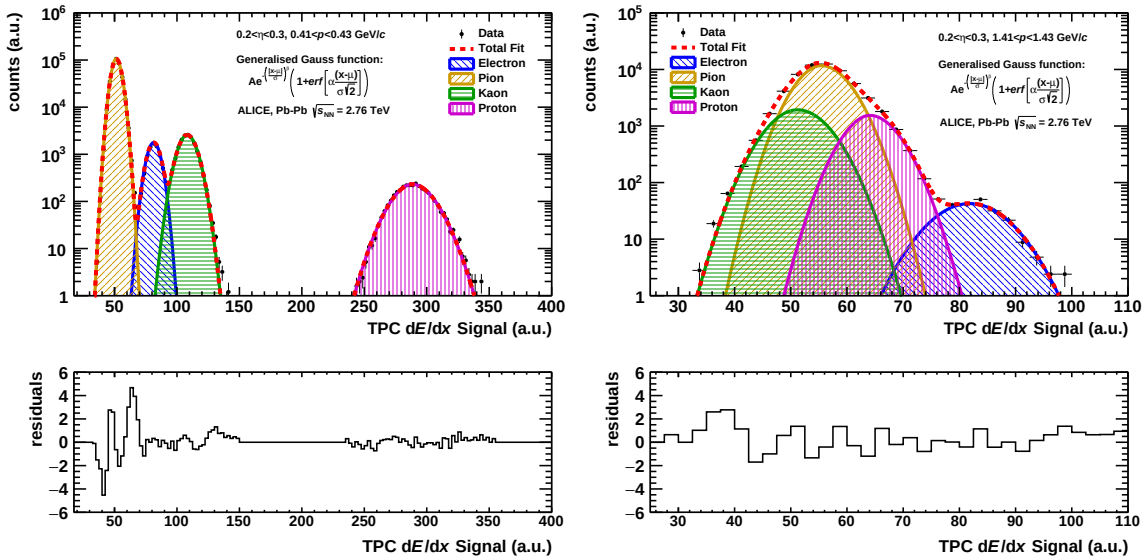

Figure 4.20.: (Upper panel) $\mathrm{d}E/\mathrm{d}x$ distributions of pions, kaons, electrons and protons fitted with the generalized Gauss function in two different momentum intervals. (Lower panel) The corresponding residual plots.

Even though the current fits of inclusive spectra are confirmed to provide excellent results in the physics output, there is still some room for improvement. For instance, to have cleaner kaon samples one can use the decay of the ϕ meson ($\phi \longrightarrow K^+K^-$, BR= 48.9$\pm$ 0.5% [4]) instead of the TOF cut which can not remove the contamination at momenta larger than 0.6 GeV/c. Furthermore, the treatment of the skewness parameter can be improved by taking into account its decreasing behavior as a function of momentum.

5. Data Analysis

This chapter is dedicated to the analysis of the event-by-event particle ratio fluctuations. Track and event selection, error estimation and the verification of the Identity Method with a MC simulation will be discussed in detail. Also, the comparison of the particle spectra obtained using the Identity Method to published results is given. Moreover, the effect of particle detection efficiency on the ν_{dyn} measure is investigated.

5.1. Data set and acceptance

In this analysis, about 13 million Pb–Pb events at $\sqrt{s_{\mathrm{NN}}} = 2.76$ TeV collected with the ALICE detector during the first LHC run in 2010, were used. The sub-detectors involved in the analysis were the TPC and ITS for tracking, particle identification and vertexing. Moreover, the two forward V0 detectors were used as triggering detectors and for the centrality estimation.

The ITS-TPC tracking system covers the mid-rapidity region ($|\eta| < 0.8$) and provides

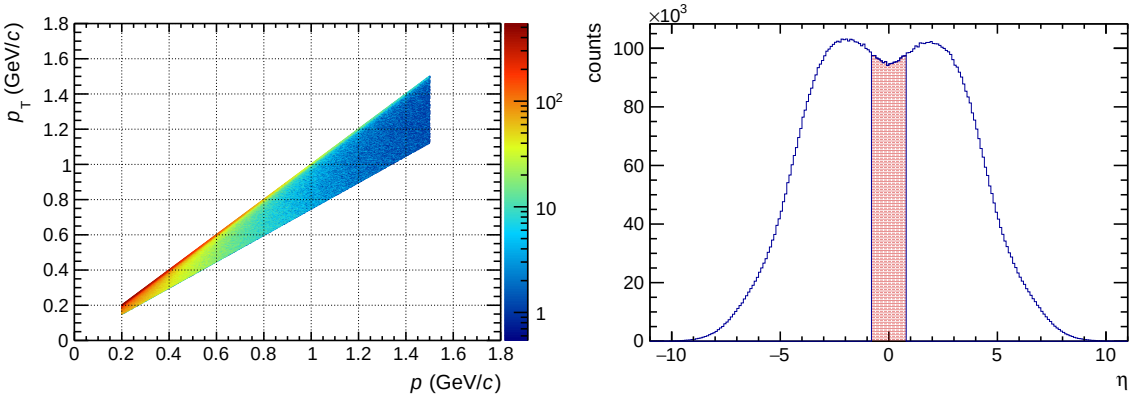

Figure 5.1.: Acceptance in momentum ($0.2 < p < 1.5$ GeV/c) and pseudorapidity ($|\eta| < 0.8$) spaces (HIJING model calculations).

charged-particle tracking and momentum reconstruction down to $p_{\mathrm{T}} = 100\,\mathrm{MeV}/c$. The ITS allows to reconstruct the collision vertex with high precision, and provides for powerful rejection of secondary charged particles. Moreover, ITS and TPC allow particle identification through measurements of the specific energy loss by ionisation ($\mathrm{d}E/\mathrm{d}x$). While PID via $\mathrm{d}E/\mathrm{d}x$ in the ITS is limited to the $1/\beta^2$ domain, the relativistic rise of the energy loss in the TPC gas allows particle identification over a wide momentum range out to several GeV/c. Therefore, in this analysis, the PID was based on the measurement of the $\mathrm{d}E/\mathrm{d}x$ in the TPC gas. The momentum range was restricted to $0.2 < p < 1.5$ GeV/c in order to minimize the systematic uncertainties due to overlaps of the particle $\mathrm{d}E/\mathrm{d}x$ distributions and also to avoid minijet contributions which may lead to additional correlations and fluctuations. Figure 5.1 illustrates the acceptance covered in momentum and pseudorapidity spaces.

5.2. Event and track selection

An online minimum bias (MB) trigger condition, which is defined as a coincidence of hits in both V0 detectors, were used for the event selection. Since the purity of the primary track selection is crucial for the analysis of ν_{dyn}, at least two hits in the outer layer of the SPD were also required to have tighter constraints on the vertex determination and thus avoid large weak decay and feed-down contaminations.

For the primary vertex determination both ITS and TPC information were used. Additionally, the event vertex is reconstructed using only TPC tracks. The event is accepted only if the z-position of that vertex is within ±10 cm from the nominal interaction point along the beam direction to keep the acceptances of all detectors as uniform as possible.

Also, an offline event selection is applied to reject undesired events such as machine-

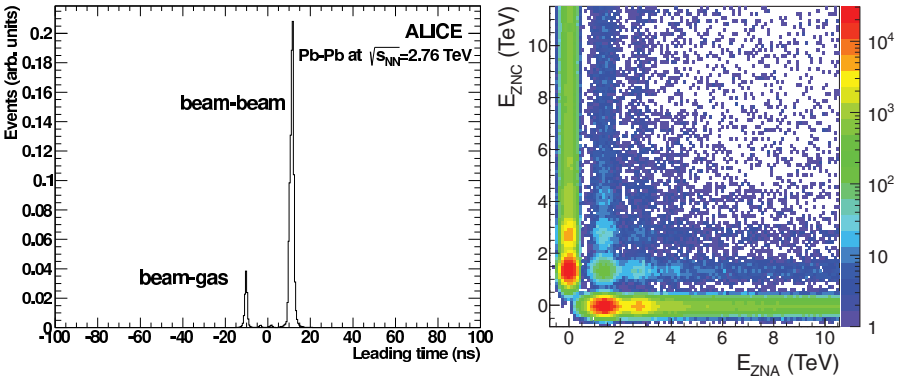

Figure 5.2.: (Left) Time distribution of signals in the V0A detector. The peaks corresponding to beam-beam, beam-gas and satellite collision events are clearly visible [80]. (Right) Correlation between signals in the two neutron zero-degree calorimeters, ZNA and ZNC. Single electromagnetic dissociation events produce a signal in only one of the calorimeters [80].

induced background events, that are caused by the lead ions in the beam interacting with the residual gas in the beam-pipe or the mechanical structures in the machine and parasitic collisions from debunched ions (Figure 5.2). These events are filtered by making use of the timing information provided by the V0 detector. Moreover, large electromagnetic (EM) fields generated by the relativistic heavy ions produce photons which later may create e^+e^- pairs. Also, one photon from the EM field of one of the nuclei may interact with the other nucleus leading to low-multiplicity events with soft particles. These physical background processes are identified and rejected correlating the response of the ZNA and ZNC detectors, as shown in the right plot of Figure 5.2 [80]. The efficiency of the event selection is calculated using the average of results obtained with HIJING and AMPT simulations. Under the aforementioned online and offline event selection criteria an event selection efficiency of about ∼97% was achieved.

Several track cuts were applied to guarantee an optimal $\mathrm{d}E/\mathrm{d}x$ and momentum resolution. For this, charged-particle tracks having at least 80 crossed rows in the TPC and having a maximum χ^2 per cluster from the track fit less than 4 were accepted. Besides, daughter tracks from reconstructed secondary weak decay topologies (kinks) were rejected. For the primary-track selection the Distance-of-Closest Approach (DCA) of the extrapolated trajectory to the primary-vertex position is restricted to less than 2 cm along the beam direction, while on the transverse plane tracks are required to fulfill the following

condition

$$dca_{xy} < 0.0182 \text{ mm} + \frac{0.0350 \text{ mm}}{p_{\mathrm{T}}^{1.01}}, \tag{5.1}$$

which takes into account the p_{T}-dependence of the impact parameter resolution. Moreover, tracks are required to be present in ITS and TPC refits.

Pseudo-rapidity (η) range	$\lvert\eta\rvert$ <0.8
Momentum (p) range	0.2<p<1.5 GeV/c
Centrality classes (%)	0-5, 5-10, 10-20, 20-30, 30-40 40-50, 60-70, 70-80
DCA to vertex on xy plane	$< 0.0182 \text{ mm} + \frac{0.0350 \text{ mm}}{p_{\mathrm{T}}^{1.01}}$
DCA to vertex along beam direction	<2 cm
TPC vertex along beam direction	<10 cm
χ^2 per cluster	<4
Number of crosseed rows is a sector	>80
Found/findable TPC clusters	>0.5
Fraction of shared clusters	<0.4
TPC and ITS refit	yes
Require hits in SPD	yes
Rejection of kink daughters	yes

Table 5.1.: Summary of the track selection criteria.

The classification of events in centrality intervals is obtained by fitting the summed amplitudes of the signals in the V0A and V0C detectors with a Glauber model [80]. The

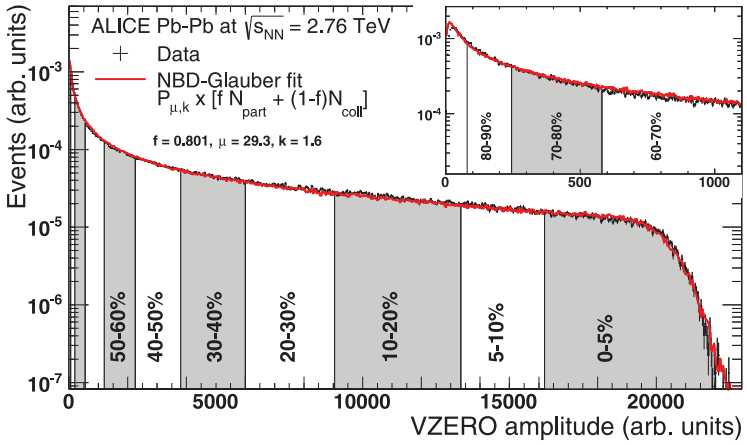

Figure 5.3.: (Black markers) Distribution of the summed amplitudes in the V0 detectors. (Red curve) the result of the Glauber model fit to the measurement. The vertical lines separate the centrality classes, which in total correspond to the most central 80% of the hadronic collisions [80].

model assumes that the number of particle-producing sources is given by $f \times N_{\mathrm{part}} + (1-f) \times N_{\mathrm{coll}}$, where N_{part} is the number of participating nucleons, N_{coll} is the number of binary nucleon-nucleon collisions and f quantifies their relative contributions. The number of particles produced per interaction is generated using a Negative Binomial Distribution (NBD) $P_{\mu,k}$, which is parametrized by μ and k, where μ is the mean multiplicity per

source and k controls the width. Figure 5.3 shows the determination of the centrality classes, which is based on the Glauber model fit on the summed amplitudes of the signals in the V0 detectors. The phase space, centrality classes and list of track quality cuts are summarized in Table 5.1.

5.3. Application of the Identity Method to ALICE data

5.3.1. ω and W distributions

Instead of identifying every detected particle event-by-event, the Identity Method calculates the moments of particle multiplicity distributions by means of an unfolding procedure using only two basic experimentally measurable event-by-event quantities, ω and W (Eq. 1.23). The step-by-step application of the Identity Method to ALICE data is as follows:

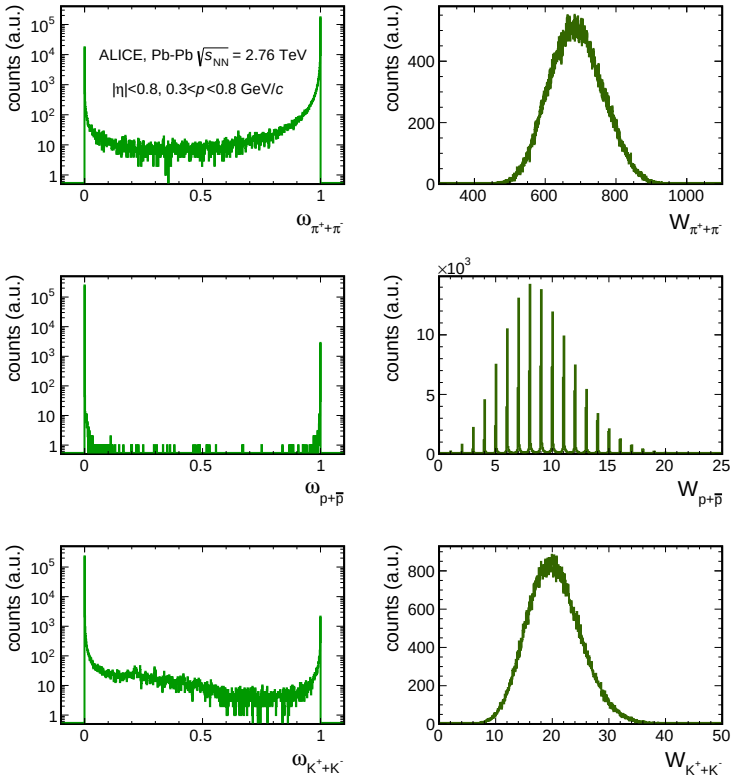

Figure 5.4.: ω and W distributions for pions, kaons and protons within the momentum range of $0.3<p<0.8$ GeV/c.

- perform the inclusive spectra fits for each centrality, pseudorapidity and momentum bin,
- store the fit parameters of each particle for a given phase space in a look-up table,
- store track-by-track momentum, centrality, pseudorapidity, event number and energy loss measurement $\mathrm{d}E/\mathrm{d}x$ information in a TTree,

- calculate ω, W quantities and subsequently the moments of particle multiplicity distributions using the TTree and the look-up table, which are the only two inputs for the TIdenty Module (see Appendix H).

As discussed in Chapter 1, the ω_j quantity is a probability measure of being particle type j for a given track. Thus, in case of perfect identification W_j is equal to N_j (total number of particle type j in a given event), i.e. it takes integer values, while this does not hold in case of misidentification. Figure 5.4 shows the ω and W distributions in the momentum interval of $0.3 < p < 0.8$ GeV/c. As expected, the W distribution of protons shows a discrete structure because proton dE/dx distributions have the least overlap. Accordingly the ω distribution is mostly peaked at either 0 or 1. On the other hand, W distributions of pions and kaons have a smooth behavior, since W values are dominated by the overlap of the dE/dx distributions, thus take non-integer values.

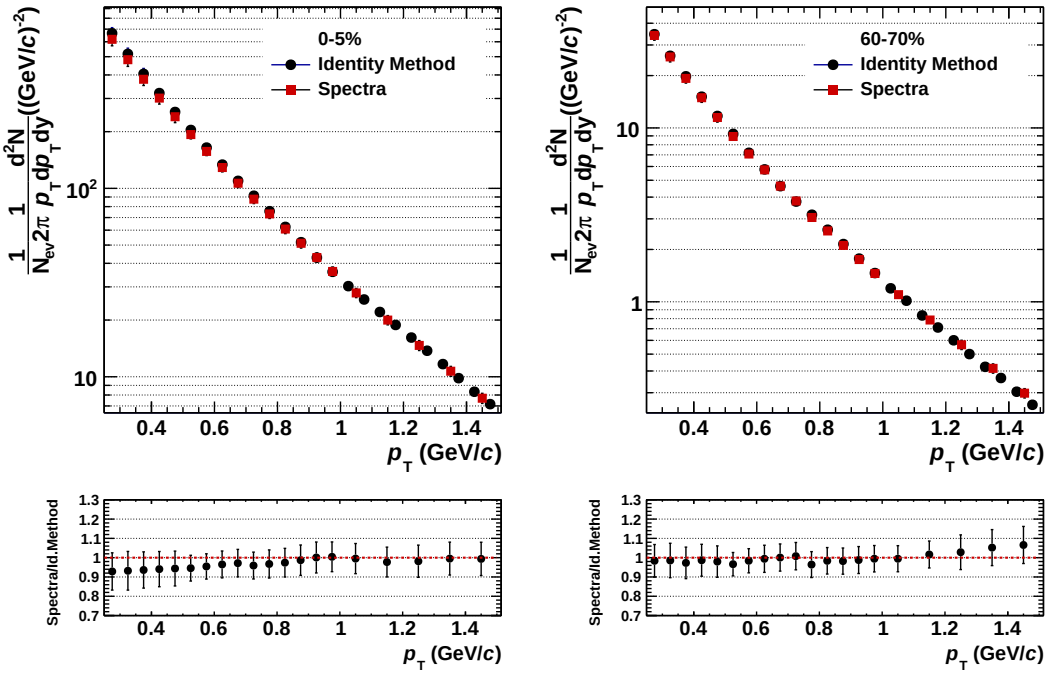

Figure 5.5.: Comparison of the published pion spectra results to the mean pion multiplicities obtained by the Identity Method.

5.3.2. Comparison to published spectra results of ALICE

Since the first moments of the W distributions is equal to the corresponding first moments of particle multiplicities for a given particle species, (see Chapter 1), one can calculate the particle spectra using the Identity Method as well. Therefore, the comparison of the particle spectra obtained with the Identity Method to the published spectra provides a significant verification of the procedure. However, the method is applied in the (p,η) space while particle spectra [81] in (p_T,y). To be consistent the following transformation was used

$$\frac{d^2N}{dydp_T} = \sqrt{1+\frac{m^2}{p_T^2\cosh^2\eta}}\frac{d^2N}{d\eta dp_T}. \tag{5.2}$$

As shown in Figure 5.5, the comparison of identified-particle mean multiplicities obtained with the Identity Method shows an excellent agreement within the systematic uncertainties with the published ALICE results. Note that the efficiency correction was applied as in the case of the published data using the efficiency matrix shown in Figure I.1.

5.3.3. MC verification test

The validity of the Identity Method is proven with a toy MC analysis in [34] under the assumption of having ideal $\mathrm{d}E/\mathrm{d}x$ spectra fits and a certain amount of overlap of the $\mathrm{d}E/\mathrm{d}x$ distributions of particle species. Here, to estimate the uncertainties stemming from the application of the method and amount of the overlap of $\mathrm{d}E/\mathrm{d}x$ distributions, a Monte-Carlo closure test was performed as an internal cross-check using the HIJING event generator and employing a GEANT3 implementation of the ALICE detector setup. First,

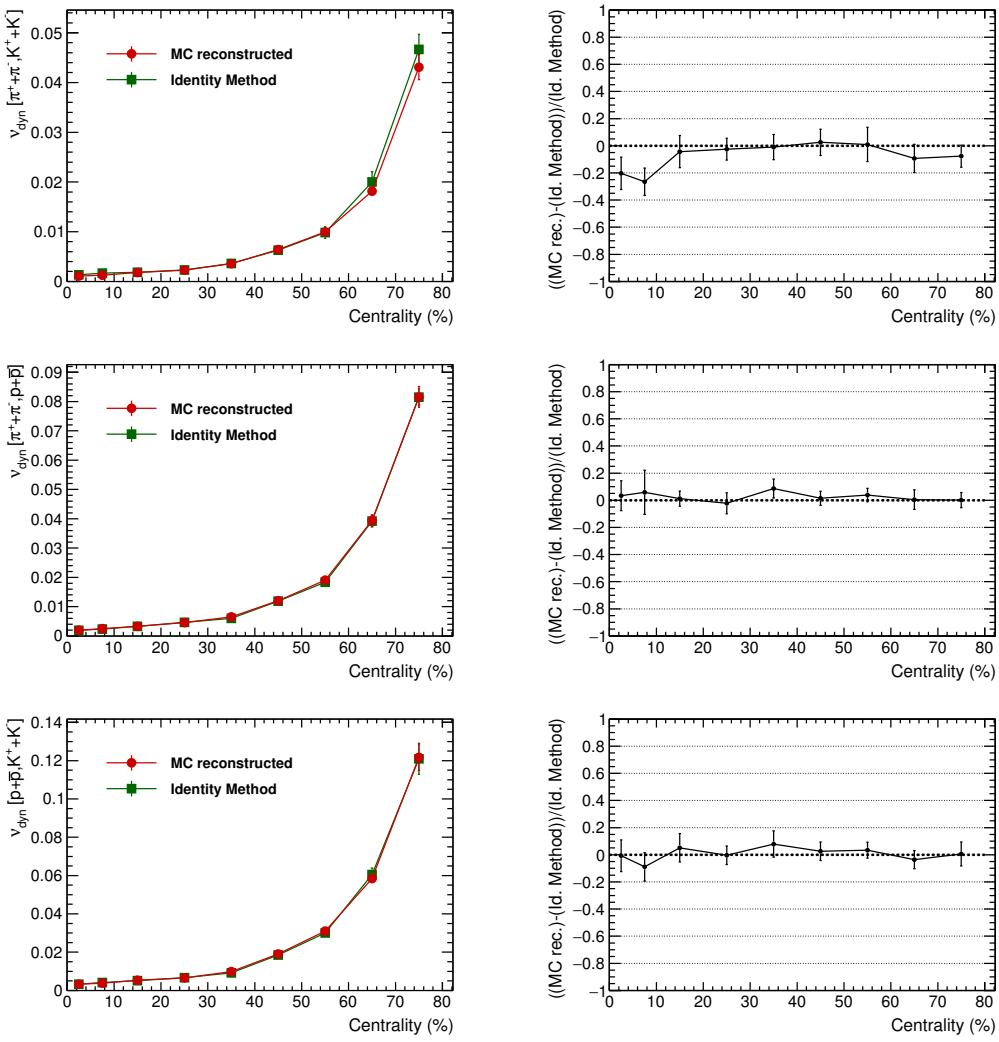

Figure 5.6.: ν_{dyn} results reconstructed with the Identity Method and calculated from MC samples (left column) and the corresponding comparison plots (right column).

the inclusive $\mathrm{d}E/\mathrm{d}x$ spectra of the MC particles were reconstructed. Second, the fits of the $\mathrm{d}E/\mathrm{d}x$ spectra were obtained in the same way as in the analysis of real data. Finally,

the ν_{dyn} values reconstructed by the Identity Method using these fits were compared to the ν_{dyn} results calculated by means of the real identity information of the MC particles, as shown in Figure 5.6. Average deviations of ∼6% for $\nu_{\mathrm{dyn}}[\pi, \mathrm{K}]$, ∼1% for $\nu_{\mathrm{dyn}}[\pi, \mathrm{p}]$ and ∼2% for $\nu_{\mathrm{dyn}}[\mathrm{K}, \mathrm{p}]$ from zero are due to the uncertainties of the fit functions.

5.4. Statistical uncertainty estimation: Subsample method

The statistical errors of the reconstructed moments of the multiplicity distributions result from the inclusive $\mathrm{d}E/\mathrm{d}x$ spectra fits and from the errors of the calculated W quantities. The elaborate derivation of the real moments makes the standard error propagation impractical. Therefore, to evaluate the statistical uncertainties the subsample approach was used. For this, the data set was subdivided into n subsamples randomly, and the ν_{dyn} values then reconstructed for each subsample, as shown in Figure 5.7. Finally the statistical error was obtained with the following formula;

$$\sigma_{\langle\nu_{\mathrm{dyn}}\rangle} = \frac{\sigma}{\sqrt{n}} \tag{5.3}$$

where

$$\langle\nu_{\mathrm{dyn}}\rangle = \frac{1}{n}\sum \nu_{\mathrm{dyn},n}, \quad \sigma = \sqrt{\frac{\sum(\nu_{\mathrm{dyn},i} - \langle\nu_{\mathrm{dyn}}\rangle)^2}{n-1}}. \tag{5.4}$$

The same procedure can be applied to the moments as well.

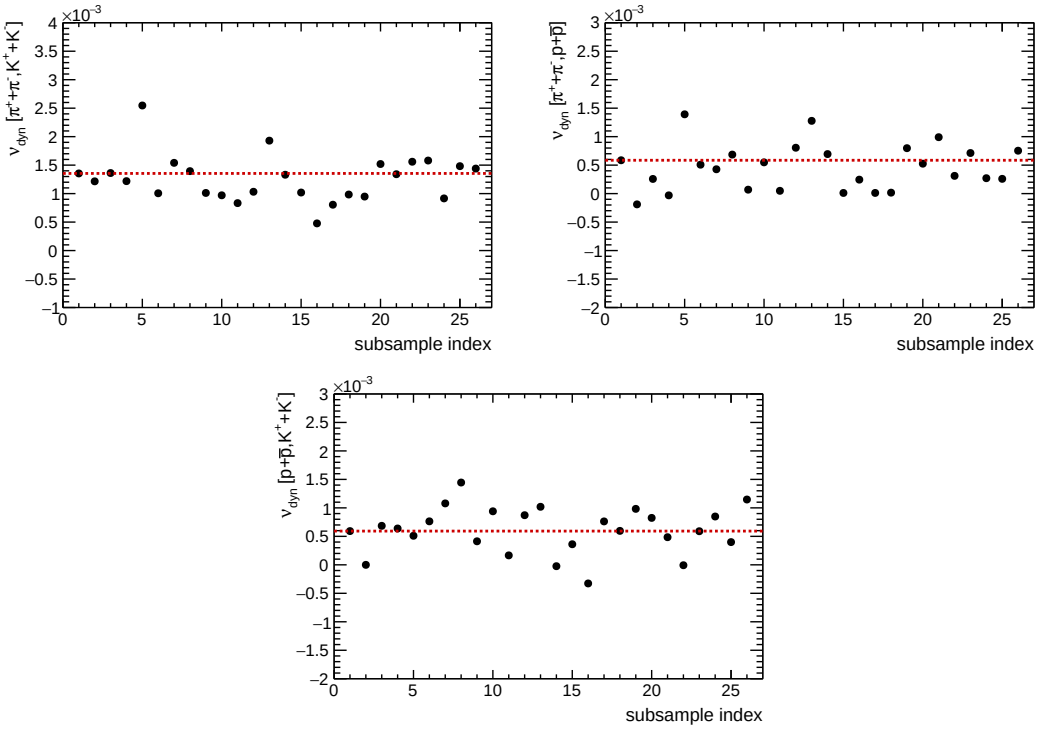

Figure 5.7.: Reconstructed values of $\nu_{\mathrm{dyn}}[\pi, \mathrm{K}]$, $\nu_{\mathrm{dyn}}[\pi, \mathrm{p}]$ and $\nu_{\mathrm{dyn}}[\mathrm{K}, \mathrm{p}]$ for most central events. Dashed red lines indicate the corresponding averaged values of ν_{dyn} over subsamples and the black markers for subsamples.

5.5. Systematic uncertainty estimation

The systematic uncertainties on ν_{dyn} have contributions from detection efficiency losses, inclusive $\mathrm{d}E/\mathrm{d}x$ spectra fits, track selection criteria and magnetic field polarity. The total systematic uncertainty was obtained by adding in quadrature the individual maximum systematic variation from each of these set of contributions.

5.5.1. Effect of detection efficiency losses

Although ν_{dyn} is known to be robust against detection efficiency losses, it may show an explicit dependence if the detector response functions differ from Binomial or Gaussian, or if the efficiencies exhibit very large variations with the detector occupancy.

For instance, binomial distribution of a single particle multiplicity can be written in

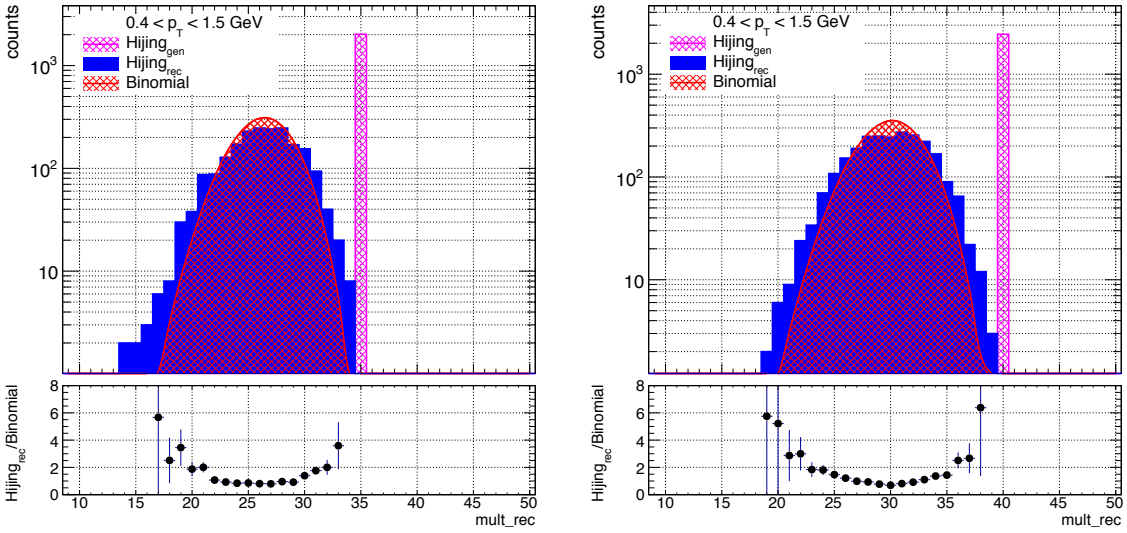

Figure 5.8.: Protons generated by the HIJING model for two different multiplicities, 35 and 40 on the top left and top right, respectively. The distribution of reconstructed protons is overlaid with a Binomial distribution. The corresponding ratios are presented in bottom panels [82].

the following form:

$$B(n;N,\varepsilon) = \frac{N!}{n!(N-n)!}\varepsilon^{n}(1-\varepsilon)^{N-n}, \tag{5.5}$$

where ε is the single particle efficiency for a given particle species, n is the measured and N is the true particle multiplicity in a given event, respectively. Also, one finds for event averages

$$\langle n\rangle = \varepsilon\langle N\rangle, \tag{5.6}$$

$$\langle n^2\rangle = \varepsilon^2(\langle N^2\rangle - \langle N\rangle) + \varepsilon\langle N\rangle. \tag{5.7}$$

By subtracting Eq. 5.6 from Eq. 5.7 and dividing both sides of the resulting expression by $\langle n\rangle^2$, one obtains the following expression:

$$\frac{\langle n^2\rangle - \langle n\rangle}{\langle n\rangle^2} = \frac{\langle N^2\rangle - \langle N\rangle}{\langle N\rangle^2}, \tag{5.8}$$

which is independent of the detection efficiency. On the other hand ν_{dyn} can be written in the following form

$$\nu_{\mathrm{dyn}}[a,b] = \frac{\langle N_a^2\rangle - \langle N_a\rangle}{\langle N_a\rangle^2} + \frac{\langle N_b^2\rangle - \langle N_b\rangle}{\langle N_b\rangle^2} - 2\frac{\langle N_a N_b\rangle}{\langle N_a\rangle\langle N_b\rangle} \tag{5.9}$$

Each term in Eq. 5.9 is independent of the particle detection efficiency under the assumption that the individual particle multiplicity distributions are binomial. However, due to detector effects, individual particle multiplicity distributions deviate from binomial distribution, as shown in Figure 5.8.

On the other hand, as seen in Figure I.1 and Figure I.2, single particle detection efficiencies have a strong momentum and weak pseudorapidity and azimuthal-angle (φ) dependence. Therefore, one also has to investigate the uncertainty resulting from the detection efficiency losses. For that, the ν_{dyn} results retrieved from full MC simulation were compared to the results from MC generator level, as shown in Figure 5.9. The resulting systematic uncertainties of less than 5% are included in the final error calculation.

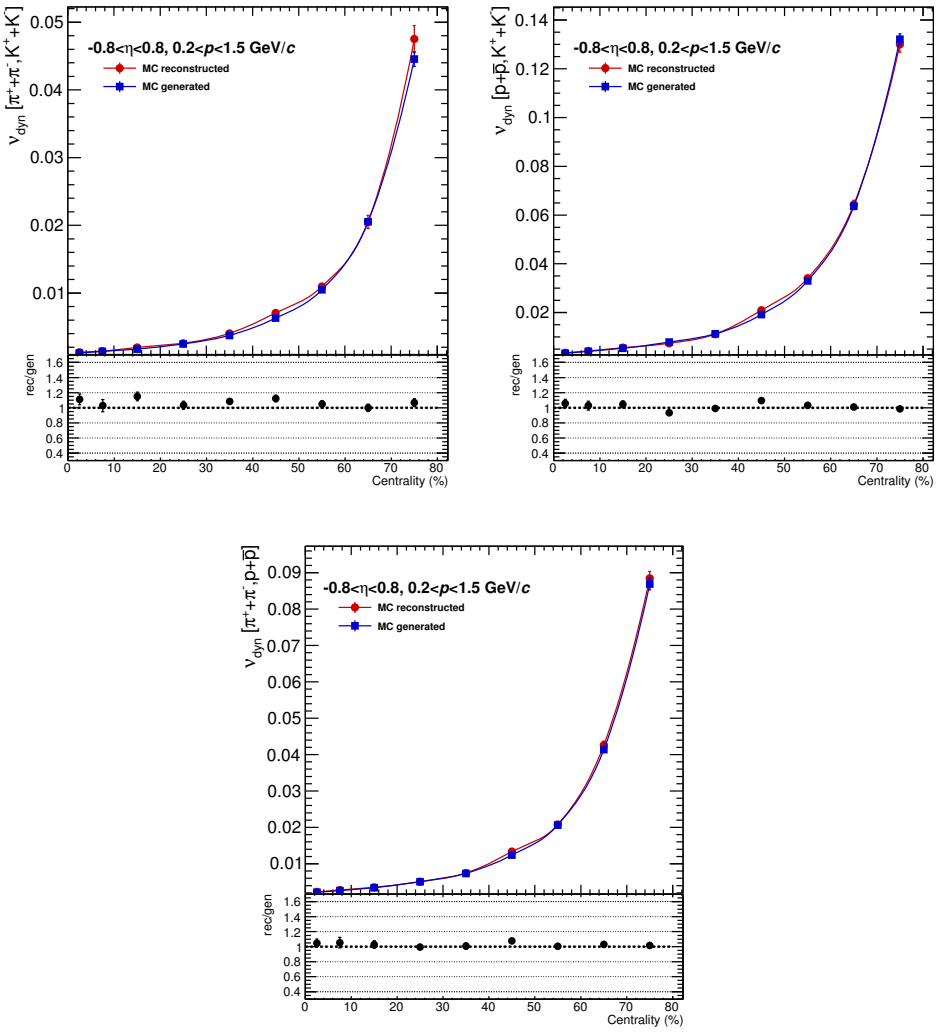

Figure 5.9.: Effect of detection efficiency losses on the ν_{dyn} results.

5.5.2. Other sources of systematic uncertainties

Other systematic uncertainty sources on the results of the ν_{dyn} are from the inclusive $\mathrm{d}E/\mathrm{d}x$ spectra fits and track selection criteria. All contributions to the systematic uncertainty for $\nu_{\mathrm{dyn}}[\pi, \mathrm{K}]$, $\nu_{\mathrm{dyn}}[\pi, \mathrm{p}]$ and $\nu_{\mathrm{dyn}}[\mathrm{K}, \mathrm{p}]$ are listed in Table 5.2, Table 5.3 and Table 5.4, respectively. Since the data points are very close to zero, errors are calculated as differences instead of ratios.

Centrality (%)	0-5	5-10	10-20	20-30	30-40	40-50	50-60	60-70	70-80
Detection efficiency	0.045	0.041	0.045	0.056	0.076	0.117	0.215	0.398	1.001
Inclusive $\mathrm{d}E/\mathrm{d}x$ fits	0.004	0.010	0.016	0.032	0.076	0.110	0.406	0.961	1.778
DCA to vertex	0.016	0.006	0.020	0.019	0.027	0.032	0.076	0.175	0.337
Vertex z-position	0.007	0.009	0.020	0.037	0.012	0.046	0.125	0.244	0.403
TPC $\chi^2/d.o.f.$	0.046	0.019	0.035	0.041	0.034	0.041	0.098	0.160	0.244
Min. TPC space points	0.010	0.002	0.018	0.020	0.008	0.031	0.058	0.100	0.151
B-field polarity	0.040	0.017	0.022	0.043	0.045	0.019	0.042	0.138	0.270
Total systematic error	0.333	0.292	0.284	0.272	0.365	0.532	1.242	2.604	5.134

Table 5.2.: Main sources of systematic uncertainties for $\nu_{\mathrm{dyn}}[\pi, \mathrm{K}]$.

Centrality (%)	0-5	5-10	10-20	20-30	30-40	40-50	50-60	60-70	70-80
Detection efficiency	0.006	0.002	0.004	0.003	0.000	0.005	0.013	0.048	0.156
Inclusive $\mathrm{d}E/\mathrm{d}x$ fits	0.004	0.005	0.005	0.006	0.010	0.014	0.033	0.067	0.116
DCA to vertex	0.031	0.009	0.014	0.016	0.028	0.040	0.080	0.188	0.427
Vertex z-position	0.022	0.007	0.014	0.008	0.022	0.074	0.037	0.176	0.477
TPC $\chi^2/d.o.f.$	0.094	0.033	0.083	0.060	0.062	0.047	0.063	0.189	0.409
Min. TPC space points	0.041	0.009	0.023	0.020	0.026	0.023	0.036	0.123	0.273
B-field polarity	0.038	0.003	0.040	0.044	0.061	0.023	0.003	0.000	0.015
Total systematic error	0.044	0.067	0.105	0.179	0.233	0.348	0.496	0.697	1.040

Table 5.3.: Main sources of systematic uncertainties for $\nu_{\mathrm{dyn}}[\pi, \mathrm{p}]$.

Centrality (%)	0-5	5-10	10-20	20-30	30-40	40-50	50-60	60-70	70-80
Detection efficiency	0.005	0.004	0.008	0.014	0.019	0.028	0.051	0.080	0.139
Inclusive $\mathrm{d}E/\mathrm{d}x$ fits	0.002	0.003	0.011	0.027	0.070	0.101	0.385	0.921	1.709
DCA to vertex	0.023	0.021	0.035	0.097	0.109	0.144	0.122	0.228	0.416
Vertex z-position	0.019	0.022	0.036	0.091	0.058	0.105	0.117	0.096	0.041
TPC $\chi^2/d.o.f.$	0.077	0.038	0.045	0.076	0.079	0.129	0.134	0.105	0.177
Min. TPC space points	0.035	0.007	0.027	0.073	0.063	0.054	0.086	0.159	0.273
B-field polarity	0.040	0.019	0.014	0.032	0.056	0.193	0.259	0.142	0.158
Total systematic error	0.134	0.151	0.210	0.318	0.402	0.501	0.982	2.176	4.060

Table 5.4.: Main sources of systematic uncertainties for $\nu_{\mathrm{dyn}}[\mathrm{K}, \mathrm{p}]$.

The largest contribution to the total systematic uncertainty is from the quality of the fits of measured particle $\mathrm{d}E/\mathrm{d}x$ distributions. It is, in particular, a big challenge to properly fit the overlap regions of the inclusive $\mathrm{d}E/\mathrm{d}x$ spectra. These regions require a good detector response shape determination i.e. good estimates of the fit parameters in a given

phase space bin. To study the influence of possible systematic shifts in the fit parameters on ν_{dyn}, the skewness and kurtosis parameters of each particle in the overlap regions were varied by about ± 0.5 %, which defines the boundaries where K-S test fails at 90% confidence level. Moreover, the error of the total fit of a given phase space was varied $\pm\sigma$ to estimate the error resulting from the fitting procedure. The most significant shift was observed for $\nu_{\mathrm{dyn}}[\pi, \mathrm{K}]$ up to 15% and the least for $\nu_{\mathrm{dyn}}[\pi, \mathrm{p}]$ up to 5%.

The systematic uncertainties due to the track selection cuts were estimated by a variation of the cut values. For instance, the systematics from contamination of weak decays and other secondaries were obtained by applying cuts on the distances between primary and secondary vertices. Moreover, the effect of magnetic field polarity was also investigated by separate analyses of data taken under two polarities. Neither of these contributions to the total systematic uncertainty exceeds 5%.

6. Event-by-event Identified Particle Ratio Fluctuations

This chapter is dedicated to a differential study of the dependence of particle ratio fluctuations on several effects such as system size, acceptance coverage, weak-decay contamination and others. The results are compared to calculations with the HIJING and AMPT event generators. Moreover, the results for the most central events are compared to the lower energy measurements at the CERN-SPS and RHIC.

6.1. Centrality dependence

The main motivation to study fluctuations with respect to centrality is to observe any system-size dependent dynamical fluctuations. The ν_{dyn} results as a function of centrality are shown in Figure 6.1 and the numerical values are presented in Table 6.1 together with the statistical and systematic uncertainties. Although the trivial multiplicity dependence of ν_{dyn} makes it difficult to draw firm physics conclusions, the sign change of $\nu_{\mathrm{dyn}}[\pi, \mathrm{p}]$ clearly indicates an increasing correlation between pions and protons going to peripheral events.

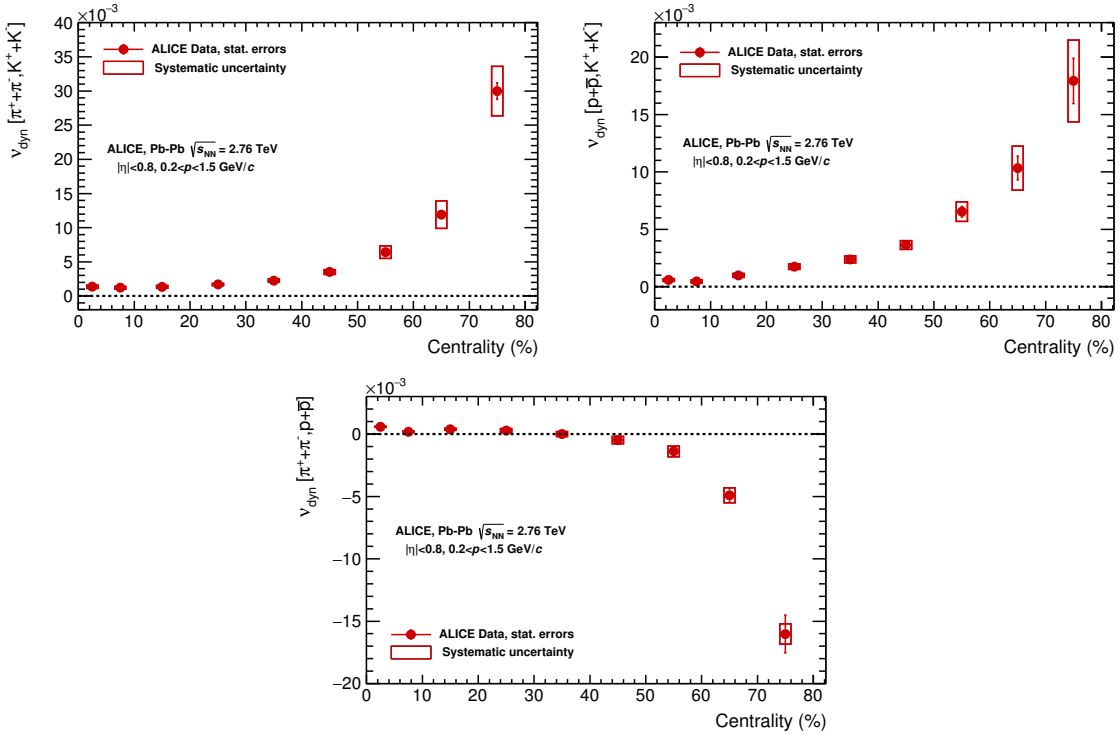

Figure 6.1.: Centrality dependence of the ALICE ν_{dyn} results and the statistical and systematic uncertainties.

Centrality (%)	$\nu_{\rm dyn}[\pi, {\rm K}]$ (10^{-3})			$\nu_{\rm dyn}[\pi, {\rm p}]$ (10^{-3})			$\nu_{\rm dyn}[{\rm K}, {\rm p}]$ (10^{-3})		
0-5	**1.35**	±0.08	±0.33	**0.59**	±0.08	±0.04	**0.59**	±0.08	±0.13
5-10	**1.22**	±0.08	±0.29	**0.19**	±0.08	±0.07	**0.46**	±0.10	±0.15
10-20	**1.35**	±0.08	±0.28	**0.38**	±0.08	±0.11	**0.98**	±0.10	±0.21
20-30	**1.69**	±0.09	±0.27	**0.29**	±0.09	±0.18	**1.76**	±0.13	±0.32
30-40	**2.27**	±0.11	±0.37	**0.01**	±0.18	±0.23	**2.39**	±0.24	±0.40
40-50	**3.52**	±0.16	±0.53	**-0.49**	±0.18	±0.35	**3.64**	±0.32	±0.50
50-60	**6.43**	±0.26	±1.24	**-1.38**	±0.24	±0.50	**6.54**	±0.47	±0.98
60-70	**11.91**	±0.53	±2.60	**-4.90**	±0.58	±0.70	**10.34**	±1.04	±2.18
70-80	**29.99**	±1.21	±5.13	**-16.02**	±1.52	±1.04	**17.93**	±1.98	±4.06

Table 6.1.: Numerical values of $\nu_{\rm dyn}$ results for different particle pairs. The first uncertainty is statistical and the second systematic.

6.2. Multiplicity scaling and comparison to HIJING and AMPT models

As mentioned in Chapter 1, the $\nu_{\rm dyn}$ measure, by definition, has an intrinsic multiplicity dependence which has to be taken into account. In this thesis, three different scaling prescriptions were investigated: charged-particle multiplicity density at mid-rapidity, $\mathrm{d}N_{\rm ch}/\mathrm{d}\eta$, number of participants, $N_{\rm part}$ and mean multiplicities of accepted particles.

For the model comparison HIJING [83, 84] and three different versions of AMPT [85] event generators were used: (i) string melting, (ii) hadronic rescattering and (iii) hadronic rescattering and string melting.

An important characteristic of HIJING is that it treats nucleus-nucleus collisions as an independent superposition of nucleon-nucleon interactions. It does not incorporate mechanisms for final-state interactions among the produced particles and therefore phenomena such as equilibrium and collectivity do not occur.

All three versions of the AMPT models use the hard minijet partons and soft strings from HIJING to describe the initial conditions. The partonic evolution is then described by the Zhang's Parton Cascade (ZPC) which is followed by a hadronisation process. At the end, the hadronic rescattering, which also includes the decay of resonances, takes place.

In the default AMPT model, after minijet partons stop interacting with other partons, they are combined with their parent strings to form excited strings, which are then converted to hadrons according to the Lund string fragmentation model [85]. In the string melting scenario, instead of the Lund string fragmentation mechanism, hadronisation is modeled via a quark coalescence scheme by combining two closest partons into a meson and three closest quarks (antiquarks) into a baryon (antibaryon). One should note that the quark coalescence model causes partons to freeze out dynamically at different times, which leads to a coexisting phase of partons and hadrons during hadronisation.

The non-scaled $\nu_{\rm dyn}$ results are shown in Figure 6.2. The ALICE data are shown by the red markers and solid black lines and colored dashed lines show HIJING and AMPT model calculations, respectively. Since the effect of finite reconstruction efficiency was added to the total systematic uncertainty, model comparisons were made on the generator level within the same acceptance as data. Both HIJING and AMPT calculations show positive values steeply increasing towards peripheral events for all three cases, while ALICE $\nu_{\rm dyn}[\pi, {\rm p}]$ results show the opposite trend. For further conclusions one has to scale

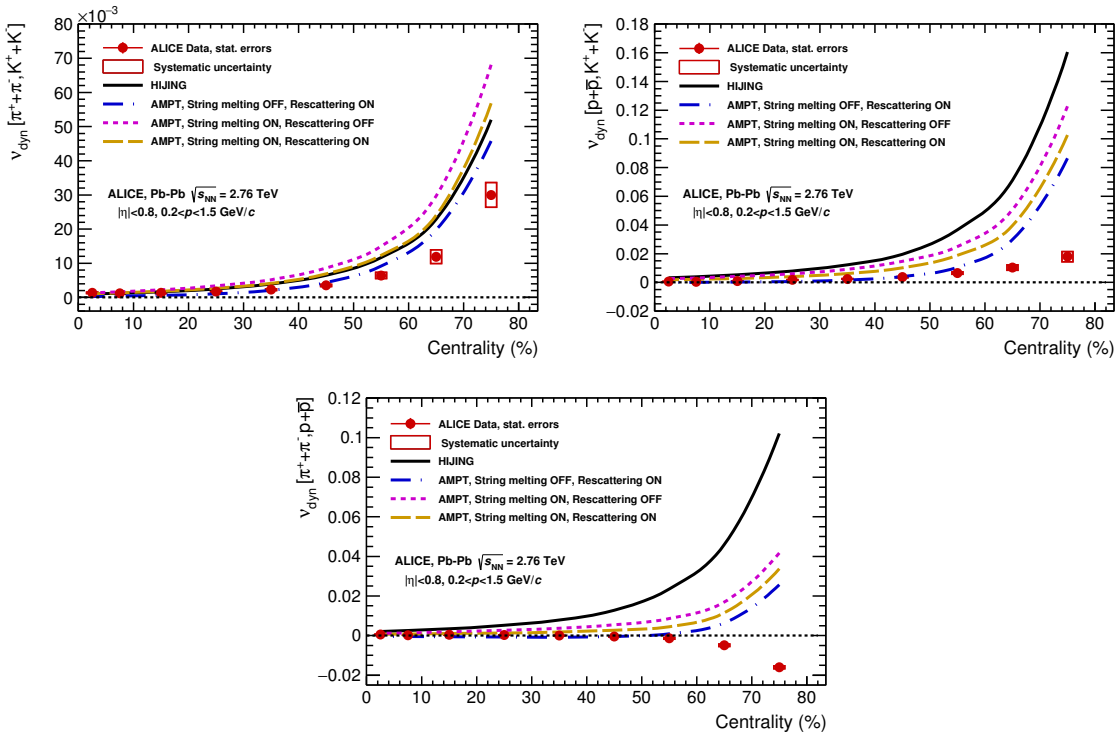

Figure 6.2.: Comparison of non-scaled ALICE ν_{dyn} results to HIJING [83] and AMPT [85] model calculations.

out the multiplicity dependence. Below the three aforementioned scaling scenarios are discussed in detail.

6.2.1. Scaling with respect to mean multiplicities of accepted particles: Link to the fluctuation measure Σ

Several scaling prescriptions based on the mean multiplicities of accepted particles were investigated in [27]. In this thesis $1/(1/\langle N_a\rangle + 1/\langle N_b\rangle)$, where $\langle N_a\rangle$ and $\langle N_b\rangle$ are the mean multiplicities of particle type a and b, respectively, is studied in view of the volume fluctuations. Here, one should note that even though this scaling has a theoretical base, it introduces an additional complication: the correction of the mean multiplicities for efficiency effects.

In high-energy collisions the volume of produced matter also fluctuates. For instance, collisions with different centralities may produce a statistical system with the same local properties such as temperature and baryonic chemical potential but with the system volume changing significantly from event to event. This implies that for a given centrality the impact parameter as well as the number of wounded nucleons fluctuate from event-to-event, thus generating a distribution, as shown in the scatter plots in Figure 6.3. and thus induces non-dynamical contributions to event-by-event fluctuation measurements. Such volume fluctuations induces non-dynamical contributions to event-by-event fluctuation measurements, and therefore must be disentangled from the dynamic ones which are of main interest. The effect of these volume fluctuations on the moments of particle multiplicity distributions are extensively discussed in [20], and a correction procedure is proposed for a given detector-specific centrality selection procedure.

Alternatively, within the grand canonical ensemble one can define quantities which are

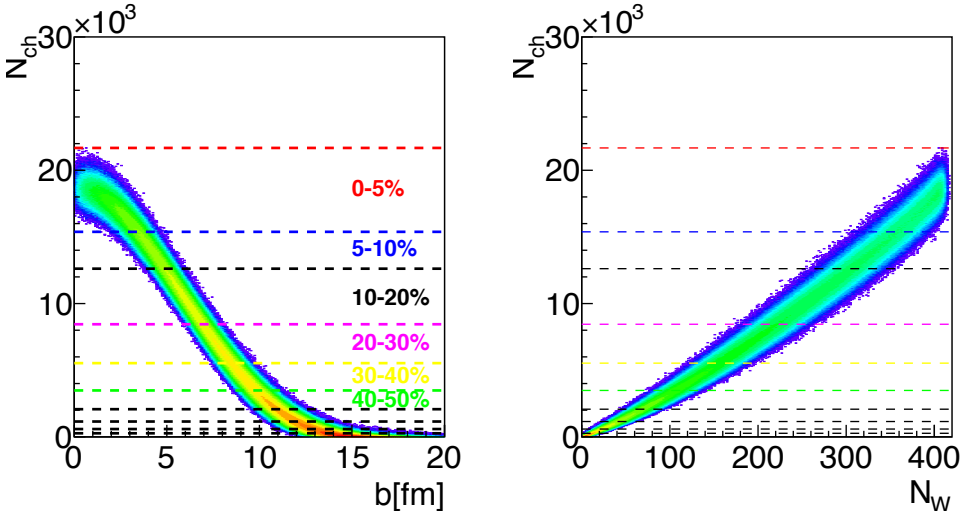

Figure 6.3.: Left Panel: Produced number of charged particles versus the impact parameter. Right Panel: Produced number of charged particles versus the number of wounded nucleons, i.e. number of participants. For a given value of the impact parameter the number of wounded nucleons and binary collisions are calculated with a Glauber Monte Carlo simulation. The corresponding centrality classes are indicated by the dashed horizontal lines [20].

free from the volume fluctuations, for instance $\nu_{\rm dyn}$. In the model of independent sources [86], extensive quantities[1] such as the mean number of particles are considered to be proportional to the number of sources, $\langle N_{\rm s}\rangle$, where $\langle N_{\rm s}\rangle$ changes from event to event. The multiplicities for particle types a and b can be expressed as

$$N_a = \alpha_1 + \alpha_2 + ... + \alpha_{N_{\rm s}}, \qquad N_b = \beta_1 + \beta_1 + ... + \beta_{N_{\rm s}}, \tag{6.1}$$

where α_k and β_k denote the contributions from the kth source. One finds the first and second moments of the multiplicity distributions as follows:

$$\langle N_a\rangle = \langle\alpha\rangle\langle N_{\rm s}\rangle, \tag{6.2}$$
$$\langle N_b\rangle = \langle\beta\rangle\langle N_{\rm s}\rangle, \tag{6.3}$$
$$\langle N_a^2\rangle = \langle\alpha^2\rangle\langle N_{\rm s}\rangle + \langle\alpha\rangle^2\left[\langle N_{\rm s}^2\rangle - \langle N_{\rm s}\rangle\right], \tag{6.4}$$
$$\langle N_b^2\rangle = \langle\beta^2\rangle\langle N_{\rm s}\rangle + \langle\beta\rangle^2\left[\langle N_{\rm s}^2\rangle - \langle N_{\rm s}\rangle\right], \tag{6.5}$$
$$\langle N_a N_b\rangle = \langle\alpha\beta\rangle\langle N_{\rm s}\rangle + \langle\alpha\rangle\langle\beta\rangle\left[\langle N_{\rm s}^2\rangle - \langle N_{\rm s}\rangle\right], \tag{6.6}$$

where $\langle\alpha\rangle$, $\langle\beta\rangle$ and $\langle\alpha^2\rangle$, $\langle\beta^2\rangle$, $\langle\alpha\beta\rangle$ are the first and second moments of the probability distributions $P(\alpha,\beta)$ for a single source. These quantities are independent of $\langle N_{\rm s}\rangle$ and play the role of intensive quantities. The details of the derivation of Eq. 6.2 – Eq. 6.6 can be found in [87]. Here, $P(\alpha,\beta)$ is assumed to be the same for all sources; that is, they are statistically identical.

[1] Intensive quantities are physical quantities which are independent of the system volume, while extensive quantities are proportional to the system volume. Accordingly, one can easily construct an intensive quantity by taking the ratio of two extensive ones. For instance, within the grand canonical ensemble the mean number of particles, $\langle N\rangle$, in a relativistic gas and the variance, $\langle N^2\rangle - \langle N\rangle^2$ are extensive quantities, thus the scaled variance, $(\langle N^2\rangle - \langle N\rangle^2)/\langle N\rangle$, is an intensive one.

The probability distribution $P_{\rm s}(N_{\rm s})$ of the source number is needed to calculate $\langle N_{\rm s}\rangle$ and $\langle N_{\rm s}^2\rangle$ and, in general, it is unknown. By substituting Eq. 6.2 – Eq. 6.6 in Eq. 1.6, one obtains

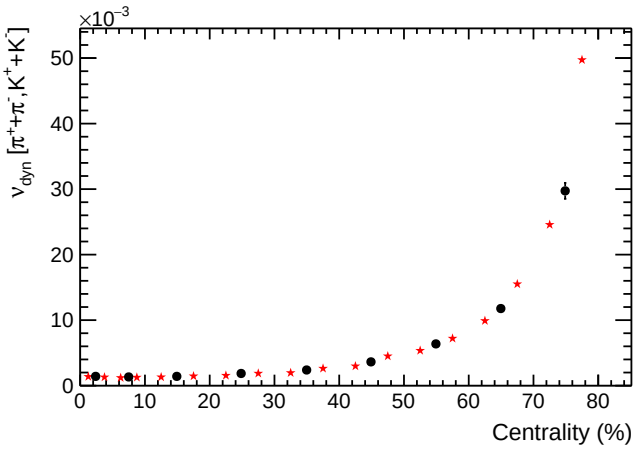

Figure 6.4.: Centrality bin-width dependence of $\nu_{\rm dyn}[\pi, {\rm K}]$ results. Centrality binning of [0, 2.5, 5, 7.5, 10, 15, 20, ... 80] is shown with black dots and [0, 5, 10, 20, 30, ... 80] is with red stars.

$$\nu_{\rm dyn}[a,b] = \frac{1}{\langle N_{\rm s}\rangle}\left[\frac{\langle\alpha^2\rangle}{\langle\alpha\rangle^2} + \frac{\langle\beta^2\rangle}{\langle\beta\rangle^2} - 2\frac{\langle\alpha\beta\rangle}{\langle\alpha\rangle\langle\beta\rangle} - \left(\frac{1}{\langle\alpha\rangle} + \frac{1}{\langle\beta\rangle}\right)\right], \tag{6.7}$$

$$= \frac{1}{\langle N_{\rm s}\rangle}\nu^*_{\rm dyn}[\alpha,\beta], \tag{6.8}$$

where $\nu^*_{\rm dyn}[\alpha,\beta]$ is the $\nu_{\rm dyn}$ quantity of the multiplicities of the particle types a and b for each source. This implies that $\nu_{\rm dyn}$ is anti-proportional to the system size, thus it is neither intensive nor extensive. On the other hand, since the terms $\langle N_{\rm s}^2\rangle - \langle N_{\rm s}\rangle$ cancel out by construction, $\nu_{\rm dyn}$ is independent from volume fluctuations, as shown in Figure 6.4. By scaling $\nu_{\rm dyn}$ with $1/(1/\langle N_a\rangle + 1/\langle N_b\rangle)$ [27] and substituting Eq. 6.2 and Eq. 6.3 one can eliminate the $1/\langle N_{\rm s}\rangle$ term, i.e. the system size dependence, and obtains

$$\frac{\nu_{\rm dyn}[a,b]}{\frac{1}{\langle N_a\rangle} + \frac{1}{\langle N_b\rangle}} = \frac{\nu_{\rm dyn}[\alpha,\beta]}{\frac{1}{\langle\alpha\rangle} + \frac{1}{\langle\beta\rangle}}. \tag{6.9}$$

Indeed there are so-called strongly intensive quantities [88] which are constructed in a way that they are independent of volume and volume fluctuations. The Σ measure [87] is an example of a strongly intensive quantity which is given as

$$\Sigma[a,b] = \frac{1}{C_\Sigma}\left[\langle N_b\rangle\omega_a + \langle N_a\rangle\omega_b - 2\left(\langle N_a N_b\rangle - \langle N_a\rangle\langle N_b\rangle\right)\right], \tag{6.10}$$

where the scaled variance ω_a and the normalization factor C_Σ are defined as

$$\omega_a = \frac{\langle N_a^2\rangle - \langle N_a\rangle^2}{\langle N_a\rangle}, \quad C_\Sigma = \langle N_a\rangle + \langle N_b\rangle. \tag{6.11}$$

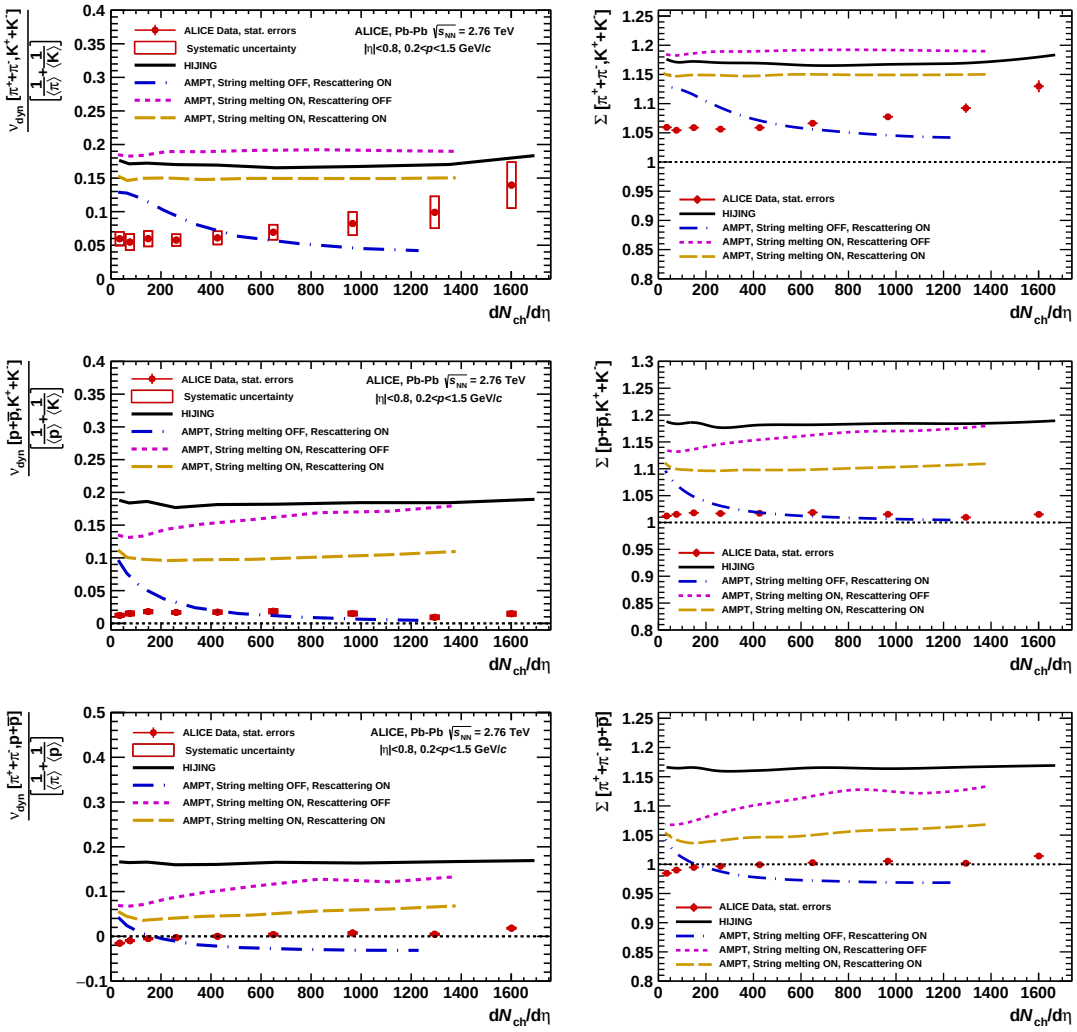

Figure 6.5.: Comparison of Σ results to the $\nu_{\rm dyn}$ results scaled by $\dfrac{1}{1/\langle N_a\rangle + 1/\langle N_b\rangle}$.

The specific choice of the normalization makes the Σ quantity dimensionless and leads to $\Sigma[a,b] = \Sigma[b,a] = 1$ in the independent particle model [88]. Also, from the definition of $\Sigma[a,b]$, it follows that $\Sigma[a,b] = 0$ in the case of absence of fluctuations of a and b, i.e., for $\omega_a = \omega_b = \langle N_a N_b\rangle - \langle N_a\rangle\langle N_b\rangle = 0$.

Moreover, by simple mathematics, the Σ measure can be related to the $\nu_{\rm dyn}$ measure by the following scaling

$$\Sigma[a,b] - 1 = \frac{\nu_{\rm dyn}[a,b]}{\dfrac{1}{\langle N_a\rangle} + \dfrac{1}{\langle N_b\rangle}}. \tag{6.12}$$

As shown in Figure 6.5, indeed Eq. 6.12 holds. Here one should note that, unlike $\nu_{\rm dyn}$, the Σ measure requires efficiency corrections. The systematic uncertainty resulting from the detection efficiency losses for Σ was found to be about 10% by comparing full MC simulation results to the results from MC generator level, as was done for $\nu_{\rm dyn}$. Therefore, this scaling requires a further study which includes a proper efficiency correction. However, as will be discussed below, the qualitative agreement with $\mathrm{d}N_{\rm ch}/\mathrm{d}\eta$ scaled results suggests

that the efficiency losses do not play a significant role.

6.2.2. The $\mathrm{d}N_{\mathrm{ch}}/\mathrm{d}\eta$ and N_{part} scalings

The STAR collaboration published K/π fluctuation results in [89] comparing $\mathrm{d}N_{\mathrm{ch}}/\mathrm{d}\eta$ and N_{part} scalings, where the former was concluded to provide better results. The main advantage of these scalings are that they do not require an additional efficiency correction and thus they preserve the basic feature of ν_{dyn} being free from the efficiency corrections.

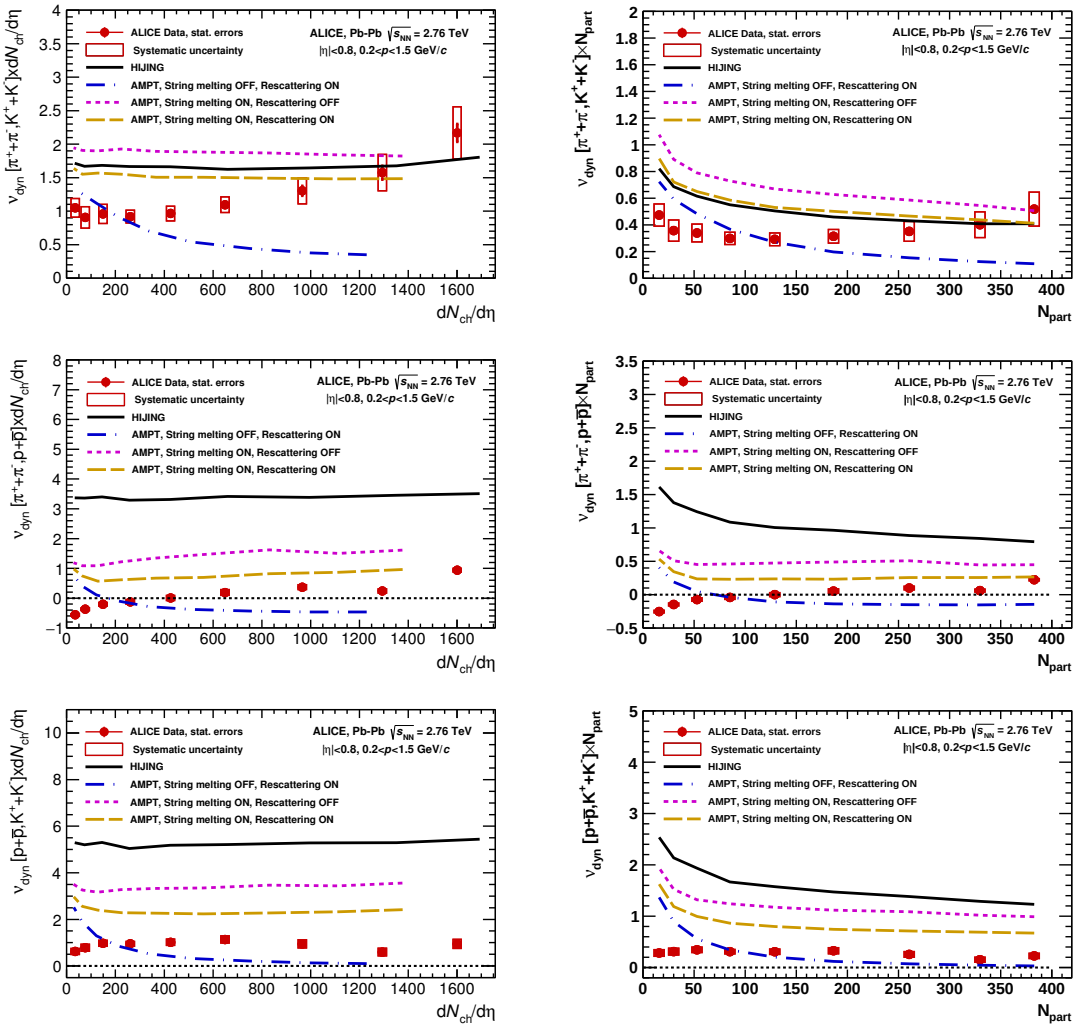

Figure 6.6.: ALICE results for ν_{dyn} scaled by $\mathrm{d}N_{\mathrm{ch}}/\mathrm{d}\eta$ (left column) and N_{part} (right column) in comparison with the HIJING [83] and AMPT [85] model calculations..

The ν_{dyn} results scaled with $\mathrm{d}N_{\mathrm{ch}}/\mathrm{d}\eta$ are shown in Figure 6.6 left column. The $\mathrm{d}N_{\mathrm{ch}}/\mathrm{d}\eta$ values for the ALICE data were taken from [80] and for the HIJING and AMPT models they were obtained by track-by-track counting of particles in a given centrality class (see Table 6.2). The $\nu_{\mathrm{dyn}}[\pi, \mathrm{K}]$ and $\nu_{\mathrm{dyn}}[\mathrm{K}, \mathrm{p}]$ are always positive across the entire centrality range, while $\nu_{\mathrm{dyn}}[\pi, \mathrm{p}]$ is negative for the most peripheral events and changes sign at mid-central events. This indicates a positive correlation between pions and protons as the

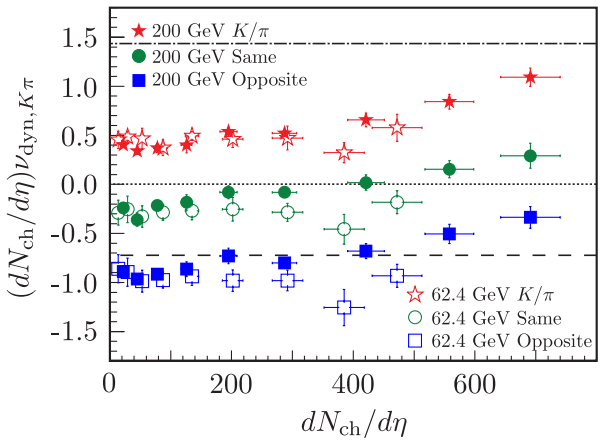

Figure 6.7.: (color online). STAR collaboration results of the $\mathrm{d}N_{\rm ch}/\mathrm{d}\eta$ scaled $\nu_{\rm dyn}[\pi,\mathrm{K}]$ for summed charges (stars), same sign (circles), and opposite sign (squares) as a function of $\mathrm{d}N_{\rm ch}/\mathrm{d}\eta$. The errors shown are statistical. The dash-dotted, dotted, and dashed lines represent HIJING calculations for summed charges, same sign, and opposite sign, respectively [89].

collision centrality decreases. The dominant source of correlated pions and protons may come from the baryonic resonances.

Moreover, the centrality dependence observed in $\nu_{\rm dyn}[\mathrm{K},\mathrm{p}]$ and $\nu_{\rm dyn}[\pi,\mathrm{p}]$ is similar: flat from central to mid-central events and approaching zero for the most peripheral events. On the other hand, $\nu_{\rm dyn}[\pi,\mathrm{K}]$ is almost independent of centrality from most peripheral to mid-central events and rises as the centrality increases. This might indicate an increasing anti-correlation between pions and kaons or can be related to the increasing dynamical fluctuations for the most central events.

Figure 6.6 also shows that HIJING results for all three cases of $\nu_{\rm dyn}$ are independent of

Centrality (%)	$\langle N_{\rm part}\rangle$	Data	HIJING	AMPT S. Melting ON Rescattering ON	AMPT S. Melting ON Rescattering OFF	AMPT S. Melting OFF Rescattering ON
0-5	1601±60	382.8±3.1	1693	1378	1377	1230
5-10	1294±49	329.7±4.6	1353	1115	1113	998
10-20	966±37	260.5±4.4	995	833	831	750
20-30	649±23	186.4±3.9	660	560	558	509
30-40	426±15	128.9±3.3	424	366	365	337
40-50	261±9	85.0±2.6	257	225	225	211
50-60	149±6	52.8±2.0	145	127	127	122
60-70	76±4	30.0±1.3	73	65	64	64
70-80	35±2	15.8±0.6	33	29	29	29

Table 6.2.: $\mathrm{d}N_{\rm ch}/\mathrm{d}\eta$ values measured in $|\eta| < 0.5$ for different centrality classes. ALICE data are taken from [80]. For HIJING and AMPT, track by track counting is performed on the generator level. $\langle N_{\rm part}\rangle$ values are obtained using the Glauber model [80].

centrality and always positive. Furthermore, HIJING over-predicts the data except for the $\nu_{\rm dyn}[\pi,\mathrm{K}]$ in the most central collisions. The centrality dependence of π/K fluctuations within the kinematic range of $|\eta| < 1$ and $0.2 < p < 0.6$ GeV/c as measured in Au–Au collisions at $\sqrt{s_{\rm NN}}$ =200 by the STAR collaboration [90] shows a similar trend, as shown in Figure 6.7.

As stated before, hadronic rescattering process produces additional resonances at the

hadronization phase thus increases the correlations between particle pairs. Hence, AMPT configuration with hadron rescattering drives the $\nu_{\rm dyn}$ values for all 3 cases towards negative values as the collision centrality increases. Particularly for $\nu_{\rm dyn}[\pi, {\rm p}]$, unlike the data, it predicts negative values i.e., larger correlations between pions and protons with increasing centrality. Moreover, it under-predicts the data for most central and over-predicts for most peripheral events for all three cases. On the other hand, the AMPT configurations with string melting shows very weak centrality dependence and over-predicts the data except for $\nu_{\rm dyn}[\pi, {\rm K}]$ in the most central events. Larger event multiplicities as achieved by the string melting mechanism without introducing any centrality dependence points to the random nature of particle production processes in the quark coalescence model.

The $N_{\rm part}$ scaling, as shown in Figure 6.6 left column, was also studied for complete-

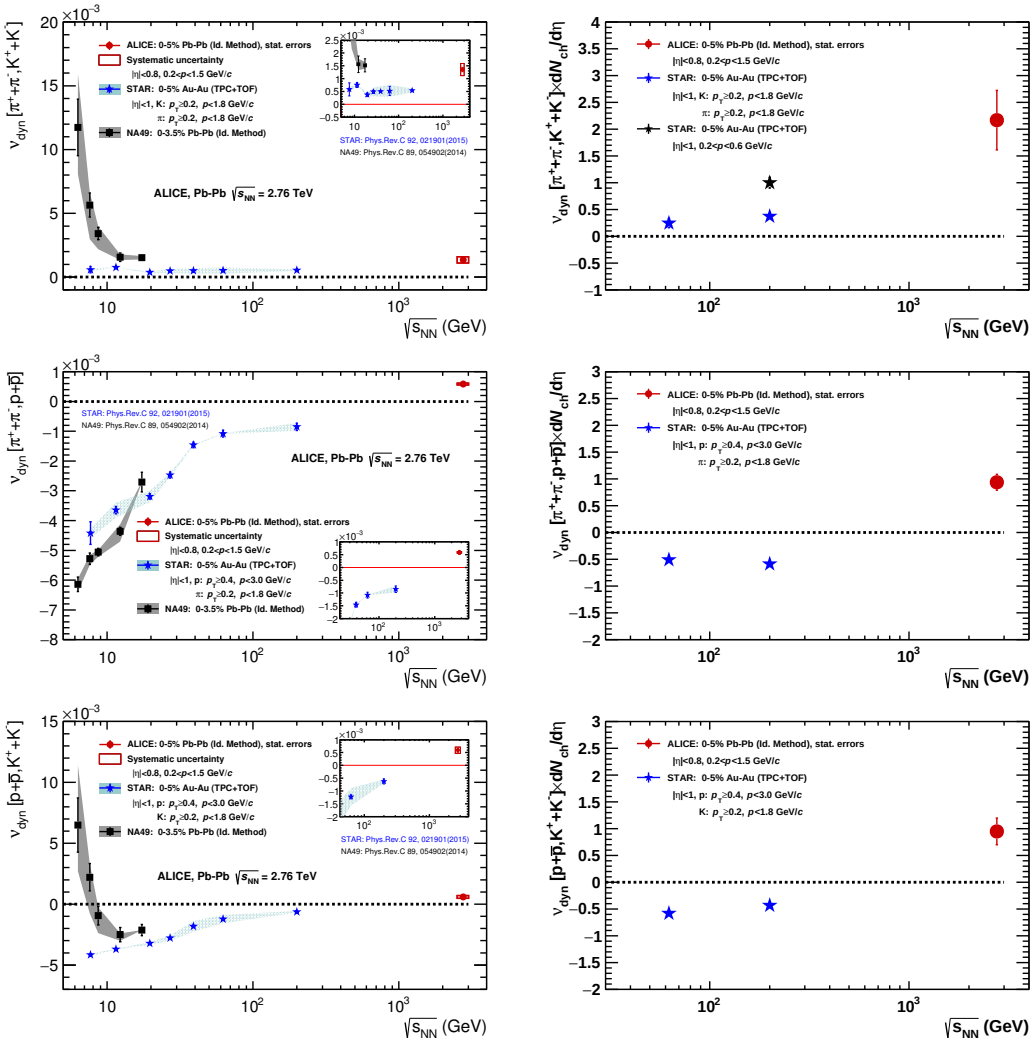

Figure 6.8.: Energy dependence of ν_{dyn} with (right) and without (left) scaled by $\mathrm{d}N_{\rm ch}/\mathrm{d}\eta$. ALICE results are shown as red solid circles. Results from the Identity Method for central Pb–Pb collisions from NA49 [28] are shown as black solid squares. Stars represent results from STAR [25] in central Au–Au collisions. STAR $\mathrm{d}N_{\rm ch}/\mathrm{d}\eta$ values were taken from [91] and data points on the top right plot with black and blue stars were taken from[89] and [25], respectively.

ness. Since $N_{\rm part}$ is not a good approximation to the mean number of sources, $\langle N_{\rm s} \rangle$, the expected behavior of the HIJING being independent of centrality is not reproduced.

Nevertheless, one could study the multiplicity dependence of ν_{dyn} in pp collisions as a crosscheck for the discrimination of N_{part} and $\langle N_{\mathrm{s}} \rangle$, since N_{part} has a fixed value of 2 in pp collisions.

6.3. Comparison to lower energy measurements at RHIC and CERN-SPS

The ALICE results for the most central Pb–Pb collisions are compared to NA49 [28] and STAR [25] data in Figure 6.8 with and without $\mathrm{d}N_{\mathrm{ch}}/\mathrm{d}\eta$ scaling. Strong phase-space coverage dependence of ν_{dyn} was studied earlier in Ref [28] to explain the discrepancies between STAR and NA49 data at low energies.

The ALICE data indicate positive results for ν_{dyn} in all three cases and thus indicates a sign change for $\nu_{\mathrm{dyn}}[\pi, \mathrm{p}]$ and $\nu_{\mathrm{dyn}}[\mathrm{K}, \mathrm{p}]$ which is also observed in the HSD [29] and UrQMD [30] model calculations. Since neither HSD nor UrQMD explicitly include the quark and gluon degrees of freedom, this observation can be attributed to the particular realization of the string and resonance dynamics used in the models [92]. Additionally, HIJING and AMPT model calculations at LHC energies predict positive values except for $\nu_{\mathrm{dyn}}[\pi, \mathrm{p}]$ in the AMPT configuration with hadronic rescattering and without string melting.

Particularly, a comparison of ALICE and the highest-energy STAR results might be of

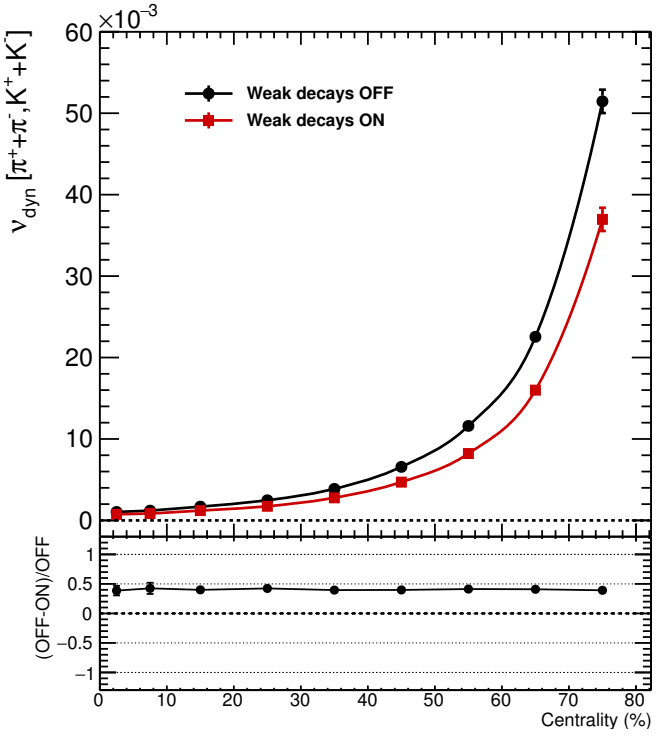

Figure 6.9.: Illustration of the effect of weak decays on $\nu_{\mathrm{dyn}}[\pi, \mathrm{K}]$ using HIJING [83] model calculations.

further interest, since they are both collider experiments and most likely sit at the cross-over region of the QCD phase diagram. For this the following differences between the two analyses should be taken into account. First, the pseudorapidity range used in ALICE

is $|\eta| < 0.8$ while for STAR it is $|\eta| < 1$. As shown in Figure 6.10, ALICE $\nu_{\mathrm{dyn}}[\pi, \mathrm{K}]$ results tend to decrease with increasing η range. Second, the primary vertex cut along the beam direction used in ALICE is 10 cm while for STAR it is 30 cm. Also, ALICE uses the ITS information in addition for the selection of primary vertex particles. That is, ALICE has stronger restrictions to suppress weak decay and feed-down contaminations. To investigate the effect of weak decays on the ν_{dyn} results, ν_{dyn} for all three cases were calculated with HIJING simulations on the generator level with and without weak decay particles. Since decay products are correlated, they drive the ν_{dyn} values towards negative values, as shown in Figure 6.9. Accordingly, STAR results most likely have a systematic shift towards lower values. Third, ALICE uses V0 detectors for the centrality selection while STAR uses TPC tracks [91]. Lastly, the momentum ranges used are different. As shown in Figure 6.8 top right, STAR results at 200 GeV/c with different momentum ranges show a significant difference.

6.4. Rapidity dependence

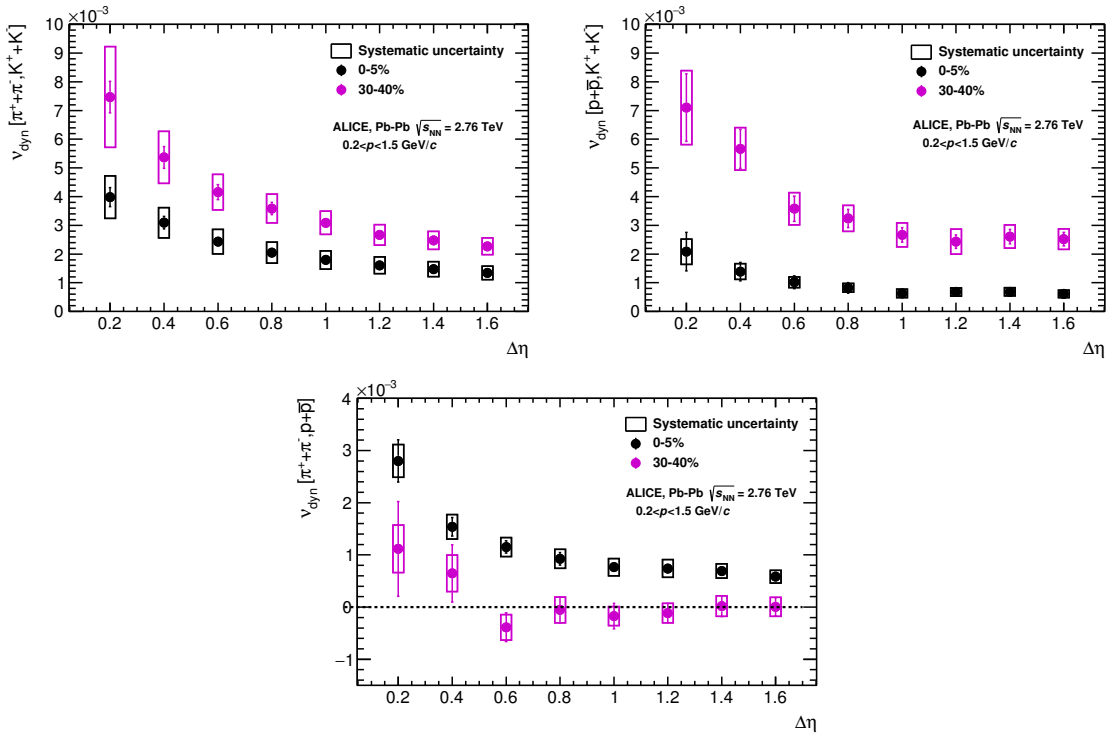

Figure 6.10.: Pseudorapidity dependence of ALICE ν_{dyn} results for two centrality classes.

As discussed previously, acceptance plays an important role in the physics interpretation of the fluctuation observables. Therefore the pseudorapidity dependence of ν_{dyn}, in comparison with Σ, was also investigated in this thesis.

By enlarging the acceptance two important contributions enter the fluctuations signals: dynamical fluctuations stemming from the underlying physics and correlations due to conservation laws. For instance, particles coming from the same source, i.e. correlated ones, most likely will not be detected together if the acceptance is too small, thus ν_{dyn} (and also Σ) results are expected to approach the Poissonian limit. However, due to the intrinsic

multiplicity dependence of ν_{dyn}, it is difficult to see this behavior, as shown in Figure 6.10. Thus, the mean number of charged particles, $\langle N_{\mathrm{ch}} \rangle$, within a given acceptance was used as a scaling factor. Since HIJING simulation results provide quite a good agreement with the ALICE data as shown in Figure 6.11, $\langle N_{\mathrm{ch}} \rangle$ values were approximated by counting the charged particles in a given acceptance in HIJING simulations on the generator level.

Figure 6.12 shows scaled ν_{dyn} and Σ results for all three cases. As expected, in both cases fluctuation signals decrease with acceptance. Here, one should note that Poissonian behavior can be due to either a random nature or an underlying physics effect. Therefore, to understand the real origin of the physics mechanism one would need a pseudorapidity coverage where the contributions from the conservation laws are clearly visible. In view of $\Sigma[\pi, p]$ one can clearly see that an η coverage less than 0.5 might be misleading.

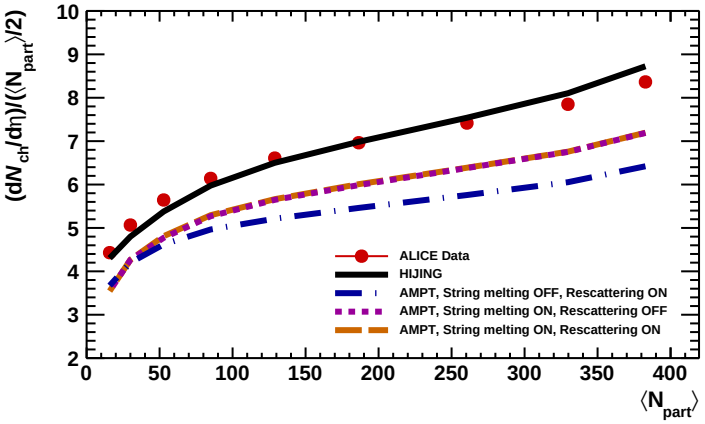

Figure 6.11.: Dependence of $(\mathrm{d}N_{\mathrm{ch}}/\mathrm{d}\eta)/(\langle N_{\mathrm{part}} \rangle/2)$ on the number of participants (N_{part}) in comparison with the AMPT [85] and HIJING [83] model calculations.

6.5. Physics discussion

The multiplicity scaling problem of ν_{dyn} measure makes it difficult to draw quantitative conclusions in comparison to small systems and model calculations. However, it is a suitable tool to gain insight into the correlations between different particle species and study dynamical event-by-event fluctuations.

Particle detection efficiency losses are considered as the most prominent challenge in the event-by-event analyses. ν_{dyn} is by construction robust against this problem, as discussed in Section 5.5.1, however the intrinsic multiplicity dependence can not be avoided. It scales with the inverse of the number of independent sources, $1/\langle N_{\mathrm{s}} \rangle$, which can not be measured experimentally, therefore it is still an open question how to scale out the multiplicity dependence. In this thesis, $\mathrm{d}N_{\mathrm{ch}}/\mathrm{d}\eta$, which is a quantity corrected for efficiency, was preferred so that the property of ν_{dyn} being free from efficiency corrections is preserved. The alternative scaling, $1/(1/\langle N_a \rangle + 1/\langle N_b \rangle)$, which was investigated in view of the strongly intensive measure Σ, has a theoretical base but it requires an efficiency correction due to the use of mean particle multiplicities, $\langle N_i \rangle$. Nevertheless, at first glance the sign of ν_{dyn} is already sufficient to deduce the relative correlation strength between particles used for the calculation of ν_{dyn}.

On the other hand, to draw further physics conclusions, ν_{dyn} results can be compared to a reference, such as model calculations, where the physics mechanisms are under control.

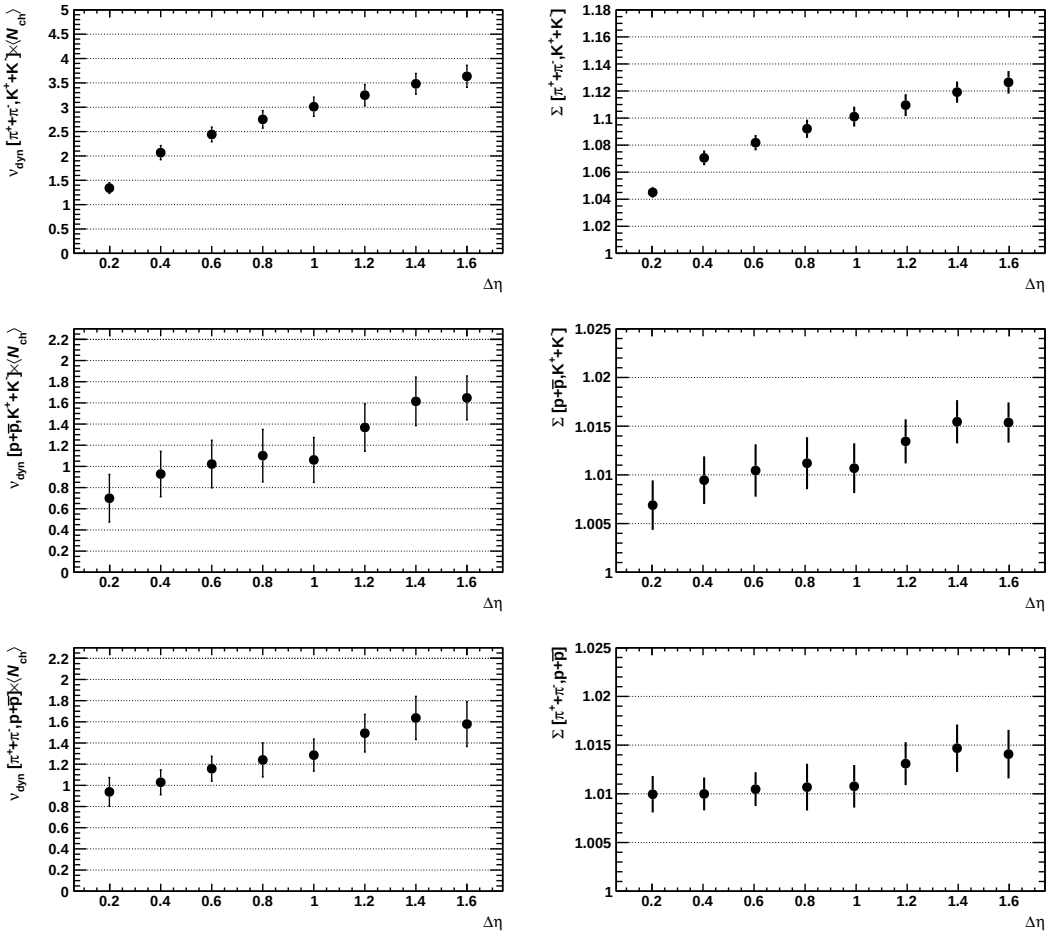

Figure 6.12.: $\Delta\eta$ dependence of Σ results in comparison with the ν_{dyn} results scaled by $\langle N_{\mathrm{ch}} \rangle$.

HIJING and AMPT models are good candidates, where the former is just a superposition of independent nucleon-nucleon collisions and the latter, in addition, includes collective effects. Accordingly, the $\mathrm{d}N_{\mathrm{ch}}/\mathrm{d}\eta$ scaled results of HIJING show no centrality dependence, while different configurations of AMPT deviate from the flat behavior, as shown in Figure 6.6. The measurement of ν_{dyn} in small systems, such as pp and p–Pb, and also at different energies would help to understand the multiplicity scaling, as well as the physics interpretation.

Moreover, when comparing to lower energy measurements one should take into account not only the multiplicity scaling but also the different acceptances and different analysis techniques. For instance, the usage of the TOF detector changes the detection efficiency loss pattern which might then effect the ν_{dyn} results (See Section 5.5.1 and Appendix G).

All in all, the study of particle ratio fluctuations using ν_{dyn} can signal the dynamical fluctuations by means of a qualitative comparison to model calculations and lower energy measurements, and also in terms of the correlation strength between particle species with respect to the Poissonian limit. To extend the current understanding, a more differential analysis of ν_{dyn} in terms of rapidity, p_{T}, and charge sign dependence as well as a study in small systems and at different collision energies is required.

Summary and Outlook

This thesis presents mainly two different analyses; (i) an offline correction procedure for the baseline fluctuations in the TPC, (ii) event-by-event identified particle ratio fluctuations in Pb–Pb collisions.

On the detector side, prior to the offline baseline correction, a detailed study of the TPC signal shape was carried out making use of the TPC Laser calibration system. The obtained results not only extended the understanding of the TPC signal shape dependencies but also maximized the performance of the offline correction procedure. Additionally, the characteristic signal shape was crosschecked with three-dimensional Garfield simulations for the first time.

Two main contributers to the baseline fluctuations in the TPC are the ion-tail and the common-mode effects. They cause a significant deterioration of the TPC $\mathrm{d}E/\mathrm{d}x$ resolution and thus the PID quality which is proportional to the track density. The resulting relative effect due to these effects reaches up to $\sim$35% worsening in the separation power of the TPC and $\sim$25% shift in the mean $\mathrm{d}E/\mathrm{d}x$ positions for the highest multiplicity events. The offline correction recovers the performance to a large extend: 25/37% for the separation power and 18/25% for the mean $\mathrm{d}E/\mathrm{d}x$ positions. In the absence of an online correction it provides the most significant improvement in the PID performance of the TPC. The method is now a standard in ALICE and being used in the offline reconstruction chain of ALICE. Besides, to have a more realistic description of the TPC detector in the Monte-Carlo (MC) simulations, both ion-tail and common-mode effects were successfully implemented in the Aliroot simulation framework. This functionality is also currently in operation and reduces systematic effects due to mismatch between data and MC.

Moreover, a functionality, which allows for tests of *online* baseline correction algorithms, was developed and implemented in the Aliroot framework. Similarly an algorithm for the correction of the common-mode effect was developed and tested successfully. It is planned to be used for the future upgrade of the TPC with Gas Electron Multipliers (GEMs), which enable continuous data readout at a rate of 50 kHz in Pb–Pb collisions in the RUN3 period of LHC running.

On the physics side, Identity Method was successfully applied to ALICE data for the first time to the analysis of event-by-event identified particle ratio fluctuations. It is currently being used also for the net-particle fluctuations and planned to be used in further event-by-event analyses in ALICE.

For the particle identification the method uses the inclusive $\mathrm{d}E/\mathrm{d}x$ distributions measured in the TPC, where the overlap regions of the inclusive spectra are also included in the calculations of the moments of the multiplicity distributions. Therefore, a detailed study of the TPC detector response was carried out, where clean particle samples retrieved from V^0 decay particles were taken as the basis. Also, the effect of the truncated mean procedure on the detector response was investigated by means of a toy simulation. To cope with the asymmetric structure of the detector response a generalised Gauss function with two additional parameters, one for the tails and one for the asymmetry, was used. It is the first time the TPC detector response is described with 5 parameters each, on a fine grid in kinematic space of 16 pseudorapidity and 9 centrality bins. Moreover, the simulated detector response was crosschecked with the data. The observed slight difference was attributed to the ion-tail and common-mode effects which are not yet included in the current official productions.

Having determined the TPC detector response, a so-called "Iterative PID" procedure was developed for the inclusive spectra fits. Each parameter of the fit function was restricted in steps making use of the joint information from the clean and MC samples, as well as the regions of inclusive spectra where there is no overlap. The resulting fit functions were then stored in a look-up table to be used as an input to the dedicated software "TIdentity Module" (Appendix H), which runs the calculation of the Identity Method. The comparison of the particle spectra obtained with the Identity Method to the published spectra was shown to agree within the systematic uncertainties.

This allowed for extracting the identified particle ratio fluctuations in Pb–Pb collisions at $\sqrt{s_{\mathrm{NN}}} = 2.76$ TeV in terms of the ν_{dyn} measure as a function of centrality and pseudo-rapidity. The results were compared to calculations with the HIJING and AMPT event generators, as well as to the lower energy measurements at CERN-SPS and RHIC for the most central events.

The intrinsic multiplicity scaling of ν_{dyn} was discussed in view of the mean multiplicities of accepted particles used for the fluctuation measurement, charged-particle multiplicity density at mid-rapidity, $\mathrm{d}N_{\mathrm{ch}}/\mathrm{d}\eta$ and number of participants, N_{part}. To keep the basic property of ν_{dyn} being free of the efficiency corrections, $\mathrm{d}N_{\mathrm{ch}}/\mathrm{d}\eta$ scaling was taken as reference. The mean multiplicity scaling, $1/(1/\langle N_a\rangle + 1/\langle N_b\rangle)$, was discussed in the scope of the strongly intensive measure Σ.

It is shown that the sign change of $\nu_{\mathrm{dyn}}[\pi, \mathrm{p}]$ going to peripheral collisions, which indicates an increasing correlation between pions and protons, is neither described in HIJING nor AMPT model calculations. Moreover, the evolution of ν_{dyn}, measured in most central collisions, with beam energy was considered. The ALICE measurements indicate that the particle production dynamics change considerably with collision centrality as well as from that observed at RHIC energies. Values of ν_{dyn} measured with all three pair combinations deviate significantly from those measured by STAR at top RHIC energy. The results for $\nu_{\mathrm{dyn}}[\mathrm{K}, \mathrm{p}]$ and $\nu_{\mathrm{dyn}}[\pi, \mathrm{p}]$ change sign relative to the values reported by the STAR collaboration. Furthermore, a re-analysis of ν_{dyn} indicates that the magnitude of ν_{dyn} is in fact dependent on the kinematical limits used in the analysis but the dependency appear too weak to explain the deviations from ν_{dyn} values measured by STAR.

A more differential study of the particle ratio fluctuations taking into account small systems, like-sign and unlike-sign particles and different collision energies would allow to draw firmer conclusions and provide links to other physics observables such as radial flow, strangeness enhancement and net-baryon fluctuations. Also, the effect of resonances and conservation laws on the particle ratio fluctuations can be studied using MC calculations, which then can be crosschecked with real data.

Appendices

A. Data Taking Model of ALICE

During the data taking process [55], the whole experiment is steered by the Experiment Control System (ECS). The ECS is responsible for the synchronization between the four ALICE online systems; Data Acquisition (DAQ), Trigger System (TRG), High-Level Trigger (HLT) and Detector Control System (DCS). The running conditions, partitioning, run type, run number and trigger settings are propagated from ECS to DCS before the start of each run. The partitioning allows different groups of sub-detectors to be read out with different triggers concurrently such that one sub-detector can only join one partition but more than one trigger cluster at a time.

A run type defines how the FEE will be configured and which subsystems are to be activated at the start of the run. A physics Run is the general run type for recording data with beam-beam collisions. The remaining run types are used for the calibration purposes (e.g. in case of TPC pedestal, pulser and laser calibration runs).

DCS: The DCS provides remote control and monitoring of all detector equipment in such a way that the whole the ALICE detector (also each sub-detector) can be operated from a single workplace, the ALICE Control Room (ACR) at LHC Point 2. The primary tasks of the DCS are to ensure safe and reliable operation of ALICE and to provide optimal operational conditions to attain high quality data. For this, the required information is retrieved from the DCS databases.

Trigger System: Since ALICE studies several physics topics using different beam conditions, a large number of trigger classes are used to select and characterize the events with respect to the requirements and the restrictions imposed by the bandwidth of the DAQ and the HLT. Trigger inputs are pulses provided by the trigger detectors so as to be synchronized to the LHC clock cycle, as distributed by the Timing, Trigger and Control (TTC) system. The trigger decision, made within in 100 ns, is provided by the Central Trigger Processor (CTP). The CTP handles this process concurrently for the different trigger clusters.

The ALICE trigger system is based on three trigger levels; Level-0 (L0), Level-1 (L1) and Level-2 (L2) with the response of accept or reject;

- **L0:** It has a fixed latency of about 1.2 μs with respect to the interaction.
- **L1a/L1r:** Each L0 can be followed by a L1 pulse after a fixed latency of about 7.7 μs with respect to the interaction time. In case of L1r the trigger sequence is terminated. If an L1a was issued, an asynchronous message containing basic event information will follow.
- **L2a/L2r:** L2 completes the trigger sequence by deciding if the triggered event should be transferred from the FEE data buffers to the DAQ. This trigger level is dispatched as an asynchronous message after a minimum time of about 96 μs, which corresponds to the TPC drift time, in order to ensure the completion of the TPC

readout. Further, L2 trigger waits for the end of the past-future protection interval (e.g. ±10 μs for the ITS and 96 μs for the TPC in case of pp) to verify that the event can be taken. The purpose of the past-future protection circuit is to ensure that the events selected for readout are not spoiled by pile-up.

The Data Acquisition: The detectors receive the trigger signals and the associated information from the CTP, through a dedicated Local Trigger Unit (LTU) interfaced to the TTC system. The readout electronics of the all detectors is interfaced to the ALICE standard Detector Data Link (DDL). At the receiving side of the DDLs there are so-called DAQ Read-out Receiver Card (D-RORC) hosted by the front-end machines, called Local Data Concentrators (LDCs). The event fragments originated by the various D-RORCs are logically assembled into sub-events in the LDCs which is also capable of local data recording, if used in stand-alone mode, and online sub-event monitoring. The LDCs ship the sub-events to a farm of machines called Global Data Collectors (GDCs) where the whole events are built from all the sub-events pertaining to the same trigger. GDCs then send these events to the Permanent Data Storage (PDS). In addition, the GDC is capable of online event monitoring.

HLT: Since the event rate is limited by the DAQ, an on-line processing is neces-

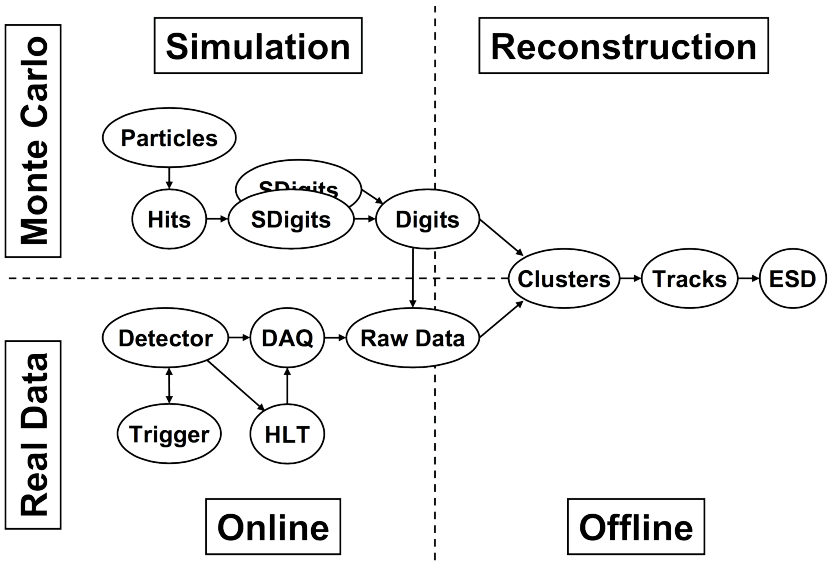

Figure A.1.: Simulation and reconstruction process in ALICE [93].

sary, in order to reduce the data size. For this purpose the HLT system was designed. The HLT allows forwarding zero-suppressed events into the DAQ data stream on an event-by-event and detector-by-detector basis. All sub-detectors submit their data into the HLT upon a L2 accept. The HLT system receives a copy of all the raw data from the LDCs. Firstly, It accepts or rejects events based on detailed online analysis by providing a trigger decision. Secondly, it selects relevant parts of the (sub-) event or regions of interest. Then it reduces the event size by applying compression techniques on the accepted and selected data. Lastly, the output is submitted to the event builders for permanent storage. A key requirement of the system is the ability to process the event analysis in real-time [94].

Reconstruction: The offline framework handles the offline analysis and the recon-

struction of the physics data coming from simulated and real interactions. This is carried out by the ALICE computer framework Aliroot which makes use of the object oriented, C++ based ROOT framework [93].

The detected hits, energy depositions at a given point and time, are stored for each detector and they are later on converted into digits taking into account the detector and associated electronics response function. As an input, the reconstruction uses the digits that are the digitized signals (ADC counts) obtained by a sensitive pad of a detector at a certain time, together with some additional information like module number, readout channel number, time bucket number, etc. The digits could be in both ROOT format, which is more convenient for development and debugging purposes, and raw data format, as they are output from the detector or can be generated from simulated special-format digits (see Fig. A.1).

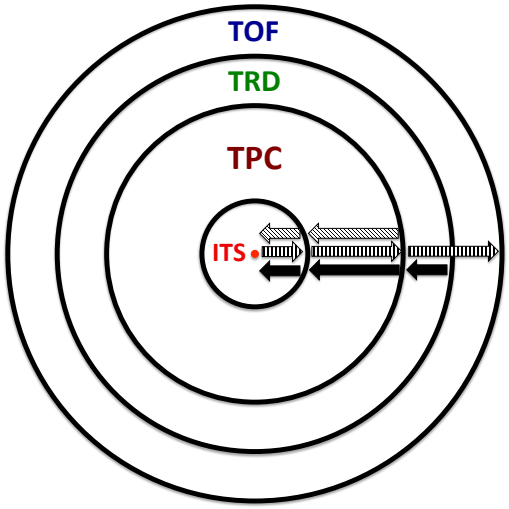

Figure A.2.: Schematic view of the three passes of the combined track finding [93].

First, a local reconstruction of clusters, containing the space point information of the particles, is performed in each detector. Then vertices and tracks are reconstructed and the particle identification is carried on. The combined track finding, which is based on the Kalman Filter approach (a method for simultaneous track recognition and reconstruction), in the central ALICE detectors consists of three steps (Fig. A.2):

1. Track seeding in the outermost pad rows of the TPC to the primary vertex through the ITS layers.

2. Tracking from the innermost ITS layer to the outer detectors; TRD, TOF, HMPID, PHOS and EMCal.

3. Refitting the primary tracks back to the primary vertex or, in the case of the secondary tracks, as close to the vertex as possible.

Finally, the outcome of the reconstruction process is kept in a structure, so-called Event Summary Data (ESD), containing the reconstructed charged particle tracks (together with the particle identification information), decays with the V^0, kink and cascade topologies and some neutral particles reconstructed in the calorimeters, as well as the global event properties [95].

B. ALICE Coordinate Systems

Global Coordinates: The ALICE coordinate system is a right-handed orthogonal cartesian system whose origin is taken to be the beam Interaction Point (IP). Its x coordinate is perpendicular to the mean beam direction such that the positive x is pointing to the center of the accelerator, y coordinate is perpendicular to the mean beam direction pointing upward and z coordinate is parallel to the mean beam direction such that positive z pointing towards the Shaft side (RB24) and negative z towards the Muon Arm (RB26).

The Azimuthal angle φ increases counterclockwise, starting from the x-axis ($\varphi = 0$)

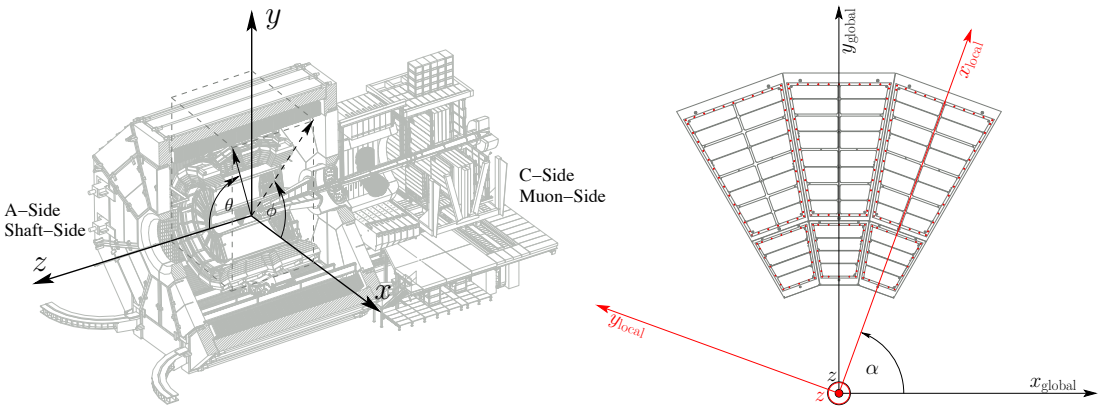

Figure B.1.: Sketch of the ALICE global (left) and local (right) coordinate systems [96, 97].

to y-axis ($\varphi = \pi/2$) for an observer standing at positive z and looking to the Muon Side. The polar angle θ increases from the z-axis to the xy plane [53, 96].

The following are the definition of some sides of the ALICE experiment:
A side : positive z (shaft side),
C side : negative z (muon side),
I side : positive x (towards LHC center, Inner),
O side : negative x (towards Jura, Outer),
U side : positive y (Up),
D side : negative y (Down).

Local Coordinates: The local offline coordinate system is used to account for the azimuthal segmentation of the central barrel detectors. It is a right handed Cartesian system which has the same origin and the same z-axis as the global system. The local system is rotated such that the x-axis is perpendicular to the sub-detectors 'sensitive plane' (TPC pad row, ITS ladder etc.). Therefore the local and global systems can be transformed into each other by a simple rotation of the angle α around the z-axis. In case of the TPC, the x-axis points radially outwards and the y-axis completes the right-handed cartesian system by being parallel to the pad rows. The transformation is done

with $\alpha = sector \times 20^{\circ}$:

$$x_g = x_l . \cos(\alpha) - y_l . \sin(\alpha) \quad \text{(B.1)}$$

$$y_g = y_l . \cos(\alpha) + x_l . \sin(\alpha) \quad \text{(B.2)}$$

A sketch of the local and global coordinate systems are shown in Fig. B.1.

C. Electron Drift and Diffusion in the TPC

Electron Drift: In microscopic level, an electron scatters isotropically with an instantaneous velocity ν immediately after the collision [64]. However, some short time later, it picks up the extra velocity u, which appears macroscopically as the drift velocity, equal to its acceleration along the field. In this sense, the drift of the electrons under the influence of an electric and a magnetic field is given by an equation of motion:

$$m\frac{d\mathbf{u}}{dt} = eE + e\left[\mathbf{u}\times\mathbf{B}\right] - K\mathbf{u}, \tag{C.1}$$

where m and e are the mass and charge of the electron and $K\mathbf{u}$ is the friction term. The ratio m/K has the dimension of a characteristic time and can be interpreted as the average time between collisions τ:

$$\tau = \frac{m}{K}. \tag{C.2}$$

In view of the fact that $t \gg \tau$, the drift velocity is taken to be constant i.e $du/dt = 0$. Thus, equation (3.2) gives:

$$\frac{\mathbf{u}}{\tau}\frac{e}{m} - \left[\mathbf{u}\times\mathbf{B}\right] = \frac{e}{m}\mathbf{E}. \tag{C.3}$$

From here, introducing the cyclotron frequency $\omega_x = (e/m)B_x$ and $\varepsilon_x = (e/m)E_x$ etc. one can conclude the drift velocity u as:

$$u = \frac{e}{m}\tau|E|\frac{1}{1+\omega^2\tau^2}\left(\mathbf{e} + \omega\tau\left[\mathbf{e}\times\mathbf{b}\right] + \omega^2\tau^2\left(\mathbf{e}\cdot\mathbf{b}\right)\mathbf{b}\right), \tag{C.4}$$

where $\mathbf{e}$ and $\mathbf{b}$ denote the unit vectors in the direction of the electric and magnetic fields respectively. The drift direction is governed by the dimensionless parameter $\omega\tau$. For $\omega\tau = 0$, the drift velocity is along the electric field. In this case the relation has the simple form:

$$\mathbf{u} = \frac{e}{m}\tau\mathbf{E} = \mu\mathbf{E}, \tag{C.5}$$

$$\mu = \frac{e}{m}\tau, \tag{C.6}$$

where μ is the scalar electron mobility.

Diffusion: As the drifting electrons are scattered on the gas molecules, their drift velocity deviates from the average due to the random nature of the collisions. In the absence of electromagnetic fields, the deviation is the same in all directions, and a point-like electron cloud starting to diffuse at time $t = 0$ from the origin in the z direction will, after

some time t, assume the following Gaussian density distribution:

$$n = \left(\frac{1}{\sqrt{4\pi Dt}}\right)^3 \exp\left(-\frac{r^2}{4Dt}\right), \tag{C.7}$$

where r is the distance to the origin; ($r^2 = x^2 + y^2 + (z - ut)^2$) and D is the diffusion constant because n satisfies the continuity equation for the conserved electron current [64]. The electric field, however, breaks the isotropy in such a way that the diffusion in drift direction and perpendicular to it are different. Hence, equation (3.8) has the form:

$$n = \left(\frac{1}{\sqrt{4\pi D_l t}}\right)\left(\frac{1}{\sqrt{4\pi D_t t}}\right)^2 \exp\left[-\frac{x^2 + y^2}{4D_t t} - \frac{(z - ut)^2}{4D_l t}\right], \tag{C.8}$$

where D_l and D_t denote the two different diffusion constants in longitudinal and transverse direction. Equation (3.8) shows that the width of the density distribution σ is given by $\sigma^2 = 2Dt$. Together with $L = ut$, the width can be written as:

$$\sigma^2 = \frac{2D}{u}L, \tag{C.9}$$

where t is the drift time of the electrons and L the length traveled during that time. However, as a characteristic measure for the diffusion in a gas, the drift length independent quantities:

$$D_{\mathrm{L}} = \frac{\sigma_l}{\sqrt{L}} = \sqrt{\frac{2D_l}{\mu E}} \tag{C.10}$$

$$D_{\mathrm{T}} = \frac{\sigma_t}{\sqrt{L}} = \sqrt{\frac{2D_t}{\mu E}} \tag{C.11}$$

derived from equation (3.6) and (3.10), are used [97]. The magnetic field reduces the transverse diffusion by the factor

$$\frac{D_{\mathrm{T}}(\omega)}{D_{\mathrm{T}}(0)} = \frac{1}{1 + \omega^2\tau^2} \tag{C.12}$$

$$\tag{C.13}$$

where $\omega = \dfrac{eB}{m}$ is the cyclotron frequency.

D. Two Photon Ionization Processes in the TPC

Laser beams are used to produce ionisation tracks in the active volume of the TPC for calibration and surveying purposes (See Section 4.2). The pulsed UV laser used has a wavelength of 266 nm which corresponds to the energy of 4.66 eV. However, the molecules taking part in the ionisation process are not the basic components of the gas mixture (Ne, CO_2, N_2) but organic impurities in the gas with the ionisation potentials of $5-8$ eV. Further, the cross section for $3-4$ photon ionisation is extremely low. The ionisation process with the lasers, therefore, is dominated by the two photon process.

Relevant processes are given in Fig. D.1. The most dominant ones being probably B and also D, if the singlet to triplet transition rate $S_1 \rightarrow T_1$ is high. The stimulated transitions from one state to another are proportional to the incoming photon flux, where the constant of proportionality is the corresponding transition cross-sections [98].

Assuming recombinations are negligible, the physics process is described with the following differential equation system;

$$\frac{dn_i}{dt} = n_e \sigma^* N, \tag{D.1}$$

$$\frac{dn_e}{dt} = (n_0 - n_e)\,\sigma_e N - n_e \sigma_i^* N - n_e/\tau, \tag{D.2}$$

where N is photon flux (photon/cm^{2}s), τ is the life time, σ is cross-section, n_0, $n_e(t)$, $n_i(t)$ are molecule densities of ground, exited and ionized states, respectively. Integration of these equations gives;

$$n_e(t) = \frac{a}{b}\left(1 - e^{-bt}\right), \tag{D.3}$$

$$n_i(t) = \sigma_i^* N \frac{a}{b}\left(T + \frac{1}{b}(e^{-bT} - 1)\right), \tag{D.4}$$

where T is the width of the laser pulse, $a = n_0 \sigma_e N$ and $b = (1/\tau + \sigma_e N + \sigma_i^* N)$. Assuming N is constant, this leads to

$$n_i\,(T) = n_0 \sigma_e \sigma_i^* N^2 \frac{T}{b}\left[1 - \frac{1}{bT}\left(1 - e^{-bT}\right)\right]. \tag{D.5}$$

For the limiting case of low photon flux and long lifetime of the intermediate state τ $\left(\gg T \sim 10^{-9}s\right)$ i.e. $bT \ll 1$, equation (3.17) yields:

$$n_i\,(T) = \frac{1}{2} n_0 \sigma_e \sigma_i^* N^2 T^2. \tag{D.6}$$

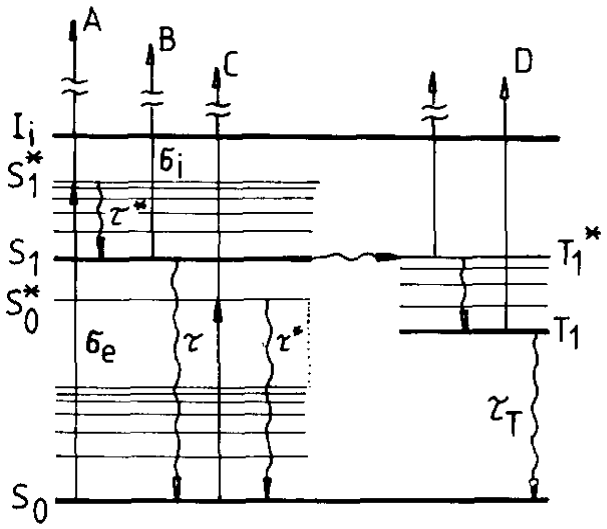

Figure D.1.: Schematic energy level diagram of complex molecule, indicating possible channels for 2-photon ionisation [98].

As a conclusion, the ionization density is proportional to the square of the photon flux N^2. That means, it is crucial that the laser intensity is stable in order to get a constant ionisation rate, which is required to use the lasers as a calibration tool [64, 97].

E. TPC Laser System: Generation and Distribution of Laser Beams

The basic principle of generating hundreds of narrow laser beams simultaneously in the TPC volume was developed for the STAR experiment at RHIC [99] and has been modified appropriately for ALICE.

The ALICE TPC laser calibration system is composed of a static optical system with a few adjustable parts. The static optics is composed of beam splitters, mirrors and bending prisms guiding the laser beam before it enters the TPC volume. The guiding system ends with cameras for the purpose of monitoring the position and intensity of the remaining beams. This information is used for the alignment of the adjustable part of the system. The adjustable part is mainly composed of remotely controllable mirrors that guide the beam into the static optical system.

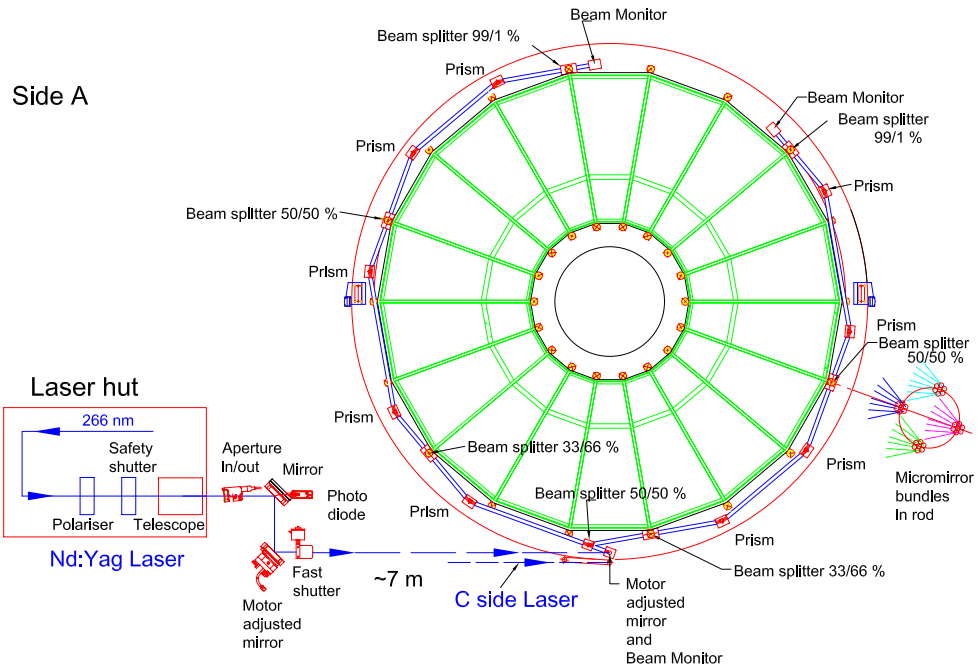

Figure E.1.: Overview of the optical elements to guide the laser beam from the laser hut to the entrance windows in the TPC field cage. The A side system is shown. The C side system is obtained by mirror symmetry in a vertical plane along the TPC axis [50].

The laser is placed in a hut outside the L3 magnet at a distance of 10 m to the TPC (Figure E.1). It is specified to provide 100 mJ/pulse of 5 ns duration and 266 nm wavelength at a repetition rate of 10 Hz. Built into the laser is also a beam expanding telescope to enlarge the beam diameter from $9-10$ mm to 25 mm and reduce the beam divergence to approximately 0.3 mrad. Close to the laser, the beam has a flat intensity profile across the beam spot which develops smoothly into a Gaussian profile after $20-30$ m.

From the laser hut, two wide laser beams exit horizontally. One beam is guided to the A-side end-plate close to its outer radius, where a mirror reflects it by 90° into a vertical plane parallel to the TPC end-plate. The other beam passes slightly lower and continues in a straight line to the C-side end-plate where likewise another 90° mirror bends it into the vertical plane parallel to this plate. After the beam is reflected into the vertical plane at the bottom of the TPC, a 50% beam splitter directs half of the beam in each direction to the laser rods, as shown in Figure E.2. The beam paths at the two TPC ends are virtually identical, except that one of the prisms on the C-side has a smaller bending angle to compensate for the beam entrance shift of 10° in ϕ.

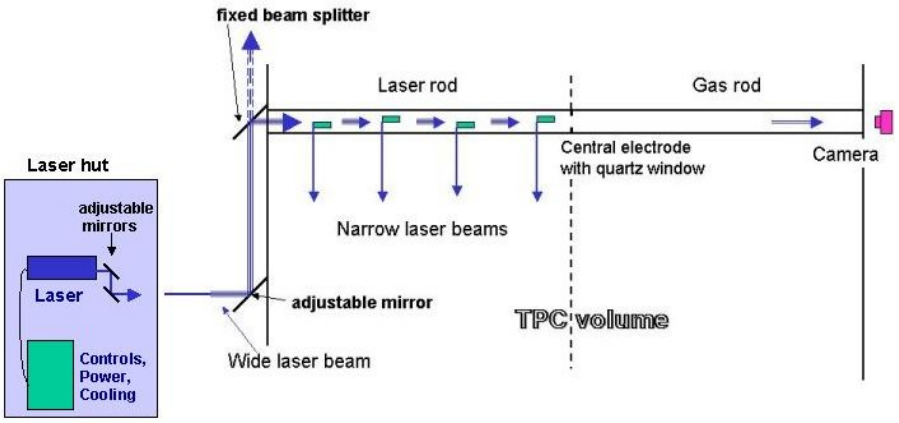

Figure E.2.: Principle of generating narrow laser rays in the TPC volume [60].

The wide beams travel along the inside of the rods as illustrated in Figure E.2 and are intersected by four micro-mirror bundles before arriving at the TPC central electrode at $z = 0$. Here, the undeflected part of the wide beam goes through an empty gas rod in the other half of the TPC. At the far end, the beam position and intensity are monitored by a camera, using the Poisson Spot technique [60].

The wide beams hit bundles of seven one-millimeter diameter micro-mirrors. The narrow beams spread out from these bundles roughly in a plane perpendicular to the wide laser beam and were rotated along their axis to give predefined azimuthal reflection angles: $2,5°$, $\pm 9,2°$, $\pm 16°$ and $\pm 31,8°$, as shown in Figure E.4. The angles were optimized such that the narrow beams cross the sector boundaries strategically, i.e. at points where alignment between sectors would benefit the most. A projection on the transverse-plane of the star-like pattern of laser rays is shown in Figure E.3.

Furthermore, beams from neighboring laser rods in ϕ are shifted slightly in z relative to each other to avoid most of the apparent beam crossings. The micro-mirror bundles, thereby, are positioned at $z = \pm 130, 850, 1690, 2470$ mm for odd laser rods and $z = \pm 100, 790, 1630, 2410$ mm for even rods [59].

Spatial Precision and Stability: The TPC calibration with laser tracks requires the knowledge of the ideal spacial position of all laser tracks. Given the mechanical tolerances, the best absolute coordinate frame for each half of the TPC is defined by the plane of the end plate. All ROCs and the plane of the CE were aligned and adjusted relative to the end plates.

In order to obtain a relative electric drift field error below 5×10^{-4}, these surfaces,

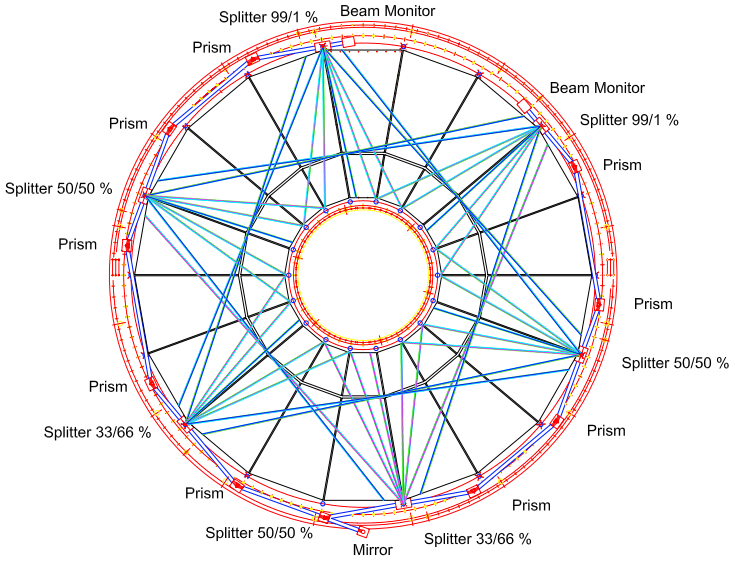

Figure E.3.: Ideal laser tracks in (r,φ) in the TPC drift volume, projected to the end-cap. The pattern repeats eight times through the full length of the TPC. [50].

as well as the 4 laser track planes on each side, were defined relative to each other to a precision of approximately 100 μm. A final precision goal of $800 - 1000$ μm for space points translate to the following requirements on spacial coordinates and angles of the laser system: $(\triangle x, \triangle y, \triangle z) \leq 800 - 1000$ μm, $(\triangle\varphi, \triangle\phi) \leq 0.4 - 0.5$ mrad [50].

The most important issue in the definition of the laser track positions is the placement of the micro-mirrors (Figure E.4). The mechanical construction errors of the micro-mirror bundles are specified to be less than 100 μm in the spacial measures and less than 1° in all reflection angles. This production tolerance of 1° results in deviations of up to 40 mm near the inner cylinder [60]. The only other deviation from the ideal rays that matters is the incidence angle of the wide laser beams on the micro-mirrors which is relatively easy to measure and keep constant due to the long lever arms in the optics system.

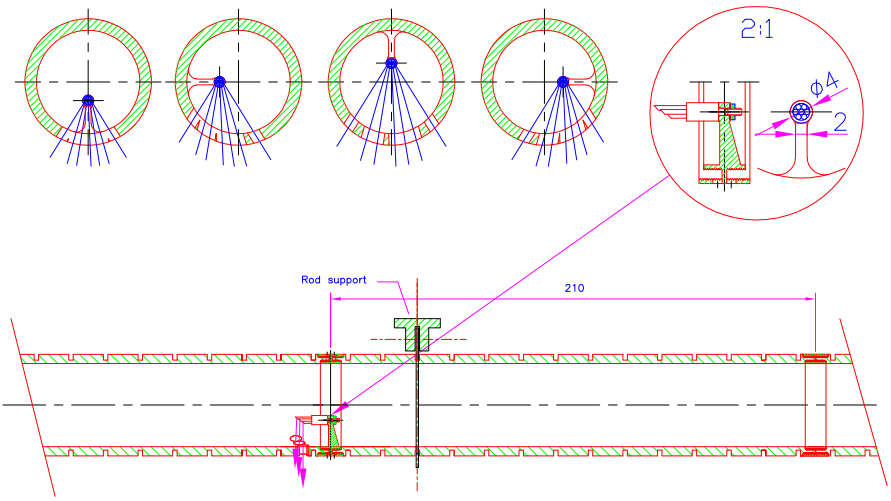

Figure E.4.: Laser rod with micro-mirror bundle and its support, as well as the position of four mirror bundles (left). Azimuthal reflection angles of each mirror bundle (right) [60].

F. Armenteros-Podolanski Space

The Armenteros-Podolanski plot [100] classifies neutral V^0 particles by considering the decay topologies. To understand the physics behind, the system has to be considered in both the laboratory and in the center of mass system as shown in Figure F.1.

In the center of mass system the two decay particles must come off back-to-back so

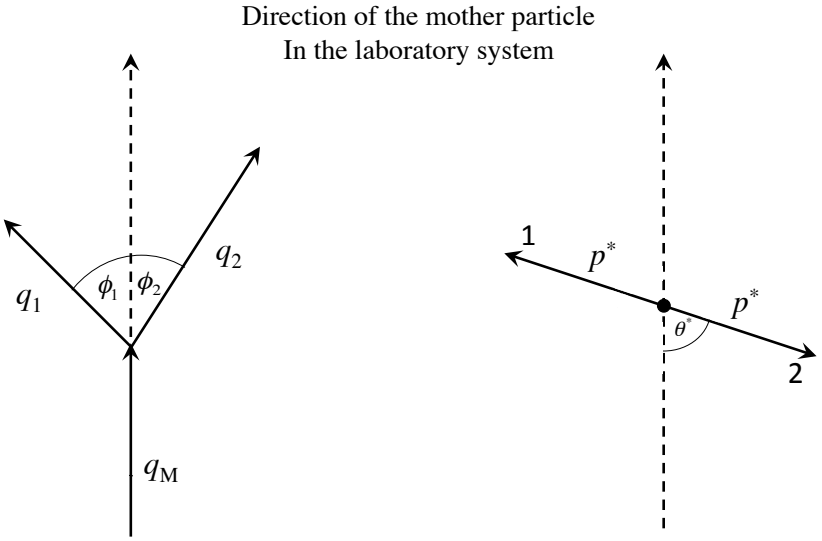

Figure F.1.: The decay of a neutral V^0 into two charged tracks in the laboratory system (left) and the center of mass system (right). Particle 1 and 2 are assumed to be the positively and negatively charged, respectively. In the center of mass system the momentum of mother particle p^*_M, is zero.

as to conserve momentum. Thus one obtains the transverse and longitudinal momentum, relative to the direction of mother particle in the laboratory system, as

$$q^*_{\mathrm{T}} = p^* sin\theta^*, \qquad q^*_{\mathrm{L}} = p^* cos\theta^* \tag{F.1}$$

where all quantities in the center of mass system are denoted by a *.

By means of Lorentz transformation

$$\begin{pmatrix} E \\ q_{\mathrm{L}} \end{pmatrix} = \begin{pmatrix} \gamma & \gamma\beta \\ \gamma\beta & \gamma \end{pmatrix} \begin{pmatrix} E^* \\ q^*_{\mathrm{L}} \end{pmatrix} \tag{F.2}$$

and using Eq. F.1, one can obtain the longitudinal and transverse momentum in the laboratory system as

$$q_{\mathrm{L}} = \gamma\beta E^* + \gamma p^* cos\theta^*, \tag{F.3}$$

$$q_{\mathrm{T}} = q^*_{\mathrm{T}} = p^* sin\theta^*. \tag{F.4}$$

where $\beta = \nu/c$ (ν is the velocity of the mother particle and c is the speed of light), $\gamma = 1/\sqrt{1-\beta^2}$ and E is the energy. Note that transverse momentum is Lorentz invariant. Here, by substituting q_{L} and q_{T} in Eq. 4.5 the α variable takes the form

$$\alpha = \frac{\gamma\beta(E_1^* - E_2^*) + 2\gamma p^* cos\theta^*}{\gamma\beta(E_1^* + E_2^*)}. \tag{F.5}$$

which also can be written as

$$\alpha = \frac{(E_1^* - E_2^*)}{m_M} + \frac{2p^* cos\theta^*}{m_M}, \tag{F.6}$$

using the energy conservation relation; $E^* = \sqrt{p_M^{*2} + m_M^2} = m_M = E_1^* + E_2^*$, where m_M is the mass of the mother particle.

Finally, by defining variables; $a = 2p^*/m_M$ and $b = (E_1^* - E_2^*)/2m_M$ and using the trigonometric relation $cos^2\theta + sin^2\theta = 1$, one obtains an equation of ellipse

$$\left(\frac{\alpha - b}{a}\right)^2 + \left(\frac{q_{\mathrm{T}}}{p^*}\right)^2 = 1 \tag{F.7}$$

which is illustrated in Figure F.2.

Moreover one can express p^* in terms mass by using the relativistic equation;

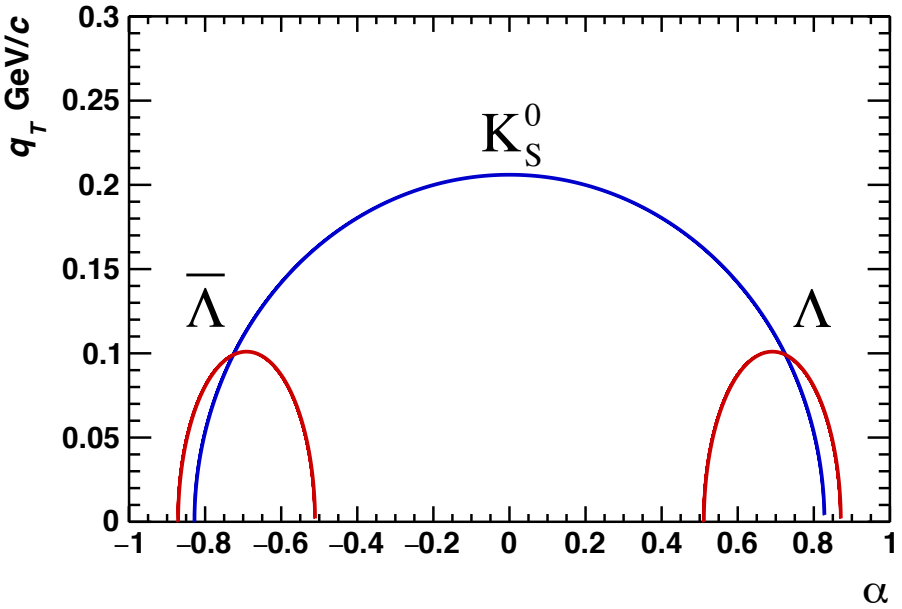

Figure F.2.: The Armenteros-Podolanski plot showing the K^0_S , Λ and $\bar{\Lambda}$ half ellipses.

$$E^2 = p^2 + m^2. \tag{F.8}$$

In the center of mass system the two decay particles of mass, m_1 and m_2 travel with momentum p_1^* and p_2^*. Therefore one can write

$$E_M^{*2} = m_M^2 = (E_1^* + E_2^*)^2 + (\overrightarrow{p_1^*} - \overrightarrow{p_2^*})^2, \tag{F.9}$$

which, using Eq. F.8, gives

$$m_M^2 = m_1^2 + m_2^2 + 2(E_1^* E_2^* - \overrightarrow{p_1^*} \cdot \overrightarrow{p_2^*}). \tag{F.10}$$

Here, Substituting for E_1^* and E_1^* by using Eq. F.8 and rearranging one obtains

$$\left[\frac{(m_M^2 - m_1^2 - m_2^2) + 2\overrightarrow{p_1^*} \cdot \overrightarrow{p_2^*}}{2}\right]^2 = \overrightarrow{p_1^{*2}}\overrightarrow{p_2^{*2}} + m_1^2 m_2^2 + \overrightarrow{p_2^{*2}} m_1^2 + \overrightarrow{p_1^{*2}} m_2^2. \tag{F.11}$$

In the center of mass system the two decay particles come off with equal and opposite momentum so as to conserve momentum, i.e. $\overrightarrow{p_1^*} = \overrightarrow{p^*}$ and $\overrightarrow{p_2^*} = -\overrightarrow{p^*}$. Thereby, one can easily get

$$p^* = \frac{1}{m_M}\sqrt{m_M^4 + m_1^4 + m_2^4 - 2m_M^2 m_1^2 - 2m_M^2 m_2^2 - 2m_1^2 m_2^2}. \tag{F.12}$$

Here, by substituting the known mass values of mother and decay particles one can calculate numerical values of Armenteros Podolanski plot, as listed in Table F.1.

Decay	m_M (GeV/c)	m_1 (GeV/c)	m_2 (GeV/c)	a	b	p^*
$K_S^0 \longrightarrow \pi^+\pi^-$	0.49770	0.13957	0.13957	0.828	0	0.206
$\Lambda \longrightarrow p\pi^+$	1.1156	0.93828	0.13957	0.180	0.691	0.101
$\bar{\Lambda} \longrightarrow \bar{p}\pi^+$	1.1156	0.13957	0.93828	0.180	-0.691	0.101

Table F.1.: Numerical values in the Armenteros-Podolanski plot.

G. Particle Identification in the Central Barrel of ALICE

PID in ITS:

The ITS is the detector closest to the beam pipe (at $r = 3.9\ cm$ in innermost layer). Its main tasks are the precise determination of primary and secondary vertices and also to contribute the ALICE global tracking (See Appendix A). The two innermost layers, SPD detectors, provide high position resolution for the primary and secondary vertex determination, while the outer four layers SDD and SSD provide a measurement of the ionization energy loss $\mathrm{d}E/\mathrm{d}x$ for the particle identification in particular for the small transverse momenta down to $\sim$100 MeV/c.

$\mathrm{d}E/\mathrm{d}x$ is calculated using a truncated mean procedure. For tracks with four

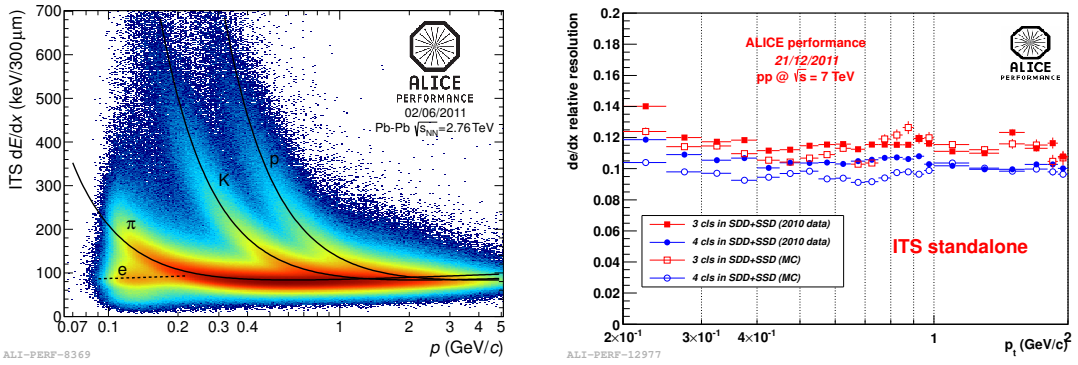

Figure G.1.: (Left) $\mathrm{d}E/\mathrm{d}x$ of charged particles vs their momentum, measured by the ITS alone. The lines are a parametrization of the detector response based on the Bethe-Bloch formula. (Right) ITS standalone $\mathrm{d}E/\mathrm{d}x$ resolution as function of p_{T} for pp at 7 TeV. Monte-Carlo and data are superimposed with different request on SDD+SSD clusters.

hits, the lowest two points are used, however, in case of three hits, the lowest point is used and the second-lowest point is added with weight 1/2. Resolutions of the order of $\sigma_{\mathrm{d}E/\mathrm{d}x} \approx 10 - 12\%$ can be achieved and the resulting $\mathrm{d}E/\mathrm{d}x$ distribution is somewhat asymmetric. Figure G.1 shows the distribution of measured truncated mean energy loss values as a function of momentum for Pb–Pb collisions at 2.76 TeV and ITS standalone $\mathrm{d}E/\mathrm{d}x$ resolution as function of p_{T} for pp collisions at 7 TeV.

PID in TOF:

TPC provides PID in the intermediate momentum range, up to 2.5 GeV/c for pions and kaons, and up to 4 GeV/c for protons, where energy loss measurements are not sufficient enough. The reference time of the event is given by a combination of the the event start time information from the T0 detector, and

the one estimated from the particle arrival times measured by TOF. In Pb–Pb collisions, for the centrality range 0-70% , the overall TOF resolution is ∼83 ps for pions with a momentum around 1 GeV/c. Using the momentum ($p = m\beta\gamma$) information provided by TPC, the mass, thus the identity, of a particle traveling the distance l in time t is calculated by

$$m = p \cdot \sqrt{\frac{t^2}{l^2} - 1}. \tag{G.1}$$

Similarly in TPC, the PID in TOF is based on "$n\sigma$" which is defined as

$$n\sigma = \frac{(t_{\text{hit}} - t_{\text{start}}) - t_{\text{exp}}(p, m, l)}{\sigma_{\text{TOF}}}, \tag{G.2}$$

where t_{hit} is the time measured by TOF, t_{start} is the event start time, $t_{\text{exp}}(p, m, l)$ is the expected time for a given mass hypothesis and $\sigma_{\text{TOF}} = \sqrt{\sigma^2_{\text{intr}} + \sigma^2_{\text{T0}} + \sigma^2_{\text{tracking}}}$ is the proper response function which depends on the intrinsic resolution of the TOF detector, tracking capabilities of ALICE and the resolution of the start time measurement of the event.

Figure G.2 illustrates the performance of the TOF detector by showing the

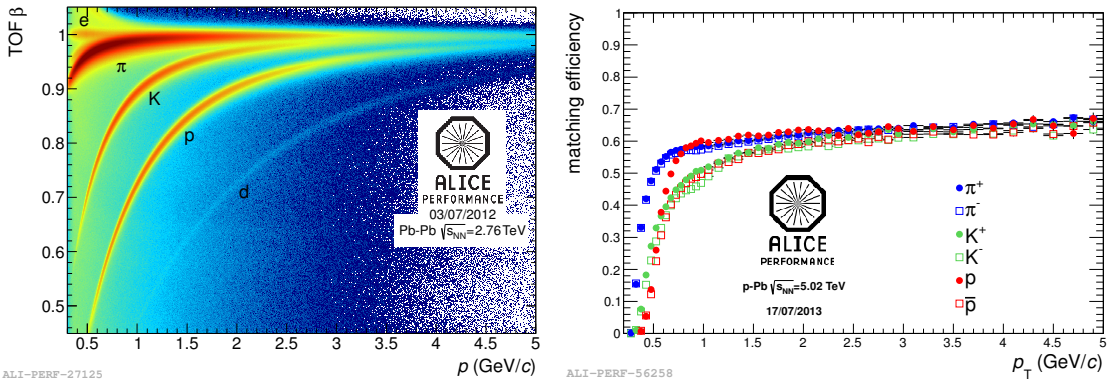

Figure G.2.: (Left) Track velocity β vs p from TOF in Pb–Pb collisions. The bands for e, π, K, p and d are clearly visible. Particles outside of these bands are tracks wrongly associated with a TOF signal. (Right) The efficiency of matching TPC tracks to TOF for pions, kaons and protons in p–Pb collisions.

measured particle velocity β distribution as a function of momentum, where the background is due to tracks that are incorrectly matched to TOF hits. The efficiency of matching TPC tracks to TOF in the 2013 p–Pb is shown in Figure G.2. At $p_{\text{T}} < 0.7$ GeV/c, the matching efficiency is dominated by energy loss and the rigidity cutoff generated by the magnetic field, while at higher p_{T} it reflects the geometrical acceptance (dead space between the sectors of TPC).

PID in TRD:

The TRD, which is composed of six layers consisting of a radiator followed by a drift chamber, provides hadron, light nuclei and electron identification in

the central barrel It allows for electron identification in the momentum region $p > 1$ GeV/c with a pion rejection factor of 100. Furthermore, it is used as L1 trigger for high p_{T} electrons to enhance the statistics of J/ψ and Υ particles and for jets.

The particle identification is based on a combination of specific energy loss and Transition Radiation (TR) . The TR in the form of X-rays is produced when a relativistic charged particle ($\gamma > 800$) traverses many interfaces of two media of different dielectric constants composing the radiator. These photons are then absorbed by the high-Z gas Xe-CO_2 (85-15). The resulting signal is a combination of absorbed TR photons and the specific energy loss dE/dx measurement. Figure G.3 shows the combined TRD signal (dE/dx and TR) as a function of momentum for p–Pb collisions.

The electron identification relies on a 2-dimensional likelihood approach, which makes it possible to distinguish between pions and electrons due to the different shapes of the signals they release in the detector. Figure G.3 shows the performance of two dimensional likelihood method (LQ2D) to identify electrons.

One should also note that, the matching efficiency between TPC tracks and TRD clusters is $\geq 85\%$ for $p_{\mathrm{T}} > 0.8$ GeV/c where the losses are mostly due to chamber boundaries.

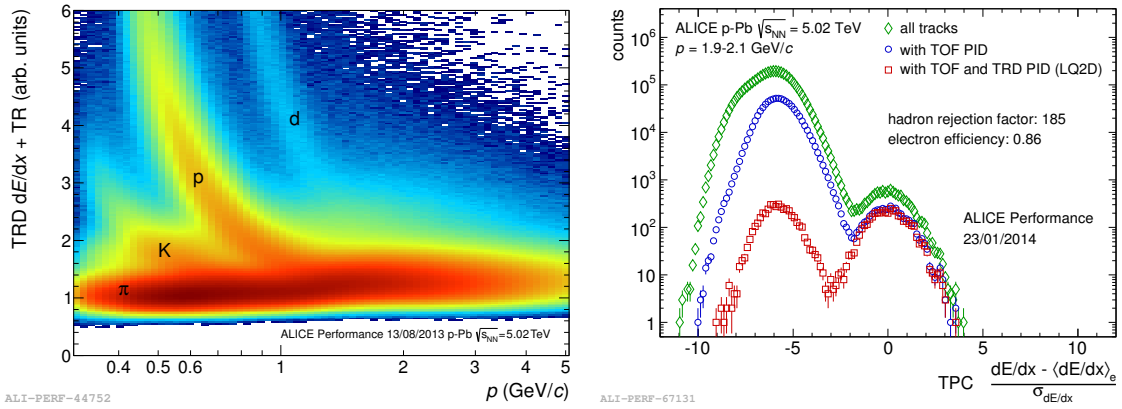

Figure G.3.: (Left) TRD truncated mean signal vs. momentum from minimum bias events in p–Pb collisions. (Right) TPC dE/dx signal relative to the electron Bethe-Bloch line for 2 GeV/c tracks and 6 TRD tracklets without any PID, with TPC PID, with TPC and TRD PID.

Combined Bayesian PID:

Bayesian PID [101] approach in ALICE aims for combining individual PID signals of each detector to take full advantage of the PID capabilities of ALICE. To this end, the independent PID information from TPC, ITS, TRD, TPC, PHOS, EMCal and HMPID are combined to express the measured signals in terms of probabilities.

The most commonly used discriminating variable for PID for a given detector is the n_σ^i variable corresponds to a "true/false" decision on whether a particle belongs to a particle type i ($i = e, \pi, \mu$,K,p). It is defined as the deviation of the measured

signal from that expected, in terms of the detector resolution σ_i:

$$n_\sigma^i = \frac{S_{\text{meas}} - S_{\text{exp}}^i}{\sigma_i}. \tag{G.3}$$

On the other hand, for a given detector with a Gaussian response, it is possible to define the conditional probability that a particle of species i will produce a signal S as

$$P(S|i) = \frac{1}{\sqrt{2\pi}\sigma_i} e^{-\frac{1}{2}(n_\sigma^i)^2}. \tag{G.4}$$

Since the PID information from each detector are independent, these probabilities , P_k (k=ITS,TPC,...), with and without Gaussian responses, can be combined as a product:

$$P(\overrightarrow{S}|i) = \prod_k P_k(S_k|i) \tag{G.5}$$

where $\overrightarrow{S} = (S_{ITS}, S_{TPC}, S_{TRD}, ...)$. However, the variable of interest is the conditional probability that the particle is of species i, given some measured detector signal, i.e. $P(i|\overrightarrow{S})$. It can be expressed using Bayes' theorem:

$$P(i|\overrightarrow{S}) = \frac{P(\overrightarrow{S}|i) \cdot C_i}{\Sigma_{j=e,\pi,\mu,...}(P(\overrightarrow{S}|j) \cdot C_j)}, \tag{G.6}$$

where $C(i)$ is the so-called prior, an *a priori* probability of measuring the particle species i and the conditional probability $P(i|\overrightarrow{S})$ is known as the posterior probability. The priors are used as a weight factor which serve as a "best guess" of the true particle yields per event.

The advantage of combined Bayesian PID is that the efficiency is higher (or equal) and the contamination is lower (or equal) than the ones given by any of the detectors stand-alone. On the other hand, the determined probabilities are very sensitive to eventual imperfections of the calibration.

H. Identity Method Code: "TIdentity Module"

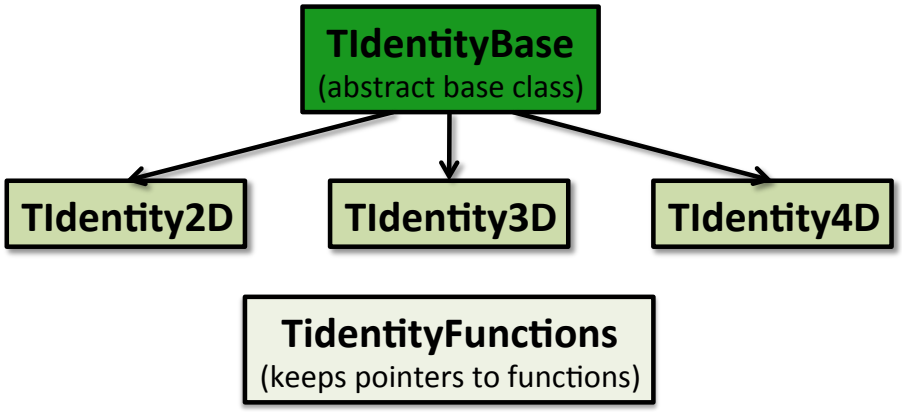

Figure H.1.: Schematic diagram of the Identity Method code.

The Identity Method code is planned to be published soon as "TIdentiy Module". The schematic diagram of the module is given in Figure H.1. The method requires a TTree object, which holds the momentum and pseudorapidity information of tracks, centrality and index of each event and a lookup table of the fit prameters of inclusive $\mathrm{d}E/\mathrm{d}x$ spectra. An example usage, which calculates the $\nu_{\mathrm{dyn}}[\mathrm{K,p}]$, is given below

```
Tidentity2D *iden = new TIdentity2D(4);     // second moments for 4 particles
iden -> SetInputDirectory("inDir");         // input data tree path
iden -> SetOutputDirectory("outDir");       // output directory
iden -> SetInputTree("dataTree");           // lookup table of fit functions
iden -> SetFunctionPointers(getFunctions); // pointer to the function
iden -> Process();                          // calculate the moments
Double_t NpNk = iden -> GetMixedMoments(proton, kaon);
Double_t Np2 = iden -> GetMoments(proton, 2);
Double_t Nk2 = iden -> GetMoments(kaon, 2);
Double_t nuKP = iden -> GetNuDyn(proton, kaon);
```

I. Particle Detection Efficiency in TPC

Single particle detection efficiencies for pions, kaons and protons as a function of pseudorapidity and azimuthal angle and momentum are shown below. Note that, here, only ITS and TPC detectors, with the track and event selection criteria introduced in Section 5.2, are used.

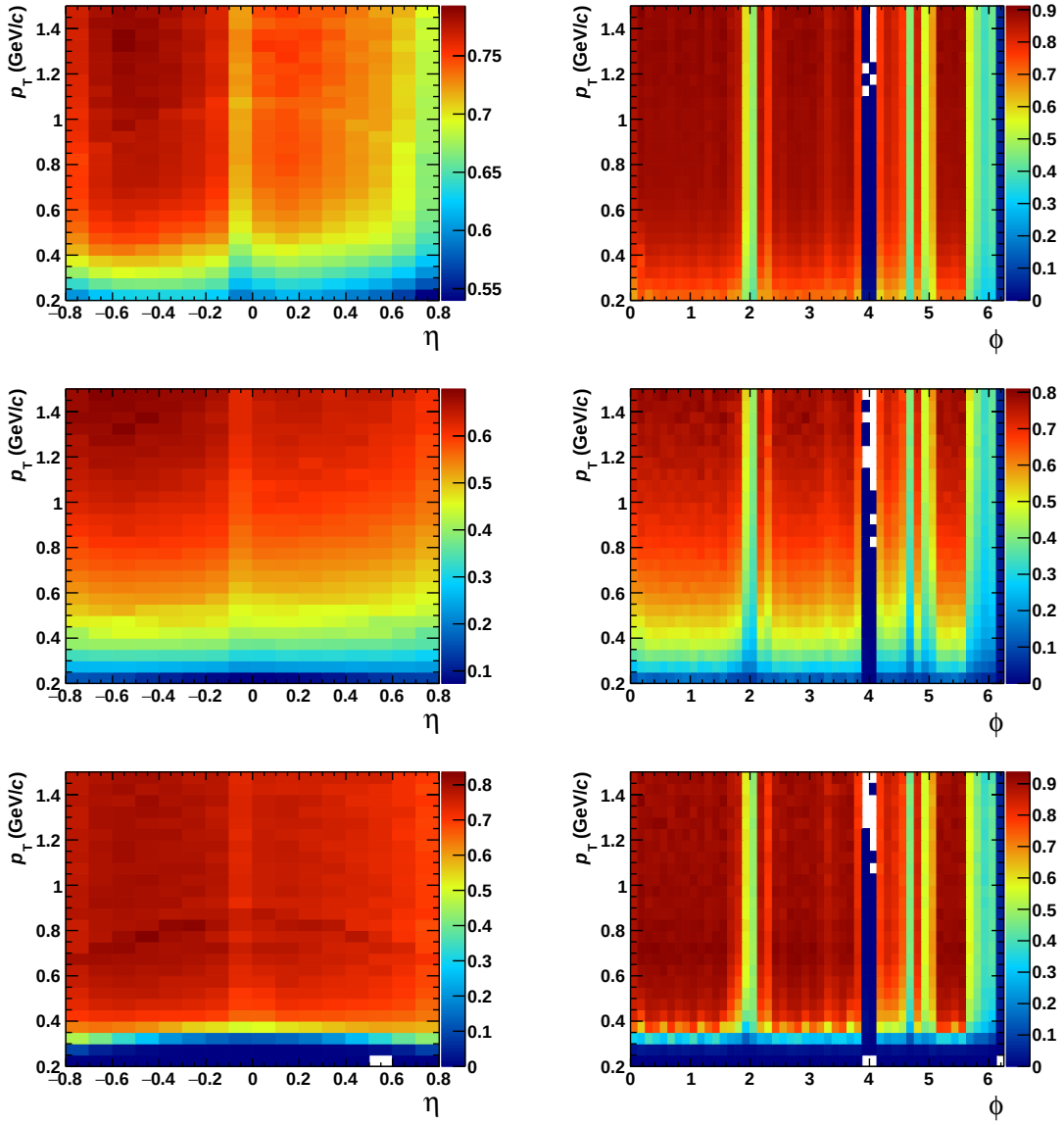

Figure I.1.: Single particle detection efficiencies for pions (first row), kaons (second row) and protons (third row). Efficiencies are shown as a function of transverse momentum vs pseudorapidity (first column) and transverse momentum vs azimuthal angle (second column).

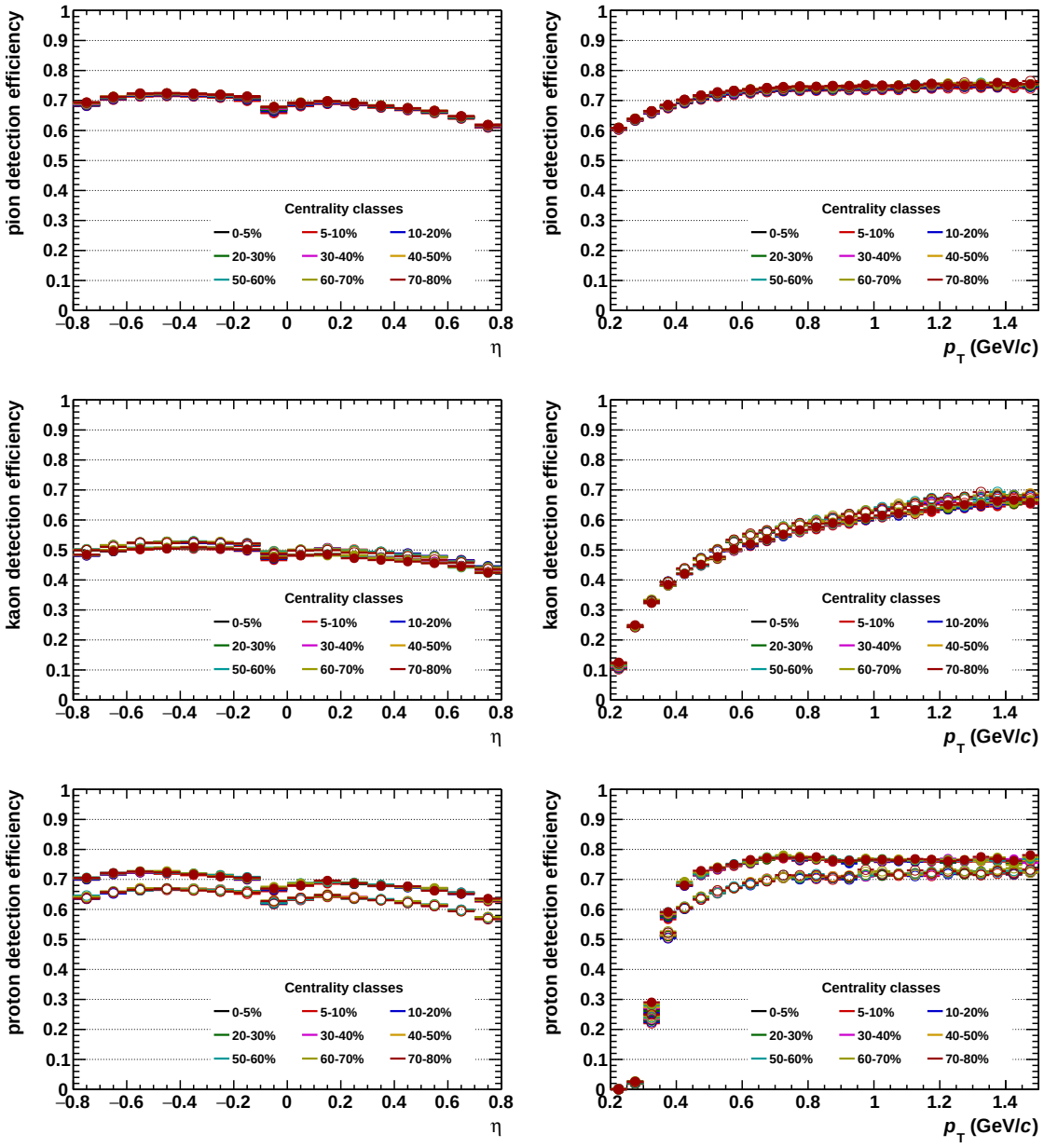

Figure I.2.: (Color Online) Single particle detection efficiencies for pions (first row), kaons (second row) and protons (third row). Efficiencies are shown as integrated over momentum (first column) and pseudorapidity (second column). Different colors show different centrality classes. Negative and positive particles are shown with open and closed circles, respectively. (Negative particles are corrected for the absorption due to interaction with the material in the detector[81].)

List of Figures

List of Tables

Glossary

$\boldsymbol{N}_{\mathrm{part}}$ The number of participants, i.e. the number of nucleons that undergo at least one collision, or in terms of the number of binary collisions among nucleons from the two nuclei (N_{coll}). vii, 104, 109–112, 114, 118

$\boldsymbol{Q}_{\mathrm{max}}$ Maximum value among all digits in a TPC cluster. 33, 36

$\boldsymbol{Q}_{\mathrm{seg}}$ Total charge on a given anode wire segment. 64

$\boldsymbol{Q}_{\mathrm{tot}}$ Sum of all digits in a TPC cluster. 33, 36

$\boldsymbol{S}_{i,j}$ Separation power between particle types i and j. 36

$\boldsymbol{T}_{\mathrm{c}}$ Critical temperature. iii, 4

$\boldsymbol{V}^0$ A name given to a neutral particle which decays into two charged tracks. 72, 77, 80, 81, 117, 123, 135

$\boldsymbol{\alpha}_{\mathrm{CM}}$ Fetch factor for the Common-mode correction which stands for the missing charge due to threshold effects. 60

$\mathbf{d}\boldsymbol{E}/\mathbf{d}\boldsymbol{x}$ specific energy loss. i, ii, 10–13, 15, 16, 19, 28, 30, 34–38, 41–43, 56, 61, 62, 64, 65, 68, 71–78, 80–82, 84–88, 90–92, 94–97, 100, 117, 139, 141, 143

$\mathbf{d}\boldsymbol{N}_{\mathbf{ch}}/\mathbf{d}\boldsymbol{\eta}$ number of charged particles per unit rapidity at mid-rapidity. 17, 23, 104, 109–112, 114, 115, 118

$\boldsymbol{\eta}$ Pseudo-rapidity. 81, 84, 113, 114

$\boldsymbol{\mu}_{\mathrm{B}}$ Baryochemical potential. 3, 7

$\boldsymbol{\nu}_{\mathrm{dyn}}$ Dynamical event-by-event fluctuations of the particle composition. i, 8–10, 12, 91, 92, 96–101, 103, 104, 106–115, 118

$\boldsymbol{p}_{\mathbf{T}}$ Transverse momentum. iv, v, 8, 9, 17, 35, 38, 43, 93, 115, 139–141

$\boldsymbol{n}_{\mathrm{PID}}$ Number of TPC clusters used for the PID calculation. 37

Aliroot ALICE offline framework. 63, 64, 66, 68, 81, 82, 86, 117, 123

ROOT An object-oriented C++ based program and library developed by CERN, which is currently being used in all major High Energy and Nuclear Physics laboratories around the world to monitor, to store and to analyze data. In the other sciences as well as the medical and financial industries, many people are using ROOT.. 47, 123

Acronyms

ACORDE ALICE COsmic Ray DEtector. 20

ACR ALICE Control Room. 121

ADC Analogue-Digital-Converter. 26, 45, 47, 58, 61, 69, 123

ALEPH Apparatus for LEP PHysics. 72, 73

ALICE A Large Ion Collider Experiment. i, ii, 9, 10, 17–21, 23, 24, 27, 29, 30, 34, 37, 38, 49, 50, 57, 63, 71, 72, 81, 91, 94, 96, 103–105, 109–114, 117, 121–123, 125, 131, 139–141

ALTRO Alice TPC Readout Chips. 25, 26

AMPT A Multi-Phase Transport Model. ii, 63, 92, 103–105, 109–111, 114, 115, 118

ARM originally Acorn RISC Machine, later Advanced RISC Machine. 27

BR Branching Ratio. 90

CE Central Electrode. 23, 24, 30, 132

CERN Conseil Européen pour la Recherche Nucléaire. i, 103, 118

CRU Common Reaout Unit. 70

CTP Central Trigger Processor. 27, 121, 122

D-RORC DAQ Read-out Receiver Card. 122

DAQ Data Acquisition. 26, 121, 122

DCA Distance-of-Closest Approach. 38, 92

DCS Detector Control System. 26, 27, 30, 121

DDL Detector Data Link. 26, 122

ECS Experiment Control System. 121

EM Electro-Magnetic. 92

EMCal ElectroMagnetic Calorimeter. 19, 71, 123, 141

ESD Event Summary Data. 123

FEC Front-end Card. 25, 26, 57

FEE Front-end Electronics. 25–27, 45, 121

FFT Fast Fourier Transform. 47, 49

FMD Forward Multiplicity Detector. 20

FWHM Full Width at Half Maximum. 25

GDC Global Data Collector. 122

GEANT GEometry ANd Tracking. 37, 42, 63, 81, 96

GEM Gas Electron Multiplier. 67

HIJING Heavy Ion Jet INteraction Generator. ii, 37, 42, 63–65, 68, 91, 92, 96, 103–105, 109–115, 118

HLT High-Level Trigger. 121, 122

HMPID High-Momentum Particle Identification Detector. 19, 71, 123, 141

HSD Hadron-String Dynamics. 9

HV High Voltage. 28

IP Interaction Point. 125

IROC Inner Read-Out Chamber. 24, 26, 35, 37, 46, 47, 49–52, 56–58, 70

ITS Inner Tracking System. 9, 17, 19, 21, 35, 38, 40, 71, 91–93, 113, 122, 123, 125, 139, 141, 142

L0 Level-0. 20, 27, 121

L1 Level-1. 27, 121, 141

L2 Level-2. 20, 27, 121, 122

LDC Local Data Concentrator. 122

LHC Large Hadron Collider. i, 5, 6, 9, 28, 67, 68, 91, 117, 121, 125

LTU Local Trigger Unit. 122

MAF Moving Average Filter. 59

MB Minimum Bias. 92

MC Monte-Carlo. 16, 63, 74–77, 81–87, 91, 96, 97, 99, 108, 117, 118

MIP Minimum-Ionizing Particle. 36, 38, 41

MRPC Multi-gap Resistive-Plate Chambers. 19

MWPC Multi-wire Proportional Chambers. 50, 52

NBD Negative Binomial Distribution. 93, 94

neBEM nearly exact Boundary Element Method. 52

OCDB Offline Calibration Data Base. 33, 46, 54, 64

OROC Outer Read-Out Chamber. 24, 26, 35, 37, 46, 47, 50, 51, 56, 58

PASA Pre-Amplifier and Shaper Chips. 25, 26, 57

PDS Permanent Data Storage. 122

PHOS PHOton Spectrometer. 19, 123, 141

PID Particle Identification. i, ii, 9, 10, 19, 37, 38, 56, 71, 73, 77, 80, 87, 117, 118, 139–142

PMD Photon Multiplicity Detector. 20

PRF Pad Response Function. 37, 52

QA Quality Assurance. 38

QCD Quantum Chromodynamics. 1–6, 17, 112

QGP Quark-Gluon Plasma. 3–5, 17

RCU Read-out Control Unit. 25–27

RHIC Relativistic Heavy Ion Collider. 9, 103, 118, 131

RICH Ring Imaging Cherenkov. 19

RMS Root Mean Square. 58

ROC Read-Out Chamber. 24, 25, 28, 30, 132

RPCs Resistive-Plate Chambers. 20

SDD Silicon Drift Detector. 19, 139

SPD Silicon Pixel Detector. 17, 92, 139

SPS Super Proton Synchrotron. 8, 103, 118

SQS Self-Quenching Streamer. 28

SSD Silicon Strip Detector. 19, 139

STAR Solenoidal Tracker at RHIC. 9, 10, 109–113, 131

T0 Time 0. 20, 139

TDR Technical Design Report. 59

TOF Time-Of-Flight. 9, 19–21, 24, 71, 78, 80, 84, 90, 115, 123, 140

TPC Time Projection Chamber. i, ii, 9, 10, 16, 19, 21, 23–35, 37, 38, 40, 42, 43, 45–50, 52–54, 56, 57, 59–63, 66, 71–77, 81, 84, 91–93, 113, 117, 118, 121–123, 125, 129, 131–133, 139–142

TR Transition Radiation. 141

TRD Transition Radiation Detector. 19–21, 24, 71, 78, 80, 123, 140, 141

TRF Time Response Function. 62, 64

TRG Trigger System. 121

TTC Timing, Trigger and Control. 121, 122

UrQMD Ultrarelativistic Quantum Molecular Dynamics. 9

UV Ultra-Violet. 29, 32, 129

V0 Vertex 0. 20, 91–94, 113

ZDC Zero Degree Calorimeter. 19

ZPC Zhang's Parton Cascade. 104

References

[1] L. P. Csernai. *Introduction to Relativistic Heavy Ion Collisions*. John Wiley and Sons Ltd, 1994.

[2] D. H. Perkins. *Introduction to High Energy Physics*. Cambridge University Press, 2000.

[3] S. Bethke. "Observation of a new boson at a mass of 125 GeV with the CMS experiment at the LHC". In: *Phys. Lett. B* (2012). DOI: doi:10.1016/j.physletb.2012.08.021.

[4] "Review of Particle Physics, Particle Data Group". In: (2014). DOI: DOI:10.1088/1674-1137/38/9/090001.

[5] P. Aurenche. *The standard model of particle physics*. 1997. arXiv: hep-ph/9712342.

[6] Murray Gell-Mann. "A Schematic Model of Baryons and Mesons". In: *Phys. Lett.* 8 (1964), pp. 214–215. DOI: 10.1016/S0031-9163(64)92001-3.

[7] D. Griffiths. *Introduction to Elementary Particles*. John Wiley and Sons, Inc., 1987.

[8] David J. Gross. "Twenty five years of asymptotic freedom". In: *Nucl. Phys. Proc. Suppl.* 74 (1999), pp. 426–446. DOI: 10.1016/S0920-5632(99)00208-X. arXiv: hep-th/9809060.

[9] A. Bazavov et al. "The chiral and deconfinement aspects of the QCD transition". In: *Phys. Rev. D* 85 (2012), p. 054503.

[10] Ulrich W. Heinz. "The little bang: Searching for quark-gluon matter in relativistic heavy-ion collisions". In: *Nucl. Phys.* A685 (2001), pp. 414–431. DOI: 10.1016/S0375-9474(01)00558-9. arXiv: hep-ph/0009170.

[11] Ulrich W. Heinz. *Concepts of heavy-ion physics*. 2004. arXiv: hep-ph/0407360.

[12] D. Antonczyk. "Detailed Analysis of Two Particle Correlations in Central Pb-Au Collisions at 158 GeV per Nucleon". PhD thesis. Technische Universität, Darmstadt, 2006. URL: https://edms.cern.ch/document/316077/1.

[13] P. Giubellino. "The ALICE detector at LHC". In: *Nucl. Instr. Meth. A* 344 (1994), pp. 27–38.

[14] S. Jeon and V. Koch. "Event-by-Event Fluctuations". In: *arXiv:hep-ph/0304012* (2003).

[15] M. Stephanov, K. Rajagopal, and E. Shuryak. "Event-by-Event Fluctuations in Heavy Ion Collisions and the QCD Critical Point". In: *Phys. Rev. D* 60 (1999), p. 114028.

[16] M. Stephanov, K. Rajagopal, and E. Shuryak. "Signatures of the Tricritical Point in QCD". In: *Phys. Rev. Lett.* 81 (1998), p. 4816.

[17] S. Sarkar, H. Satz, and B. Sinha. *The Physics of the Quark-Gluon Plasma, Introductory Lectures*. Springer Verlag, 2010. DOI: 10.1007/978-3-642-02286-9.

[18] B Schaefer, J. Pawlowski, and J. Wambach. "The Phase Structure of the Polyakov–Quark-Meson Model". In: *Phys. Rev. D* 76 (2007), p. 074023.

[19] B. Friman et al. "Fluctuations as probe of the QCD phase transition and freeze-out in heavy ion collisions at LHC and RHIC". In: *arXiv:1103.3511* (2011).

[20] P. Braun-Munzinger, A. Rustamov, and J. Stachel. "Bridging the gap between event-by-event fluctuation measurements and theory predictions in relativistic nuclear collisions". In: *Nuclear Physics A* 960 (2017), pp. 114–130.

[21] M. Gaździcki and S. Mrowczynski. "A Method to study 'equilibration' in nucleus-nucleus collisions". In: *Z. Phys.* C54 (1992).

[22] H. Heiselberg. "Event-by-event physics in relativistic heavy ion collisions". In: *Phys. Rept.* 351 (2001), p. 161.

[23] M. I. Gorenstein and M. Gaździcki. "Strongly Intensive Quantities". In: *Phys. Rev. C* 84 (2011), p. 014904.

[24] NA49 Collaboration. "Energy dependence of particle ratio fluctuations in central Pb+Pb collisions from $\sqrt{s_{\mathrm{NN}}} = 6.3$ to 17.3 GeV". In: *Phys. Rev. C* 79 (2009), p. 044910.

[25] STAR Collaboration. "Energy dependence of Kπ, pπ, and Kp fluctuations in Au–Au collisions from $\sqrt{s_{\mathrm{NN}}} = 7.7$ to 200 GeV". In: *Phys. Rev. C* 92 (2015), p. 021901.

[26] C. Pruneau, S. Gavin, and S. Voloshin. "Methods for the study of particle production fluctuations". In: *Phys. Rev. C* 66 (2002), p. 044904.

[27] Koch V. and Schuster T. "Energy dependence of K/π fluctuations in relativistic heavy-ion collisions". In: *Phys. Rev. C* 81 (2010), p. 034910.

[28] NA49 Collaboration. "Phase-space dependence of particle-ratio fluctuations in Pb–Pb collisions from 20A to 158A GeV beam energy". In: *Phys. Rev. C* 89 (2014), p. 054902.

[29] E. L. Bratkovskaya et al. "Fluctuations of the K/π ratio in nucleus-nucleus collisions: Statistical and transport models". In: *Phys. Rev. C* 79 (2009), p. 024907.

[30] M. Bleicher et al. "Relativistic hadron-hadron collisions in the ultra-relativistic quantum molecular dynamics model". In: *J. Phys. G* 25 (1999), p. 1859.

[31] M. Gaździcki et al. "Identity method to study chemical fluctuations in relativistic heavy-ion collisions". In: *Phys. Rev. C* 83 (2011), p. 054907.

[32] M. I. Gorenstein. "Identity method for particle number fluctuations and correlations". In: *Phys. Rev. C* 84 (2011), p. 024902.

[33] A. Rustamov and M. I. Gorenstein. "Identity method for the determination of the moments of multiplicity distributions". In: *Phys. Rev. C* 86 (2012), p. 044906.

[34] A. Rustamov and M. I. Gorenstein. "Identity method for the determination of the moments of multiplicity distributions". In: *Phy. Rev. C 86, 044906* (2012). DOI: 10.1103/PhysRevC.86.044906.

[35] ALICE Collaboration. "ALICE: Physics Performance Report, Volume I". In: *J. Phys.* G30 (2004), pp. 1517–1763. DOI: 10.1088/0954-3899/30/11/001.

[36] P. Kuijer. "The Alice experiment at the CERN LHC". In: *Nuclear Physics B* 117 (2003), pp. 62–64.

[37] E. Vercellin. “The ALICE experiment at the LHC”. In: *Nuclear Physics A* 805 (2008), p. 511.

[38] CMS Collaboration. “Evidence for collectivity in pp collisions at the LHC”. In: *Phys. Lett. B* 765 (2017), pp. 193–220.

[39] ALICE Collaboration. *Technical Design Report of the Inner Tracking System*. German. CERN/LHCC 99-12. 1999. URL: https://edms.cern.ch/document/398932/1.

[40] ALICE Collaboration. *Technical Design Report of the Time Projection Chamber*. CERN/LHCC 2000-001. 2000. URL: https://edms.cern.ch/document/398930/1.

[41] ALICE Collaboration. *Technical Design Report of the Transition Radiation Detector*. German. CERN/LHCC 2001-021. 2001. URL: https://edms.cern.ch/document/398057/1.

[42] ALICE Collaboration. *Technical Design Report of the Time of Flight System*. German. CERN/LHCC 2000-012. 2000.

[43] ALICE Collaboration. *Technical Design Report of the High Momentum Paricle Identificatino Detector*. German. CERN/LHCC 98-19. 1998.

[44] ALICE Collaboration. *The Electromagnetic Calorimeter Addendum to the Technical Proposal*. CERN-LHCC-2006-014. 2006. URL: http://aliceinfo.cern.ch/Collaboration/Documents/EMCal.html.

[45] ALICE Collaboration. *Technical Design Report of the Photon Spectrometer*. German. CERN/LHCC 99-4. 1999. URL: https://edms.cern.ch/document/398934/1.

[46] ALICE Collaboration. *Technical Design Report of the Zero Degree Calorimeter (ZDC)*. CERN/LHCC 99-5. 1999. URL: https://edms.cern.ch/document/398933/1.

[47] ALICE Collaboration. *Technical Design Report of the Photon Multiplicity Detector (PMD)*. CERN/LHCC 99-32. 1999. URL: https://edms.cern.ch/document/398931/1.

[48] ALICE Collaboration. *Technical Design Report on Forward Detectors: FMD, T0, V0*. CERN-LHCC-2004-025. 2004. URL: https://edms.cern.ch/document/498253/1.

[49] ALICE Collaboration. “Study of cosmic ray events with high muon multiplicity using the ALICE detector at the CERN Large Hadron Collider”. In: *JCAP* 01 (2016), p. 032. DOI: 10.1088/1475-7516/2016/01/032.

[50] ALICE TPC Collaboration. “The ALICE TPC, a large 3-dimensional tracking device with fast readout for ultra-high multiplicity events”. In: *Nucl. Instr. Meth. A* 622 (2010), p. 316.

[51] L. Musa. “The Time Projection Chamber for the ALICE experiment”. In: *Nuclear Physics A* 715 (2003), pp. 843c–848c.

[52] C. Garabatos. “The ALICE TPC”. In: *Nucl. Instr. Meth. A* 535 (2004), p. 197. DOI: 10.1016/j.nima.2004.07.127.

[53] C. Lippmann and D. Vranić. *Alice TPC Numbering Conventions*. URL: http://lippmann.web.cern.ch/lippmann/TPC/num.pdf.

[54] L. Musa et al. "The ALICE TPC front end electronics". In: *IEEE Nuclear Science Symposium*. Vol. 5. 2003, pp. 3647–3651. DOI: 10.1109/NSSMIC.2003.1352697.

[55] ALICE Collaboration. "The ALICE experiment at the CERN LHC". In: *JINST* 3 (2008), S08002. DOI: 10.1088/1748-0221/3/08/S08002.

[56] R. Veenhof. "Choosing a gas mixture for the ALICE TPC". In: *ALICE-INT-2003-29* (2003). URL: https://edms.cern.ch/document/470838/1.

[57] Y. Kalkan, M. Arslandok, R. Veenhof, et al. "Cluster ions in gas-based detectors". In: *JINST 10 P07004* (2015). DOI: 10.1088/1748-0221/10/07/P07004.

[58] N. A. Kalinina et al. "Investigation of Self-Quenching Streamer Discharge in a Wire Chamber". In: *Nucl. Instr. Meth.* 177 (1980), pp. 385–397.

[59] G. Renault et al. *The laser of the ALICE time projection chamber*. 2007. arXiv: nucl-ex/0703042.

[60] B.S. Nielsen et al. *Design Note on the ALICE TPC laser calibration system*. ALICE-INT-2002-022. INT. ALICE-INT-2002-022, 2002. URL: https://edms.cern.ch/document/350420/1.

[61] D. Vranić. private communication.

[62] A. Dainese and N. Carrer. "A parameterization of the Kalman filter track reconstruction in the ALICE TPC". In: *ALICE-INT-2003-011* (2003).

[63] Y. Belikov et al. "TPC tracking and particle identification in high-density environment". In: *arXiv:physics/0306108* (2003).

[64] W. Blum and L. Rolandi. *Particle Detection with Drift Chambers*. German. Springer-Verlag, 1994.

[65] Hans Bichsel. "A method to improve tracking and particle identification in TPCs and silicon detectors". In: (2006).

[66] Alexander Philipp Kalweit. "Production of Light Flavor Hadrons and Anti-nuclei at the LHC". PhD thesis. Technische Universität, Darmstadt, 2012.

[67] ALICE Collaboration. "Performance of the ALICE experiment at the CERN LHC". In: *International Journal of Modern Physics A* 29 (2014), p. 1430044. DOI: 10.1142/S0217751X14300440.

[68] *ROOT Data Analysis Framework*. URL: https://root.cern.ch/.

[69] S. Rossegger and W. Riegler. "Signal shapes in a TPC wire chamber". In: *Nucl. Instr. Meth. A* 623 (2010), pp. 927–930.

[70] Stefan Rossegger. "Simulation and Calibration of the ALICE TPC Including Innovative Space Charge Calculations". PhD thesis. CERN-THESIS-2009-124, 2009.

[71] R. Renfordt. private communication.

[72] *Quality Assurance (QA) for tthe ALICE-TPC*. URL: http://aliqatpc.web.cern.ch/aliqatpc/data/.

[73] *Garfield - simulation of gaseous detectors*. URL: http://garfield.web.cern.ch/garfield/.

[74] "A nearly exact Boundary Element Method (neBEM)". In: (). URL: http://nebem.web.cern.ch/nebem/.

[75] Christof Roland. “Flavor Fluctuations in Central Pb–Pb Collisions at 158 GeV/Nucleon”. PhD thesis. Johann Wolfgang Goethe-Universität, Frankfurt am Main, 1999.

[76] B. Mota et al. “Performance of the ALTRO chip on data acquired on an ALICE TPC prototype”. In: *Nucl. Instruments and Methods in Physics Research A* (2004). DOI: 10.1016/j.nima.2004.07.179.

[77] *Detector Description and Simulation Tool*. URL: http://cds.cern.ch/record/1082634.

[78] ALICE Collaboration. *Upgrade of the ALICE Time Projection Chamber*. CERN-LHCC-2013-020. 2014. URL: http://cds.cern.ch/record/1622286/files/.

[79] P.G. Kuijer for the ALICE collaboration. “Commissioning and Prospects for Early Physics with ALICE”. In: (2009). DOI: doi:10.1016/j.nuclphysa.2009.10.011.

[80] ALICE Collaboration. “Centrality determination of Pb–Pb collisions at $\sqrt{s_{\mathrm{NN}}}$ =2.76 TeV with ALICE”. In: *Phys. Rev. C 88 044909* (2013).

[81] “Centrality dependence of π, K, and p production in Pb–Pb collisions at $\sqrt{s_{\mathrm{NN}}} = 2.76$ TeV”. In: *Phys. Rev. C* 88 (2013), p. 044910.

[82] A. Rustamov. private communication.

[83] M. Gyulassy and X. N. Wang. “HIJING 1.0: A Monte Carlo program for parton and particle production in high energy hadronic and nuclear collisions”. In: *Comput. Phys. Commun.* 83 (1994), p. 307.

[84] W.-T. Deng, X.-N. Wang, and R. Xu. “Hadron production in p+p, p+Pb, and Pb+Pb collisions with the hijing 2.0 model at energies available at the CERN Large Hadron Collider”. In: *Phys. Rev. C* 83 (2011), p. 014915.

[85] Z.-W. Lin et al. “Multiphase transport model for relativistic heavy ion collisions”. In: *Phys. Rev. C* 72 (2005), p. 064901.

[86] A. Bialas, M. Bleszynski, and W. Czyz. “Multiplicity Distributions in Nucleus-Nucleus Collisions at High Energies”. In: *Nuclear Physics B* 111 (1976), p. 461.

[87] M. Gaździcki, M. I. Gorenstein, and M. Mackowiak-Pawlowska. “Normalization of Strongly Intensive Quantities”. In: *Phys. Rev. C* 88 (2013), p. 024907.

[88] M. Gaździcki and M. I. Gorenstein. “Strongly Intensive Quantities”. In: *Phys. Rev. C* 84 (2011), p. 014904.

[89] STAR Collaboration. “K/π Fluctuations at Relativistic Energies”. In: *PRL 103, 092301* (2009).

[90] STAR Collaboration. “K/π Fluctuations at Relativistic Energies”. In: *PRL* 103 (2009), p. 092301.

[91] STAR Collaboration. “Systematic Measurements of Identified Particle Spectra in pp, d+Au and Au+Au Collisions from STAR”. In: *Phys. Rev. C* 79 (2009), p. 034909.

[92] M.I. Gorenstein et al. “Fluctuations of the K/π ratio in nucleus-nucleus nollisions: Statistical and Transport Models”. In: *Phys. Rev. C* 79 (2009), p. 024907.

[93] ALICE Collaboration. *ALICE Technical Design Report of the Computing*. CERN-LHCC-2005. 2005.

[94] V. Lindenstruth, C. Loizides, D. Rohrich, et al. "Real-time TPC analysis with the ALICE High-Level Trigger". In: *Nucl. Instr. Meth. A* 534 (2004), pp. 47–52. DOI: 10.1016/j.nima.2004.07.057.

[95] *ALICE Offline Bible*. http://aliweb.cern.ch/Offline/AliRoot/Manual.html.

[96] L. Betev and P. Chochula. "Definition of the ALICE Coordinate System and Basic Rules for Sub-detector Components Numbering". In: *ALICE-INT-2003-038* (2003).

[97] Jens Wiechula. "Commissioning and Calibration of the ALICE-TPC". PhD thesis. Johann Wolfgang Goethe-Universität, Frankfurt am Main, 2008.

[98] H. J. Hilke. "Detector calibration with lasers – A review". In: *Nucl. Instr. Meth. A* 252 (Dec. 1986), pp. 169–179. DOI: 10.1016/0168-9002(86)91177-0.

[99] A. Lebedev. "A laser calibration system for the STAR TPC". In: *Nucl. Instr. Meth. A* 478 (2002), pp. 163–165.

[100] J. Podolanski and R. Armenteros. In: *Phil. Mag. 45* 13 (1954).

[101] ALICE Collaboration. "Particle identification in ALICE: a Bayesian approach". In: *Eur. Phys. J. Plus 131* (2016), p. 168.

Acknowledgements

This work would have not been possible without the support of many people to whom I would like to express my gratitude. First of all, I would like to thank Prof. Dr. Harald Appelshäuser and Prof. Dr. Cristoph Blume for giving me the opportunity to perform my research in this fascinating experiment. I consider myself extremely lucky to have worked with Harald. He is an excellent supervisor. His support in every kind of issue as well as guidance in both TPC project and physics analysis have been priceless. I would also like to thank Prof. Dr. Marcus Bleicher for the fruitfull discussions in regarding of the theoretical aspects.

In particular, I am heartily thankful to my supervising tutor Marian Ivanov, whose supervision in the TPC project from the preliminary to the concluding level enabled me to develop an understanding of the TPC detector and also to improve my programming skills which then helped me a lot in the physics analysis. Without his guidance I could not have imagined to get to this point.

My gratitude to all the people in the TPC group at CERN: Christian Lippmann, Chilo Garabatos, Danilo Vranic and Thomas Morhardt. Throughout the two years period I spent at CERN, I have gained deep insight into the TPC; thanks in particular to Christian Lippmann and Chilo Garabatos. It was a wonderful experience to work with them. Likewise, many thanks to Rob Veenhof for introducing me to the Garfield simulations. I also appreciate the discussions with him about the detector physics and many other aspects, where his guidance, full of wisdom, has been invaluable. I would also like to thank Kai Schweda, who has been the TPC offline project coordinator, for his constant support and motivating positive spirit.

Many thanks to the members of the ALICE group at the Institut für Kernphysik in Frankfurt. It has been a very friendly and supportive atmosphere to work in. I especially owe my deepest gratitude to Rainer Renfordt and Jens Wiechula for their constant help in countless aspects. Moreover, I owe special thanks to Benjamin Dönigus for his constant help in particular during the physics analysis.

Further special thanks to Anar Rustamov. I greatly appreciate not only for the physics discussions but also the guidance, support and in particular invaluable friendship. Likewise many thanks to my student colleagues Mahmut and Irem Ozdemir, together with Anar Rustamov and Rainer Renfordt, they have been like a family to me in Germany.

Lastly, I would like to thank Rainer Renfordt, Anar Rustamov, Benjamin Dönigus, Kai Schweda and Chilo Garabatos for proofreading the thesis, and Markus Köhler, Yvonne Pachmayer, Luisa Bermann and, once again, Rainer Renfordt for helping me writing the German summary of the thesis.

Curriculum Vitae

Mesut Arslandok

PERSONAL DATA

Address:	Hasenhain 10, 69221 Dossenheim, Germany
Nationality:	Turkish
Date of birth:	10.11.1983
Place of birth:	Kayseri/Turkey

EDUCATION

Ph.D. in Physics 2011-2017
Institut für Kernphysik (IKF), Goethe University, Frankfurt, Germany

M.Sc. in Physics 2009-2011
Goethe University, Frankfurt, Germany

M.Sc. study in Physics 2008-2009
Boğaziçi University, Istanbul, Turkey

B.Sc. in Mathematics with minors in Physics 2003-2008
Yıldız Technical University (YTU), Istanbul, Turkey

High School 1996-2002
Sema Yazar Anatolian High School, Kayseri, Turkey

AWARDS

Best Poster Award 2015
XXV International Conference on Ultrarelativistic Nucleus-Nucleus Collisions, Kobe, Japan

Giersch-Excellence-Award 2015
Stiftung Giersch and Helmholtz Graduate School for Hadron and Ion Research, Frankfurt, Germany

Turkish Education Foundation Honor Award 2008
Istanbul, Turkey

Highest ranked student of the year in the Faculty of Arts and Science 2008
B.Sc. in Physics (GPA: 3.84/4.0), Yıldız Technical University, Istanbul, Turkey

Highest ranked student of the year in the Faculty of Arts and Science 2007
B.Sc. in Mathematics (GPA: 3.86/4.0), Yıldız Technical University, Istanbul, Turkey

RESEARCH

Publications

- M. Arslandok (for the ALICE collaboration) **"Event-by-event identified particle ratio fluctuations in Pb–Pb collisions with ALICE using the Identity Method", Proceedings of Quark Matter 2015**
  Nucl.Phys. A956, 870-873 (2016)
- Y. Kalkan, M. Arslandok, R. Veenhof et al. **"Cluster ions in gas-based detectors"**
  JINST 10 P07004 (2015)
- 153 publications by ALICE. A comprehensive list can be found at:
  https://inspirebeta.net/author/profile/M.Arslandok.1

Conference and Seminar Presentations

- **"Event-by-event fluctuation analyses in view of the ALICE TPC upgrade"**
  XII Workshop on Particle Correlations and Femtoscopy, Nikhef, Amsterdam, Netherlands, June 16, 2017
- **"Centrality and pseudorapidity dependence of identified-particle ratio fluctuations in Pb–Pb collisions in ALICE"**
  Spring Meeting of Deutsche Physikalische Gesellschaft (DPG), Münster, Germany, March 31, 2017
- **"Event-by-event dynamical fluctuations of K/π, p/π and K/p in Pb–Pb collisions with ALICE"**
  XI Workshop on Particle Correlations and Femtoscopy (WPCF), Warsaw, Poland, November 4, 2015
- **"Event-by-Event identified particle ratio fluctuations in Pb–Pb collisions with ALICE using the Identity Method (Best poster award, Flash talk)"**
  XXV International Conference on Ultra-relativistic Nucleus-Nucleus Collisions, (Quark Matter 2015), Kobe, Japan, October 3, 2015
- **"Event-by-event fluctuations measured with ALICE at the LHC"**
  The 31st Winter Workshop on Nuclear Dynamics (WWND), Colorado, USA, January 28, 2015
- **"Ion-tail and Common-mode effect corrections for the ALICE TPC"**
  RD51 Collaboration Meeting, CERN, Geneva, Switzerland, December 10, 2014
- **"Signal shapes in the ALICE TPC"**
  International Workshop on Advanced Detectors (IWAD) and RD51 Collaboration Meeting, Kolkata, India, October 29, 2014
- **"Event-by-event particle multiplicity fluctuations in Pb-Pb collisions with ALICE"**
  Spring Meeting of Deutsche Physikalische Gesellschaft (DPG), Frankfurt, Germany, March 18, 2014
- **"Offline signal tail-correction for the ALICE TPC"**
  Spring Meeting of Deutsche Physikalische Gesellschaft (DPG), Dresden, Germany, March 3, 2013
- **"Drift velocity calibration with the laser system of the ALICE TPC"**
  Spring Meeting of Deutsche Physikalische Gesellschaft (DPG), Münster, Germany, March 21, 2011

Theses and Other Research Works Carried Out

- **"Online drift velocity calibration with the laser system of the ALICE-TPC"**
  Master Thesis, Goethe University, Frankfurt, Germany, 2011
- **"Introduction to the ALICE TPC and noise studies"**
  CERN Summer School Project, Geneva, Switzerland, 2008
- **"Integrability and Korteweg-de Vries (KdV) equation"**
  B.Sc. Thesis in Physics, Yıldız Technical University (YTU), Istanbul, Turkey, 2008
- **"Introduction to the module theory"**
  B.Sc. Thesis in Mathematics, Yıldız Technical University (YTU), Istanbul, Turkey, 2007

PROFESSIONAL EXPERIENCE

TPC detector expert in ALICE 2011-2014
As CERN user based at CERN, Geneva, Switzerland

- TPC Detector Operation
- Development of calibration algorithms for the ALICE TPC
- Code development for GOOFIE (Gas prOportional cOunter For drIfting Electrons)
- Investigation of electric field distortions using the Laser System of the TPC
- Junk event filtering; Online algorithm which detects extremely noisy events on the raw data level
- Simulation of the SAMPA readout chip for the TPC upgrade with GEM (Gas Electron Multiplier)

Master thesis project conducted at GSI Helmholtzzentrum 2010-2011
GSI Helmholtzzentrum für Schwerionenforschung, Darmstadt, Germany
Online Drift Velocity Calibration with the Laser System of the ALICE TPC

SCHOOLS AND COURSES

EDIT (Excellence in Detectors and Instrumentation Technologies) School 2015
INFN - Laboratori Nazionali di Frascati, Italy
CERN-Fermilab Hadron Collider Physics Summer School 2015
CERN, Geneva, Switzerland
Introductory Statistics School 2013
DESY, Hamburg, Germany
Soft Skill Course: Career and Leadership 2012
Imperial College London & Helmholtz Association
GridKa School 2011
Karlsruhe Institut of Technology (KIT), Karlsruhe, Germany
International School on Quark-Gluon-Plasma and Heavy Ion Collisions 2011
Torino, Italy
Soft Skill Course: Communication and Presentation Skills 2011
Imperial College London & Helmholtz Association
Soft Skill Course: Research Skills Development 2010
Imperial College London & Helmholtz Association
CERN Summer School 2008
Geneva, Switzerland
CIMPA Summer School ALS&S 2007
Galatasaray University, Istanbul, Turkey

TEACHING AND OUTREACH

Advanced Lab Course: Measuring the Lifetime of Cosmic Ray Muons 2013-2014
Goethe University, Frankfurt, Germany
Advanced Lab Course: Statistics 2010-2011
Goethe University, Frankfurt, Germany
CERN official guide 2012-present
CERN, Geneva, Switzerland
ALICE detector official guide 2012-present
CERN, Geneva, Switzerland

ASSOCIATIONS & AFFILIATIONS

H-QM Helmholtz Research School for Quark Matter Studies 2011-2017
Frankfurt, Germany
HGS-HIRe for FAIR, Helmholtz Graduate School for Hadron and Ion Research 2011-2017
Frankfurt, Germany
Member of DPG (German Physics Society) 2011-present

LANGUAGES

Turkish: *Mother tongue*
English: *Fluent*
German: *Intermediate-B1*

TECHNICAL SKILLS

OS: *Windows, Linux, Mac OS X*
Programming: *C/C++, Fortran, Java, ROOT, Aliroot, GARFIELD, Bash-Shell*